8-10-2015

Amylin Structure, Aggregation and Pancreatic β Cell Toxicity

Sharadrao Patil
University of Connecticut - Storrs, sharadrao.patil@uconn.edu

Amylin Structure, Aggregation, and Pancreatic β Cell Toxicity

Sharadrao Maruti Patil, PhD

University of Connecticut, 2015

In most type 2 diabetes patients, amyloid plaques have been found juxtaposed with membranes of pancreatic β-cells. These plaques are composed of amyloid fibrils of the 37 residue endocrine hormone amylin and cause distinct changes in cell membrane morphology associated with the destruction of β-cells. Research is still ongoing to identify the toxic species involved and the mechanisms by which mature fibrils or oligomers cause cytotoxicity. The projects undertaken were designed to study the molecular structural features of amylin, mechanism of amyloid aggregation and, to develop cytotoxicity inhibitors. We determined the structure of human amylin bound to SDS micelles using NMR. In this membrane mimetic environment amylin adopts an α- helix structure for residues 5-28, with a kink between residues 18 and 22. The last nine C-terminal residues are unfolded. Paramagnetic spin probe data suggest the segment between residues 5 and 17 is within the hydrophobic lipid environment while residues 20-29 remain at the lipid-solvent interface. Experimental techniques such as total internal reflection fluorescence microscopy, fluorescence assays and cytotoxicity assays were undertaken to study fibrillization and the effect of designed cytotoxicity inhibitors. Microscopy experiments demonstrate three types of aggregate growth processes: globular seed formation, unidirectional fibril elongation and fibril thickening. The three aggregation processes are suggestive of secondary nucleation mechanisms. Lastly, three amylin peptide analogs were designed to inhibit fibrillization via electrostatic charge repulsion. The three analogs fibrillize poorly on their own and inhibit fibril elongation of WT-amylin at physiological salt concentrations. The most effective inhibitor Arg-1, inhibits amylin fibrillization and cytotoxicity with a potency comparable to other types of fibrillization inhibitors described in the literature.

Amylin Structure, Aggregation, and Pancreatic β Cell Toxicity

Sharadrao Maruti Patil

B. Pharm., Shivaji University, 2003

MS, University of Massachusetts, 2007

A Dissertation

Submitted in Partial Fulfillment of the

Requirements for the Degree of

Doctor of Philosophy

at the

University of Connecticut

2015

APPROVAL PAGE

Doctor of Philosophy Dissertation

Amylin Structure, Aggregation, and Pancreatic β Cell Toxicity

Presented by

Sharadrao Maruti Patil, B. Pharm., MS

Major Advisor _____
Dr. Andrei Alexandrescu

Associate Advisor _____
Dr. Victoria Robinson

Associate Advisor _____
Dr. Nathan Alder

Associate Advisor _____
Dr. Olga Vinogradova

University of Connecticut

2015

ACKNOWLEDGEMENTS

I consider myself privileged to have been able to spend the past few years in graduate school at UCONN. To my advisor Dr. Andrei Alexandrescu- thank you for accepting me into your lab and giving me the opportunity to do research. I am grateful to you for supporting and mentoring me through these past years. To my committee members Dr. Victoria Robinson, Dr. Nathan Alder, Dr. Olga Vinogradova, and Dr. Eric May - thank you, not only for taking the time to attend my presentations and read my manuscripts but also for your support, guidance and helpful feedback.

I have had the pleasure of working with exceptional colleagues over the years- Dr. Robyn Croke, Dr. Suman Jha, Dr. Sarah Sheftic, Andrew Mehta, Jason Gibson and Fred Knolling. The knowledge I have gained from you is invaluable. Robyn Croke-I would especially like to thank you for being a patient teacher and showing me the ropes. Suman Jha- I am grateful to you for being a wonderful mentor and a close friend.

I would also like to thank Dr. Carol Norris, Dr. David Knecht for being patient with me during the initial stages of learning TIRF microscopy. Thanks to Geetali Pradhan and Gaurav Joshi for useful discussions on fluorescence microscopy and cell biology. Thanks to Dr. Vitaliy Gorbatyuk and Dr. Martha Morton for taking time to teach and help at every stage of my protein NMR learning experience. I would also like to thanks Dr. Marie Cantino and Stephen Daniels for all the help and making Electron Microscopy such an enjoyable and exciting experience.

I know I am incredibly blessed to have a family that has supported and encouraged me all along. To my parents- you are my inspiration. You taught me to always strive to do my best and that nothing would be impossible. I couldn't have done this without you and words cannot express my gratitude to you.

This thesis is dedicated to Dr. Ashok Cholli and Dr. Jayant Kumar for their support, encouragement and for giving me an opportunity to explore an exciting field of NMR.

Table of Contents

List of Tables

List of Figures

List of Publication

1. S.M. Patil, S. Xu, S.R. Sheftic, and A.T. Alexandrescu, Dynamic alpha-helix structure of micelle-bound human amylin, J. Biol. Chem., 284 (2009), 11982-11991.

2. S.M. Patil, A. Mehta, S. Jha, and A.T. Alexandrescu, Heterogeneous amylin fibril growth mechanisms imaged by total internal reflection fluorescence microscopy, Biochemistry, 50 (2011), 2808-2819.

3. S. Jha, S.M. Patil, J. Gibson, C.E. Nelson, N.N. Alder, and A.T. Alexandrescu, Mechanism of amylin fibrillization enhancement by heparin, J. Biol. Chem. 286 (2011) 22894-22904.

4. Croke, R. L., Patil, S. M., Quevreaux, J., Kendall, D. A. and Alexandrescu, A. T., NMR determination of pK_a values in α-synuclein. Protein Science, (2011), 20: 256–269.

5. Suman Jha, Jessica M. Snell, Sarah R. Sheftic, Sharadrao M. Patil, Stephen B. Daniels, Frederick W. Kolling, and Andrei T. Alexandrescu, pH Dependence of amylin fibrillization, Biochemistry, 53 (2014), (2), 300-310.

CHAPTER I: Introduction

Amyloids

Amyloid Diseases are characterized by fibrillar deposits of amyloidogenic proteins. Amyloid deposits are associated with some 30 diseases including Alzheimer's [1], Parkinson's [2], dialysis-related amyloidosis [3], type 2 diabetes [4], Huntington's Disease, systemic amyloidosis, and light-chain amyloidosis. Some amyloids have physiologically normal functions such as hormone storage [5] and bacterial biofilm formation [6]. The name amyloid comes from early mistaken identification of the substance as starch (Amylum) based on iodine staining techniques. Amyloids are formed by a variety of unrelated peptides & proteins but have similar morphologies by electron microscopy (Fig. 1.1A). The characteristic amyloid structures include long un-branched fibers of diameter 5-10 nm with a twist at about 100 nm along the growth axis. The characteristic property of amyloid is the green birefringence under polarizing microscope after binding to Congo Red dye. Amyloid deposits are found in a number of protein misfolding diseases characterized by fibrillar protein deposits, in which protein monomers form intermolecular β-sheets running along the length of the fibrils. Amyloid fibril growth shows typical nucleation kinetics. Amyloid fibrils are insoluble and are resistant to proteases and extreme treatments.

Amyloid aggregation is entropically disfavored until a critical nucleus is formed. In order to generate a long-range fibril like order in such structures, a critical number of molecules must be present such that the favorable enthaplic terms associated with their regular stacking can most effectively offset the accompanying loss of configurational entropy [7]. The effective peptide concentration, pH, and ionic strength also contribute towards such aggregation kinetics. Once a critical nucleus is formed aggregation is energetically favorable due to stable, and ordered fibrillar

structure formation. Initially a smaller number of nuclei are formed, this phase is called as "lag phase" and there is a delay before macro-aggregates (fibrils) are detected. Ones the nucleus is formed, fibril growth proceeds rapidly by further association of either monomers or oligomers with these nuclei. Protein monomer dissociation is more unfavorable at this stage and the monomer association with a growing surface and polymerization is close to irreversible. Fibrillization continues until the monomer concentration is sufficiently low. This stage is characterized as a plateau phase, where an apparent steady state is reached. The rate of fibril formation is governed by number of factors such as seeding which provides nucleation sites (surfaces for further aggregation) and eliminates the lag time. A typical amyloid fibrillization curve is shown below in Fig. 1.1B.

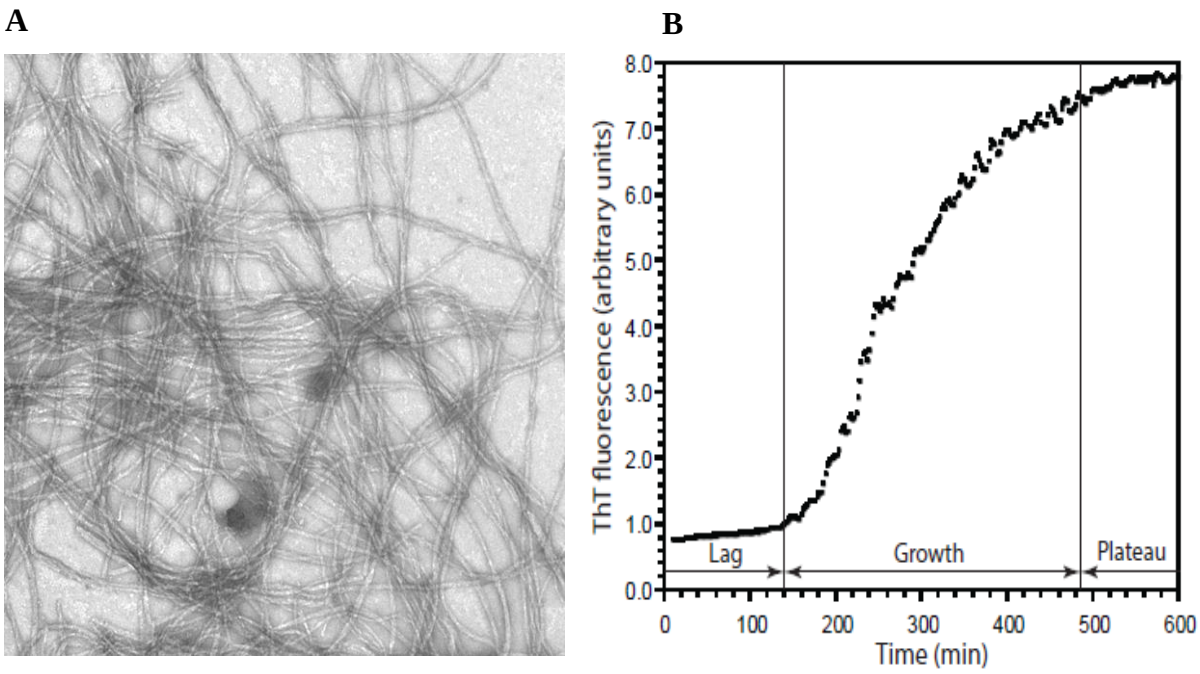

Figure 1.1 Amyloid fibrils and fibrillization kinetics. (A) Negatively stained electron microscopy image of amyloid fibrils. (B) Kinetic curve depicting a typical amyloid fibrillization (20 μM amylin in 20 mM phosphate buffer at pH 7.4, 2% Dimethyl sulfoxide (DMSO) and at 25 °C temperature).

Amyloid and Type 2 diabetes mellitus

Type 2 diabetes affects over 315 million people worldwide and is thought to cost upward of $250 billion dollars a year in the United States alone. One of the hallmarks of type 2 diabetes, found in 90% of patients, is the formation of extracellular amyloid aggregates composed of amylin. The endocrine hormone amylin also called as Islet Amyloid polypeptide (IAPP), appears to have key roles in diabetes pathology [8, 9]. The amyloids cause changes in the morphology of the pancreatic β-cells [8] and aggregates of amylin are toxic when added to cultures of β-cells, suggesting that the amyloid deposits found *in situ* may be responsible for β-cell death [10, 11]. In several transgenic mouse and rat models expression of human amylin has been found to correlate with β-cell apoptosis and diabetes-like symptoms [12], although considerable controversy remains on whether the fibrils themselves or smaller aggregates of amylin constitute the toxic species [13-16]. The amyloid deposits accumulate in the interstitial fluid between islet cells and are usually juxtaposed with the β-cell membranes[8]. Genetic evidence that indicates amylin is directly involved in pathology includes a familial S20G mutation that leads to early onset of the disease [17] and produces an amylin variant that aggregates more readily [18, 19].

Amylin is a 37 residue (~4 KDa) peptide hormone synthesized by the β-cells of the pancreas. It is involved in the metabolism of sugar and is secreted along with insulin. Amylin controls metabolic functions in concert with insulin by controlling glucose levels and gastric emptying. Amylin inhibits glucagon secretion and induces a feeling of satiety after a meal [8, 9]. After being expressed as pro-amylin in response to increased glucose concentrations, amylin undergoes post-translational modification inducing removal of 9 residues from the N-terminus and 19 residues from the C-terminus. Subsequently the C-terminus is enzymatically amidated and a

Cys 2-Cys 7 disulfide bond is formed. These post-translational modifications are necessary for the physiological activity of amylin. The amyloidogenic propensity of amylin also increases as it undergoes post-translational modifications [20]. The amino acid sequence of amylin after post-translational modifications is shown below.

NH_3-**KCNTATCATQ RLANFLVHSS NNFGAILSST NVGSNTY**-NH_2

In patients afflicted with type 2 diabetes, amylin is found in fibrillar deposits in the pancreas. These deposits are thought to be responsible for islet cell toxicity during type 2 diabetes progression. Under normal conditions amylin is synthesized and processed in the secretary granules and released along with insulin. Circulating amylin levels increase in a number of pathological conditions, including obesity, syndrome X, pancreatic cancer, and renal failure [20]. Normal human fasting amylin levels range from 1-10 pM, whereas post prandial levels increases to 5-20 pM. In obese insulin-resistant individuals amylin levels are reported up to 50-70 pM [21]. Amylin levels together with insulin are raised initially in type 2 diabetes but fall as the disease progresses to a stage where the pancreatic islets of Langerhans β-cells that synthesize amylin no longer function [8]. The concentration of amylin in the storage vesicles of β-pancreatic cells is much higher, where it is stored in concentrations of 0.1-4 mM together with insulin. At these high concentrations, aggregation may be prevented due to binding of amylin to insulin, or storage in the form of unprocessed 67 residue pro-peptide. The low pH of the storage granules (pH 5.5) as compared to the extracellular matrix (pH 7.4) may also slow down the aggregation of amylin, as studies from our lab and others have shown that amylin fibrillization is enhanced going from acidic to neutral pH [22, 23]. The schematic representation of the potential relationship of islet dysfunction, islet amyloid, and β-cell destruction in type 2 diabetes mellitus is shown in Fig. 1.2.

Autopsy studies of human pancreases obtained from type 2 diabetes patients show the presence of amyloid plaques in the interstitial spaces between β-cells in the islets of Langerhans and mature amylin is the major constituent of these plaques. The mechanism of amylin misfolding that leads to amyloid formation is still unclear and investigation of the structural properties of amylin during the early stages of fibrillization should clarify the pathway to fibrillar structure [24, 25]. Detailed structural models are available for Aβ [26] and αS [27] bound to SDS micelle mimetics of membranes. For amylin there were models of peptide fragments 1–19 [28], 20–29 [29], and 17–29 [30] bound to micelles but no structural model for the complete hormone was

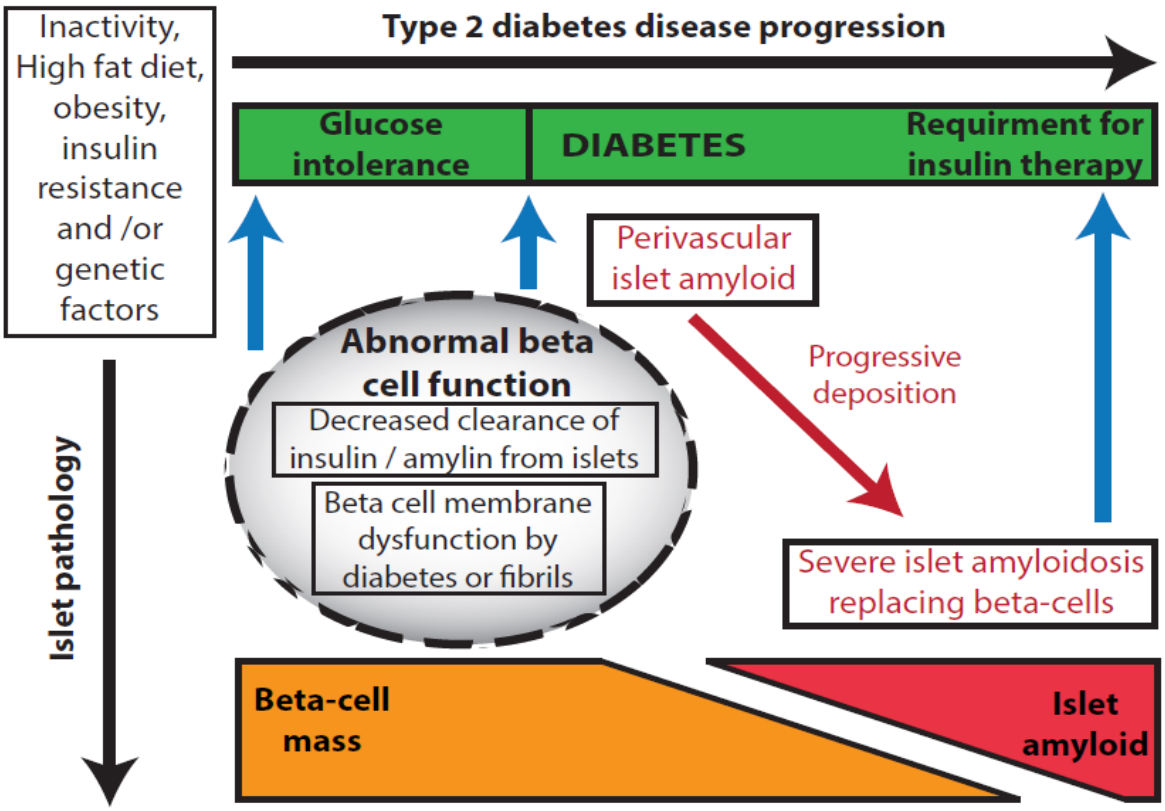

Figure 1.2 Schematic representation of the potential relationship of islet dysfunction, islet amyloid, and pancreatic β-cell destruction in the pathophysiology of type 2 diabetes mellitus (adapted from [31]).

available. This turns out to be particularly important as the interplay between structure and dynamics in amylin only comes to light when considering the whole molecule. In chapter II of my thesis I discuss the solution structure of human amylin bound to SDS micelles. The structural data is complemented with information on dynamics and data on the immersion of amylin into micelles.

Molecular structure data for amylin prompted our attention towards investigating amyloid fibrillization mechanics and the prevention of cytotoxicity. The projects focused on studying the fibrillization using fluorescence microscopy and spectroscopy along with the study of amyloid toxicity to mouse pancreatic cells. The application of fluorescence microscopy technique called total internal reflection fluorescence microscopy (TIRFM) to the study of individual amyloid fibrils was pioneered by the Goto lab who used the technique to study growth process of amyloid fibrils formed by the Alzheimer's disease peptide Aβ(1-40), glucagon, and β2-microglobilin a protein involved in kidney dialysis-related amyloidosis [32-36]. The pioneering studies of amyloid by TIRFM provided important information on the kinetics of individual fibril growth starting from seeds, and on the unidirectional polarity of fibril elongation which is consistent with an amyloid structure in which β-strands pair predominantly in parallel along the length of the fibril [34, 35]. Chapter III of the thesis describes the use of TIRFM to image the aggregation of amylin. Previous TIRFM studies of Aβ (1-40), glucagon, and β-microglobulin looked at fibril elongation starting from seeded solutions, that is mature fibrils were fragmented by sonication to provide nucleation sites for fibril growth [32, 34, 35]. Because amylin fibrillization is very fast, and because we wanted to examine the seeding processes, the reactions in our work were not seeded. Our data emphasize that amylin fibrillization proceeds through multiple mechanisms involving a mixture of fibril types, and emphasizes the importance of heterogeneous or secondary nucleation [32, 37-

39] in amylin aggregation.

Consideration of amyloid structures suggests that like-charges, replicated along the fibril axis by the intermolecular β-sheet pairing of monomers, should energetically disfavor self-association through electrostatic repulsion [40, 41]. Conversely, compensation of charges displayed on fibril surfaces may be important in the interactions of amyloids with polyanions such as heparan sulfate proteoglycans and membrane lipid bilayers [40, 42, 43]. Replacements of single charged residues can have large effects on fibrillization kinetics as shown with amyloid-beta[41], α-synuclein [44, 45], and amylin[46]. Amylin represents a particularly favorable system for investigating the roles of electrostatic charges in fibrillization, since the core of the intermolecular β-sheet fibril structure has only His18 as pH-titratable group. Introduction of single charged amino acids in the portion of the amylin sequence that forms the fibril core has been shown to markedly inhibit fibrillization [46].

We therefore thought to exploit the property of electrostatic repulsion by designing peptide variants that incorporate a string of residues with like charges into the amylin sequence. The designed peptide Arginine-variant 1 (Arg-1), substitutes four arginines for WT-amylin residues Asn14-Val17. The second analog, Arginine-variant 2 (Arg-2), substitutes four arginine residues for residues Phe23-Ile26 in the center of the amyloidogenic segment. A third peptide, the Membrane Trojan analog (Mem-T) was conceived as an inhibitor of the interactions of WT-amylin with cell membranes, rather than as a fibril elongation inhibitor. Chapter IV of the thesis examines the ability of the designed amylin analogs Arg-1, Arg-2 and Mem-T to form fibrils using a kinetic assay that employs the amyloid-specific fluorescent dye thioflavin T (ThT), and by imaging the reaction products with transmission electron microscopy (TEM). We investigated the ability of

peptide analogs to inhibit fibril formation when added in *trans* to WT-amylin, and characterized the concentration dependence of inhibition. We also investigated the ability of the above mentioned peptide inhibitors to inhibit fibrillization and in turn suppress cytotoxicity towards a mouse model of β-pancreatic cells when challenged with WT-amylin.

The projects undertaken successfully address the gaps between previous research on amylin in relation to type 2 diabetes. The NMR structure of amylin in presence of SDS micelle provides an insight into the peptide membrane interactions of the full length amylin peptide. The detailed molecular level study of possible amylin-membrane interaction could be significant in order to derive the possible membrane oligomer structures and fibril nucleation processes. The earlier studies of amyloids using TIRFM has provided an important information on kinetics of individual fibril growth starting from a seed. The TIRFM studies from our lab investigated the kinetics of individual fibril growth started without the initial seeding processes. Therefore, our microscopy study provides a real-time images of the fibril nucleation and the initial seed formation along with the effect of charge on the kinetics of fibril formation. In the concluding project, we designed amyloid cytotoxicity inhibitors and the results represent a new electrostatic-based approach to inhibit amyloid fibrillization and toxicity. The results point towards the possibility of rational design of more potent amyloid inhibitors.

CHAPTER II: NMR Structure of Micelle-bound Human Amylin

Excerpted from: S.M. Patil, S. Xu, S.R. Sheftic, and A.T. Alexandrescu, Dynamic alpha-helix structure of micelle-bound human amylin, J. Biol. Chem. 284 (2009), 11982-11991.

Abstract

To better understand the structural basis for the interactions between amylin and membranes, we determined the NMR structure of human amylin bound to membrane mimetic SDS micelles. The first four residues in the structure are constrained to form a hairpin loop by the single disulfide bond in amylin. The last nine residues near the C terminus are unfolded. The core of the structure is an α-helix that runs from about residues 5-28. A distortion or kink near residues 18-22 introduces pliancy in the angle between the N- and C-terminal segments of the α-helix. Mobility, as determined by ^{15}N relaxation experiments, increases from the N to the C terminus and is strongly correlated with the accessibility of the polypeptide to spin probes in the solution phase. The spin probe data suggest that the segment between residues 5 and 17 is positioned within the hydrophobic lipid environment, whereas the amyloidogenic segment between residues 20 and 29 is at the interface between the lipid and solvent. This orientation may direct the aggregation of amylin on membranes, whereas coupling between the two segments may mediate the transition to a toxic structure.

Introduction

A recurrent theme for amyloidogenic proteins is that toxicity appears to be exerted through membrane-bound oligomers that form pores and disrupt ion balance across membranes [7, 9, 47-49]. Experimental evidence for such oligomers has been found for the amyloid-β (Aβ) peptides [50], which cause Alzheimer disease, and for α-Synuclein (αS), the protein involved in Parkinson disease [51]. The similar toxic effects exerted by these amyloidogenic molecules may have a common structural and physical basis. Detailed structural models were available for Aβ [26] and αS [27] bound to SDS micelle mimetics of membranes. For amylin there were models of peptide fragments 1–19 [28], 20–29 [29], and 17–29 [30] bound to micelles but as of yet no model of the complete hormone. This was particularly important because the interplay between structure and dynamics in amylin only comes to light when considering the whole molecule. The solution structure of human amylin bound to SDS micelles is described in this chapter. The structure is complemented with information on dynamics and he data on immersion of amylin into micelles.

Materials and Methods

Materials - Recombinant human amylin (0.5 mg, lot number 718071NAM) and ^{15}N-amylin (1 g, lot number 70507) were from rPeptide (Bogart, GA). The peptides were expressed in *Escherichia coli* and differ from human amylin by not having an amidated C-terminus. SDS (electrophoresis grade) was from Bio-Rad. D_2O, d_{25}-SDS, d_4-acetic acid, d_6-methanol, $MnCl_2$, and 16-doxyl-stearic acid were from Aldrich.

NMR Sample Preparation - 1 mg of ^{15}N-amylin was used for all heteronuclear NMR studies. Sample 1 was prepared by taking up 0.5 mg of lyophilized ^{15}N-amylin powder in a 0.25 ml 90% H_2O, 10% D_2O solution of 100 mM d_{25}-SDS, 60 mM acetic acid, pH 4.6, to give a final amylin

concentration of 0.5 mM. Sample 1 was used for NMR assignments, structure determination and relaxation studies. Sample 2 was prepared by dissolving 0.5 mg of amylin into 0.66 ml of the solution described above to give a final concentration of 0.2 mM. Sample 2 was divided into aliquots and used for the paramagnetic quenching studies with Mn^{2+} and 16-doxyl-stearate. Sample 3 was prepared by dissolving 0.5 mg of amylin at natural isotope abundance in 99.96% D_2O containing 100 mM SDS, and 60 mM d_4-acetate, pH 4.2. An internal 2,2-dimethyl-2-silapentane-5-sulfonate standard was used for chemical shift referencing.

NMR Spectroscopy - All NMR experiments were done on a 600-MHz Varian Inova spectrometer equipped with a cryogenic probe. Pulse programs were implemented from the Varian ProteinPack. A temperature of 37 °C was used for all experiments. NMR assignments were based on three-dimensional HNHA, HNHB, TOCSY-HSQC (70-ms mixing time), and NOESY-HSQC (100- and 200-ms mixing times) experiments. Spin systems were first grouped by amino acid type using through-bond scalar connectivities. Sequence-specific assignments were then made using dαN and dNN sequential walks [52] using NOESY-HSQC data. Stereospecific assignments for glycine methylene hydrogens were obtained from an HNHB spectrum as described in the literature [53]. Stereospecific assignments for side chain β-methylene hydrogens were made based on qualitative comparisons of the relative sizes of $^3J_{NH\alpha}$ couplings in HNHB spectra [54] and intraresidue HN-Hβ and Hα-Hβ NOEs in short mixing time NOESY experiments [55]. Assignments for micelle-bound amylin have been deposited with the BMRB under accession number 16105.

Structure Determination - A summary of the restraints used to calculate the NMR structures of micelle-bound amylin and of the statistics relating to the qualities of the structures is given in Table 2.1. Distance restraints were grouped into four ranges (strong 1.8–2.7, medium 1.8–3.5, weak 1.8–

5.0, and very weak 1.8–5.5 Å) based on the intensities of cross-peaks in the NOESY spectra. Backbone ϕ angle dihedral restraints of -60 ± 30° were included for 22 residues with $^{3}J_{HNH\alpha}$ couplings [56] smaller than 6 Hz. Side chain χ1 restraints were included for eight residues based on HNHB coupling data and NOE data from short mixing time NOESY experiments [55]. Standard α-helix hydrogen bond restraints were included for 17 residues with $^{3}J_{HNH\alpha}$ couplings and Hα secondary shifts in the α-helix range. Of the 17 residues, 8 could be identified in one-dimensional ^{1}H NMR spectra as experiencing hydrogen exchange protection for up to 30 min when amylin was dissolved in d_{25}-SDS micelles suspended in D_2O (Thr-9, Gln-10, Leu-12, Ala-13, Leu-16, Leu-27, Ile-26, and Ser-20). For the remaining 9 residues, spectral crowding precluded unambiguous information on exchange protection in one-dimensional spectra. We calculated control structures with hydrogen bond restraints included for only the 8 amides unambiguously protected. These structures showed slightly decreased precision (the backbone r.m.s.d. increased from 1.4 to 1.7 Å for residues 6–27 and from 0.4 to 0.5 Å for residues 6–17). Despite the lower precision, there were no systematic changes in structure, and the NMR ensemble calculated with the full complement of hydrogen bonds fell within the breadth of the conformational ensemble calculated with less hydrogen bonds. We feel that the inclusion of all 17 hydrogen bond restraints is justified by the NOE and $^{3}J_{HNH\alpha}$ coupling data that support hydrogen-bonded α-helical structures for the residues in question, and by the consistency of the hydrogen bonds with preliminary structures calculated without these restraints. The final NMR structure calculations started from 500 conformations with randomized ϕ, ψ angles. Structures were calculated with the program X-PLOR (version 3.851) [57] according to a published protocol [58]. The 30 lowest energy structures with no distance violations greater than 0.3 Å or dihedral violations greater than 3° were kept for

analyses. The coordinates were deposited with the Protein Data Bank accession code 2KB8.

^{15}N Relaxation Studies of Amylin Dynamics - ^{15}N relaxation data were obtained using ^{1}H-^{15}N correlation experiments from the Varian Protein Pack based on published methods [59]. Longitudinal relaxation data were obtained from eight spectra collected with T_1 relaxation periods of 20, 50, 130, 210, 310, 500, 700, and 1000 ms. To measure time constants for transverse relaxation, eight T_2 relaxation periods of 10, 30, 50, 70, 90, 110, 150, and 190 ms were used. Pre-acquisition delays of 2 s were used between transients. T_1 and T_2 values were determined from nonlinear least squares fits of the intensity decay as a function of relaxation period to Equation 2.1,

$$I = I_0 \cdot \exp(-\tau/T_{1,2}) \qquad \text{(Eq. 2.1)}$$

Where, I is the intensity for relaxation period τ; I_0 is the initial amplitude; and $T_{1,2}$ is the time constant for either T_1 or T_2 relaxation. Uncertainties in the T_1 and T_2 values were taken as the standard errors of the fits. ^{1}H-^{15}N NOE values were calculated as the ratio of intensities in an experiment recorded with proton saturation for 4 s to a control experiment where the saturation period was replaced with an equivalent 4-s delay as shown in Equation 2.2,

$$\text{NOE} = I(s)/I(c) \qquad \text{(Eq. 2.2)}$$

Uncertainties in the NOE values were calculated as shown in Equation 2.3,

$$\sigma\,\text{NOE} = I(s)/I(c)\sqrt{\left(\frac{\Delta I(s)}{I(s)}\right)^2 + \left(\frac{\Delta I(c)}{I(c)}\right)^2} \qquad \text{(Eq. 2.3)}$$

where, $\Delta I(s)$ and $\Delta I(c)$ indicate the root mean square base-line noise in the spectra with and without saturation [60].

Table 2.1 Statistics for the 30 best micelle-bound amylin structures[a].

NMR Restraints (total)				341
Distance (total)				311
Intraresidue				34
Sequential (|i-j| = 1)				129
Short Range (1 < |i-j| < 5)				113
Long Range (5 ≤ |i-j|)				1
Hydrogen bonds (17*2)				34
Dihedral (total)				30
(ϕ angle)				22
(c1 angle)				8
Residual restraint violations [b]				
Distance (Å)				0.044 ± 0.005
Dihedral (°)				0.73 ± 0.16
RMS deviations from ideal geometry				
Bonds (Å)				0.0034 ± 0.0003
Angles (°)				0.71 ± 0.02
Improper torsions (°)				0.55 ± 0.03
Non-bonded energies (kJ/mol)				
Van der Waals energy [b]				28 ± 6
Lennard-Jones energy [c]				1 ± 12
Ramachandran regions	favored	allowed	gen. allowed	disallowed
residues 1-37	69.7 %	20.6 %	7.2 %	2.4 %
residues 6-27	95.5 %	4.5 %	0.0%	0.0%
Coordinate precision rmsd (Å)				
NMR ensemble to average			Cα, C, N	all heavy
residues 1-37			3.66 ± 0.76	4.29 ± 0.80
residues 6-27			1.36 ± 0.45	1.80 ± 0.42
residues 6-17			0.40 ± 0.14	1.00 ± 0.19
residues 18-27			0.77 ± 0.23	1.33 ± 0.32

[a] Values are reported as the means over the final 30 structures ± 1 s.d. These final lowest-energy structures had no NOE violations greater than 0.3 Å or dihedral violations greater than 3°.

[b] The energy was calculated using the X-PLOR [57] F_{repel} function with van der Waals interactions and atomic radii set to 0.8 times their CHARMM values [61].

[c] Calculated using the CHARMM empirical energy function [61].

S^2 order parameters describing the amplitudes of internal motions [62] were calculated with the program TENSOR 2.0 [63] assuming isotropic rotational diffusion [27] for the amylin-micelle complex. To obtain a value for the global correlation time for rotational diffusion, we restricted our analysis to residues 5–17, which had ^{1}H-^{15}N NOE values greater than 0.55, $^3J_{HNH\alpha}$ couplings smaller than 6 Hz, and Hβ chemical shifts consistent with stable α-helix structure. Using this subset of residues, we obtained a correlation time of 6.7 ns for global tumbling, which was used to calculate S^2 values for individual residues.

Paramagnetic Studies of Amylin Positioning in SDS Micelles - Separate experiments on 0.2 mM amylin in 100 mM SDS were performed with 16-doxyl-stearate and $MnCl_2$. 16-Doxyl-stearate was prepared as a 100 mM stock solution in d_6-methanol. The stock solution was used to bring the concentration of sample 2, to 1.85 mM in 16-doxyl-stearate. The aggregation number of SDS micelles is about 60 [64], so that a 100 mM SDS solution corresponds to a micelle concentration of 1.85 mM, or 1 spin probe per micelle. In a second experiment the concentration of 16-doxyl-stearate was raised to 9.2 mM corresponding to five spin probes per micelle. Experiments with paramagnetic Mn^{2+} were done at concentrations of 0.2 and 1 mM $MnCl_2$, corresponding to ratios of 1:1 and 5:1 of the paramagnetic ion to amylin. ^{1}H-^{15}N HSQC spectra were used to measure paramagnetic quenching. For each experiment a separate control experiment was recorded to obtain cross-peak intensities in the absence of paramagnetic agents.

CD Spectroscopy - Circular dichroism experiments were carried out on an Applied Photophysics II*-180 instrument with samples maintained at a temperature of 37 °C. Far-UV wavelength scans from 280 to 180 nm were collected on 250 μL volume samples held in a 1-mm path length cuvette. The samples contained 35 μM amylin in 60 mM acetic acid, pH 4.6, and varying concentrations of SDS.

Results

Amylin Adopts an α-Helical Structure in the Presence of SDS Micelles - Although human amylin forms fibrils rapidly in water [23], it is soluble and stable for at least 2 months in 100 mM SDS at an acidic pH of 4.6. The ^{1}H-^{15}N HSQC spectrum of amylin under these conditions is shown in Fig. 2.1.

Fig. 2.2*A* shows CD spectra of amylin with increasing concentrations of SDS at pH 4.6. In the absence of SDS, the CD spectrum of amylin looks roughly like that for an unfolded protein. Weak minima at 208 and 222 nm together with the lack of a pronounced minimum at 195 nm, however, are more indicative of a mixture of random coil and nascent α-helix conformations. The nascent α-helix structure in the absence of SDS probably corresponds to that characterized in detail by NMR for unfolded rat amylin [65]. In the presence of 5 mM SDS, there is already significant α-helix structure in the peptide. Under the conditions of our study (37 °C, pH 4.6), the critical micelle concentration of SDS in acetate buffer is about 2 mM. As the SDS concentration is raised from 5 to 10 mM, the amount of α-helix structure starts to plateau (Fig. 2.2*A*), and there are only small further changes in the CD spectrum between 10 and 100 mM SDS (Fig. 2.2*A*). We chose 100 mM SDS for our studies because this value corresponds to a micelle concentration of ~2 mM (the number of SDS molecules per micelle is expected to be ~60). Compared with the 0.5 mM amylin concentration, 100 mM SDS ensures an excess of micelles to peptide so that each micelle should have only one molecule of amylin bound. Pulse-field gradient NMR experiments [66] give a diffusion constant for amylin in complex with SDS that within experimental error was the same as that obtained for the complex formed between SDS and Aβ-(1–40), a 40-residue peptide of similar size to the 37-residue amylin ($D^{\text{amylin}}/D^{\text{A}\beta}$ 0.99 ±0.06). This observation suggests that

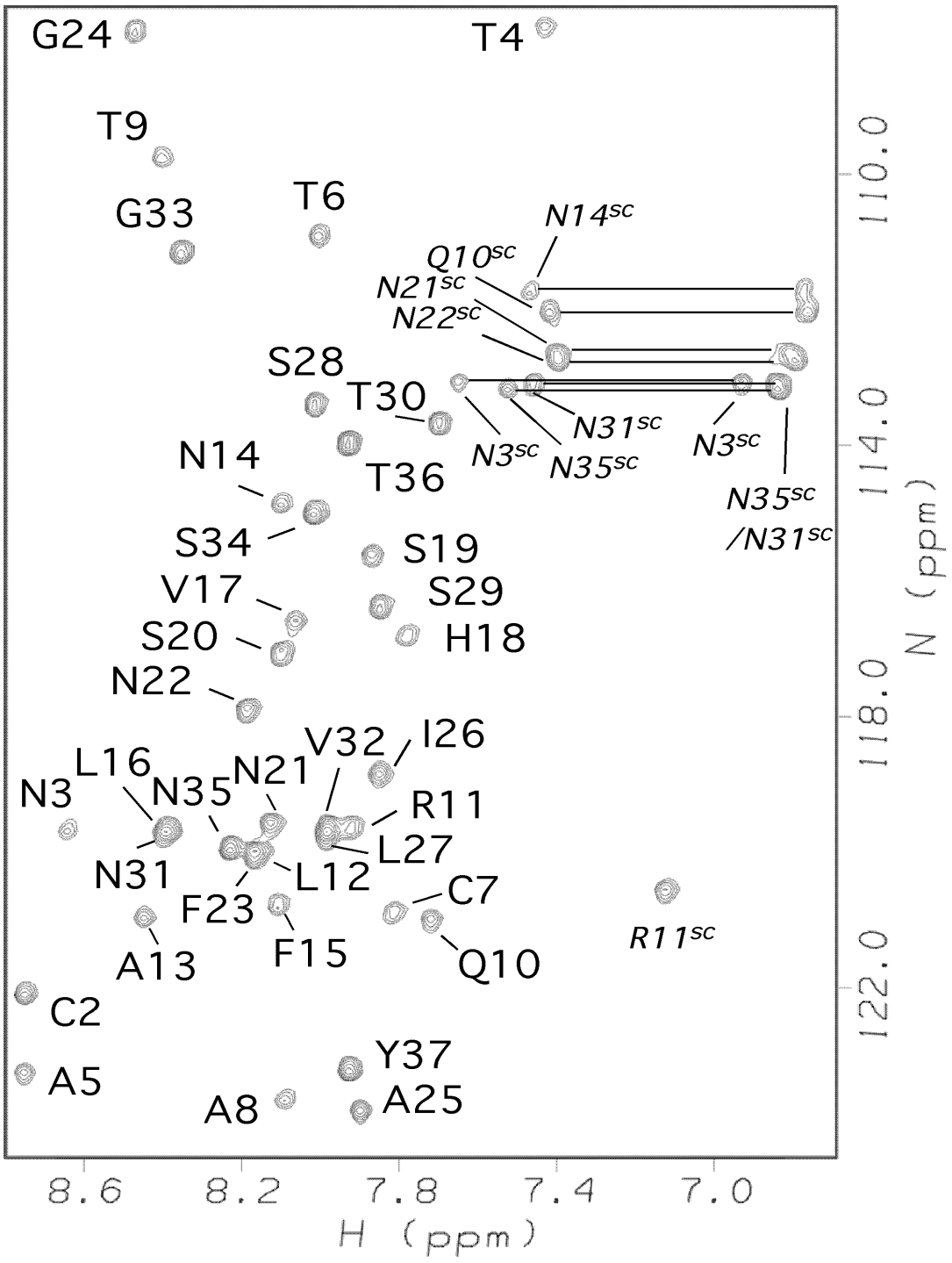

Figure 2.1 ^{1}H-^{15}N HSQC spectrum of micelle-bound amylin annotated with backbone NMR assignments. Side-chain correlations are indicated with the superscript 'SC'. Conditions: 0.5 mM ^{15}N-amylin, 100 mM SDS, 60 mM acetate, pH 4.6, 37 ^{o}C.

like Aβ [67], amylin binds to micelles as a monomer at the large 100 mM SDS concentration used for this study. In addition to work at pH 4.6, we also obtained CD data at pH 10.8 in the presence of SDS. His-18, the only side chain in amylin that titrates in the physiological range, should lose its positive charge between pH 4.6 and 10.8. The CD spectrum between 200 to 280 nm showed very little difference between the two pH values. In the 180–200 nm range, the spectrum at pH 10.8 lacked the large positive band associated with α-helix structure and was noisier, possibly due to light scattering caused by increased aggregation at pH 10.8.

Fig. 2.2*B* shows the sequence profile of $^{3}J_{\mathrm{HNH\alpha}}$ couplings calculated from an HNHA experiment [56]. Couplings below 6 Hz indicative of ϕ dihedral angles in the α-helix range occur for all residues between 5 and 28, except 18 and 22. On average the group of couplings between residues 5 and 17 is smaller than that for residues 23–28. Fig. 2*C* shows the difference between random coil values [68] and the Hα chemical shifts of amylin. The secondary shifts for the region between residues 5 and 28 are positive, typical of α-helix structure. The secondary shifts show a periodicity of 3–4 residues, also consistent with α-helix structure [69, 70]. Periodicity is also observed for the HN chemical shifts (Fig. 2.2*D*), and this type of periodicity has been attributed to α-helix curvature [71, 72]. The secondary Hα shifts, which are the most sensitive to secondary structure, appear to be on a gradient decreasing from residues 8 to 28 (Fig. 2.2*C*). The data suggest a higher stability for α-helix structure in the N-terminal half of amylin. Fig. 2.2*E* summarizes the short range NOEs observed for amylin. The NOEs are indicative of α-helix structure. There is a break in the pattern near residues 18-22, consistent with a discontinuity in the α-helix structure. Although there is overlap of HN chemical shifts within this segment (Fig. 2.1) that precludes the detection of HN-HN NOEs, other types of NOEs predicted for an α-helix structure such as

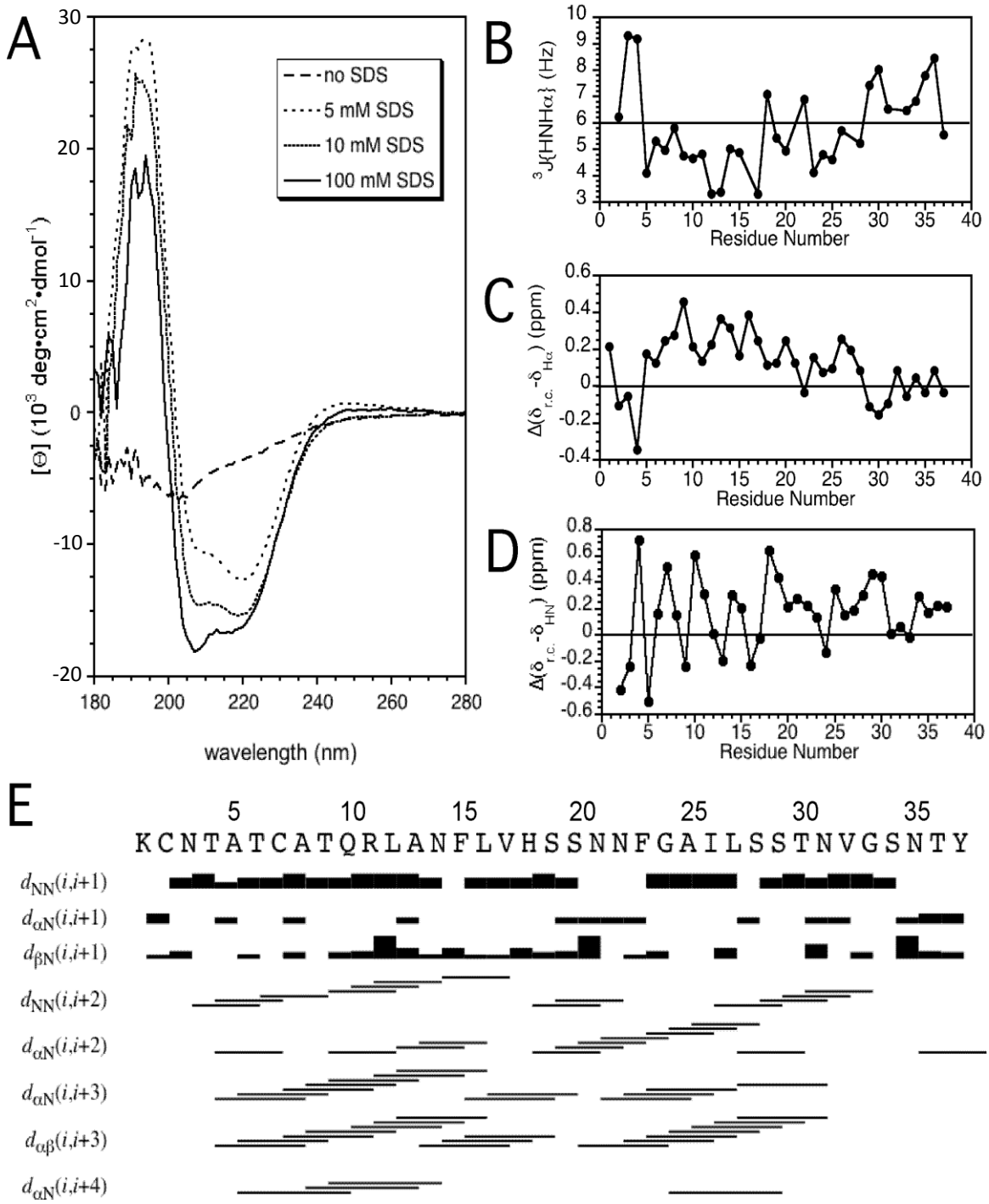

Figure 2.2 Data illustrating the α-helix structure of micelle-bound amylin. (A) CD spectra of amylin at 0, 5, 10, and 100 mM concentrations of SDS. (B) $^{3}J_{HNH\alpha}$ couplings obtained from a 3D HNHA experiment. (C) Secondary Hα chemical shifts calculated as the difference between micelle-bound amylin and 'random coil' values [68]. (D) Periodicity of HN chemical shifts illustrated as the difference from 'random coil' values [68]. (E) Summary of short-range NOEs.

dαN(*i*,*i*+3), dαN(*i*, *i* + 4), and dαβ(*i*, *i* + 3) are weak or missing. Moreover between residues 5 and 28, His-18 and Asn-22 are the only two sites with $^{3}J_{HNH\alpha}$ values above 6 Hz, consistent with a departure from α-helix structure in this segment. Although not apparent in the semi-quantitative plot (Fig. 2.2*E*), α-helix NOEs are weaker for the 22-28-residue segment compared with the 5-17-residue segment.

NMR Solution Structure of Micelle-bound Amylin - The NMR structure of amylin is shown in Fig. 2.3. Information on experimental restraints used to calculate the NMR structure ensemble and parameters related to the quality of the structures are given in Table 2.1. At the N-terminus, residues1-4 are constrained to a hairpin topology by a disulfide bond between Cys-2 and Cys-7. The Cys-7 part of the disulfide is in the α-helix and is ordered, giving a nonaveraged side chain χ1 of -60°. The Cys-2 residue is disordered. The last 8 residues between Thr-30 and Tyr-37 are also disordered. The core of the structure consists of an α-helix running from residues 5 to 28. Most of the members of the NMR ensemble have a kink or bend in the α-helix between residues 18 and 22. When the NMR ensemble is superposed on the mean backbone coordinates of the entire α-helix (residues 6-27), the resulting root mean square deviation (r.m.s.d.) of 1.4 Å is rather large (Fig. 2.3*A* and Table 2.1). Consequently, we did a systematic search for residue ranges that would improve the r.m.s.d., and we found that the precision of the structure improves if the segments 6-17 (Fig. 2.3*B*) and 18-27 (Fig. 2.3*C*) are considered separately. Leaving out segment 18-22 did not improve the fit significantly compared with that obtained for residues 6-27. This indicates that the poor r.m.s.d. when the whole helix is considered is because of an uncoupling of the relative orientations of the 6-17- and 18-27-residue segments rather than disorder in the middle of the helix. We used the MolMol program [73] to calculate a value of 30 ±18° for the inter-helical angle between segments 6-17 and 18-27.

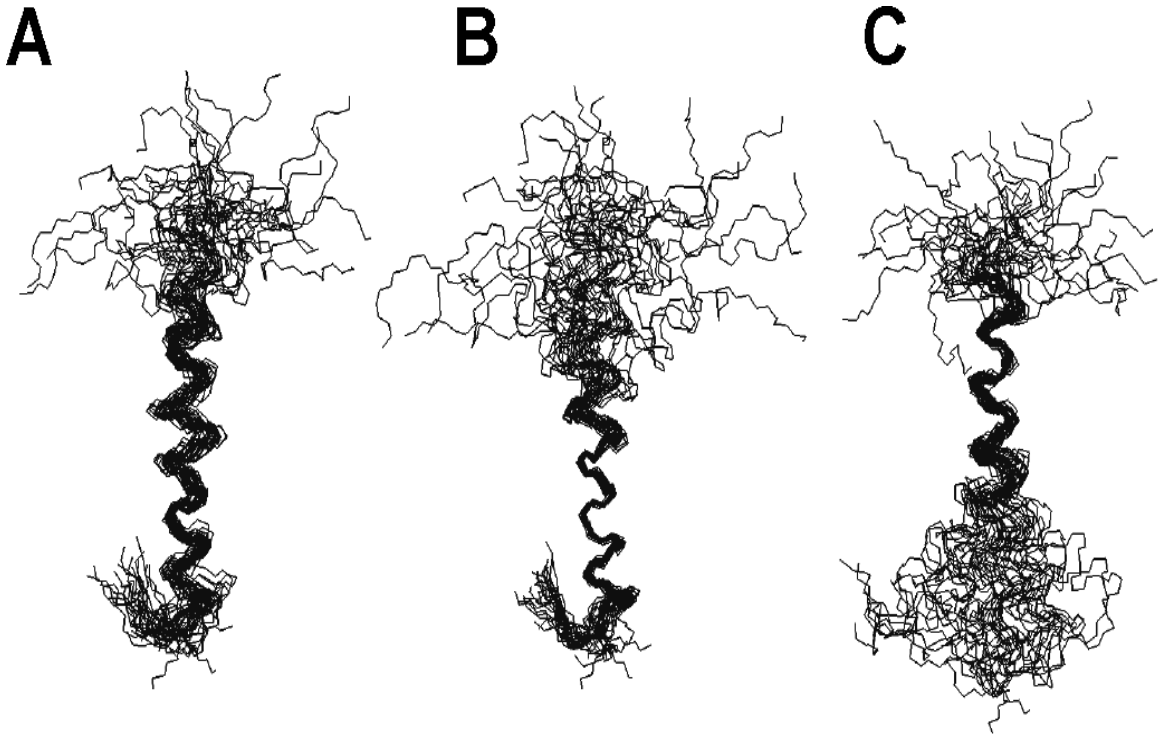

D

	6 - 27	6 - 17	18 - 27	
1	11	21	31	
KCNTATCATQ	RLANFLVHSS	NNFGAILSST	NVGSNTY	human
KCNTATCATQ	RLANFLIRSS	NNLGAILSPT	NVGSNTY	cat
KCNTATCATQ	RLANFLVRTS	NNLGAILSPT	NVGSNTY	dog
KCNTATCATQ	RLANFLVHSN	NNLGPVLSPT	NVGSNTY	hamster
KCNTATCATQ	RLANFLVRSS	NNLGPVLPPT	NVGSNTY	rat/mouse
KCNTATCVTQ	RLADFLVRSS	SNIGAIYSPT	NVGSNTY	Chicken
KCNTATCATQ	RLTNFLVRSS	HNLGAALPPT	KVGSNTY	Degu/Guinea pig
KCNTVTCATQ	RLANFLIHSS	NNFGAIFSPP	SVGS	Rabbit
KCNTATCVTQ	RLADFLVRSS	NTIGTVYAPT	NVGSATY	Green Puffer
KCGTATCETQ	RLANFLAPSS	NKLGAIFSPT	KMGSNTY	Cow

Figure 2.3 NMR structure of micelle-bound amylin and sequence conservation relative to the human protein. (A) Ensemble of the 30 best NMR structures overlaid on the mean Cα, N, and C' backbone atom coordinates of residues 6 to 27. (B) Structures fitted to the backbone mean of residues 6 to 17. (C) Structures fitted to the backbone mean of residues 18 to 27. (D) Sequences of the 10 closest homologs of human amylin obtained from a BLAST [74] search against the Swiss-Prot [75] database. Residues that differ with respect to the human sequence are shown in inverse type.

The organization of the micelle-bound amylin structure into subdomains is reminiscent of that seen with αS and the Alzheimer Aβ-(1- 40) peptide. In the presence of SDS micelles αS folds into an α-helix hairpin structure [27, 76]. The Aβ-(1– 40) peptide when bound to SDS micelles adopts an α-helical structure with a kink between residues 26 and 28 [26]. The two helical segments 15-24 and 28-36, flanking the kink superpose well individually but have different orientations relative to each other with an inter-helical angle of 48 ±15° [26].

Generally the kinks in micelle bound structure correspond with locations of turns adopted by these proteins in amyloid fibril structure[77]. Of the two α-helix segments, residues 6-17 gave a more precise structure than residues 18-27 (Fig. 2.3, *B* and *C*, and Table 2.1). This is consistent with the magnitudes of the $^{3}J_{\mathrm{HNH}\alpha}$ couplings (Fig. 2.2*B*) and Hα secondary shifts (Fig. 2.2*C*), which suggest the α-helix structure is more stable in the 6–17-residue segment. As described below, micelle-bound amylin shows a gradient of backbone dynamics, with the 6-17-residue segment corresponding to the least flexible part of the polypeptide chain. The structural precision and dynamics of micelle-bound amylin correlate with the amino acid sequence conservation in amylin homologues. Fig. 2.3*D* shows the sequences of the 10 closest homologues of human amylin identified in a BLAST search [74] against the Swiss-Prot data base [75]. The N-terminal half of amylin, which has the highest avidity for membranes [78], shows the highest sequence conservation. The C-terminal part of amylin, which in human amylin is the most amyloidogenic [78, 79], has the lowest sequence conservation.

Dynamic Properties of Micelle-bound Amylin - Fig. 2.4 shows ^{15}N relaxation data for micelle-bound amylin. The experimental relaxation parameters T_1 (Fig. 2.4*A*), T_2 (Fig. 2.4*B*), and the ^{1}H-^{15}N NOE (Fig. 2.4*C*) suggest a gradient of increasing flexibility from the N- to the C-terminus.

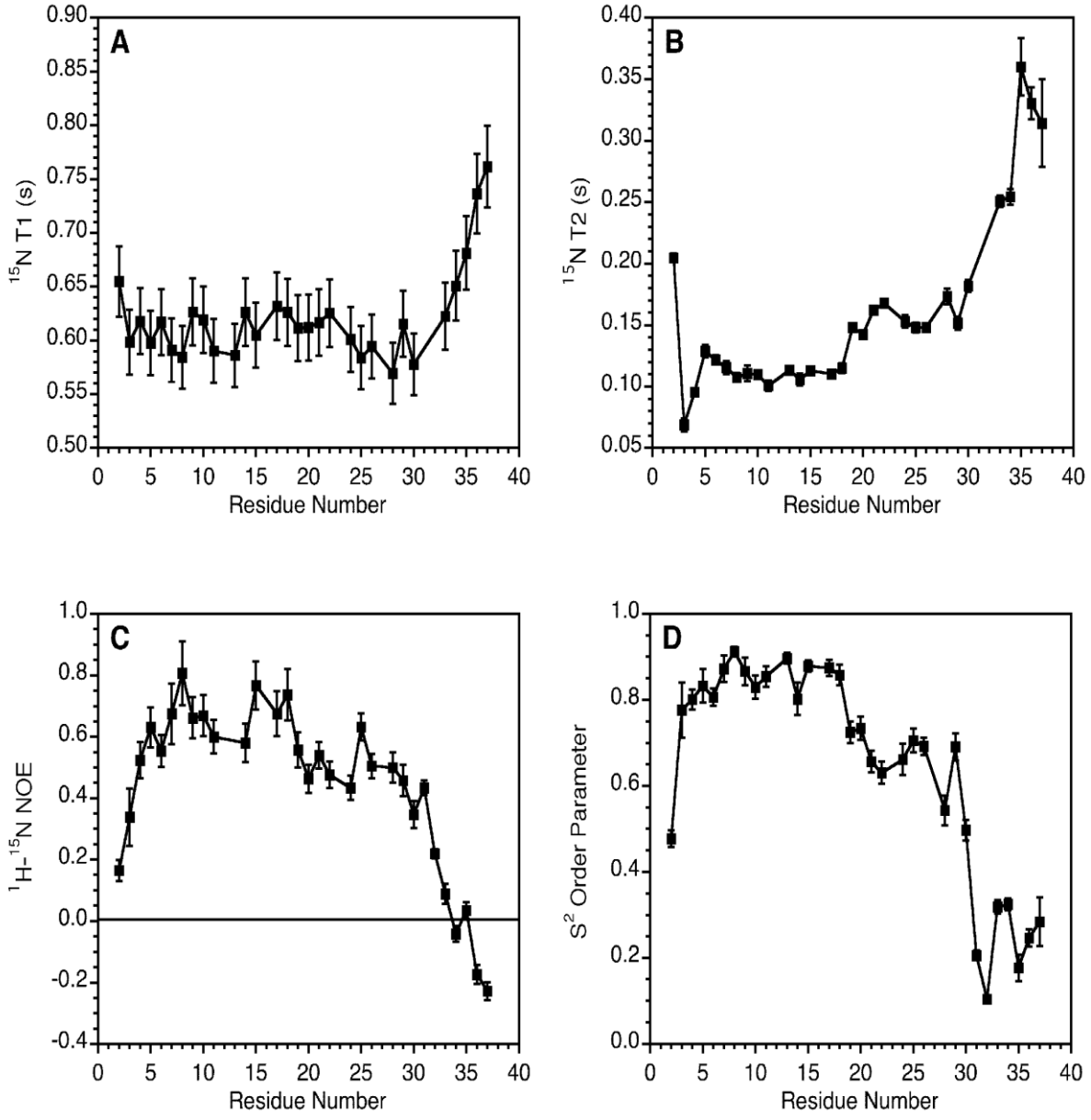

Figure 2.4 Dynamics of micelle-bound amylin (A) ^{15}N T_1 values. (B) ^{15}N T_2 values. (C) ^{1}H-^{15}N NOEs. (D) S^2 order parameters calculated [63] from ^{15}N relaxation data using an isotropic model of rotational diffusion for the amylin-micelle complex. Errors in S^2 values were calculated with the TENSOR program [63] using 100 Monte Carlo simulations to probe the uncertainty in internal mobility due to errors in the experimental relaxation data.

Calculations to obtain a correlation time for global rotational diffusion were done with the program TENSOR 2.0 [63] using data for the least flexible segment between residues 5 and 17. The calculations assuming isotropic tumbling since, amylin is bound to a roughly spherical micelle

[27], gave a global correlation time of 6.7 ns. For comparison, free SDS micelles have a correlation time of ~5.5 ns at 35 °C [80], and the correlation time of a complex formed between SDS micelles and a 22-residue peptide similar in size to the 37-residue amylin was 6.6 ns [81]. Although the agreement observed is good, we note that the correlation time of SDS micelles depends on a

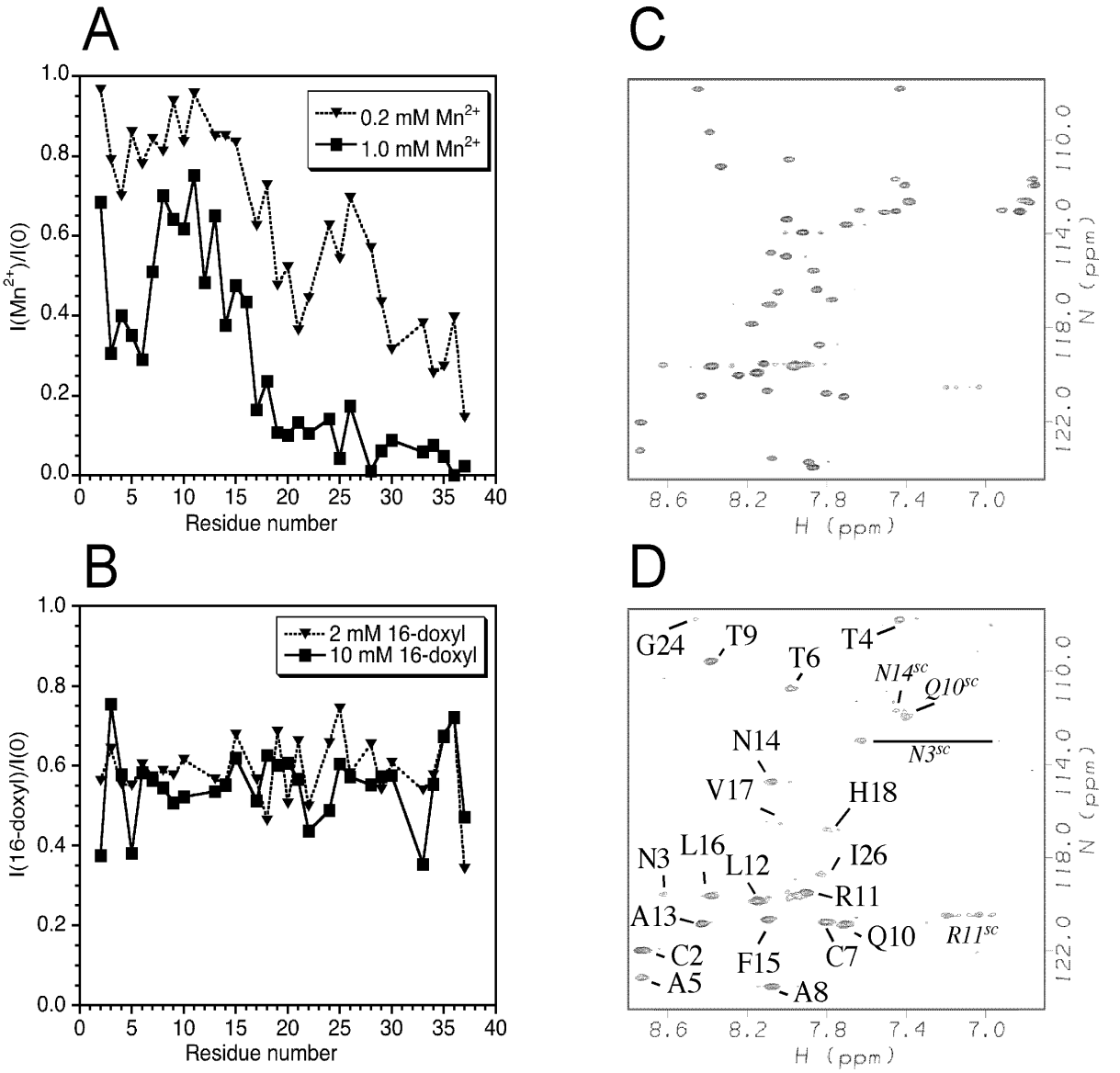

Figure 2.5 Spin probe studies of amylin positioning in SDS micelles. (A) Effects of $MnCl_2$ on ^1H-^{15}N HSQC cross-peak intensities. (B) Effects of 16-doxyl-stearate on cross-peak intensities. (C) Control ^1H-^{15}N HSQC of micelle-bound amylin showing intensities in the absence of paramagnetic spin probes. (D) Spectrum in the presence of 1.0 mM $MnCl_2$. The correlations that persist are labeled. Side-chain correlations are indicated with the superscript 'SC'.

number of variables, including detergent concentration, ionic strength, and the molecules complexed to the micelle [82]. Nevertheless, the 6.7 ns rotational correlation time is most consistent with amylin binding to the SDS micelles as a monomer. The TENSOR2.0 program [63] was used to calculate S^2 order parameters, which describe the amplitudes of internal motions on the fast ps to ns time scale. The data are shown in Fig. 2.4*D* and suggest a subdivision of amylin dynamics into three subdomains. The segment running from residues 4 to 18 has the lowest mobility with all S^2 values greater than 0.8. Residues 19-30 have S^2 values between 0.7 and 0.5. Finally, the last 7 residues have S^2 values smaller than 0.4. Only two residues Asn-3 and Thr-4 required $R2_{ex}$ exchange broadening terms (2 Hz) to account for the experimental relaxation data.

Positioning of Amylin in the SDS Micelle - Fig. 2.5 shows the results of paramagnetic quenching experiments used to define the interactions of amylin with SDS micelles. Paramagnetic Mn^{2+} provides a probe of surface accessibility to bulk solution. At a 1:1 ratio of Mn^{2+} to amylin, the C-terminal half of the protein is already substantially broadened (Fig. 2.5*A*). The 30-37-residue segment, which is unstructured, experiences the most severe quenching. The 21-29-residue segment, although α-helical, experiences more broadening than the 5-17-residue segment. At a 5:1 ratio of Mn^{2+} to amylin, most of the backbone HN signals from residues after Val-17 are barely visible. The 2-16-residue segment survives even at this higher concentration of Mn^{2+}, indicating it is immersed in the micelle (Fig. 2.5, *C* and *D*). Interestingly, the 2-16-residue segment also shows at least partial protection of side chain amide protons. Each of the side chains of Asn-14, Arg-11, Gln-10, and Asn-3 has at least one HN proton inaccessible (Fig. 2.5*D*). In addition to Mn^{2+} we also looked at paramagnetic quenching with 16-doxyl-stearate (Fig. 2.5*B*). This lipid has a spin label near the ω-end of the detergent chain, so the paramagnetic probe should be incorporated near

the hydrophobic center of the micelle. In contrast to Mn^{2+}, the 16-doxyl probe caused little specific quenching, except perhaps for residues 2, 5, and the glycine at position 33. These data suggest that although amylin is immersed below the surface of the micelle, it does not traverse to its center.

Discussion

In this study we report NMR assignments, the solution structure, and dynamics of amylin when bound to SDS micelles. Although SDS micelles are not physiological, their relatively small size makes them amenable to high resolution structure studies by NMR. Indeed, the most detailed structural models available for the amyloidogenic proteins Aβ [26] and α-synuclein [27] in membrane-like environments came from work with SDS micelles. We envision that the micelle-bound structure of amylin will pave the way for studies with more realistic membrane mimetics like bilayers or vesicles.

Aspects of the amylin NMR structure related to its dynamic and micelle-binding properties are highlighted in Fig. 2.6. Fig. 2.6*A* shows a ribbon representation of the NMR structure color coded according to the S^2 order parameters derived from ^{15}N relaxation data (Fig. 2.4). Micelle-bound amylin folds into an α-helix running from about residue 5 to 28. The structure is not uniformly stable but shows a ramp of increasing flexibility toward the C terminus (color coded from blue for rigid, to red for flexible). Residues 5-17 form the most rigid part of the α-helix, and disorder increases from residues 18 to 28. Residues 1-4 are constrained to form a hairpin turn by the Cys-7-Cys-2 disulfide bond, and residues ~30-37 are unfolded. We note that in contrast to the recombinant peptide studied here, amylin *in vivo* undergoes post-translational processing that results in an amidated C-terminus. Amidation is required for amylin activity [8], presumably due to the interactions of the hormone with its receptors. Because the last 8 residues in the micelle

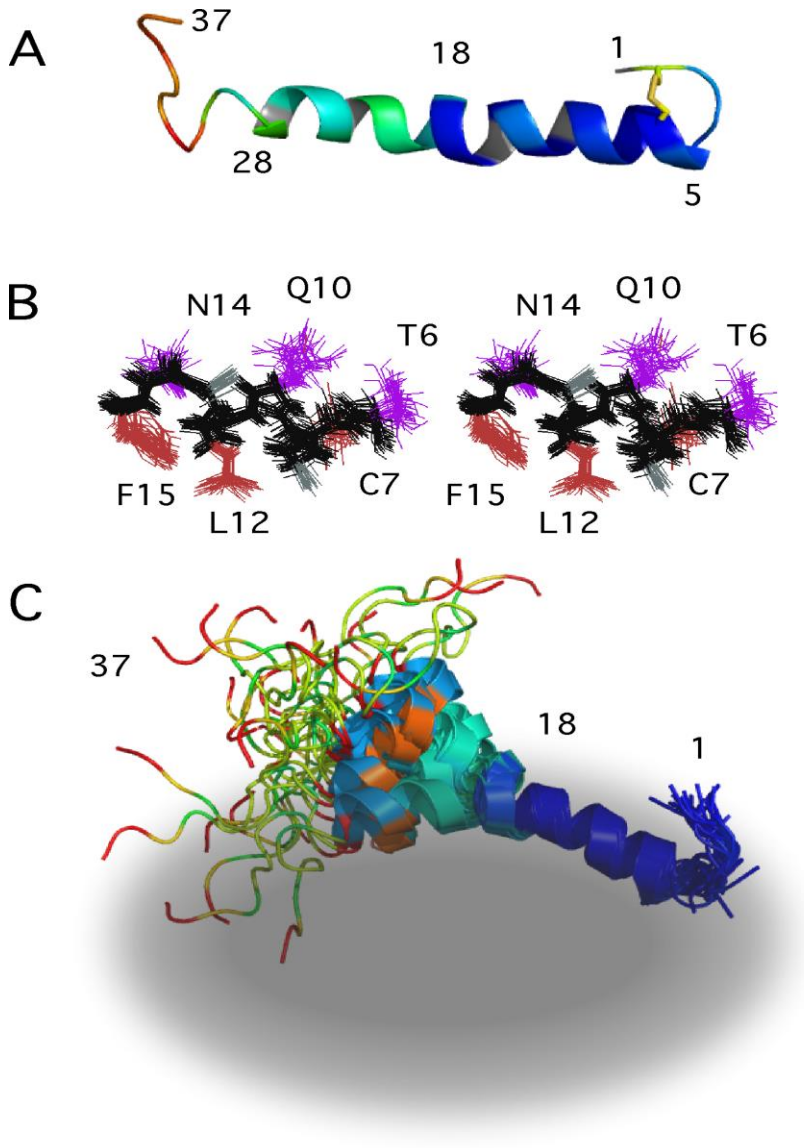

Figure 2.6 Properties of the micelle-bound amylin structure. (A) Ribbon diagram of the NMR structure color-coded according to S^2 order parameters (data from Fig. 2.4D). The color ramp ranges from blue (large S^2, rigid) to red (small S^2, flexible). The side-chains of Cys2 and Cys7 are shown in yellow to illustrate the disulfide bond. (B) Stereo-pair (cross-eyed) showing the precision of side-chain conformations for residues 6-16 is similar for the hydrophobic (brown) and hydrophilic (violet) faces of the helix. (C) Schematic diagram illustrating the structure of micelle bound amylin. The ensemble of 30 NMR structures were superposed on the mean backbone coordinates of residues 6-17, and the ribbon diagrams were color-coded according to spin probe accessibility with 1.0 mM $MnCl_2$ (data from Fig. 2.5A). The color ramp ranges from blue for backbone amides protected from the spin probe to red for amides that experience large NMR peak intensity losses in the presence of 1 mM $MnCl_2$. The gray ellipsoid illustrates an SDS micelle. The micelle and peptide are not drawn to scale, and we do not have quantitative information on the distance the peptide penetrates into the micelle. The schematic is simply to illustrate that based on spin probe data the N-terminal half of the peptide is immersed into the micelle, and that immersion correlates with the dynamic properties of the peptide (Fig. 2.6B).

bound amylin structure are disordered, we think it is unlikely that amidation has a role in the interaction of the peptide with membranes. In our structure the α-helix of amylin has a kink or discontinuity near residues 18–22. The micelle-bound states of other amyloidogenic proteins, kinks or distortions from α-helix conformations also correlate with the locations of turns in the fibrillar β-sheet structures [77]. Thus in micelle-bound Aβ the first 15 residues are disordered and a kink in the α-helix occurs in the 26–28-residue region [26]. The first 15 residues are also disordered in Aβ fibrils, and a reverse turn occurs between residues 26 and 30 [83]. The micelle-bound state of α-synuclein consists of a broken helix with an interruption of α-helical conformations near residues 42-44 [27]. This location roughly corresponds to a turn between strands β1 and β2 in the fibril structure, and more generally regions of α-synuclein with small S^2 order parameters [27] in the micelle bound structure appear to correlate with gaps between β-strands in a recent model of α-synuclein fibrils [84]. For amylin, residues 12-17, 22-27, and 30-37 are thought to make up the strands of β-sheet in amyloid fibrils of the peptide [24]. The strands correspond to the dynamic subdomains of micelle-bound amylin identified in the current work, and the discontinuity in the α-helix structure near residues 18-22 corresponds to a turn in the putative fibril structure. These observations suggest that intrinsic sequence turn propensities may have roles in determining β-sheet topology in the fibrils.

NMR structure of a 1-19-residue fragment of human amylin in dodecylphosphocholine micelles also identified α-helix structure between residues 7 and 17 [28]. The difference from our structure at the C terminus is probably due to end fraying effects in the fragment. A second 20-29-residue fragment in SDS micelles adopted a structure consisting of a series of reverse turns [29]. A third 17-29-residue fragment showed NMR and CD evidence for weakly stable α-helix structure [30]. A model for intact amylin in large unilamellar vesicles is available from EPR studies [78]. This work

identified α-helix structure running from residues 9 to 22. The helix starts later than position 5 in our structure. This may result from the substitution of the cysteines at positions 2 and 7 with alanines for the EPR studies. Although the helix ends at position 22 in the EPR study rather than 28 in this work, the data are consistent with our dynamic structure of amylin. The EPR experiments measure mobility and accessibility of the spin labels introduced into amylin [78]. Although residues 23-28 are in an α-helix conformation according to the NMR data (Fig. 2.2, *B-D*), both mobility (Fig. 2.4*D*) and solvent accessibility (Fig. 2.5*A*) are increased in this region compared with the 5–17-residue segment.

As noted for micelle-bound α-synuclein [27], protein backbone dynamics are highly correlated with the degree of immersion of individual sites into the micelle. Indeed, conformational restriction of segments of the polypeptide chain bound to micelles is a common theme in peripherally bound proteins [85]. Although amylin binds roughly parallel to the micelle surface, the degree of immersion varies from site to site based on accessibility to paramagnetic Mn^{2+}. The S^2 order parameters of amylin (Fig. 2.4*D*) are linearly correlated with the quenching data obtained at 0.2 mM Mn^{2+}, with an R^2 of 0.73. This indicates that 73% of the variance in S^2 values can be explained by the variance in solvent exposure of amylin. The strong correlation probably arises because the lower dielectric constant of the micelle environment should favor hydrogen bonding of polar groups in the polypeptide backbone [9]. Greater immersion in the micelle would thus increase the stability of hydrogen-bonded α-helix structure and decrease backbone mobility. Interestingly, our paramagnetic quenching data with Mn^{2+} show that some of the NH-containing side chains in amylin are at least partially protected from solvent by the micelle. A stereo pair illustrating the side chain conformations of residues 6-17 is shown in Fig. 2.6*B*. The *brown* side chains in Fig. 2.6*B* are hydrophobic and should point toward the interior of the micelle, whereas the *violet* hydrophilic side chains should be oriented toward the solvent [78]. Fig.

2.6*B* shows that the precision of the side chains in the NMR ensemble is similar for the two faces of the amphipathic α-helix, which seems consistent with the paramagnetic quenching data that suggest hydrophilic residues in the 5–17-residue region are partially immersed in the micelle. Consistently, amylin monolayer insertion depth measurements using EPR indicate that the center of the stable α-helix of amylin is immersed 6-9 Å below the lipid head groups, with the immersion depth decreasing from the N to the C terminus of the helix. Monolayer experiments are also consistent with an insertion of the N-terminal part of amylin into lipid membranes [86].

A highly schematic model illustrating our results on the binding of amylin to SDS micelles is shown in Fig. 2.6*C*. The *gray ellipsoid* in Fig. 2.6*C* represents an SDS micelle. The *ribbon diagram*s in Fig. 2.6*C* illustrating the NMR ensemble are color coded according to spin probe accessibility, with *blue* representing inaccessible and *red* representing accessible. The segment between residues 5 and 17 is immersed just below the surface of the micelle, stabilizing α-helical structure and dampening the dynamics of this region. The Cys-7-Cys-2 disulfide directs residues 1-4 to form a hairpin turn that presumably brings Lys-1 near the surface of the micelle to avoid burying a positively charged group in a hydrophobic environment. The N-terminal part of amylin thus acts as a "hook" anchoring the hormone to the micelle.

Although amylin can bind to phospholipids as a monomer [86], we are unaware of such an interaction in the normal function of amylin. At the same time amylin needs to bind to transmembrane receptors [87] and to cross the blood-brain barrier [88] so the hydrophobic character of the N-terminal part of the hormone could facilitate those functions.

At the end of the 5-17-residue segment, residues 18-28 show a gradient of diminishing protection from paramagnetic quenching and increased backbone dynamics. Presumably these

residues are located at the interface between the micelle and solvent. Although residues 18–28 are in α-helical conformations, the axis of the helix shows considerable variance relative to the 5–17-residue segment with an average inter-helix angle of 30 °C. The ability of the N-terminus to insert into membranes could facilitate the assembly of amylin into toxic aggregates. Anchoring in the membrane would work to increase the effective concentration of amylin and would reduce the entropic cost of self-association by orienting molecules within the plane of the membrane lipid bilayers [9]. The dynamic character of the 22–29-residue segment would allow induced fit association, and its placement at the interface between lipids and solvent may nucleate aggregation. Under the conditions of the present studies, amylin is very stable, but we have an excess of SDS micelles to peptide. When the peptide predominates, with different types of lipids or under slightly different solution conditions, membranes could catalyze amylin aggregation [89-91].

The gradient in dynamics, the correlation of the helices when coordinates are fitted over the entire 5-28-residue region, and the presence of a few short range NOEs that span the 18-22- residue region suggest that although there is flexibility in the relative orientation of the α-helical segments 5-17 and 18-28, their structures remain coupled. This is important because although our work provides a model for amylin peripherally associated to membranes, a toxic pore composed of oligomeric amylin would have to traverse the membrane lipid bilayers. Presumably, aggregation of the amyloidogenic 20-29-residue segment results in the transmission of a conformational switch to the 5-17-residue segment that allows it to traverse the membrane bilayer. Structural coupling between the amyloidogenic and membrane-immersed segments could thus facilitate the transition to a toxic state when membrane-bound amylin oligomerizes.

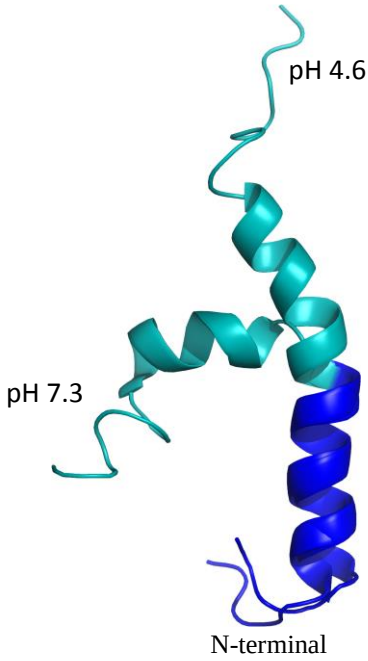

Figure 2.7 Human amylin structure at pH 4.6 superimposed on top of human amylin structure at pH 7.3 highlighting the difference between intrahelical angles (PDB code 2KB8 and 2L86).

Subsequent NMR structural studies of amylin in SDS micelles at physiological pH show structural similarities with our structure done at acidic pH. An α-helix was found running from residues 7-17, and residues 21-28. In addition to the similarities to our structure, the 3_{10} helix was found between residues Gly33-Asn35. The biggest difference was in the angle between the two α-helical segments separated by the kink near His 18. In the neutral pH structure this angle constrained to 85° compared to 30° in our structure (fig. 2.7). The C-terminal region of the peptide in neutral and acidic pH remains unstructured [92]. The higher intra helical angle identified for the structure of micelle bound amylin at neutral pH, resembles to the structure of amylin and the related mutant pramlintide determined later in fluorinated organic solvents [93], suggesting the kink in the helix between residues 17-22 is not enforced by membrane binding. Structural similarity have also been

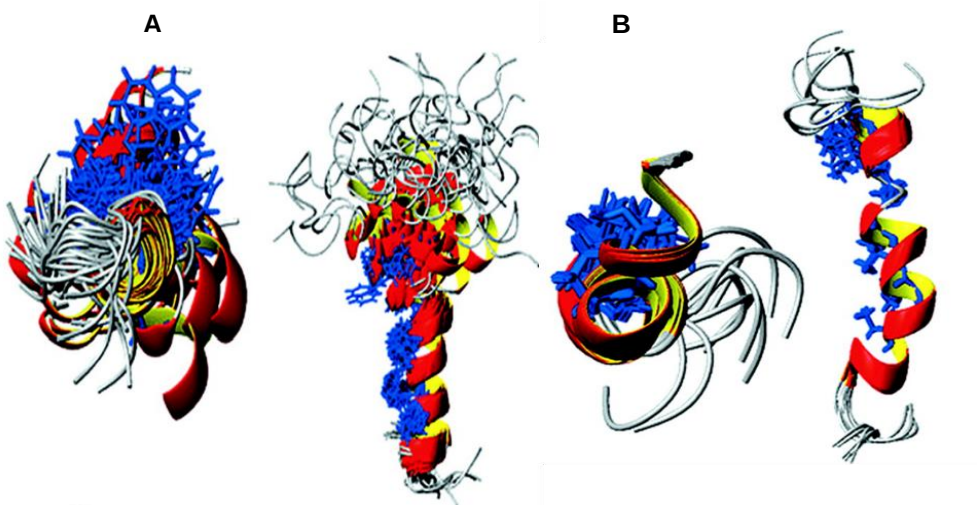

Figure 2.8 The 3-dimensional structures of human amylin in presence of SDS micelle (A), rat amylin in the presence of DPC micelles (B). The hydrophobic residues that have been implicated in coiled-coil interactions (blue) stabilize the amylin oligomer (adapted from Westermark et.al. [4, 94]).

found between the rat amylin structure determined in the presence of DPC micelle and our human amylin structure bound to SDS micelle (fig. 2.8) [4, 94]. The interaction of the peptide with the lipid membrane is of significant interest as it increases the rate of peptide aggregation which can in turn result in membrane disruption [90, 91]. The NMR structure of a truncated version of a truncated version of human amylin (human amylin 1-19) showed that protonation of His 18 causes a change in its membrane binding topology from a buried to a surface associated state [28] a phenomenon that was also with β-cell membranes as demonstrated by a H18R human amylin 1-19 mutant [95]. The higher intra helical angle between residues 18-22 and the charge on His-18 at physiological pH correlate with higher fibrillization propensity and cytotoxicity of human amylin. Therefore, the effects of charge on amylin fibrillization are discussed in next chapter of this thesis.

CHAPTER III: Heterogeneous Amylin Fibril Growth Mechanisms Imaged by Total Internal Reflection Fluorescence Microscopy

Excerpted from : S.M. Patil, A. Mehta, S. Jha, and A.T. Alexandrescu, Heterogeneous amylin fibril growth mechanisms imaged by total internal reflection fluorescence microscopy, Biochemistry 50 (2011) 2808-2819.

Abstract

Total internal reflection fluorescence microscopy has been used to visualize the fibrillization of amylin. Data were obtained at acidic pH where fibrillization is hindered by the charging of histidine-18 and at slightly basic pH where the loss of charge on the histidine promotes aggregation. The experiments show three types of aggregate growth processes. In the earliest steps globular seeds are formed with some expanding radially during the course of the reaction. The dimensions of the globular seeds as well as their staining with the amyloid-specific dye thioflavin T indicate that they are plaques of short fibrils. The next species observed are fibrils that invariably grow from large globular seeds or smaller punctate granules. Fibril elongation appears to be unidirectional, although in some cases multiple fibrils radiate from a single seed or granule. After fibrils are formed, some show an increase in fluorescence intensity that we attribute to the growth of new fibrils alongside those previously formed. All three aggregation processes are suggestive of secondary (heterogeneous) nucleation mechanisms in which nucleation occurs on preformed fibrils. Consistently, electron micrographs show changes in fibril morphology well after fibrils are first formed, and the growth processes observed by fluorescence microscopy occur after the corresponding solution reactions have reached an initial apparent plateau. Taken together, the results highlight the importance of secondary nucleation in the fibrillization of amylin, as this could provide a pathway to continued fibril growth once an initial population of fibrils is established.

Introduction

We used TIRFM in conjunction with the amyloid specific dye ThT to follow the growth processes of individual amylin aggregates. At the interface between a medium with a large refractive index (glass slide) and a medium with a small refractive index (aqueous solution), laser excitation can be used to induce a thin 100-200 nm electromagnetic field called an "evanescent wave" in the medium with the smaller refractive index [33, 96, 97]. This narrow illumination field can be used for TIRFM imaging of objects lying along the plane of the coverslip [33]. Compared to conventional fluorescence microscopy, background fluorescence from fluorophores in bulk solution decreases exponentially with distance from the slide-solution interface in TIRFM [97]. While TIRFM has the same resolution as light microscopy, the exquisite sensitivity of the technique makes it possible to detect single molecules.

The amyloid-specific dye ThT was used to image the fibrils. Binding of ThT to amyloid fibrils causes marked changes in the fluorescence spectrum of the dye. These include red shifts in the excitation maximum from 385 to 450 nm and in the emission maximum from 445 to 482 nm and a large increase in quantum yield when the dye is bound to the amyloid cross-β structure [98]. These properties make ThT ideal for imaging amyloid fibrils by TIRFM, since fluorescence from the free dye in solution is minimal and the dye is specific to amyloid fibrils [33]. Conversely, aggregates that lack the specific cross-β sheet structure of amyloid fibrils will be invisible to TIRFM imaging using ThT. Alternatively, fluorescent dyes can be covalently attached to amyloidogenic proteins to image their fibrillization [99-101]. Amyloid fibril imaging by TIRFM has provided important information on the kinetics of individual fibril growth and on the unidirectional polarity of fibril elongation [34, 35, 99-101] predicted by fibril structure composed

primarily of parallel β-sheets.

Previous TIRFM studies looked at fibril elongation starting from seeded solutions; that is, mature fibrils were fragmented by sonication to provide nucleation sites for fibril growth [32, 34, 35]. Amylin fibrillization is fast and we also wanted to investigate seed formation, therefore the reactions in the present work were not seeded. Because we were interested in the effects of charge on amylin fibrillization, we obtained TIRFM data under acidic conditions close to those the hormone experiences when it is stored in β-cell secretory granules, and near the neutral pH conditions amylin is exposed to when it is released into the extracellular matrix [23]. Data on the growth of individual aggregates on the surface of a slide monitored by TIRFM were compared to snapshots sampling the population of aggregates that develop in solution using the higher resolution afforded by EM. Kinetics of individual fibrillar aggregates measured by TIRFM were compared with fibrillization kinetics in solution measured by fluorescence spectroscopy. Our results indicate that amylin fibrillization proceeds through multiple mechanisms involving a mixture of fibril species and emphasize the importance of secondary nucleation [32, 37-39] in amylin fibrillization.

Material and Methods:

Sample Preparation. Human amylin containing an amidated C-terminus and a Cys2-Cys7 disulfide bond was purchased from Anaspec (Cat. No. 60254-05; San Jose, CA). The peptide, which was >95% pure, was supplied as a dry powder in 0.1 mg amounts sealed in glass vials. Because the peptide is poorly soluble in water, samples were dissolved in 10% acetonitrile (ACN) according to the manufacturer's suggestion. A 20 mM sodium phosphate buffer was used for studies at pH 8 while a 60 mM sodium citrate buffer was used for experiments at pH 4. Additional

experiments were done in which the peptide was initially dissolved in 100% Dimethyl sulfoxide (DMSO) before adjusting the samples to a final concentration of 4% (v/v) DMSO in aqueous buffers. Amylin solutions were used immediately or stored at 80 °C. Unless otherwise specified, the final amylin concentrations in all samples was 100 μM. This peptide concentration was chosen because it gave the best results for TIRFM experiments in terms of the number of fibrils formed and the speed of the fibrillization reactions. The samples additionally contained the metal chelator EDTA at a 0.5 mM concentration and the bacteriostatic compound sodium azide at a 0.05 mM concentration. Before use in fibrillization reactions, the solutions were sonicated continuously for 5 min in an ice bath at a power of 75% using a Fisher Scientific Sonic Dismembrator Model 500.

TIRFM Experiments. Fibrils were imaged using the fluorescent dye ThT (Ultrapure, Anaspec; San Jose, CA) which was included in the samples at a concentration of 5 μM. Samples of ~30 μL were inserted in the space between the glass slides (Fisher Cat. No. 12-544-1) and a clean coverslip (Fisher Cat. No. 12542-C; Pittsburgh, PA), was affixed on two edges with double-sided tape. The assembly was sealed with Dow Corning high-vacuum grease and placed on the microscope with the coverslip facing the objective. Glass coverslips were cleaned by soaking for 1 h in 2:1 (v/v) HNO_3: HCl, washing with water, and rinsing three times with deionized water. Coverslips were stored in 70% ethanol and dried before use. Glass slides were prepared in the same way except they were cleaned with a 1% (w/v) Alconox solution.

Fibril growth was imaged using a TIRFM system integrated into an Andor Revolution XD Spinning Disk Confocal instrument with a Nikon TiE inverted microscope. ThT excitation was achieved at 405 nm, using the available laser line on our instrument closest to the excitation maximum of 450 nm for amyloid-bound ThT [98]. Excitation profiles for amyloid-bound ThT

recorded on a standard fluorescence spectrophotometer were used to establish that excitation at 405 nm leads to an ~50% loss in fluorescence intensity compared to excitation at 450 nm. Although this results in a loss of sensitivity, ThT excitation at 405 nm can still be used to visualize fibrils. To selectively monitor fluorescence from amyloid-bound ThT which has an emission maximum of 482 nm,[98] we used a 483 (16 nm bandpass filter from Semrock (Rochester, NY). Images were recorded with an Andor 897 iXon EMCCD camera using an oil immersion TIRF lens (1.49 NA, 100x, Nikon). Samples were maintained at a temperature of 24 ±1 ℃ during the experiments. We did additional experiments on a Leica TCS SP2 laser confocal scanning microscope to verify that the seed like aggregates imaged by TIRFM were detected due to ThT fluorescence. For these experiments we excited the sample at a fixed wavelength of 458 nm and scanned through the emission spectrum which had a maximum at 483 nm, consistent with the fluorescence maximum of amyloid-bound ThT [98]. Image analysis, including calculations of fibril lengths and seed diameters, was performed with ImageJ software from the NIH [102]. Briefly, the "set scale" utility of ImageJ was used for calibration according to the resolution of our camera which was 133 nm/pixel. The line utility was then used to measure the length or diameters of objects. Curved fibrils were approximated by line segments, and their lengths were calculated from the sum of the segments. To characterize kinetics, fibrils were observed every 2 h of the 48 h experiment at pH 4 and every 1 h of the 23 h experiment at pH 8. When measuring kinetics, we excluded any species that appeared between consecutive TIRFM images collected 5 or 15 min apart and then maintained a constant size, since these are likely to represent aggregates that have precipitated from solution onto the coverslip [34, 35].

EM Experiments. Samples containing 100 μM amylin at pH 8 or pH 4 were incubated at 25 °C,

and aliquots of the reaction were removed for imaging after 0.5, 5, 10, 20, and 170 h (1 week). Aliquots were immediately transferred to 400-mesh carbon coated Maxtaform Cu/Rh grids (Ted Pella Inc., Redding, CA) and stained with a 1% (w/v) solution of uranyl acetate. EM images were recorded using an AMT XR-40 (2048 x 2048 pixel) camera that was side-mounted on a FEI Tecnai BioTWIN G^2 Sprit transmission electron microscope. At least five images were obtained for each sample and time point, and the most representative images were analyzed.

Fibrillization Kinetics in Solution. The time course of fibrillization in solution was monitored in duplicate using 200 μL samples of amylin, contained in white polystyrene clear bottom 96-well plates (Corning Inc., Corning, NY). Plates were covered with a clear polyester sealing tape (Fisher Scientific, Agawam, MA) to prevent evaporation. Samples had 100 μM amylin concentrations for consistency with the TIRF experiments and 10 μM ThT (Sigma; St. Louis, MO). To look at the effects of predissolving amylin in different organic solvents, we compared amylin dissolved in pure ACN and brought up in buffer to a final concentration of 10% (v/v) ACN to amylin dissolved in pure DMSO and brought up to a concentration of 4% (v/v) DMSO. All experiments were done without agitation, at a temperature of 25 °C. ThT fluorescence was recorded at 1 min intervals for 30 h using excitation at 440 nm and emission at 490 nm on a Fluoroskan Ascent 2.5 fluorescence plate reader.

Results

TIRF Microscopy of Amylin Fibrillization at pH 4 and 8- Fibrillization of amylin is enhanced at pH 8 compared to pH 4 due to the loss of the positive charge on His18, which lessens electrostatic repulsion between the amylin monomers packed in fibrils. These effects are physiologically relevant since amylin is stored at pH 5.5 in the secretory granules of pancreatic β-

cells but is exposed to pH 7.4 when it is released into the extracellular matrix [23]. To look at the effect of pH on fibrillization, we obtained TIRFM data at pH 4 and 8, where His18 in amylin fibrils is fully charged and fully uncharged, respectively.

Fig. 3.1 shows 42 x 42 μm sections of the 68 x 68 μm TIRFM images collected. The earliest images obtained after 45 min (Fig. 3.1A, C) are compared with images at the end of the reactions: 48 h at pH 4 (Fig 3.1B) and 23 h at pH 8 (Fig. 3.1D). The first images at both pH values show mostly round "seeds" (Fig. 3.1A, C), even though no attempt was made to seed the reaction by fragmenting preformed fibrils [33-35]. Because amylin fibrillization is fast, some seeds and a few fibrils already formed during the 45 min lag time of the experiment between dissolution of the peptide and TIRFM imaging. In addition to seeds, we observed smaller punctate "granules". The term 'seed' is used to describe aggregates with a round, nonfibrillar morphology for consistency with previous studies [33-35] and because the growth of the fibrils we see by TIRFM invariably starts from these aggregates. As shown below, the dimensions of the seeds together with their binding of the amyloid-specific dye ThT (which is a prerequisite for TIRFM observation) indicate they correspond to plaques of short fibrils rather than the oligomeric nuclei that initiate fibril growth through primary nucleation mechanisms. The number of seeds initially observed at pH 8 (Fig. 3.1C) was larger than at pH 4 (Fig. 3.1A). As the reaction progressed, more fibrils formed at pH 8 (Fig. 3.1D) than at pH 4 (Fig. 3.1B) and the fibrils at pH 8 were more clustered (Fig. 3.1D). The smallest objects we could identify were about 0.2 μm (200 nm) as the resolution of our camera is 133 nm/pixel. Although we counted objects with sizes between 0.2 and 0.5 μm as small seeds, we caution that we cannot easily distinguish between a round seed and an elongated fibril morphology for objects smaller than about 0.5 μm.

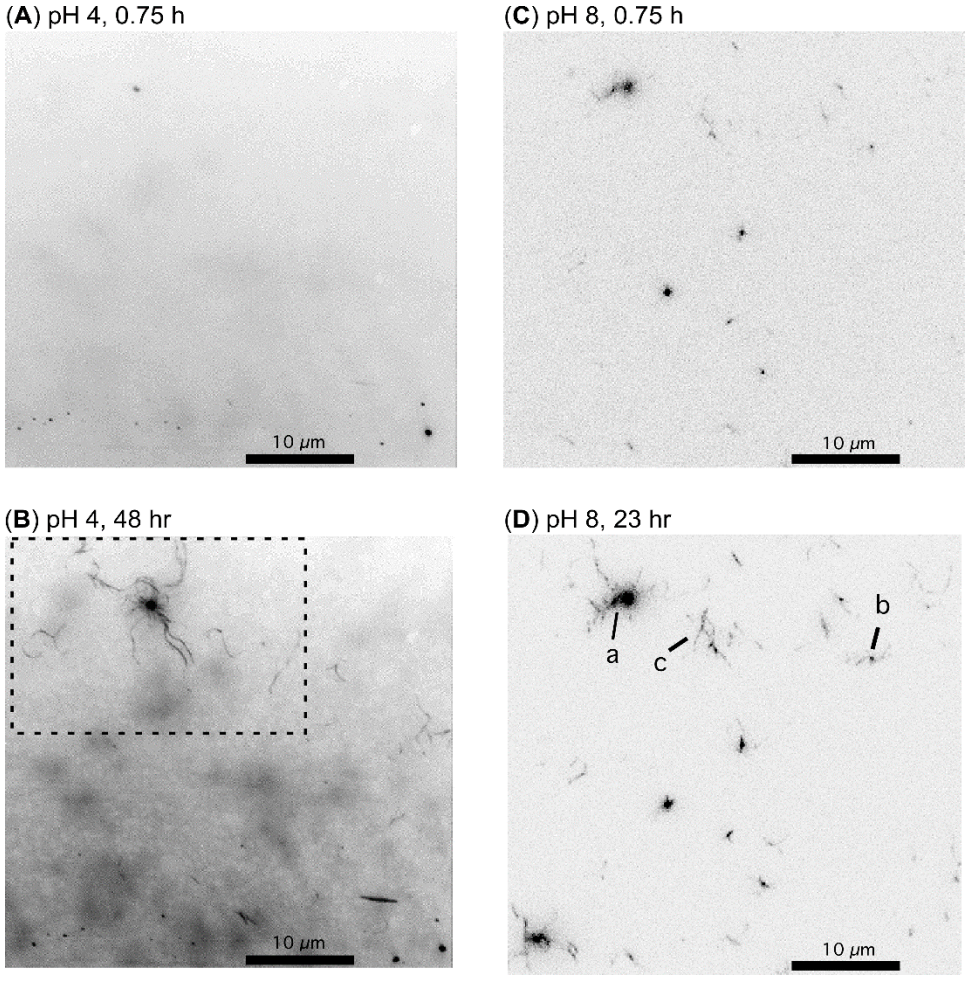

Figure 3.1. TIRFM images of human amylin at pH 4 (A, B) or pH 8 (C, D) showing the initial (A, C) and final stages of the reactions (B, D). Images were color inverted so that white corresponds to nonfluorescent material and black to fibril-induced ThT fluorescence. The dashed box in (B) corresponds to the area shown in Fig. 3.4. In panel D, **a** is an example of a large seed, **b** is an example of a small seed (granule) with at least two faint fibrils emanating from it, and **c** is an example of a fibril.

Fig. 3.2 compares the distributions of seed and fibril lengths at the end of the reactions, when no further changes were seen in the TIRFM images. Qualitatively, we have seen between a 2- and 5-fold increase in the numbers of seeds and fibrils at pH 8 compared to pH 4 in multiple TIRFM experiments. A quantitative assessment is not possible because we are not observing a macroscopic average. The number of individual aggregates varies between experiments or even when different sections of a slide are compared. The distributions of seeds and fibril lengths,

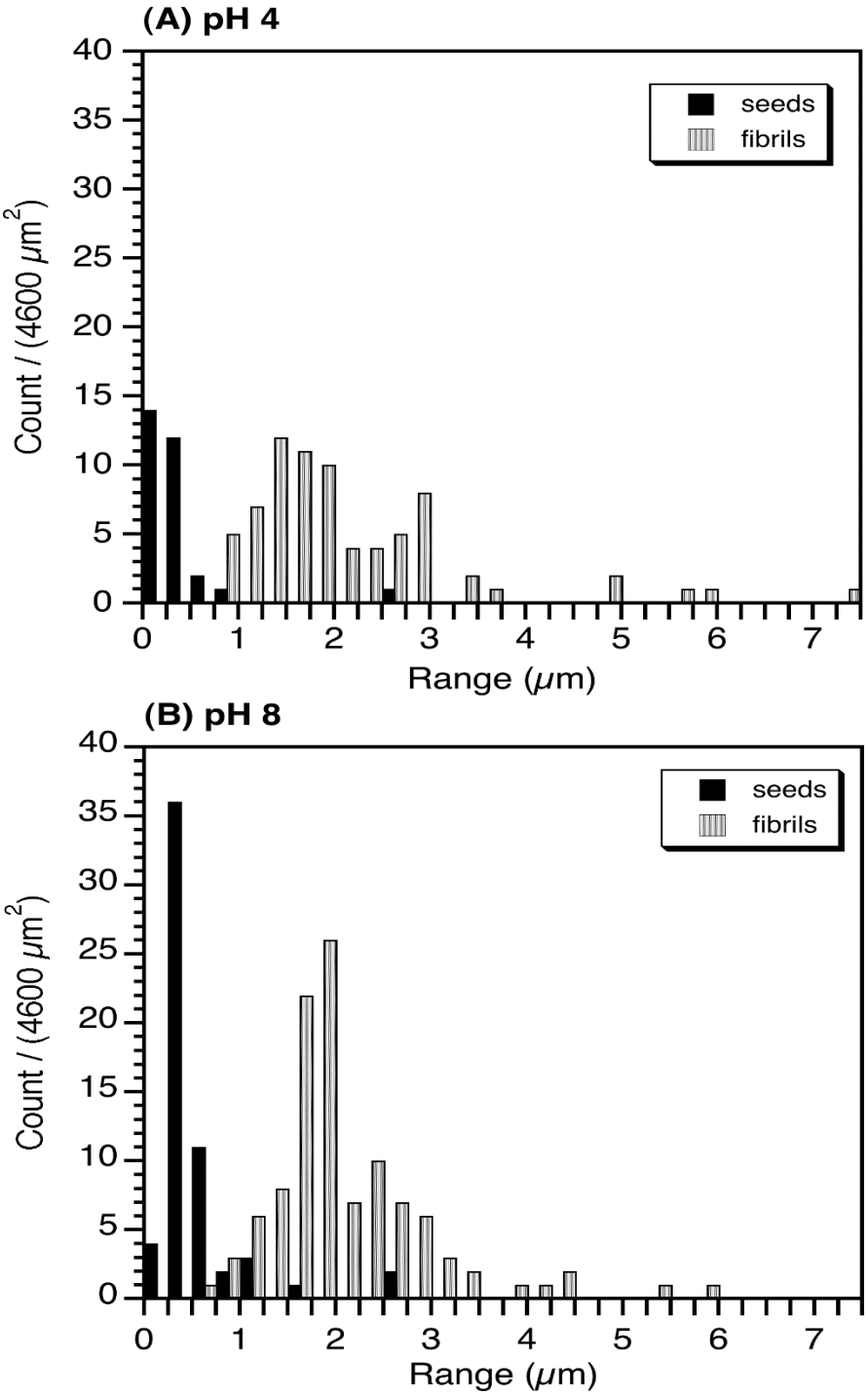

Figure 3.2. Distributions of seeds and fibrils at the last time points of the TIRF experiments (A) at pH 4, after 48 h of incubation and (B) at pH 8, after 23 h of incubation. By these times fibril growth processes had subsided for each of the samples.

however, show similar patterns in multiple experiments. At both pH values there were about twice as many fibrils as seeds at the end of the reaction, while seeds were the dominant species at the start of the reaction. The average fibril lengths when the reactions reached completion were ~2 μm at both pH values although a small number of fibrils as long as 57 μm were observed (Fig. 3.2). Seed diameters were on average about 50% larger at pH 8 (0.56 μm, 60 samples) compared to pH 4 (0.34 μm, 29 samples) while fibril lengths were the same. The distributions of seed sizes fell of more rapidly than fibrils (Fig. 3.2), suggesting that large seeds are unstable or disfavored.

Seeds Observed by TIRFM Correspond to Plaques of Short Fibrils. Fig. 3.3 shows a small seedlike object with a 0.15 μm diameter imaged by EM that is comparable to the 0.35 μm diameter of seed b in the TIRFM image of Fig. 3.1D. The subsequent EM images in Fig. 3.3 shown progressively higher magnifications of the areas indicated by the rectangles. As the resolution of the EM images increases, the globular seed can be seen to be composed of a cluster of small wormlike fibrils. Atomic Force Microscopy (AFM) studies reported that in the initial stages of amylin fibrillization globular oligomers are formed with an average length of 23 nm. The oligomers grew in height from 2 to 6 nm before elongating into fibrils [103]. The sizes of the oligomers observed by AFM are some 10-100 times smaller than the smallest 0.2 μm sized aggregates discernible by TIRFM. In EM images of amylin fibrillization reactions we see some fibrils as short as 10-20 nm, but these have an elongated rather than a globular morphology. For objects shorter than about 10 nm it would be difficult to distinguish between a fibrillar and globular morphology. Globular aggregates that could correspond to the types of oligomeric intermediates seen by AFM were not seen by EM under the conditions of our study. The oligomeric species observed by AFM elongated into fibrils in about 30-60 min [103]. This time scale is on the order

of our 20-45 min dead time for preparation of samples for our EM and TIRFM experiments. Moreover, the AFM studies were done with 10 μM amylin concentrations, [103] which should result in slower fibrillization kinetics than at the 100 μM amylin concentrations used for this work. Some of the seeds observed by TIRFM grow over periods of 10-20 h, a rate much slower than the lifetime of the globular oligomers observed by AFM [103]. Moreover, nearly all of the seeds observed by TIRFM persisted at the ends of the 24 h (pH 8) or 48 h (pH 4) experiments, whereas for a primary nucleation mechanism, the population of oligomeric species should decrease at the

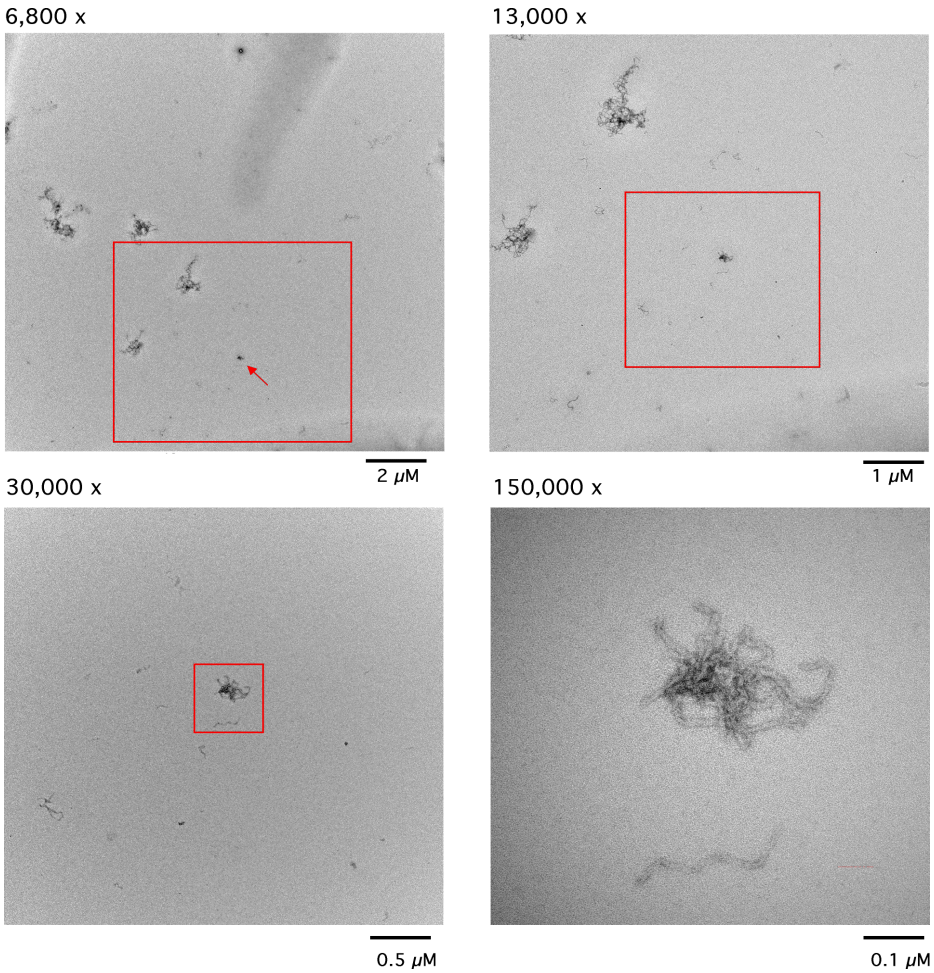

Figure 3.3. Electron micrographs of a granule-like seed (arrow) with a diameter of ~0.15 μm that at increasing magnification can be seen to be comprised of a cluster of fibrils. The EM data were recorded for a 100 μM amylin sample that was aggregated for 5 h at pH 8.

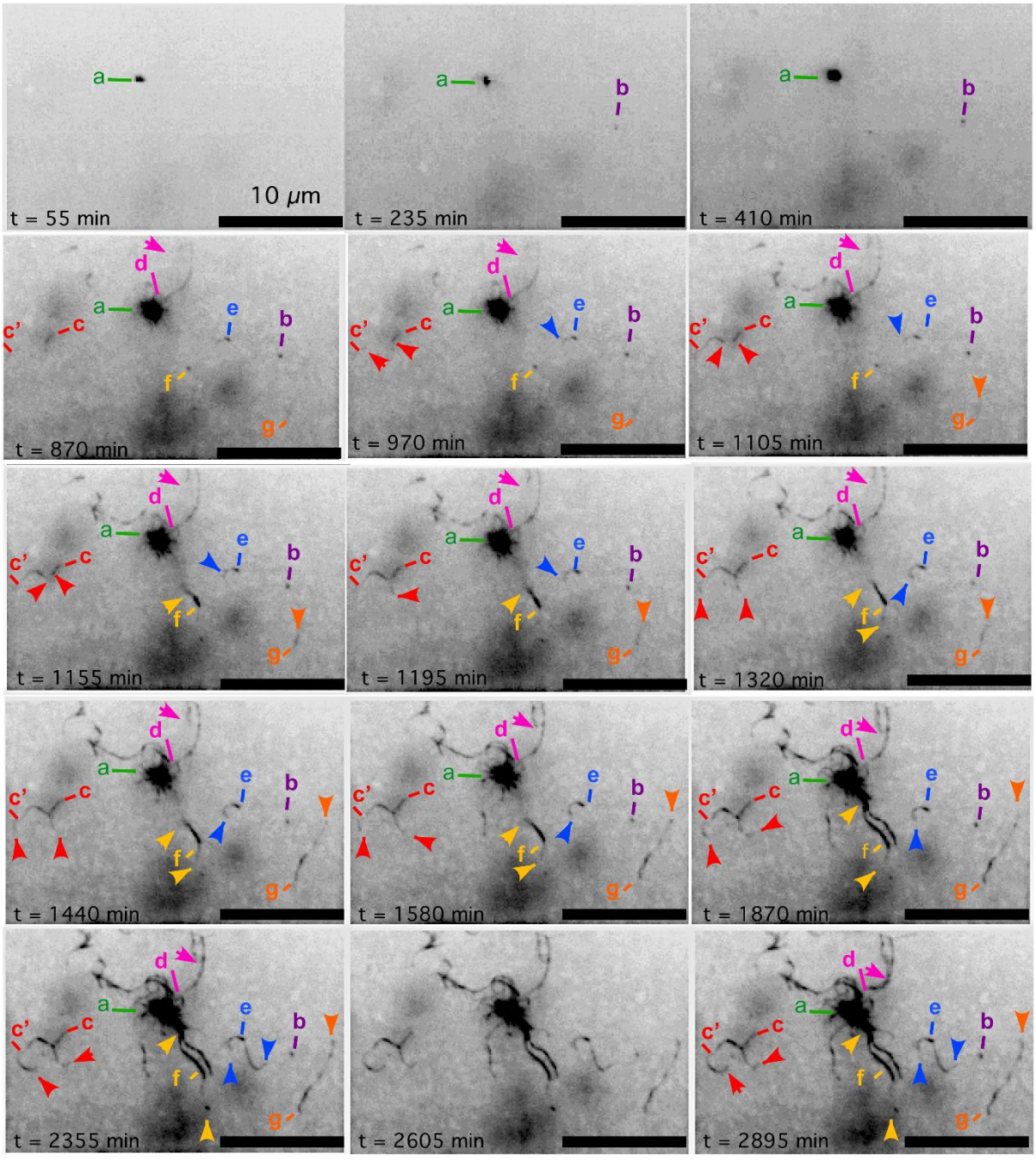

Figure 3.4. Snapshots of amylin fibril growth at pH 4 imaged by TIRFM. The time each image was obtained after transfer of dissolved amylin to a glass slide is given in the lower left-hand side of the panels. The data are from a total of 568 time points, recorded every 5 min for 2895 min (2 days). The time from preparing the sample to the first image collection was 45 min. Letters illustrate different species observed as described in the text. Lines are drawn to the location where each aggregate is seen at the earliest time point. Arrows indicate the ends of fibrils at the indicated time points.

expense of fibrils during the course of the reaction [103]. Finally, the detection of species by TIRFM through ThT fluorescence requires that amylin is assembled in a cross-β conformation. The specific changes in ThT fluorescence when the dye binds fibrils generally do not occur when the dye binds oligomers [104]. We therefore conclude that the seeds observed by TIRFM are plaques of short fibrils. The seeds observed by TIRFM can clearly act as nucleation sites for fibril growth, since all of the fibrils we observed start from small seeds or granules. The growth processes, however, are more consistent with a secondary or heterogeneous nucleation mechanism than with the primary or homogeneous nucleation events that lead to the formation of the initial fibrils following the lag phase of fibrillization.

TIRF Microscopy Reveals Three Distinct Mechanisms of Aggregation. Fig. 3.4 shows snapshots of an amylin aggregation reaction at pH 4. The data are illustrated for pH 4 because fibrillization kinetics are slower and there are fewer fibrils under these conditions, making it easier to show key steps in the reaction. Aggregation mechanisms were similar at pH 8, except where noted. The principal differences were that at pH 8 more fibrils formed and these were more clustered. The time course of aggregation in Fig. 3.4 suggests three distinct aggregation mechanisms: seed growth, fibril elongation, and fibril thickening. The three types of aggregation mechanisms are discussed in detail below.

Radial Seed Growth. The first species observed in experiments at both pH 4 and 8 are seeds illustrated by aggregates **a** and **b** in Fig. 3.4. After fibrils started to grow, few if any new seeds were observed. Some seeds such as **a** grew in intensity and expand radially with time, while the majority like **b** remained unchanged as the reaction progressed. The globular morphology of the seeds is different from the elongated morphology of amyloid fibrils, [105] and to our knowledge

radial expansion of fibrillar aggregates has not been previously described.

A number of seeds such as **a** sprouted fibrils as they grew, developed a coarse frayed periphery, and eventually lost their globular appearance. Other seeds showed a similar change to a coarser morphology but had no fibrils extending from them. The majority of seeds such as **b** stayed constant over the course of the reaction. The observation that some seeds became frayed as fibrils start to form, together with the distribution data in Fig. 3.2 showing that smaller seeds predominate, suggests that large seeds are unstable and that the fibril morphology is preferred as the aggregation reaction progresses.

Fibril Elongation. Fibrils either extended from large seeds such as fibril **d** or grew in apparent isolation (**c, e,** and **g**). On closer inspection, all fibrils can be traced back to small seeds or granules that have a larger fluorescence intensity than the fibrils that grow from them. In Fig. 3.4, the granule starting points of the fibrils are indicated by lines pointing to their origin, whereas the ends of the growing fibrils are identified with arrows.

In previous TIRF studies with Aβ and β2 microglobulin, fibril growth was observed to be unidirectional [34, 35]. By contrast, previous AFM studies of amylin observed bidirectional growth of amylin fibrils, with elongation occurring from both ends [106]. We see apparent growth in multiple directions of the fibrils shown in Fig. 3.4. For example fibril **e** slowly forms the top of the question-mark-shaped fibril between 870 and 1440 min. The bottom part of the question mark of fibril **e** then grows very rapidly after 1870 min. The top of fibril **f** grows toward seed **a** between 870 and 1870 min, but a fainter new arm of **f** extends in the opposite direction between 1320 and 2105 min. By contrast, fibril **g** grows in one direction, and fibril **c** is formed from the merging of the two branches **c** and **c**' after 1155 min. After **c** and **c**' have come together both the bottom-most

arm and the arm on the left (**c**') continue to grow in opposite directions, albeit at different rates. For all the fibrils that show apparent multidirectional growth (e.g., **c**, **e**, **f**) the elongation of the different branches is asynchronous with respect to the starting time and occurs at different rates. Moreover, all of the fibrils start to grow from a granule or small seed that appears as a nodule of higher fluorescence intensity than the fibrils that extends away from the origin (shown by the fluorescence intensities in Fig. 3.5). For fibril **c**, **e**, and **f** the initial granules can be seen as early as 870 min. We think the data in Fig. 3.4 are more consistent with multiple fibrils growing unidirectionally from a single seed. First, the extension of different arms occurs at different times during the reaction (for example, fibril **f**). Second, the elongation of different arms occurs with different rates. Third, growth in multiple directions in rosette-like bundles is observed from larger seeds such as **a**.

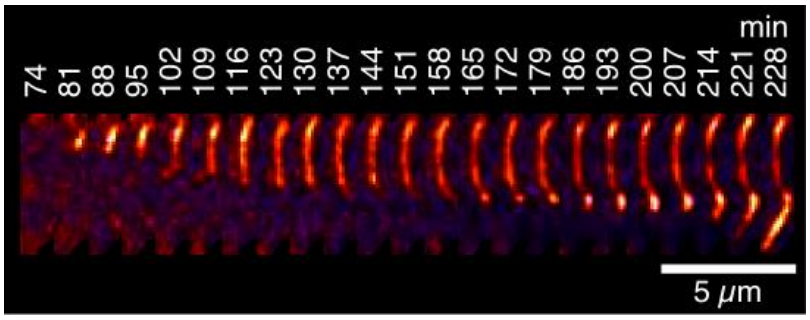

Figure 3.5 Fibril elongation from a seed. Figure showing an individual seed growth over time.

Fibril Thickening- The third process evident in the TIRFM data is an increase in the fluorescence intensity of some of the fibrils during the course of the reaction. We attribute this observation to growth of new fibrils along the templates provided by preformed fibrils, in a mechanism analogous to the "heterogeneous nucleation mechanism" first described for sickle cell hemoglobin fibrils [37]. Heterogeneous nucleation, also called "secondary nucleation", has been previously shown to play a role in amylin fibrillization based on kinetic studies [38, 39].

The intensity increases in preformed fibrils are best illustrated by fibril **d**, which is first observed in faint outline by 870 min (Fig. 3.4). The fibril appears between two images collected in a 5 min interval and as such is likely to represent a fibril that has precipitated from solution [34, 35]. Consequently, we have no information on the growth of fibril d before ~870 min. Once deposited on the slide, fibril **d** continues to grow slowly to close a lariat-like loop until 1870 min. In addition to these elongation processes, the fluorescence of fibril **d** becomes markedly more intense between 870 and 2895 min. The same type of increase in intensity is also seen for a number of the other fibrils including fibril **c** between 1195 and 2895 min. For reference, seed **b** maintains roughly the same intensity from the time it is first observed at 235 min to the end of the reaction at 2895 min, and fibril **g** shows little change in intensity between 1440 and 2895 min.

Fibrils are often observed in aligned bundles in high-resolution AFM and EM images. Since these structures are often wound around each other in a supercoil, it is unlikely they are formed by fibrils sticking together. One mechanism that could account for the growth of fibrils in bundles is the heterogeneous nucleation mechanism first proposed for sickle-cell hemoglobin fibrils [37]. Fibrils are first formed by homogeneous (or primary) nucleation during the lag time of the reaction and then elongate during the growth phase [37, 107]. After an initial population of fibrils are formed, additional heterogeneous (or secondary) nucleation sites can became available along the length of preformed fibrils. These can promote the growth of new fibrils using the original fibrils as templates [37]. An alternative to this mechanism is that the strands in a bundle could grow simultaneously. Evidence for this mechanism was obtained from AFM imaging of amylin fibril growth on a mica surface [103]. On the basis of the TIRFM data, both types of mechanisms appear to have a role in amylin fibrillization. Fibril **f**, for example, is one of the most

intensely fluorescent in Fig. 3.4. The high fluorescence intensity of fibril f is maintained as it grows upward toward seed a, from 870 to 1870 min. An exception is in the frame at 1155 min, where a small thin, possibly frayed extension is seen for fibril **f** that grows in advance of the thicker fibril. To a good approximation, however, the growth of fibril f is consistent with a mechanism where if its stronger fluorescence intensity is due to a bundle rather than a single fibril, the strands in the bundle grow at the same time. In contrast to fibril **f**, the fibrils **c** and **d** start out as faint strands that increase in intensity with time, which is more readily explained by a template-assisted growth mechanism rather than simultaneous growth of strands in a bundle of fibrils. The increase in intensity of fibrils **c** and **d** is not distributed evenly throughout the fibril but appears to occur in patches or nodules that suggest the presence of multiple heterogeneous nucleation sites along the length of a fibril.

At the resolution of TIRFM we cannot accurately determine the width of fibrils [34]. Oscillation of fluorescence intensity could occur from fibrils diffusing in and out of the TIRFM illumination field. The changes we observe happen on time scales of hours (Fig. 3.4), however, and we see increases in fluorescence intensity rather than the variations that would be expected if the fibrils were moving in and out of the evanescent field. Differential binding of ThT to the fibrils is another explanation that seems unlikely to account for the increase in fluorescence intensity since the initial staining of the fibrils occurs in less than 5 min. One possibility we cannot exclude is that preformed fibrils could be undergoing a conformational change that leads to increased ThT fluorescence. That the fluorescence increases occur progressively along the length of the fibrils and with rates similar to fibril growth seems more consistent with the formation of new fibrils than with changes in the properties of preformed fibrils.

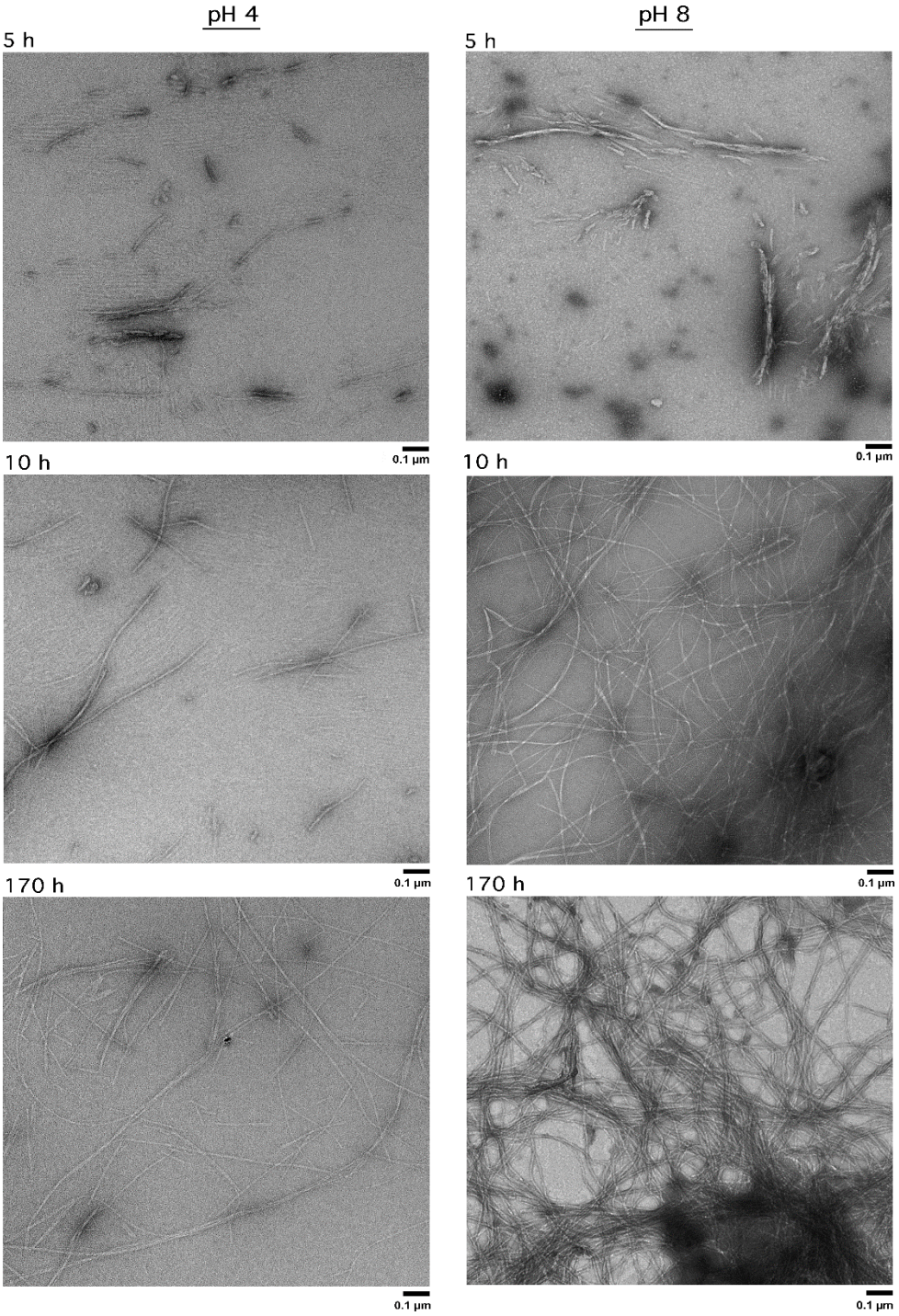

Figure 3.6. Time course of amylin fibrillization followed by EM. The panels on the left side show fibrils grown at pH 4 and the right side fibrils grown at pH 8. Images were sampled after solution incubation periods of 5 h (top), 10 h (middle), and 1 week (bottom). In contrast to the TIRFM (Fig. 3.4), we cannot track the same aggregates over time by EM. To give a representative description, the images shown are the most typical of 510 images from different regions of the EM grid prepared for each time point and pH. All images are at a magnification of 68,000x.

Comparison of Fibril Growth by TIRFM and EM. In contrast to TIRFM where we can watch individual aggregates grow on the surface of a slide, EM can be used to image fibrils at high resolution after growth in bulk solution and transfer to a copper grid for uranyl acetate staining and imaging. We obtained EM images of amylin fibrils after aggregation times of 0.5, 5, 10, 20, and 170 h (1 week). For each time point we recorded five images from different areas of the grid and show the most representative for time points at 5, 10, and 170 h in Fig. 3.6. Although EM is not suited for quantifying the amount of aggregates, we saw a qualitative increase in the number of fibrillar species with time, and more fibrils were formed at pH 8 than pH 4.

At the earliest time points in the reaction, between 0.5 and 5 h, the fibrils at pH 4 form sheets of very thin fibrils together with a smaller number of short robust fibrils (Fig. 3.6). The fibrils formed during comparable times at pH 8 have a more frayed appearance (Fig. 3.6). By 10 h, the sample at pH 4 shows a larger number of long fibrils together with the thin sheets of fibrils observed at earlier time points. In the pH 8 samples the fibrils formed by 10 h are longer and are more often arranged in curved coiled ribbon structures compared to the sticklike fibrils seen at pH 4. The last set of images in Fig. 3.6 show the samples after 1 week (170 h), well after changes in TIRFM images had subsided (24-48 h). In the last time points, the fibrils at pH 8 reach lengths of 12 μm while at pH 4 some fibrils as short as 0.05-0.1 μm are still observed together with long fibrils (Fig. 3.6). Note that these shorter fibrils at pH 4 would be too small to be resolved by TIRFM. The fibrils in the final time point at pH 8 are arranged in dense meshworks and have an average width of 14.4 ± 5.6 nm compared to 6.8 ± 1.9 at pH 4, consistent with previous reports that amylin fibrils at pH 8 are thicker than at pH 4 [23].

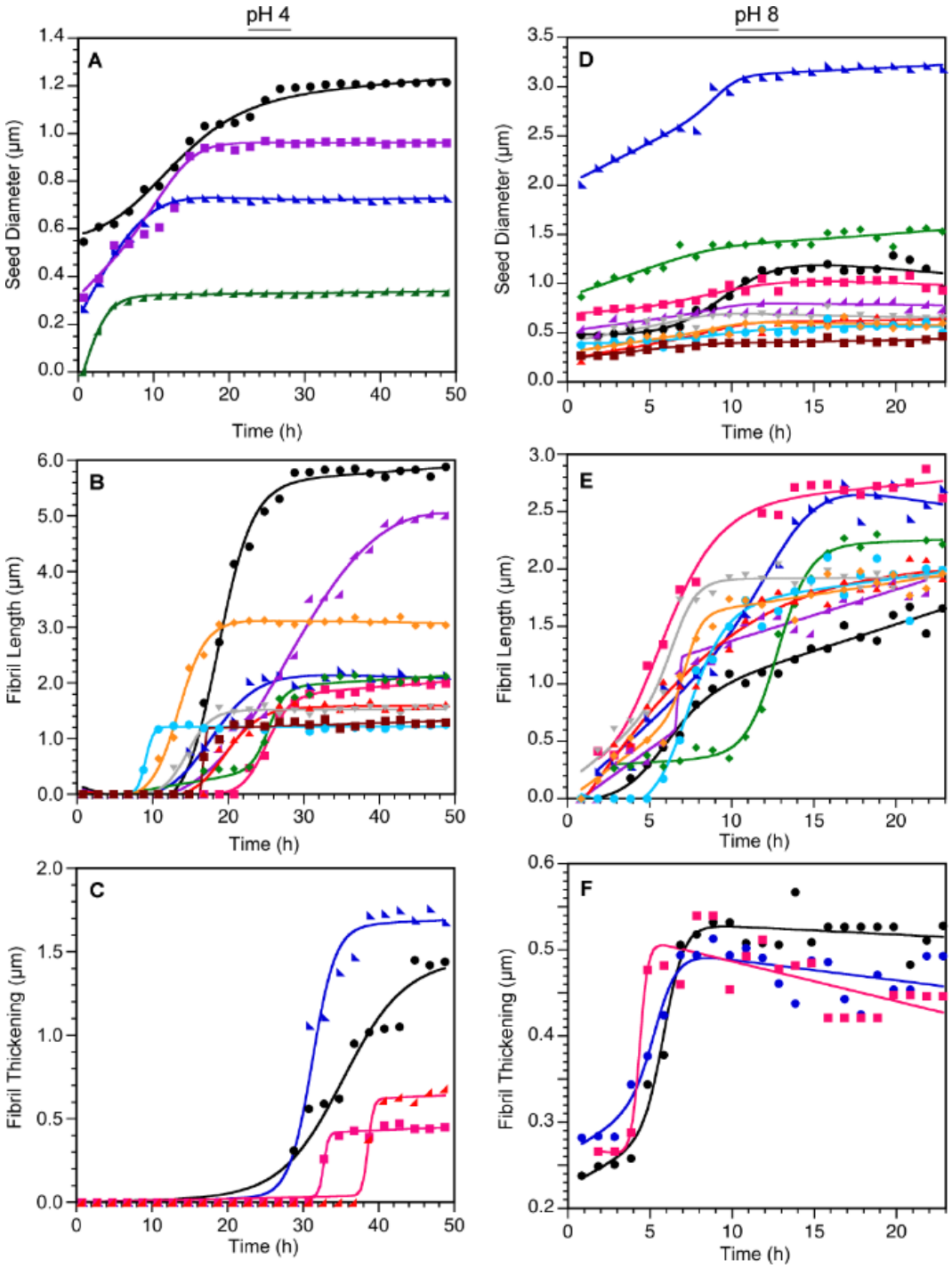

Figure 3.7. Kinetics of individual seed growth, fibril elongation, and fibril thickening from TIRFM data at pH 4 (A, B, C) and pH 8 (D, E, F). The data for each fibril were fitted to a six-parameter equation[38] in order to extract lag times, growth rates, and maximal length parameters, which are given in Table 3.1.

Kinetics of Individual Aggregate Growth. Fig. 3.7 shows growth curves for seeds, fibrils, and the process we attribute to fibril thickening at pH 4 and 8. Kinetic parameters obtained from least-squares fits of the data are summarized in Table 3.1. Under both conditions seed growth is observed first followed by fibril elongation and fibril thickening. Because many of the seeds we looked at were already present at the start of the reaction, we consider the lag time for seed formation undefined in the TIRFM experiment. On the basis of solution experiments, the lag times for fibrillization under the conditions of the TIRFM experiments (samples in 10% acetonitrile) are about 30 min (Fig. 3.8 , Table 3.1), which is shorter than the ~45 min dead time of the TIRFM experiments. The apparent average lag time for species with a distinct fibrillar morphology by TIRFM is much longer: about 4 h at pH 8 (Fig. 3.7B) and 14 h at pH 4 (Fig. 3.7D). We note that in the earliest stages of the TIRFM experiments most of the ThT fluorescence is due to seeds, which are likely to be composed of plaques or clusters of fibrils too small to be resolved by TIRFM. Fibril thickening had the longest lag times between 26 and 37 h at pH 4 and between 3 and 4 h at pH 8 (Fig. 3.7 C and F). Radial seed growth had the slowest rate, fibril elongation rates were intermediate, and fibril thickening rates were the fastest (Table 3.1). Comparing the reactions at the two pH values, all processes had longer lag times and slower growth rates at pH 4 compared to pH 8 (Table 3.1).

At the completion of the reactions we could measure the maximum dimensions of the individual aggregates used to characterize fibrillization kinetics by TIRFM. The averages of these values are given in Table 3.1. We saw no correlation between growth rates and the final sizes of individual seeds or fibrils. The final dimensions for the thickening process are shorter than for elongation because the increases in fluorescence intensity often occurs in patches along the length of a fibril, and we only characterized the growth kinetics of uninterrupted segments.

Fibrillization Kinetics in Solution. Fig. 3.8 shows kinetic data for amylin fibrillization in solution. The reactions were carried out at the same 100 μM amylin concentration and 25 °C temperature as the TIRFM experiments. For one set of experiments monomeric amylin was initially dissolved in ACN and brought up in buffer to a final concentration 10% ACN (v/v). This set of conditions is the same as for the TIRFM and EM experiments shown in Fig. 3.1-3.7. We also looked at amylin that was initially dissolved in DMSO [23] and brought up in buffer to a final concentration of 4% DMSO (v/v). The first 10 h of the reactions shows a sigmoidal profile typical of a nucleated fibrillization reaction consisting of a lag time, a growth phase, and a plateau [107, 108]. This portion of the data were fitted to a six parameter model [108] to obtain the kinetic parameters for the solution reactions given in Table 3.1. The lag times obtained in solution are much shorter than the lag times for fibril growth obtained for the fibrils imaged by TIRFM. The rates of fibril growth are slower for individual fibrils but within a factor of 2 of the solution rates (Table 3.1). Part of the reason for this difference is that in the TIRFM experiment we are measuring the kinetics of the longest fibrils in the reaction (18 μm), whereas the majority of the fibrils formed in the early stages of the reaction are too short to be discerned as such at the resolution of the TIRF microscope (<0.5 μm). When considering differences in elongation rates between the experiments, it is also important to note that in solution we are measuring only ThT fluorescence, which does not distinguish between the species with different morphologies or different growth processes observed by TIRFM.

At time points following the initial leveling off of fluorescence after 10 h, the solution reactions show behavior that deviates from standard fibrillization time curves. In 4% DMSO solvent, there is a decrease in fluorescence following the initial plateau. It has been argued that

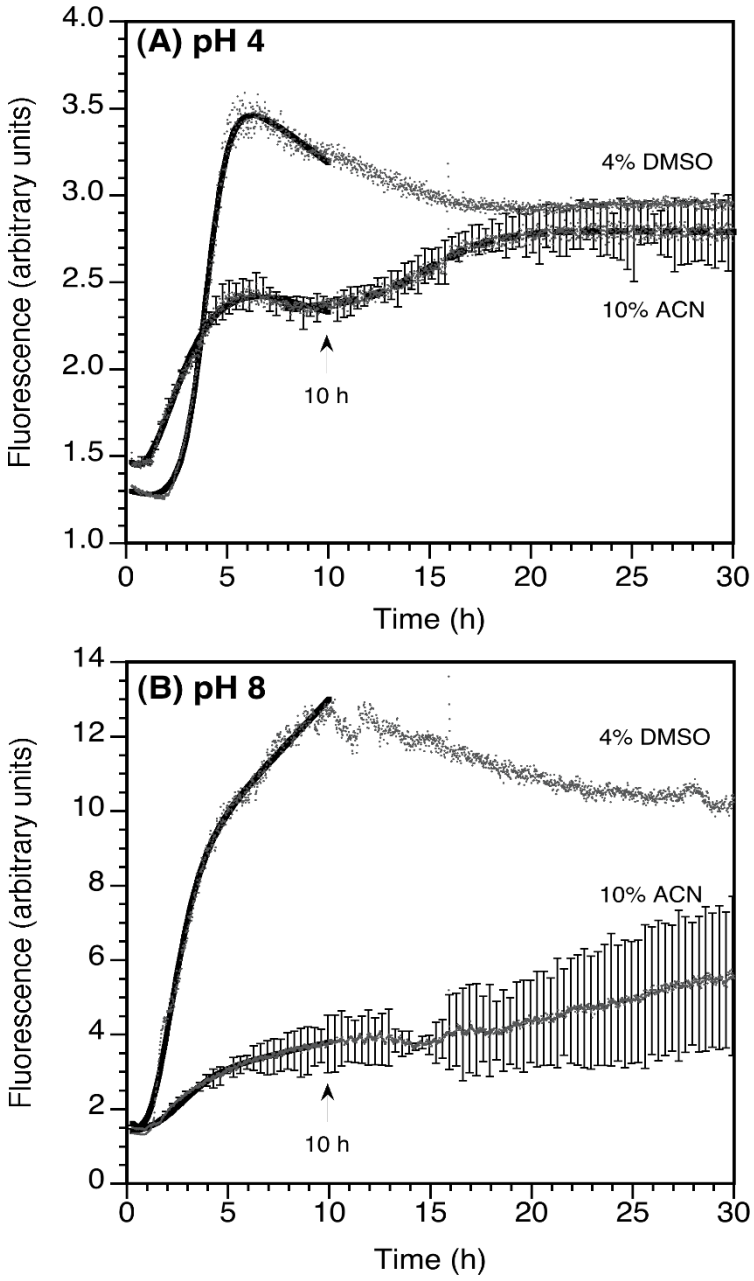

Figure 3.8 Kinetics of fibrillization in solution followed by ThT fluorescence at pH 4 (A) or pH 8 (B). For each pH, samples were initially dissolved in ACN and brought up in buffer to a final concentration of 10% (v/v) ACN or in DMSO and brought up to a final concentration of 4% (v/v) DMSO. The data for each set of conditions are averages of duplicate measurements. Representative errors are shown for 5% of the data points in the ACN experiments, and errors in kinetic parameters from the duplicate data sets are given in Table 3.1. The data for the first 10 h only were fitted to a six-parameter equation [108] to obtain values for lag times and rate constants which are given in Table 3.1. For the pH 4 data in the presence of 10% CAN, we separately fitted the data between 8 and 30 h to a second sigmoidal transition (dashed curve). For the other experiments the data beyond 10 h do not define a sigmoidal transition and were not fit.

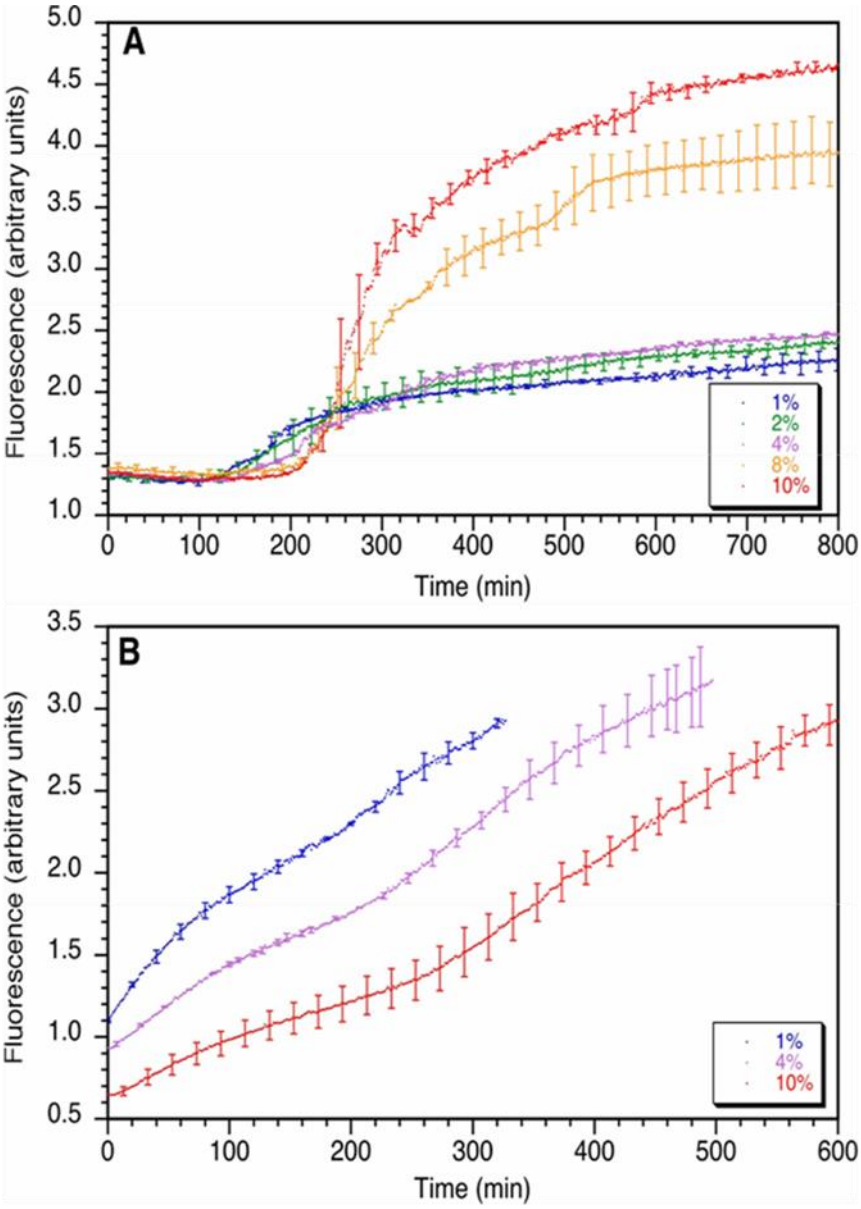

Figure 3.9 Effects of solvents used to dissolve amylin on fibrillization reactions. (**A**) Varying DMSO concentrations. Starting from a stock solution of amylin in pure DMSO, samples were diluted with 20 mM phosphate buffer (pH 8) to the DMSO concentrations indicated. The amylin concentration for all experiments was 5 µM, ThT was 10 µM, and all experiments were done at a temperature of 25 ºC. Lag times and rates increased with increasing DMSO concentration. Lag times: 108, 119, 135, 209, 215 min. Rates: 4.7 x 10^{-3}, 3.8 x 10^{-3}, 4.6 x 10^{-3}, 7.2 x 10^{-3}, 9.8 x 10^{-3} min^{-1} between 1 and 10% DMSO. (**B**) Varying ACN concentrations. The amylin concentration was 100 µM in 60 mM citrate buffer (pH 4) at 25 ºC. Note that all reactions with ACN show biphasic transitions. With increasing ACN concentration the rate of the first transition decreases about two fold while the second transition rate appears constant. Rate 1: 9.0 x 10^{-3}, 5.1 x 10^{-3}, 4.5 x 10^{-3}; rate 2: 2.0 x 10^{-3}, 2.6 x 10^{-3}, 1.5 x 10^{-3}. Apparent lag times for the second transition increase from 1 to 10% ACN (180, 230, 260 min), while for the first transition they could not be accurately defined. Errors are from duplicate measurements and are shown for 5% of the data in both A and B.

once fibrils have formed the solution is no longer homogeneous so that fluorescence measurements become erratic and are of questionable value [109]. At amylin concentrations below 20 μM the plateaus in 4% DMSO are nearly flat, suggesting that the decreasing plateau at 100 μM amylin may be due to an increase in the turbidity of the samples accompanying the formation of insoluble fibrils. For the 10% ACN solvent, we see a reproducible increase in fluorescence following the initial fluorescence plateau. This increase in fluorescence following an initial steady state is observed for fibrillization reactions where the amylin concentration is as low as 5 μM and suggests that fibrils continue to form after the first 10 h of the reaction. At pH 4 this is manifested as a second sigmoidal curve that starts after the first apparent plateau is reached (Fig. 3.8A). Note that the increase in florescence intensity during the second sigmoidal phase is about 40% of the increase in the first sigmoidal phase that occurs within the first 10 h of the reaction. At pH 8 we also see a continuing increase in fluorescence after the initial sigmoidal phase, with a shallower apparently linear time dependence that does not subside by 30 h (Fig. 3.8B). In this case as well, the increase in fluorescence between 10 and 30 h is about 70% of the increase in fluorescence during the first 10 h of the reaction. The increases in ThT fluorescence during the second stage of the reaction suggests that fibrils are formed through secondary nucleation, catalyzed by the initial population of fibrils that grew during the first 10 h.

If we compare the time course of the individual aggregates measured by TIRFM to the solution data, the largest seeds that we could measure accurately at pH 4 formed between 0 and 20 h (Fig. 3.7A), a time that extends beyond the first 10 h sigmoidal phase of the solution reaction in 10% ACN (Fig. 3.8A). Fibrils grew between 9 and 40 h (Fig. 3.7B)-a time that also extends past the first and into the second sigmoidal phase of the reaction in solution (Fig. 3.9A). Consequently,

Table 3.1. Growth Rates of ThT-Sensitive Amylin Aggregates[a].

Conditions	Lag time (h)	Growth rate (μm/h)	Max length (μm)	Species average
pH 4				
seed diameter	N.D.[e]	0.27 ± 0.04	0.81 ± 0.18	4
fibril elongation	14.14 ± 1.54	0.56 ± 0.09	2.60 ± 0.51	10
fibril thickening	31.3 ± 2.4	1.75 ± 0.76	1.08 ± 0.31	4
solution (10% ACN, pt 1)[b,c]	0.59 ± 0.35	1.20 ± 0.02	N.A.[f]	N.A.[f]
solution (10% ACN, pt 2)[b,d]	11.93 ± 2.09	0.74 ± 0.25	N.A.[f]	N.A.[f]
solution (4% DMSO)[b]	2.56 ± 0.34	1.70 ± 0.30	N.A.[f]	N.A.[f]
pH 8				
seed diameter	N.D.[e]	0.70 ± 0.09	1.06 ± 0.26	10
fibril elongation	4.31 ± 1.11	0.73 ± 0.18	2.10 ± 0.13	9
fibril thickening	4.18 ± 0.25	2.35 ± 0.83	0.48 ± 0.02	3
solution (10% ACN)[b]	0.42 ± 0.01	1.15 ± 0.01	N.A.[f]	N.A.[f]
solution (4% DMSO)[b]	0.04 ± 0.04	1.32 ± 0.01	N.A.[f]	N.A.[f]

[a] Rates for the different growth processes were obtained by nonlinear least-squares fits of the kinetic curves in Fig. 3.7 and 3.8 as described [108]. Rate constants are reported as means ±1 standard error. Note that the uncertainties for the TIRF data describe the variation between individual aggregates (Fig. 3.7) while for the solution data (Fig. 3.8) they were obtained from duplicate measurements of solution population-weighted averages.
[b] The units for the fibril growth rates from solution experiments are fluorescence intensity (arbitrary units)/h. For solution experiments, except 10% ACN at pH 4 , kinetic parameters were calculated by considering only the first 10 h of the reactions which show a sigmoidal time dependence characteristic of fibrillization.
[c] Kinetic parameters derived from the first part of the reaction between 0 and 10 h.
[d] Kinetic parameters derived from the second part of the reaction between 8 and 30 h.
[e] Not determined since many of the seeds are already visible in the first images recorded at both pH 4 and pH 8. The dead time for the TIRF experiments was ~45 min.
[f] Not applicable.

the lag times and elongation rates of the fibrils observed by TIRFM are in much better agreement with the kinetic parameters obtained from the second phase of the solution reaction (Table 3.1). The increases in fluorescence intensities of the fibrils imaged by TIRFM occur between 20 and 40

h (Fig. 3.4 and 3.5C), well past the first 10 h sigmoidal phase of the solution reaction (Fig. 3.8A).

Finally, the changes in fibril morphology and association by EM (Fig. 3.6) occur on slower time scales than the first 10 h transition seen for the solution reaction at pH 4 with 10% ACN (Fig. 3.8A).At pH 8 where fibrillization is faster, the growth of individual seeds (Fig. 3.7C) and fibrils (Fig. 3.7D) is more comparable to the solution rates (Fig. 3.8B), but asynchronicity is still observed, with some individual fibrils imaged by TIRFM growing after the first fluorescence plateaus is reached in bulk solution. In the presence of 4% DMSO, the rate of fibrillization is increased and the reactions reach a larger ThT fluorescence plateau, suggesting that more fibrils are formed than with 10 % ACN (Fig. 3.8). We found that increasing the DMSO concentration between 1% and 10% (v/v) promotes fibrillization primarily by increasing the elongation rate of the reaction (Fig. 3.9). Thus, DMSO appears to act as a catalyst for fibrillization. By contrast, at large concentrations (≥95%) DMSO disaggregates fibrils to monomers. Given the differences in solution reaction profiles between samples dissolved in 10% ACN and 4% DMSO, we collected additional TIRFM data to examine the time dependence of fibrillization of a 100 μM amylin sample at pH 8 in 4 % DMSO (Fig. 3.9). Compared to samples in 10 % ACN, the sample in 4% DMSO fibrillized much faster and the appearance of fibrils was more abrupt, resembling a phase transition. Most fibrils formed in 2 h in the TIRFM experiment-a time more in line with the reaction in solution (Fig. 3.8B). We saw examples of all three growth mechanisms observed with 10% ACN: seed growth, fibril elongation, process with 4% DMSO. These observations suggest primary nucleation is favored over secondary nucleation in 4% DMSO compared to 10 % ACN. The organic phases such as dichloromethane, chloroform, or lipids have been shown to accelerate the fibrillization of a 20-29 fragment of amylin and shift the balance from secondary to primary nucleation mechanisms [39].

Discussion

TIRFM shows three types of amylin fibrillization processes: seed growth, elongation, and fibril thickening. Seeds are the earliest species seen and are likely to consist of plaques of short fibrils based on their size, growth rates, and ThT binding. Fibrils invariably elongate from small seeds or granules, except for some rare cases where we see fibrils apparently branch from other fibrils in a mechanism similar to that observed in TIRFM studies of glucagon fibrillization [32]. Fibril elongation appears to be unidirectional, if we consider that multiple fibrils can grow in opposite directions with different rates, starting from a common seed. A third type of process is manifested as a progressive increase in the fluorescence intensity of preformed fibrils. We attribute the fluorescence intensity increases to template-assisted growth of fibrils alongside preformed fibrils. The fluorescence intensity increases often occur in patches, suggesting that multiple secondary nucleation sites can occur along the length of a fibril. We also see instances of fibrils that grow with a uniformly high fluorescence intensity from start to finish (upper branch of fibril **f** in Fig. 3.4), which could be consistent with the simultaneous growth of strands in a bundle of fibrils as has previously seen in AFM experiments [103].

Although the three types of aggregation processes (seed growth, fibril elongation, and fibril thickening) manifest themselves differently by TIRFM, they may occur by the same mechanism, namely heterogeneous or secondary nucleation. This seems consistent with the time course of the growth processes imaged by TIRFM and EM, which for samples in 10% ACN occur after the completion of the main phase of the reaction in bulk solution. In the classical nucleation mechanism, aggregation is initially disfavored by entropy since association involves loss of rotational and translational degrees of freedom for the monomers. The time required to form the

"critical nuclei" that propagate polymerization is manifested as a lag time, during which aggregation is not detected [37]. Once critical nuclei are formed in a process called "homogeneous" or "primary" nucleation, the reaction enters a growth phase as the loss of entropy for the monomers is compensated by the gain in enthalpy due to the formation of new noncovalent interactions when the monomers become incorporated into the growing fibril [37]. The reaction proceeds, reaching an eventual plateau. In a double nucleation mechanism, fibrils can form through homogeneous or primary nucleation steps but can also be initiated by heterogeneous or secondary nucleation on the surfaces of preformed fibrils [37, 110]. Additional mechanisms that could play a role in secondary nucleation include branching of fibrils or fragmentation of fibrils in a way that introduces new sites for incorporation of monomers [39].

Our proposal of heterogeneous nucleation of amylin fibrillization in the current study has been confirmed recently by Goto lab using TIRFM and fluorescently tagged amylin. Their findings using ThT and Alexa 532-amylin confirms that amylin fibrillization takes place at both ends of a short fibril or seed. The study also confirms the increase in fluorescence of the preformed fibrils that we have reported in our study, corresponds to the lateral binding of Alexa532-amylin [111] to the preformed fibrils. Studies by the Miranker lab, looking at the dependence of polymerization kinetics on monomer and seed concentrations, established that secondary nucleation is the predominant mechanism of amylin fibrillization in aqueous solution [38, 39]. Additional amyloidogenic proteins for which secondary nucleation appears to play important roles in fibrillization include Aβ, [112] prion protein, [113] β2-microglobulin, [114] insulin, [115] and glucagon [32]. One strategy to inhibit fibrillogenesis is to develop compounds that interfere with the formation of the primary nuclei needed for fibril formation. However, if primary and secondary

nucleation have a different structural basis, interfering with primary nucleation may not be effective in controlling secondary nucleation once a population of fibrils has been established. The possible mechanisms for inhibition of fibrillization and hence cytotoxicity are discussed in next chapter of this thesis.

CHAPTER IV: Charge-Based Inhibitors of Amylin Fibrillization and Toxicity

Abstract:

To test the hypothesis that repulsion of like-charges is one of the main forces opposing amyloid fibril assembly, we designed peptides that substitute strings of positively or negatively charged residues in the sequence of the amyloidogenic hormone amylin, which contributes to type 2 diabetes pathology. Peptide Arg-1 substitutes four positively charged arginine residues for the segment of amylin that forms the end of strand β1 and Arg-2 the beginning of strand β2, in structural models of amylin fibrils. A third variant Mem-T that substitutes negatively charged aspartate residues for the segment with the largest avidity for membranes was designed to interfere with the ability of amylin to disrupt membranes. All three of the charge-loaded peptides fibrillize poorly on their own and inhibit fibril elongation of WT-amylin at physiological salt concentrations. The inhibition of fibril elongation rates is dependent on salt concentration indicating the analogs affect WT-amylin through electrostatic interactions. Arg-1 protects against WT-amylin cytotoxicity towards the MIN6 mouse model of pancreatic β-cells, Arg-2 protects against cytotoxicity at higher concentrations, while Mem-T has no effect. Although Mem-T inhibits fibril elongation rates like the other two analogs, it decreases the lag times for WT-amylin fibrillization possibly due to complementary electrostatic interactions between the negative charges in the analog and the positive charges in the WT peptide. The most effective inhibitor Arg-1, inhibits WT-amylin fibril elongation rates with an IC_{50} of ~1 μM and cytotoxicity with an IC_{50} of ~50 μM, comparable to other types of amylin fibrillization inhibitors reported in the literature. These studies suggest that electrostatic interactions can be exploited to develop new types of inhibitors of amyloid fibrillization and toxicity.

Introduction

Amyloidoses are protein misfolding diseases characterized by fibrillar protein deposits, in which protein monomers form intermolecular β-sheets running along the length of the fibrils. In type 2 diabetes, the positively charged 37-residue hormone amylin, the subject of the present study, misfolds into cationic fibrils that have been implicated in the destruction of the pancreatic β-cells that make insulin and amylin, thus contributing to pathology.

Consideration of amyloid structures suggests that like-charges, replicated along the fibril axis by the intermolecular β-sheet pairing of monomers, should energetically disfavor self-association through electrostatic repulsion [40, 41]. Conversely, compensation of charges displayed on fibril surfaces may be important in the interactions of amyloids with polyanions such as heparan sulfate proteoglycans and membrane lipid bilayers [40, 42, 43]. Replacements of single charged residues can have large effects on fibrillization kinetics as shown with amyloid-beta [41], α-synuclein [44, 45], and amylin [46]. Amylin represents a particularly favorable system for investigating the roles of electrostatic charges in fibrillization, since the core of the intermolecular β-sheet fibril structure has only one pH-titratable group, His18.

We have extensively characterized the pH dependence of amylin fibril formation, due to the acid-base equilibrium of His18 [116]. The histidine has a pK_a lowered to 5.0 in the fibrils compared to the random coil value of 6.5 [116]. The lowered pK_a is due to electrostatic repulsion between positively charged His18 residues on neighboring molecules in the fibril and the hydrophobic environment of the residue in the amyloid structure. The lowered pK_a indicates that protonation of His18 is energetically unfavorable for fibril formation. As such, His18 acts as an electrostatic switch, inhibiting fibrillization in its charged state at acidic pH and favoring

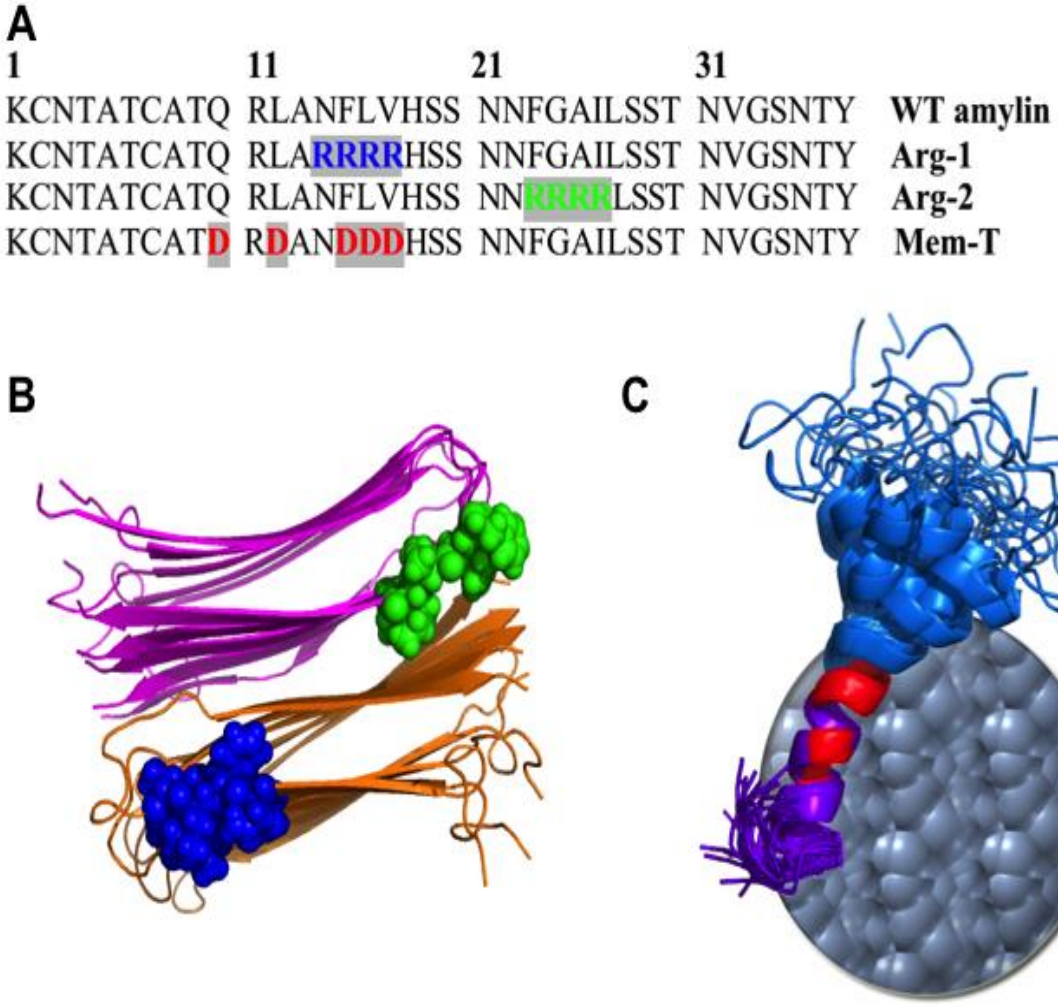

Figure 4.1 Design of fibrillization inhibitors. (A) Sequences of WT-amylin and three peptide analogs that incorporate strings of positive or negative charges in the amylin sequence. (B) Model of the stacked β-hairpin structure of amylin fibrils based on ssNMR [25]. Positively charged arginine residues are shown as spheres that are positioned at the end of strand β1 in Arg-1 (blue), or in the hairpin turn followed by the start of strand β2 in Arg-2 (green). (C) Solution NMR model of micelle-bound amylin, in which the N-terminal residues 5-17 are embedded in the hydrophobic environment of the micelle [117]. The Mem-T peptide incorporates five aspartate residues in this region (red) in order to interfere with membrane binding through electrostatic repulsion between negatively-charged residues on the peptide and lipid head-groups.

fibrillization in its uncharged state at neutral pH. The charged state of His18 also affects the morphology of amylin fibrils as determined by EM (please see Fig. 3.6) [23, 116, 118]. At

physiological pH where His18 is uncharged, WT-amylin forms a greater number of fibrils, the fibrils are longer, have a more twisted morphology, and are more likely to be laterally associated into bundles than the fibrils formed at acidic pH when His18 is charged. The morphological features of WT-amylin at acidic pH are replicated in the H18R-amylin mutant, which substitutes the histidine with a positively-charged arginine [116]. The presence of a charged arginine at position 18 in H18R-amylin lowers cytotoxicity to MIN6 β-cells compared to WT-amylin, which has an uncharged histidine at a physiological pH of 7.4 (Fig. 4.2) [95, 116]. Similar results were obtained with a S20K variant of amylin. The S20K mutation fibrillizes much more slowly than WT-amylin, partly due to the introduction of a positive charge in a segment of the peptide that participates in the hairpin turn of the fibril structure [46]. Moreover, the S20K mutant peptide inhibits fibrillization of WT-amylin when added in *trans* [46].

These observations suggest that the introduction of single charged amino acids in the portion of the amylin sequence that forms the fibril core can markedly inhibit fibrillization. We therefore thought to exploit these properties by designing peptide variants that incorporate a string of residues with like charges into the amylin sequence, as shown in Fig. 4.1. The first peptide Arginine-variant 1 (Arg-1), substitutes four arginines for WT-amylin residues Asn14-Val17 (Fig. 4.1A). These residues are part of strand β1 (blue spheres in Fig. 4.1B) in the model of the amylin fibril structure determined by ssNMR [25]. The protofilament building block of the amylin fibril structure has two C_2-symmetry related stacks of intermolecular β-sheets (shown in orange and purple in Fig. 4.1B) [25].

The positively charged residues introduced in the Arg-1 variant would be on the surface of the protofilament. In our design, we envisioned that Arg-1 would act as a fibril extension inhibitor.

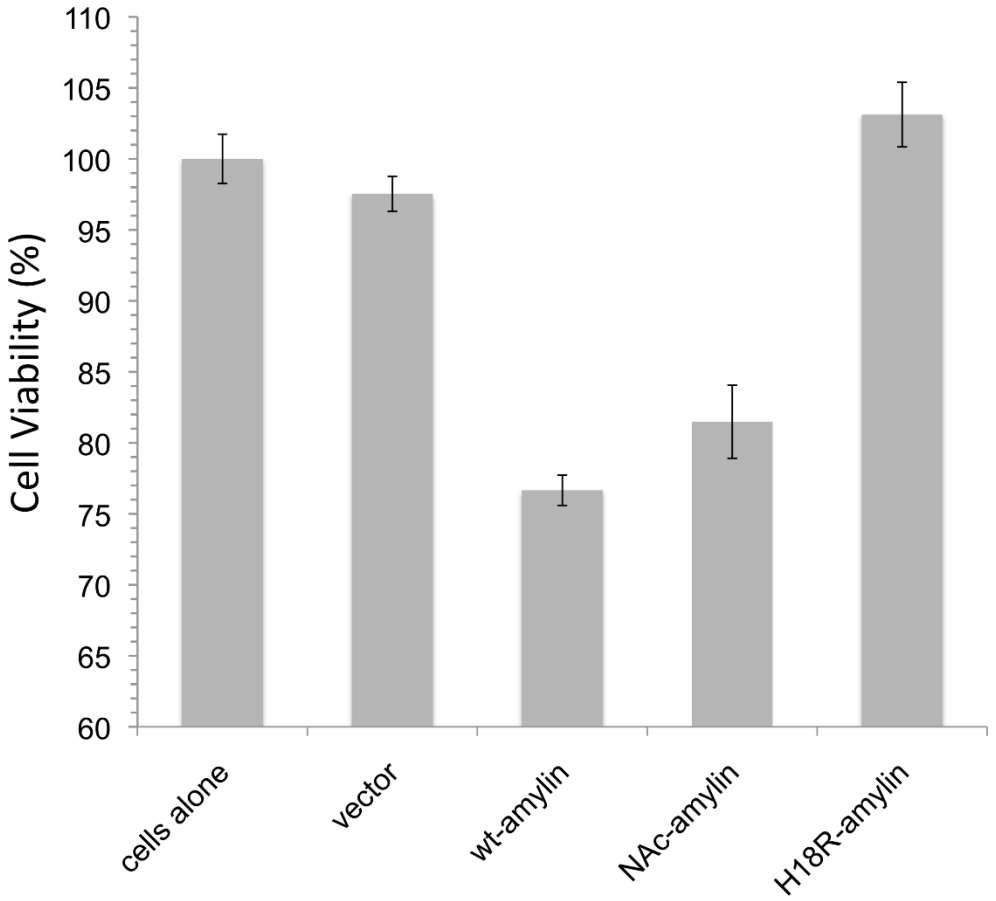

Figure 4.2 Cytotoxicity experiments using cultures of a MIN6 mouse insuloma model of β-pancreatic cells. Data are expressed as means ± S.E.M from triplicate measurements. Peptides were prepared as stock solutions in DMSO and were freshly added to the cells to give a final peptide concentration of 80 μM as measured with a micro-BCA assay, and a final DMSO concentration of 1% (v/v). The vector control contained 1% DMSO only, which was present in all experiments except the cells alone control wells. (adapted from [116])

The highly amyloidogenic segment between residues Ser20-Ser29 [4, 79] is retained in the sequence, and would allow the peptide to attach to growing fibrils of WT-amylin, whereas the four arginines in Arg-1 would disfavor addition of monomers through electrostatic repulsion with the positively charged residues Arg11 and His18 in the WT-sequence. It is important to note that since the C-terminus of amylin is naturally amidated, there are no negatively charged residues in the sequence of WT-amylin (Fig. 4.1A). In a second analog, Arginine-variant 2 (Arg-2), four arginine residues are substituted for residues Phe23-Ile26 in the center of the amyloidogenic segment. In

the fibril structure [25] this corresponds to the end of the β-hairpin and the start of strand β2 (green spheres in Fig. 4.1B). The design objectives for Arg-2 were the same as for the Arg-1 peptide but the string of four arginine residues are positioned in the interior of the protofilament structure as opposed to the surface (Fig. 4.1B). A third peptide, the "Membrane Trojan" analog (Mem-T) was conceived as an inhibitor of the interactions of WT-amylin with cell membranes, rather than as a fibril elongation inhibitor. The motivation for the design of the Mem-T analog was studies that suggest the species responsible for amylin toxicity may not be amyloid fibrils but soluble oligomers that form membrane-spanning pores, thus compromising intracellular ion homeostasis and cellular integrity [4, 119]. The Mem-T analog (Fig. 4.1C) was conceived based on our NMR structure of WT-amylin bound to membrane mimetic SDS micelles [117]. In the NMR structure, the Ala5-Val17 segment is positioned in the hydrophobic environment of the micelle based on paramagnetic probe studies[117]. The Ala5-Val17 has the highest avidity for lipid membranes based on a number of studies [4, 86]. We thus envisioned that the Mem-T analog would be able to form mixed oligomers on the surfaces of membranes with WT-amylin, through the His18-Tyr37 segment, on the surfaces of membranes but that membrane penetration of the mixed oligomers would be blocked through electrostatic repulsion between the negatively charged aspartates in the Mem-T peptide and the negatively charged phosphate groups of the membrane lipid bilayer (Fig. 4.1C).

In the present work we examined the ability of the three amylin analogs Arg-1, Arg-2 and Mem-T to form fibrils using a kinetic assay that employs the amyloid-specific fluorescent dye thioflavin T (ThT), and by imaging the reaction products with transmission electron microscopy (TEM). We investigated the ability of peptide analogs to inhibit fibril formation when added in

trans to WT-amylin, and characterized the concentration dependence of inhibition. Because we expected the three designed peptides to exert their effects through electrostatic interactions, we looked at the effects of NaCl concentration on inhibition. Finally, we examined the ability of the peptide inhibitors to suppress cytotoxicity in a MIN6 mouse model of β-pancreatic cells when challenged with WT-amylin.

Materials and Methods

Materials-Human WT-amylin was from Biopeptide (San Diego, CA). The Arg-1, Arg-2 and Mem-T peptides were custom-synthesized by NeoBioLab (Woburn, MA). All peptides were synthesized with an amidated C-terminus, which occurs as a natural post-translational modification in human WT-amylin. The peptides were purified to >95%, supplied as dry powders, and were taken up in 100% DMSO to form 1.1 mM peptide stock solutions that were stored in aliquots at -80 °C before use. Freshly thawed aliquots of the stock solutions were lyophilized and re-dissolved to the desired peptide concentration in 1 % (v/v) DMSO for cytotoxicity experiments and 2 % (v/v) DMSO for all other experiments. Ultrapure grade Thioflavin T was from AnaSpec (Fremont, CA). The Alamar Blue dye to measure cell viability in cytotoxicity assays and DMEM cell culture medium were from Invitrogen (Carlsbad, CA). All other chemicals, used for buffer preparations were from Fisher (Pittsburgh, PA).

ThT Assays of Fibrillization Kinetics - The time course of fibrillization in solution was monitored using 100-200 μL samples of WT-amylin and analog peptides contained in white polystyrene clear bottom 96-well plates (Corning Inc., Corning, NY). Plates were covered with a clear polyester sealing tape (Fisher Scientific, Agawam, MA) to prevent evaporation. Stock solutions of WT amylin and inhibitor peptides were prepared in 100% DMSO, which dissolves

and disaggregates amylin, and stored at -80°C when not in use. Starting from the 100% DMSO stock solutions, samples for fibrillization reactions were prepared to contain final concentrations of 20 μM amylin (except where noted otherwise) and 10 μM ultrapure ThT in 20 mM sodium phosphate buffer, pH 7.4, with 2% (v/v) DMSO. Amylin was the final component added, in order to reduce the dead time for the reactions. The plates ware incubated at 25 °C without agitation. Fluorescence intensity was recorded at 2-min intervals with excitation at 440 nm and emission at 490 nm on a Fluoroskan Ascent 2.5 fluorescence plate reader. Fibrillization reactions for the peptides alone were performed in triplicate, and for analog-peptide inhibition of WT-amylin in duplicate, to estimate experimental uncertainties in kinetic parameters.

Transmission Electron Microscopy - Samples containing 80 μM concentrations of WT-amylin and the three analogs were incubated without agitation at a temperature of 37°C in 20 mM phosphate buffer (pH 7.4). For the inhibition reactions, samples contained WT-amylin at an 80 μM concentration, together with 160 μM of Arg-1, Arg-2 or Mem-T analogs. Aliquots from the reactions were removed after 2 days for EM imaging. The aliquots were blotted onto carbon-coated 400-mesh Maxtaform copper grids (Ted Pella Inc. Redding, CA) for 1-3 min, followed by negative staining with 1 % uranyl acetate. EM images were recorded on an FEI Tecnai G^2 Spirit BioTwin transmission electron microscope equipped with an AMT XR-40 camera.

Cytotoxicity Assays - Amylin samples were prepared by dissolving lyophilized peptides in 100% DMSO to 8 and 12 mM concentrations for WT-amylin and the analogs, respectively. Peptide concentrations were measured using the Micro BCA Protein Assay kit (Thermo Scientific, Rockford, IL). Stock solutions were diluted with FBS (fetal bovine serum)-free DMEM (Dulbecco's Modified Eagle Medium) to final concentrations of 40, 80 and 160 μM. The solutions

were sonicated continuously for 5 min at 75% amplitude before use. FBS was added in the final step, to a concentration of 15% (v/v). The final DMSO concentration for all cytotoxicity experiments was 1% (v/v).

Cytotoxicity was measured using the mouse insuloma 6 (MIN6) cell line model of β-pancreatic cells, which was a gift from Dr. Anil Rustgi (University of Pennsylvania). Cells were seeded at a density of 20,000 per 100 μL in black clear-bottom 96-well plates. The cells were grown in DMEM with 15% FBS, 25 mM glucose, 2 mM L-glutamine, 500 mM sodium pyruvate, 55 μM β-mercaptoethanol, 1000 units/ml penicillin, and 100 μg/ml streptomycin, for 20 h at 37 °C in a humidified incubator with 5% CO_2. The culture medium was then removed and replaced with fresh medium containing WT-amylin and/or inhibitor peptides. The cells were incubated for another 24 h followed by the addition of 10% (v/v) of the redox indicator dye AlamarBlue at the concentration supplied by the manufacturer (Invitrogen). Fluorescence, due to the reduction of AlamarBlue by viable cells was measured after 6 h using, excitation and emission wavelengths of 544 and 590 nm, respectively. Cell viability was calculated from the ratio of AlamarBlue fluorescence in treated to untreated cells. Uncertainties were calculated from the standard errors of measurements done in triplicate.

Results

Incorporation of Charged Residues Inhibits Fibrillization. The three amylin analogs Arg-1, Arg-2, and Mem-T considered in this work, substitute strings of like-charged amino acids for segments of the amylin sequence. We first compared fibrillization of the analogs and WT-amylin (Fig. 4.3). At a physiological salt concentration of 150 mM NaCl and peptide concentration of 20 μM, we could only detect fibrillization for WT-amylin and Arg-1. The change of ThT fluorescence

between the start and steady-state plateau of the reactions is 30-fold larger for WT-Amylin compared to the Arg-1 peptide (Fig. 4.3A). The lag-time for the Arg-1 analog (210 min) is increased about 2-fold compared to WT-amylin (120 min) while the elongation rate for Arg-1 (0.0068 min^{-1}) is reduced about 30% compared to WT-amylin (0.010 min^{-1}). At the 20 μM peptide concentrations used for these experiments we did not detect any fibrillization with the Arg-2 or Mem-T peptides (Fig. 4. 3A). With a 20-fold higher peptide concentration of 400 μM, we observed weak fibrillization of Mem-T (Fig. 4.3B orange to red) but Arg-2 still failed to fibrillize (Fig. 4.3B light to dark green). The fibrillization of Mem-T at the larger 400 μM peptide concentration was highly salt dependent. In the absence of salt only a very weak signal for fibrils was detected (orange in Fig. 4.3B). Fibrillization was stimulated at physiological salt concentrations and above (red in Fig. 4.3B), as expected for a mechanism in which charge-repulsion for the Mem-T analog is abated when the charges become screened by salt. At a physiological salt concentration of 150 mM NaCl, the fibrillization of 400 μM Mem-T (lag time of 10,000 min, elongation rate of $6.1 \pm 1.4 \times 10^{-6}$ min^{-1}) was still much weaker than that of WT-amylin at a 20 μM peptide concentration (lag time 120 min, elongation rate of 0.0100 ± 0.0001 min^{-1}). The Arg-2 peptide did not form fibrils under any of the conditions tested (Fig. 4.3).

EM images of the aggregates present after 2 days were consistent with the kinetics data (Fig. 4.4). WT-amylin formed large amounts of fibrils (Fig. 4.4A). By contrast Arg-1 formed much fewer fibrils; the section of the grid shown in Fig. 4.4B has a relatively high number to aid visualization. The image in Fig. 4.3B clearly shows that the Arg-1 formed a larger proportion of short fibrils than WT-amylin. For Arg-2 (Fig. 4.4C) and Mem-T (Fig. 4.4D) we only detected amorphous aggregates with non-fibrillar morphologies. Taken together, these observations

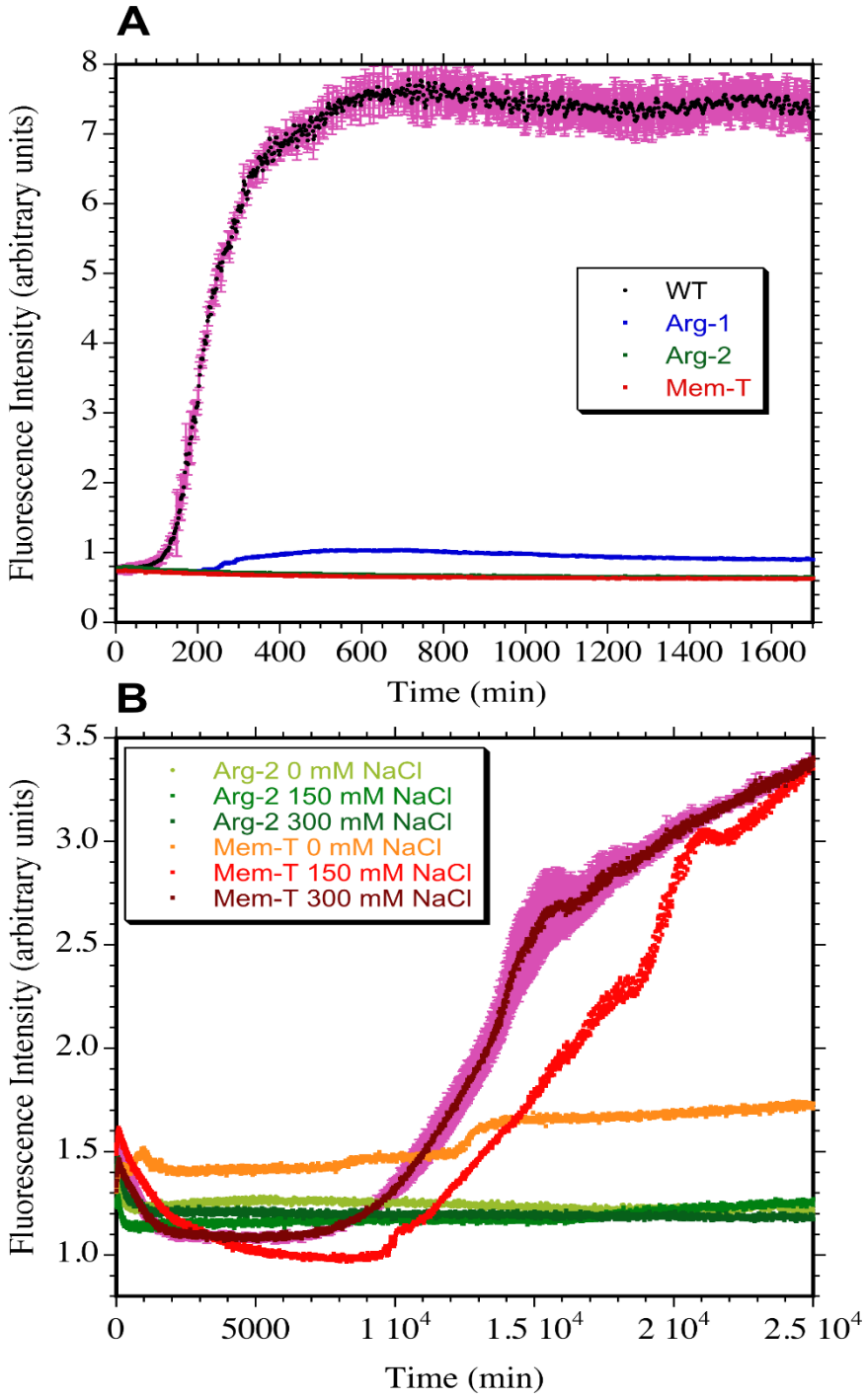

Figure 4.3 Fibrillization kinetics of WT and charged amylin variants. (**A**) Reaction profiles for 20 μM peptide concentrations in the presence of 150 mM NaCl. (**B**) Reaction profiles for 400 μM concentrations of Arg-2 and Mem-T at the indicated salt concentrations.

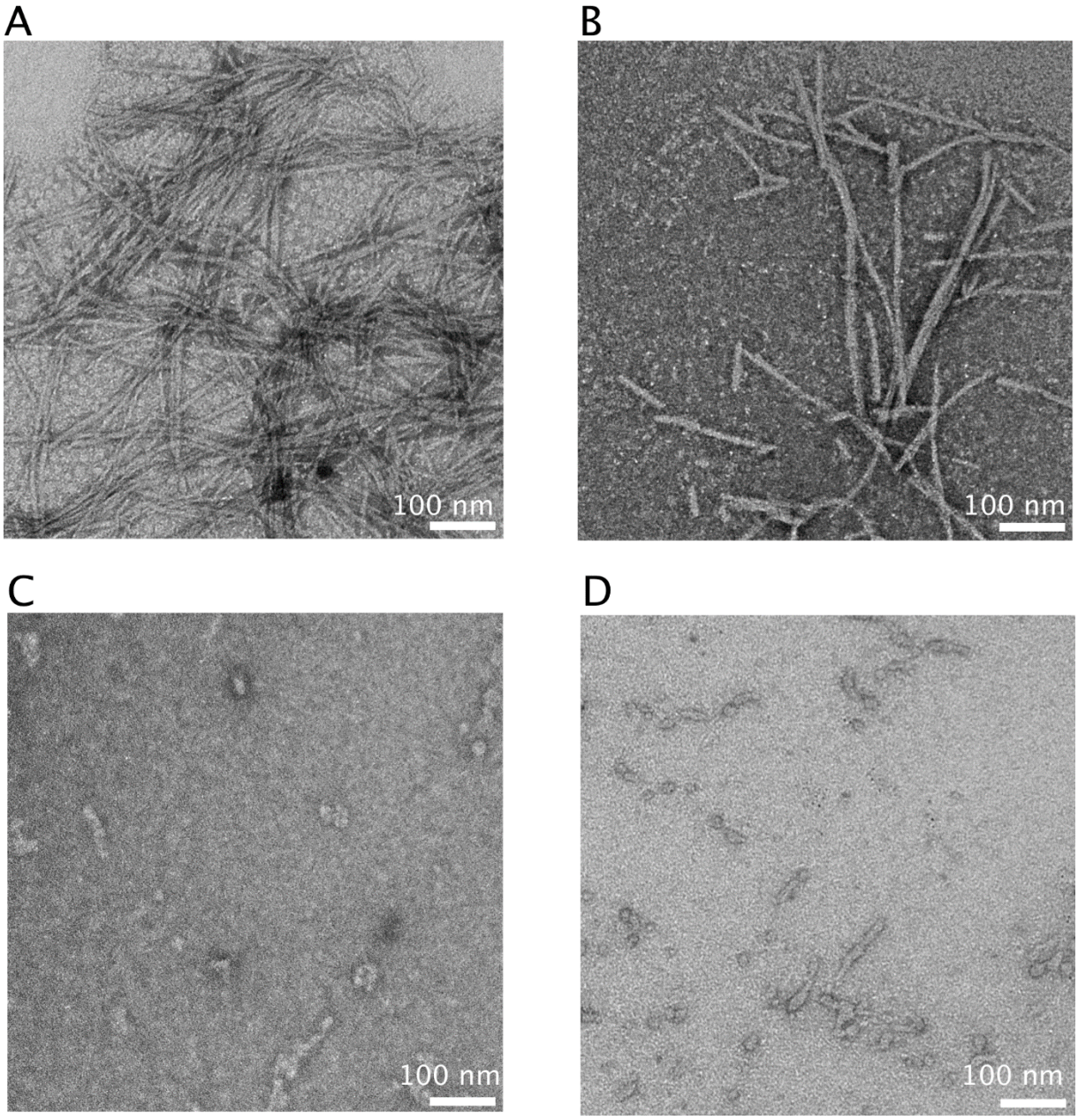

Figure 4.4 TEM images of aggregates formed by WT and charged amylin variants. (**A**) WT-amylin, (**B**) Arg-1, (**C**) Arg-2, (**D**) Mem-T after incubation for 2 days in 20 mM phosphate buffer, pH 7.4, at a temperature of 37 ºC. All peptide concentrations were 80 µM.

indicate that the introduction of charged residues in amylin analogs strongly interferes with their ability to form fibrils. The increased lag times and reduced elongation rates in the kinetic assays indicate that the charged residues inhibit fibrillization (Fig. 4.3). EM imaging shows, compared to

WT-amylin, Arg-1 forms fewer fibrils with shorter lengths, while Arg-2 and Mem-T form few if any fibrils (Fig. 4.4).

Charge-Loaded Peptide Analogs Inhibit Fibrillization of WT-amylin. We next examined whether the charge-loaded analog peptides affected the fibrillization of WT-amylin when added in *trans* (Fig. 4.5). In spite of their poor ability to fibrillize on their own, each of the three analogs affects the kinetics of WT-amylin fibrillization indicating that the analogs interact with the WT peptide. The most readily apparent effect is that fibrillization rates are reduced with increasing concentration of the analogs, manifested by a reduction in the slopes of the growth part of the reactions compared to WT-amylin alone. With Arg-1 there is also a reduction in the steady-state fluorescence plateaus with increasing concentration of the inhibitor (Fig. 4.5A). Fibrillization lag times are increased with increasing concentrations of the Arg-2 peptide (Fig. 4.5B) but decrease at high concentrations of the Mem-T analog (Fig. 4.5C).

Fig. 4.6 shows the effects of analog peptide concentrations ranging between 0.001 and 120 μM on the kinetic parameters for the fibrillization of 20 μM WT-amylin. All three peptides reduce fibril elongation rates. The Arg-1 and Arg-2 inhibitors cause an 8-10 fold reduction in elongation rates, as conceived in the design of the peptides as fibril-elongation inhibitors. Mem-T shows a smaller 4-fold reduction in elongation rates (Fig. 4.6A). Although Mem-T was conceived as an inhibitor of the interactions of WT-amylin with membranes, the substitution of a string of negatively charged aspartate residues in the N-terminal half of the amino acid sequence inhibits fibril elongation, probably by the same mechanism as the introduction of positively charged arginine residues in the Arg-1 and Arg-2 analogs. That inhibition of fibril elongation is weaker

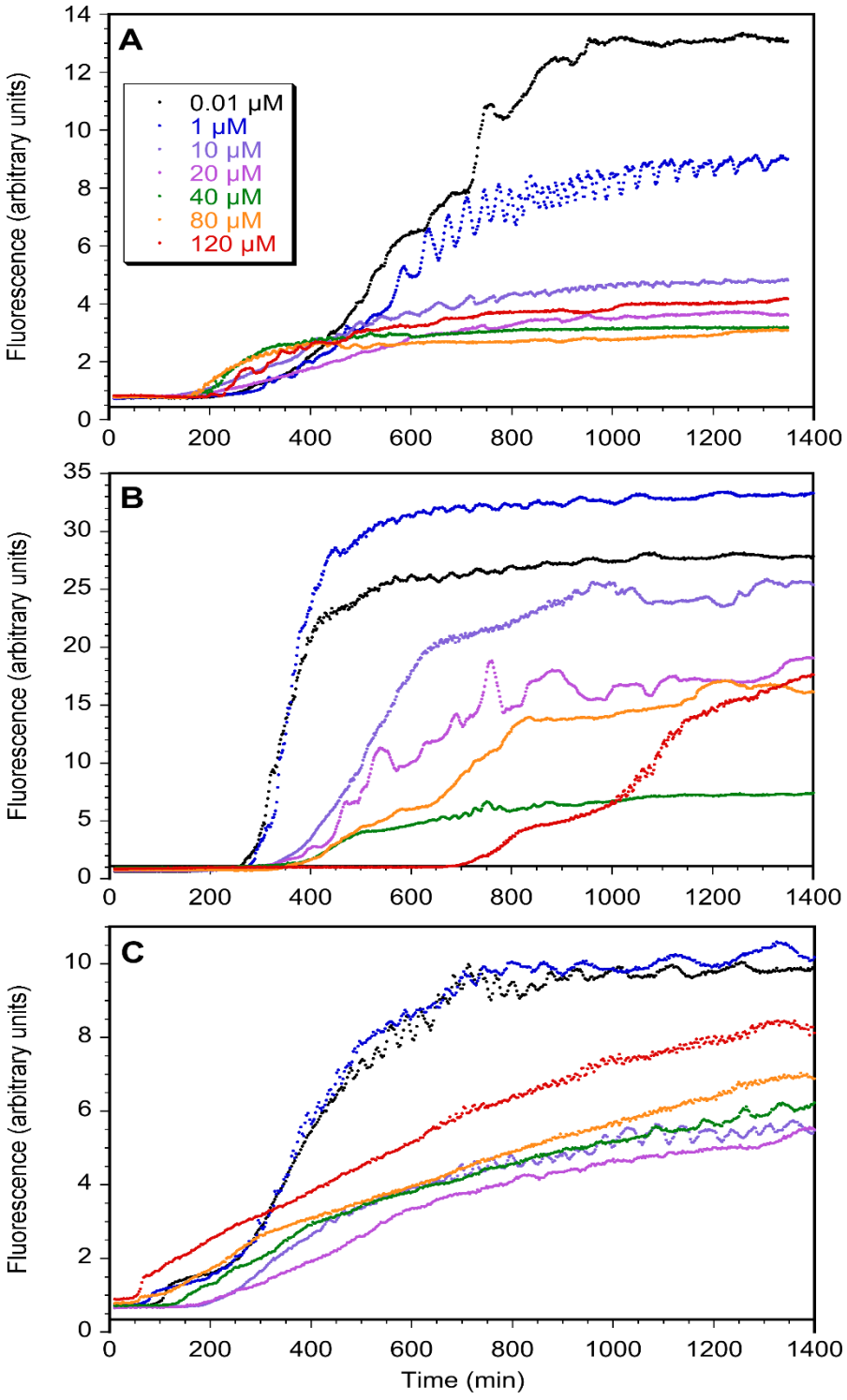

Figure 4.5 Effects of peptide inhibitors at the indicated concentrations on the fibrillization of 20 μM WT-amylin: (**A**) Arg-1, (**B**) Arg-2, (**C**) Mem-T. All reactions were done in the presence of 150 mM NaCl.

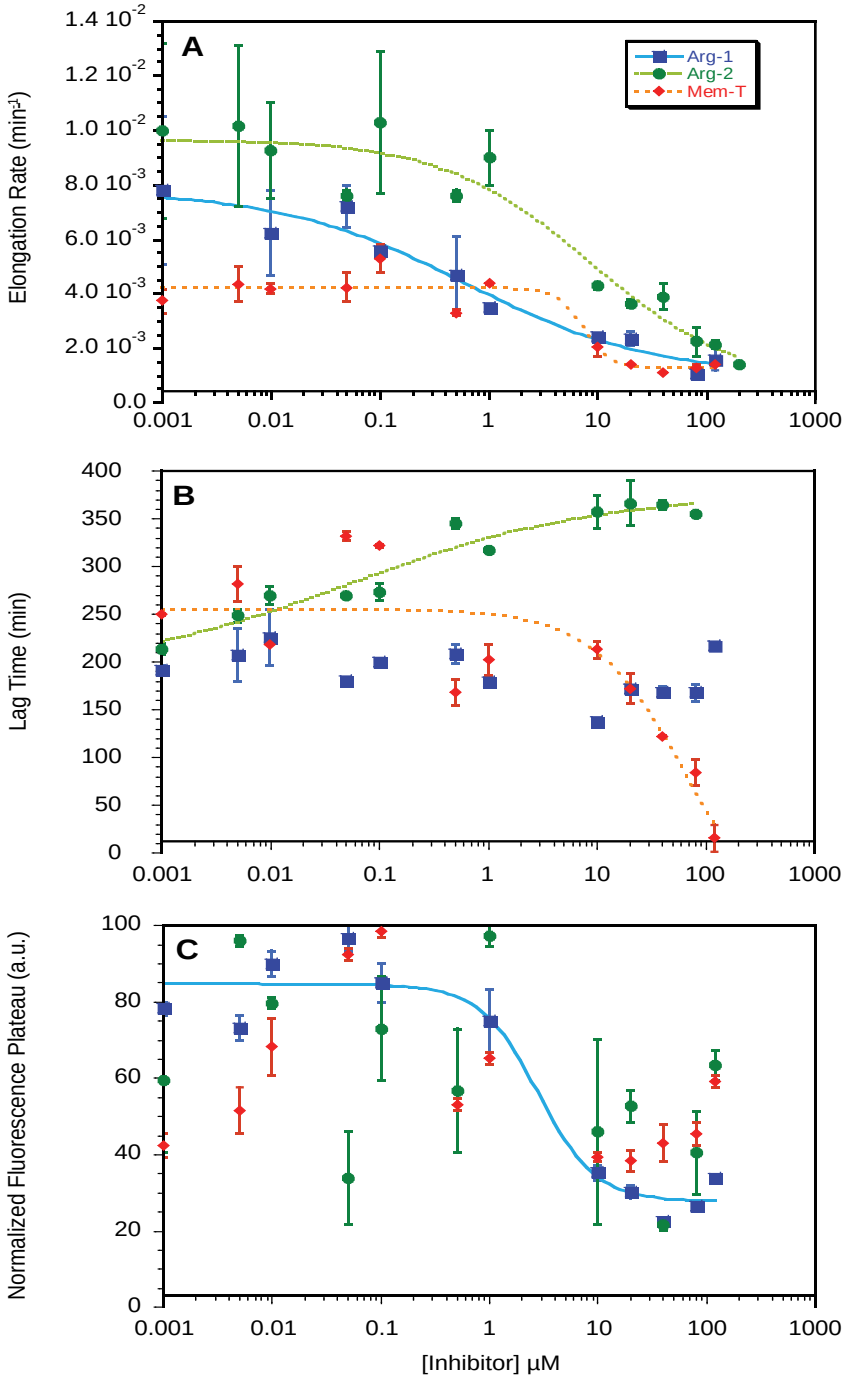

Figure 4.6 Effects of peptides added *in trans* on parameters describing the fibrillization kinetics of 20 µM WT- amylin: (**A**) elongation rates, (**B**) lag times, (**C**) fluorescence plateaus. Inhibition data from Arg-1, Arg-2, and Mem-T are shown in blue, green, and red, respectively. All experiments were done in duplicate in the presence of 150 mM NaCl. The data points are average values for the kinetic parameters, and the uncertainty bars are standard errors of the mean calculated from the duplicate reactions. Curves represent four-parameter non-linear least squares fits of the inhibition data to the IC_{50} equation [120] (when these could be fitted).

with Mem-T than with the arginine analogs, is likely a consequence of WT-amylin being an entirely cationic peptide with no negatively charged residues at neutral pH. Thus electrostatic repulsion would be expected to be stronger between the intrinsic positively charged sites in WT-amylin and the introduced positive charges in the two arginine inhibitors than with the negative charges in the Mem-T analog. An IC_{50} analysis of the inhibition data was performed to obtain quantitative information on the fibrillization of WT-amylin as a function of the concentrations of the charge-loaded analog peptides (Fig. 4.6). The Arg-1 concentration-dependence for the inhibition of WT-amylin fibril elongation rates gives an IC_{50} value of 0.6 ± 0.5 µM. For Arg-2 and Mem-T, the IC_{50} values are ~10 µM (Fig. 4.6A). In addition to effecting elongation rates, Arg-2

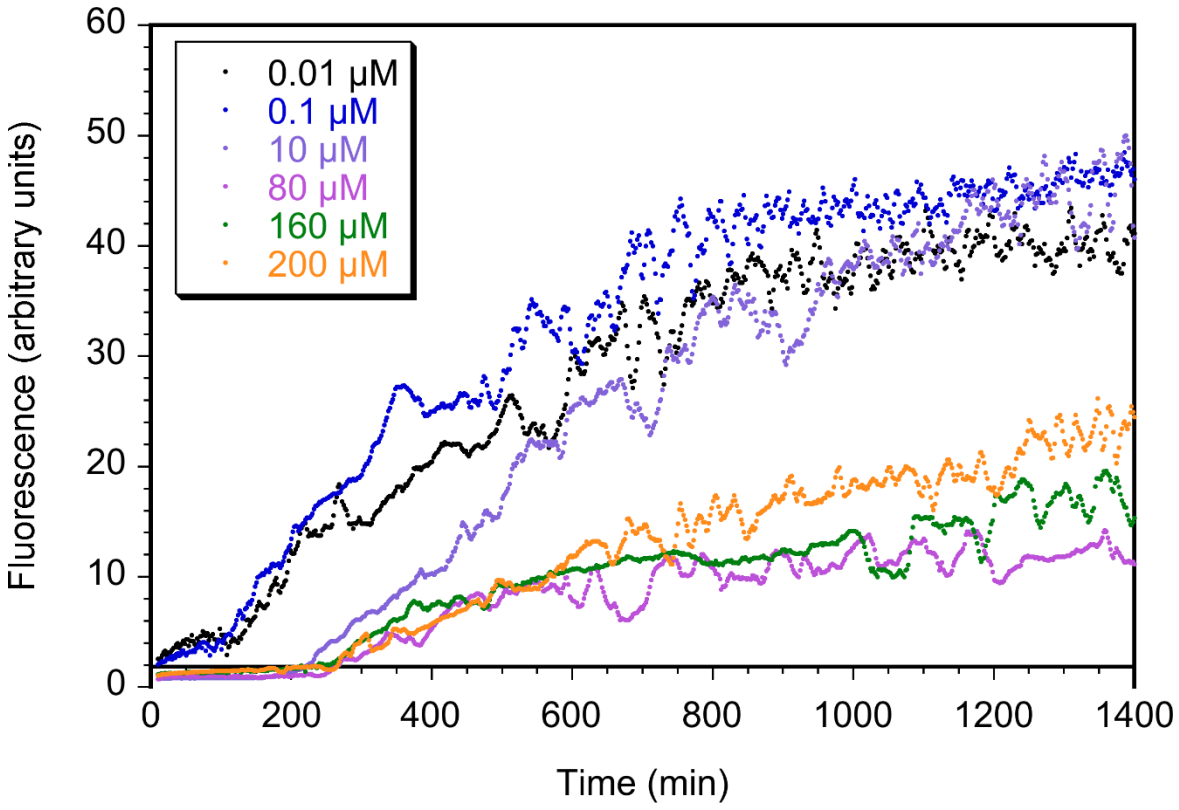

Figure 4.7 Representative kinetic traces for the fibrillization of WT-amylin at the larger peptide concentration used for the cytotoxicity assays (80 µM amylin), and the indicated concentrations of the Arg-1 inhibitor.

increases the lag times for WT-amylin fibrillization with an IC_{50} of ~0.1 μM. This indicates that Arg-2, in addition to inhibiting fibril elongation, inhibits the nucleation step of the reaction (Fig. 4.6B). By contrast, Mem-T causes a reduction in lag times at high concentrations of the analog (>10 μM) suggesting that it promotes the nucleation of WT-amylin. The half-maximal concentration for this effect was about 70 μM. The reduction in lag times with Mem-T is reminiscent of what we previously observed with negatively charged heparin polysaccharides which enhance fibrillization of WT-amylin [43], and may occur because the negative charges in Mem-T complement the positive charges in the cationic amylin peptide, thereby facilitating fibril nucleation. With increasing Arg-1 concentration, there were no effect on the lag times within experimental uncertainty when the experiments were done with a 20 μM concentration of WT-amylin (Fig. 4.6B). When the reactions were done at a larger WT-amylin concentration of 80 μM, the concentration used for cytotoxicity experiments (see below), we saw increases in lag times with increasing Arg-1 concentration as well as decreases in elongation rates and steady-state fluorescence plateaus (Fig. 4.7 and 4.8). The effects of Arg-1 may be masked at the lower 20 μM WT-amylin concentration as fibrillization lag times increase with decreasing peptide concentration. Within experimental uncertainty, steady-state fluorescence plateaus were only observed to decrease with the Arg-1 analog, with an IC_{50} of 2.8 ± 1.7 μM (Fig. 4.6C).

TEM imaging of WT-amylin fibrils formed in the presence of the charge-loaded analogs showed that the morphology of the fibrils is preserved compared to WT-amylin (Fig. 4.9). In the presence of the least effective inhibitor Mem-T, the fibrils of WT-amylin were indistinguishable from those formed with WT-amylin alone (Fig. 4.10A, 4.10D). In the presence of the effective analogs Arg-1 (Fig. 4.10B) and Arg-2 (Fig. 4.10C), we observed somewhat fewer fibrils and a

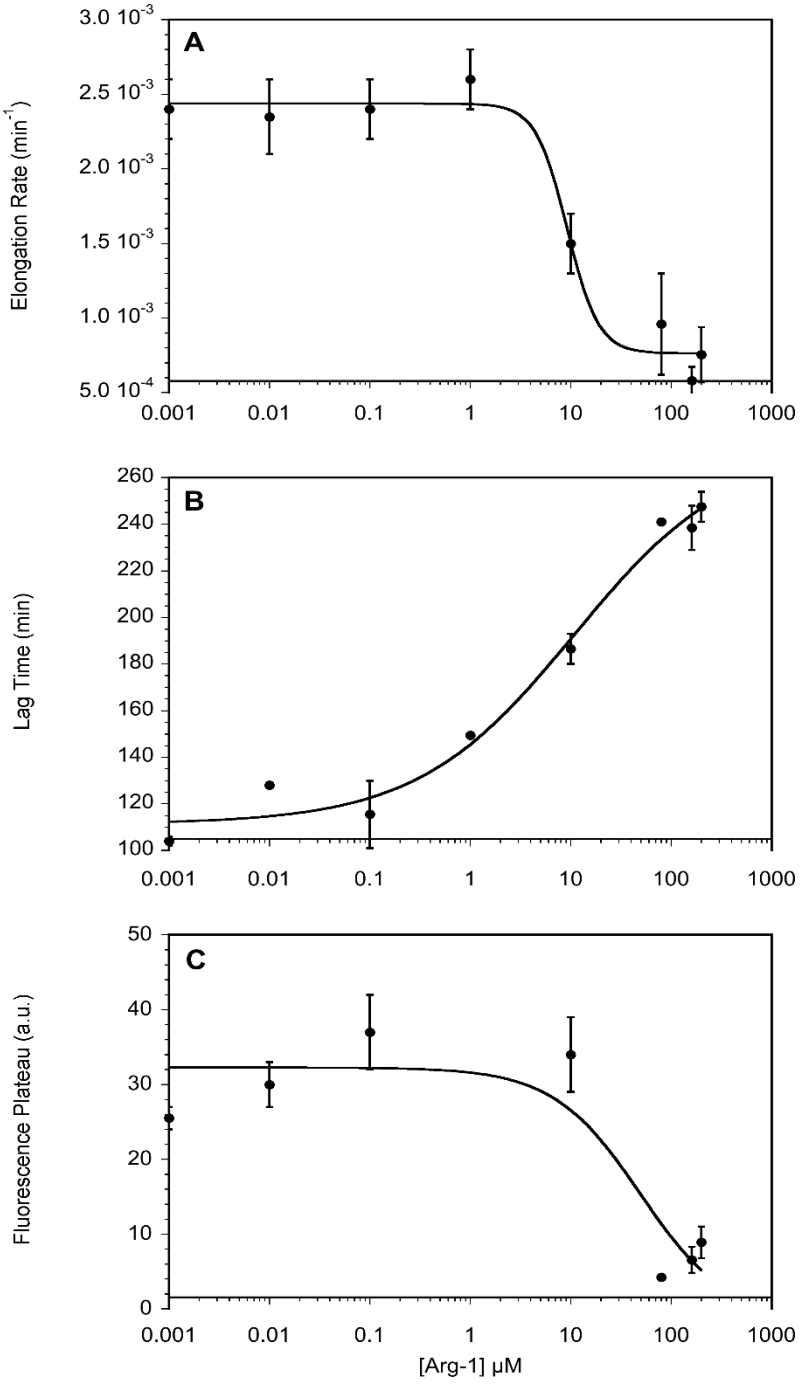

Figure 4.8 Dependence of kinetic parameters for the fibrillization of 80 μM WT-amylin (see Fig. 4.7) on the concentration of Arg-1 inhibitor. Experiments were done in duplicate in the presence of 150 mM NaCl. Data points are average values for the kinetic parameters, uncertainty bars are standard errors calculated from the duplicate reactions, and curves are four-parameter fits of the inhibition data to the IC_{50} equation. The IC_{50} values were 9.1 ± 5.2 μM for the elongation rates (**A**), 11.0 ± 12.4 μM for the lag times (**B**), and 50 ± 80 μM for the steady-state fluorescence plateaus.

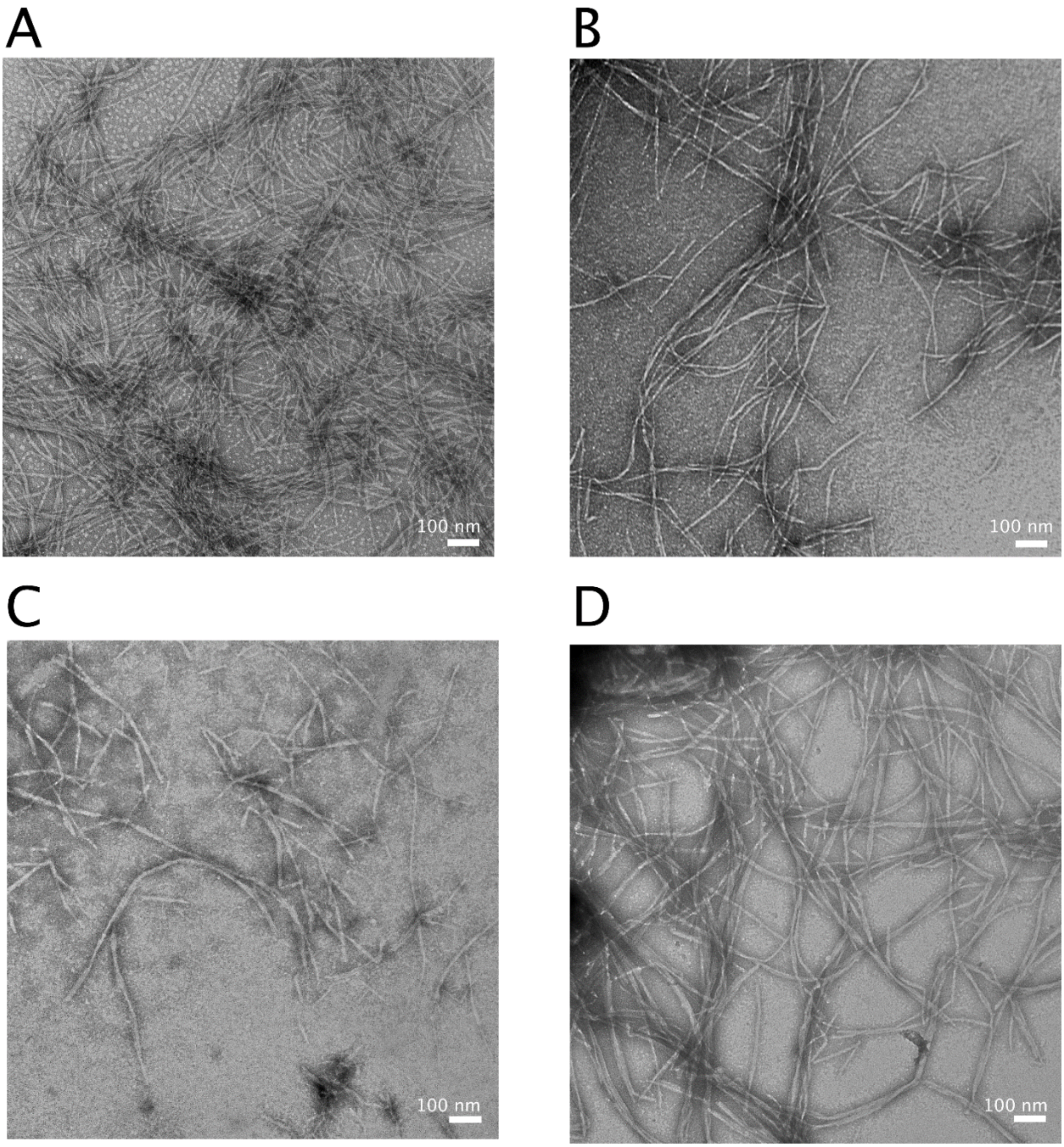

Figure 4.9. TEM images of fibrils formed from 80 μM WT-amylin in the presence or absence of inhibitor peptides. (**A**) WT-amylin alone, (**B**) with 160 μM Arg-1, (**C**) with 160 μM Arg-2, (**D**) with 160 μM Mem-T. Aliquots were removed for EM imaging 24 h after the fibrillization reactions were started. Reactions were carried out in 20 mM sodium phosphate (pH 7.4), 1% DMSO (v/v) at 37 °C.

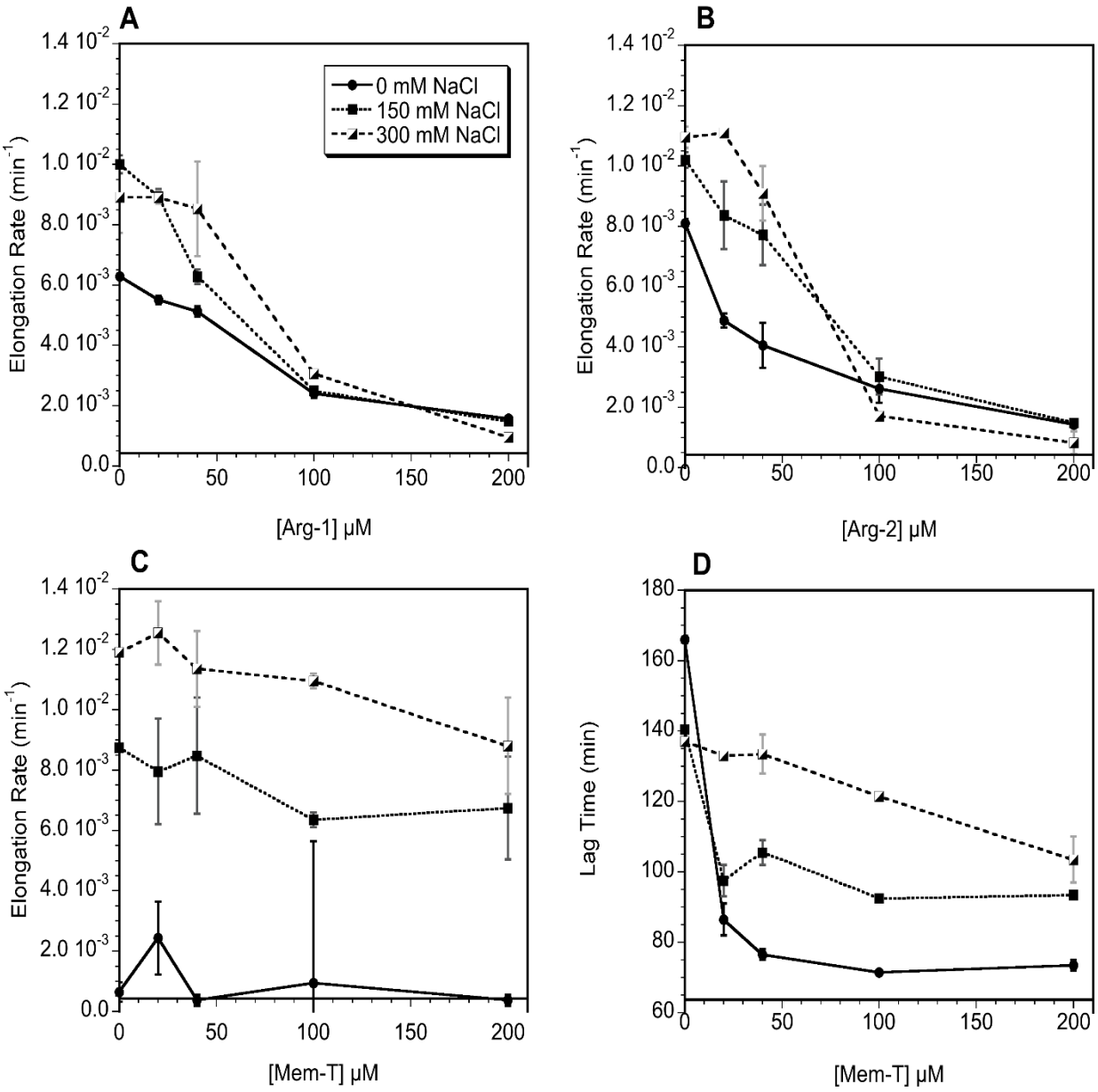

Figure 4.10 Salt-dependence on the effectiveness of charge-based inhibitor peptides. Elongation rates with Arg-1 (**A**), Arg-2 (**B**), Mem-T (**C**) and lag times with Mem-T (**D**).

greater amount of short fibrils compared to when WT-amylin was fibrillized alone. The increase in the amount of short fibrils is consistent with the greater potency of the Arg-1 and Arg-2 peptides as inhibitors of WT-amylin fibril elongation rates. Thus, while Arg-1 and Arg-2 peptides do not stop

fibrillization, they appear to inhibit fibril elongation as manifested by the smaller amounts of fibrils and the greater proportion of short fibrils in the presence of the inhibitors.

Salt Modulates the Inhibition of WT-amylin Fibrillization by Charge-loaded Analogs. Since we expected the charge-loaded amylin analogs to inhibit fibrillization through electrostatic repulsion we looked at the effects of salt, which should screen charges. Fig. 4.10A shows the effects of NaCl concentration on the most potent inhibitor Arg-1. Although we have too few data points to accurately determine IC_{50} values, the experiments clearly show that larger Arg-1 concentrations are required to decrease elongation rates with increasing salt concentration. This is the expected result for an inhibition mechanism that involves electrostatic repulsion, as the charges become increasingly screened with increasing salt concentration. A very similar effect is seen with Arg-2 (Fig. 4.10B) but with the least effective inhibitor Mem-T, salt effects on elongation rates are reduced close to the uncertainties of the measurements (Fig. 4.10C). The shortening of fibrillization lag times with the Mem-T peptide, however, shows a strong salt concentration dependence indicating that the enhanced nucleation of WT-amylin fibrils in the presence of Mem-T occurs through electrostatic interactions (Fig. 4.10D).

It is interesting to consider that the data in Fig. 4.10A and 4.10B indicate that the reduction in elongation rates with Arg-1 and Arg-2 is more effective at physiological salt concentration or higher than in the absence of salt. This is because the fibrillization of WT-amylin, in the absence of any inhibitors, is enhanced with increasing ionic strength [121]. A 7-fold reduction in elongation rates is seen as the concentration of Arg-1 is increased between 0 and 200 μM at 150 mM NaCl. In the absence of salt, there is only a 4-fold reduction over the same inhibitor concentration range (Fig. 4.10A).

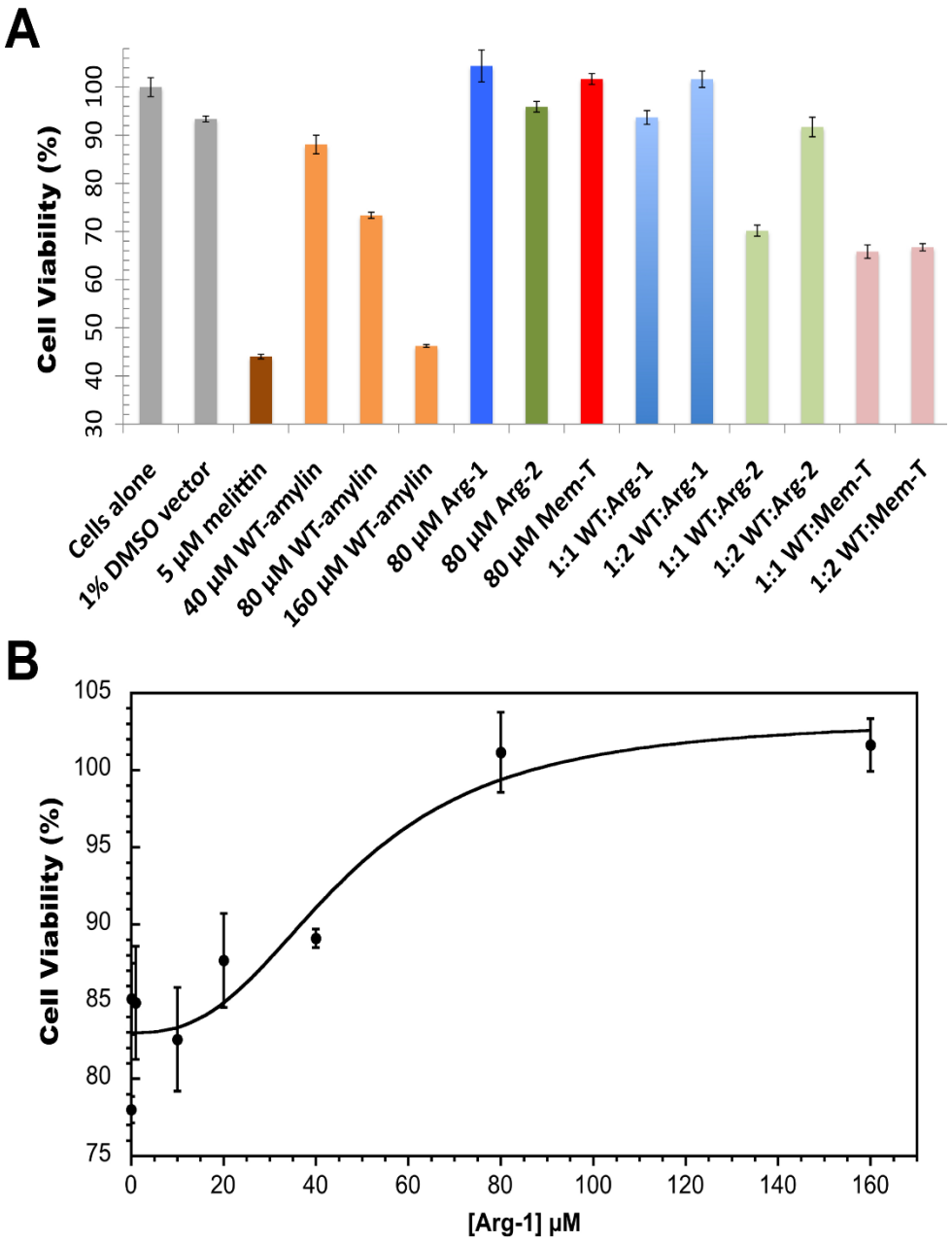

Figure 4.11 Effects of charge-based inhibitors on amylin cytotoxicity. (**A**) Cytotoxicity of WT-amylin and analogs towards a MIN6 mouse insulinoma cell models of β-pancreatic cells. Gray, cells-only, defined as 100% cell viability and 1% DMSO vector used for all experiments except the first; brown, positive melittin control; orange, WT-amylin at different concentrations; blue, green, red -cells challenged with 80 μM Arg-1, Arg-2, Mem-T respectively; light blue, green, red - cells challenged with 80 μM WT-amylin and the indicated molar ratios of the respective inhibitors. (**B**) Viability of MIN6 cells challenged with 80μM WT-amylin as a function of Arg-1 concentration. The cell viability data were fit to an IC_{50} value of 47 ± 17 μM Arg-1. All data points are averages from measurements performed in triplicate and the uncertainties are the associated SEMs.

Arg-1 and Arg-2 are Inhibitors of WT-amylin Cytotoxicity Towards β Cells. We next looked at the effects of the charge-based amylin analogs on the cytotoxicity of WT-amylin towards a MIN6 model of pancreatic β-cells (Fig. 4.11). In control experiments, all three analog peptides show no toxicity towards the MIN6 cells (dark blue, green, red in Fig. 4.11A), giving viabilities comparable to untreated cells (gray in Fig. 4.11A). We next did a concentration series challenging the MIN6 cells with 40, 80, and 160 μM WT-amylin (orange in Fig. 4.11A). As the concentration of WT-amylin is increased, cell viability drops to about 45% in the presence of 160 μM WT-amylin, comparable to the value obtained with the potent toxin bee-venom melittin, which was used as a positive control (brown in Fig. 4.11A). We chose an 80 μM concentration of WT-amylin for the inhibitor studies, as a compromise between detecting a sufficient signal in the assay (~25% cytotoxicity) and minimizing the WT-amylin peptide concentration, since this would require lower concentrations of the inhibitors to counteract the effects of WT-amylin. The Arg-1 analog protects against WT-amylin at a stoichiometric ratio of the two peptides: 80 μM Arg-1 for MIN6 cells challenged with 80 μM WT-amylin (light blue bars in Fig. 4.11). The Arg-2 analog is less effective than Arg-1, and only protects against cytotoxicity at a 2:1 inhibitor: WT-amylin molar ratio (160 μM Arg2: 80 μM WT amylin, light green in Fig. 4.11A). The Mem-T analog failed to protect against WT-amylin cytotoxicity (pink in Fig. 4.11A).

For the most potent analog, Arg-1, we looked in detail at the inhibitor concentration dependence of cytotoxicity for MIN6 Cells challenged with 80 μM WT-amylin (Fig. 4.11B). The inhibitor concentration data were fit with an IC_{50} value of 47 ± 17 μM. This value is comparable to other WT-amylin cytotoxicity inhibitors reported in the literature, such as oligopyridylamide [122] and diarylated thiophene [123] α-helix mimetics (IC_{50} values of ~7 μM and ~50 μM estimated from the data in Fig. 4.3D of [122] and Fig. 4.4B of [123], respectively).

Discussion

The motivation for the studies described in this work was to see if electrostatic charge repulsion could be exploited to design new types of inhibitors of amylin fibrillization and cytotoxicity. Our work [116, 118] and that of others [23, 124, 125] has shown that charging of His18 in amylin at low pH can markedly inhibit fibrillization. The effects of charging His18 at low pH can be recapitulated in the H18R mutant of amylin at neutral pH, and this substitution results in an amylin peptide that is not cytotoxic to β-cells [95, 116]. Moreover, addition of a single charged lysine residue in the S20K mutation was reported to result in much slower fibrillization and to inhibit fibrillization of the WT-amylin peptide when the mutant peptide was added in *trans* [46]. Stimulated by these observations we designed three peptide analogs that substitute a string of 4-5 charged residues for neutral residues in the amylin sequence. The Arg-1 and Arg-2 analogs substitute four positively charged arginine residues for segments of the amylin that form the end of strand β1 and the beginning of strand β2, respectively, in the model of the amylin fibril structure derived from ssNMR [25] (Fig. 4.1B). The Arg-1 and Arg-2 analogs were designed as inhibitors of fibril elongation. The Mem-T peptide which was designed to interfere with the membrane insertion of mixed Mem-T:WT-amylin oligomers substitutes five negatively charged aspartate residues for the segment of the peptide that has the highest avidity for membranes[4, 86] and that is embedded in the hydrophobic environment of membrane-mimetic micelles in the solution NMR structure of amylin (Fig. 4.1C) [117]. In this work we characterized the ability of the peptides to form fibrils by themselves, the concentration dependence of their inhibition of WT-amylin fibrillization, and their inhibition of WT-amylin cytotoxicity towards the MIN6 mouse model of pancreatic β-cells.

In the cytotoxicity assays, Arg-1 was more potent than Arg-2 in protecting β-cells from WT-amylin, while the Mem-T analog offered no protection (Fig. 4.11). Protection of cytotoxicity from WT-amylin was achieved at a stoichiometric ratio with the Arg-1 analog but required a two-fold molar excess with the Arg-2 peptide (Fig. 4.11). The origins of these differences are unclear but Arg-1 also serves as a more potent inhibitor of fibril elongation rates than Arg-2, with an IC_{50} of 0.60 ± 0.47 μM for Arg-1 compared to 8.6 ± 8.2 μM for Arg-2 (Fig. 4.6A). The greater potency of Arg-1 compared to Arg-2 could be a structural effect. In the ssNMR model of amylin protofibrils [25] the four substituted arginines would be positioned at the surface of the structure in Arg-1, whereas they would be placed in the interior between the two C2-symmetry related stacks of β-sheets in Arg-2 (Fig. 4.1B). Alternatively, the greater effectiveness of Arg-1 as an inhibitor may be related to its relatively better ability to form fibrils on its own, whereas Arg-2 did not form fibrils even at high concentrations of the peptide and salt. In other words, the capacity of Arg-1 to form fibrils although weakened compared to WT-amylin, may make it better able to associate with the latter, thereby allowing it to better exert its inhibitory effects on fibril elongation.

The lack of protection against WT-amylin cytotoxicity with Mem-T could indicate that the design strategy of interfering with oligomer insertion into membranes did not work. Another possibility, is that Mem-T could work at higher concentrations than the highest 2:1 Mem-T: WT-amylin ratio tested in this work. Since we do not know the optimum Mem-T: WT-amylin stoichiometry ratio for the putative mixed oligomers on which the design strategy was based, it's conceivable that Mem-T could work at a larger molar excess to WT-amylin than used in this work. Like Arg-1 and Arg-2, Mem-T acts as an inhibitor of WT-amylin fibril elongation rates with an IC50 of 7.4 ± 6.6 μM. The reduction in elongation rates with Mem-T is only about half of that for

the arginine-peptides, and in contrast to the arginine peptides Mem-T decreases the lag times for WT-amylin fibrillization. The stimulation of the nucleation step for WT-amylin fibrillization, as manifested by the reduced lag times observed at high concentrations of Mem-T (Fig. 4.6B), may be why this analog is as ineffective as a cytotoxicity inhibitor. The enhanced fibril nucleation of WT-amylin at high concentrations of Mem-T is most likely due to the insertion of negative charges in this analog which could complement the positive charges in the WT peptide. An alternative way to design a peptide that could interfere with membrane insertion of mixed oligomers, would be to disrupt the α-helix that interacts with the hydrophobic component of membranes (Fig. 4.1C) by inserting prolines rather than negatively charged residues. This could have the desired effect of interfering with membrane insertion of mixed oligomers, while avoiding the stimulation of the nucleation of WT-amylin due to the negative charges in the Mem-T analog.

For the most effective analog Arg-1, we determined IC_{50} values of 1-10 μM from the inhibitor concentration-dependence of the kinetic parameters for WT-amylin fibrillization (Fig. 4.6 and 4.8). These values are comparable to those of other fibrillization inhibitors reported in the literature, for example small molecules containing heterocyclic groups (IC_{50} = 1 μM) [126] and α-helix peptidomimetics (IC_{50} = 8 μM) [122, 123, 127]. We also looked at the Arg-1 concentration dependence of the inhibition of WT-amylin cytotoxicity and obtained an IC_{50} of 47 ± 17 μM. Although there is a dearth of similar studies for amylin inhibitors in the literature we were able to estimate a comparable IC_{50} of ~7 μM from the data reported (Fig. 4.3D) for the IS5 oligopyridylamide α-helix mimetic inhibitor of amylin cytotoxicity[122]. For the $A\beta_{1-42}$ peptide involved in Alzheimer's disease, a number of different types of inhibitors give IC_{50} values in the range between 10 and 100 μM in cell cytotoxicity assays [128-130]. A problem with the MIN6

cells used in this paper, is that a relatively high concentrations of WT-amylin is needed to give a significant cytotoxicity signal, as shown by the concentration series represented by the orange bars in Fig. 4.11. Under the conditions of this study (1% DMSO so as to not perturb cell membranes) 10%, 25% and 50% cytotoxicity is achieved with WT-amylin concentrations of 40, 80, and 160 μM WT-amylin, respectively. Because of the large amounts of WT-amylin needed to detect a sufficient cytotoxicity signal, large concentrations of inhibitor peptides were needed to protect from WT-amylin. One possibility is to use another β-cell model, such as the INS-1 cell line but with this system as well concentrations in the range between 5 and 50 μM WT-amylin were needed to give 50% cytotoxicity [122, 123]. A more sensitive cytotoxicity assay would allow the use of lower WT-amylin concentrations and possibly lower inhibitor concentrations.

It is currently uncertain which states of amyloidogenic proteins are harmful to cells. In the case of amylin, amyloid fibrils could exert their cytotoxic effects by perforating β-cell membranes or by disrupting the network of interactions with other cells in the islets (α, ε, δ, PP) that are necessary for the β-cells to function [4]. Many investigators have proposed that soluble oligomers rather than fibrils are responsible for the deleterious effects of amyloidogenic proteins. Annular oligomers could form membrane-spanning pores that would allow unregulated ion transport between the cell and its environment disrupting cellular homeostasis [4, 48, 131]. Because intermediates would be present at low concentrations and would be short-lived, oligomeric precursors to amyloids have proven difficult to isolate and their properties are ill-defined [4, 132]. Oligomers also pose the difficulty that because they are transiently formed, they could interconvert to fibrils during the cytotoxicity measurements, making a definite assignment of their role in pathology equivocal [4, 14]. In yet another proposed mechanism, it is not the oligomers or fibrils

themselves, but the process of fibril growth that could be responsible for cytotoxicity, by inducing membrane damage [133]. For the three analogs described in the paper we do see a positive correlation between inhibition of fibril elongation rates and protection against WT-amylin cytotoxicity to β-cells (Fig. 4.6A and 4.11). Although Arg-1 and Arg-2 were designed as fibril elongation inhibitors, the two analogs together with Mem-T also have effects on the lag times for the reactions, and could conceivably protect against WT-amylin cytotoxicity through a different mechanism. To unequivocally prove that Arg-1 and Arg-2 act as fibril elongation inhibitors and that Mem-T can interfere with membrane disruption by WT-amylin will require additional studies.

The current results with the charge-based inhibitors are encouraging because they potentially represent a new electrostatic-based approach to inhibit amyloid fibrillization and toxicity. Clearly, the efficacy of these first-generation inhibitors could be improved. Possible strategies include substituting charged residues for the segments that form the earliest secondary structure during misfolding [134], using structural models of amylin fibrils to substitute charged residues for residues that face the surface or core of the fibril, substituting charged residues in both strands that form the amylin fibril β-hairpin structure [25, 135], and combining charge-based substitutions with other approaches such as the introduction of H-bond blockers [136, 137].

CHAPTER V: Future Directions

This thesis has explored the molecular structure of human amylin, real-time fluorescence imaging of amyloid fibrillization, and the development of possible amyloid cytotoxicity inhibitors.

Throughout different animal species, amylin sequences are strongly conserved with the most notable variation occurring in the residues 20-29 region (Fig 2.3D). The proline residue in amylin sequence of certain species such as rat, mouse and dog in the 20-29 residue amyloidogenic region inhibits aggregation and these animals are not susceptible to type 2 diabetes. This fact has been used in the development of the FDA-approved drug pramlintide (Symlin®) for diabetes. It has been shown that proline mutations outside the amyloidogenic region of amylin (proline substitutions at positions 17, 19, and 30) result in a large inhibition of amyloid propensity and the loss of amyloid fiber stability [133]. Conversely, the S20G mutation in human amylin had been shown to fibrillize faster than the WT amylin and cause an early onset of type 2 diabetes [17].

Molecular dynamics simulation data is available for human amylin, S20G amylin, I26P amylin, and rat amylin [138]. These simulation studies show marked differences in secondary structures of mutated versus non mutated amylin. The simulation studies demonstrate varying helical populations as well as flexibility in the C-terminal region of mutated human amylin [138]. The intra helical angle for our SDS micelle-bound amylin structure is ~30°, whereas the intra helical angle for the mutated S20G amylin by molecular dynamics study samples two angles, one at 40° degree and the other at 90° [139]. The same study also reported that the simultaneous loss of both hydrogen bonds between Leu16 and Ser20 in S20G amylin coincides with the large fluctuations in backbone dihedral angles near His18 in one trajectory. An amidated version of human amylin aggregates significantly faster (~9 times) than the non-amidated variant [20], which

suggests an intrahelical angle of 85° found in micelle-bound NMR structure [92] of amidated form is significant in protein misfolding processes. These studies suggest that along with electrostatic interactions, intrahelical angle also plays a key role in aggregation, since, these L-shaped structures coincide with faster aggregation rate [139]. Generally, kinks in micelle-bound structure correspond with locations of turns adopted by the amyloidogenic proteins in fibril structure [77]. The conformational preorganization of the S20G mutant monomer into the overall fibril topology might reduce the cost of conformational search for aggregation. A molecular dynamic simulations for amylin has also found evidence for a metastable beta hairpin structure which has been proposed to be responsible for the initial seeding of fibrils [102].

In view of these structural variations, it is important to determine the NMR structures of S20G amylin variant, and what might be the driving force behind its higher fibrillization propensity. It would be informative to investigate the structural differences between our designed Arg-1 and Mem-T analogs by NMR to see how structural difference from the wild type correlate with their effectiveness as inhibitors and thereby rationally design improved inhibitors. Further fluorescence microscopy investigations could be done to determine how the inhibitors interact with and inhibit wild type amylin fibrillization. The specific techniques that could be applied towards these investigations include TIRFM. By using fluorescently tagged peptides [111] one could investigate the designed charged inhibitors Arg-1 and Mem-T to see the fibrillization inhibition in real time.

Studies have shown that human amylin dimerizes when in a highly α-alpha helical state [140] and this dimer is an on-pathway intermediate for fibril formation. AFM imaging of various amyloidogenic proteins have shown the possible oligomeric assembly in presence of lipid

membranes [141]. As of now molecular structure of the hypothesized pore forming oligomer is not available for any amyloidogenic protein. NMR studies from our lab and others have shown that human amylin monomers associate with the cell membrane [117, 142]. In addition, multiple factors such as protein concentration, cholesterol and lipids, glycosaminoglycans, temperature, and pH play a crucial role in the formation of amyloids [43, 143, 144]. It might be possible to stabilize oligomeric pore complexes for detailed structural studies, by controlling one or more of these variables while maintaining the peptide concentration high enough in the vicinity of the membrane to create microenvironments that favor stable oligomer formation. A helical wheel representation has been proposed for the pore complex, were the hydrophobic residues (shown in blue, Fig. 2.7) of human amylin are oriented toward the surrounding lipids to form a stable pentameric oligomer pore structure [145]. Such oligomeric structures could be characterized by CD, fluorescence resonance energy transfer (FRET), and electron microscopy techniques [146, 147]. Since, the fibrillization rates of our designed inhibitors are very low as compared to amylin (Fig. 4.3 A), a CD experiment could be a good starting point to determine the helical content within each of the designed inhibitor peptides for comparison. ThT fluorescence assays could be used to monitor the effect of lipids or micelle membranes on fibrillization kinetics, in conjunction with cytotoxicity assays in order to establish the correlation between a specific fibrillization stages and the maximal cytotoxicity effect. Amylin analog peptides with a fluorescent tag attached to a specific amino acid such as N-terminal lysine or by using unnatural amino acids such ring-substituted phenylalanine at residue F15 within α-helical region of human amylin could be used [111, 148] to access the lateral binding of peptide in oligomeric form in lipid membrane environment.

Excerpted from: S. Jha, S.M. Patil, J. Gibson, C.E. Nelson, N.N. Alder, and A.T. Alexandrescu, Mechanism of amylin fibrillization enhancement by heparin, J. Biol. Chem. 286 (2011) 22894-22904.
I performed NMR, Electron microscopy and TIRFM (Figures A1-1, A1-4, and A1-6)
Dr. Suman Jha performed NMR and Fluorescence assays (Figure A1-1, A1-2, A1-3, and A1-5)
Dr. Suman Jha and Dr. Jason Gibson performed Cytotoxicity assays (Figure A1-7)

Appendix I: Mechanism of Amylin Fibrillization Enhancement by Heparin.

Abstract

We characterized the interaction of amylin with heparin fragments of defined length, which model the glycosaminoglycan chains associated with amyloid deposits found in type 2 diabetes. Binding of heparin fragments to the positively charged N-terminal half of monomeric amylin depends on the concentration of negatively charged saccharides but is independent of oligosaccharide length. By contrast, amylin fibrillogenesis has a sigmoidal dependence on heparin fragment length, with an enhancement observed for oligosaccharides longer than four monomers and a leveling off of effects beyond 12 monomers. The length dependence suggests that the negatively charged helical structure of heparin electrostatically complements the positively charged surface of the fibrillar amylin cross-structure. Fluorescence resonance energy transfer and total internal reflection fluorescence microscopy experiments indicate that heparin associates with amylin fibrils, rather than enhancing fibrillogenesis catalytically. Short heparin fragments containing two- or eight-saccharide monomers protect against amylin cytotoxicity toward a MIN6 mouse cell model of pancreatic β-cells.

Introduction

Although there has been much progress in understanding the biophysical and structural basis of amyloid diseases from studies on purified amyloidogenic polypeptides [7], the amyloid deposits found *in situ* often interact or are associated with a variety of cofactors [42]. In the case of amylin, accessory molecules that could play a role in modulating pathology include insulin [149, 150], membrane lipids [9, 150], metals such as zinc [151], and glycosaminoglycans (GAGs) [152-155]. GAGs are a class of heterogeneous negatively charged oligosaccharides composed of seven different types of repeating disaccharide units [156]. GAGs and proteoglycans, particularly those composed of dermatan and heparan sulfate, are found ubiquitously in amyloid deposits formed *in situ* [157], and the heparan sulfate proteoglycan (HSPG) perlecan has been shown to co-localize with pancreatic amylin deposits isolated from patients with type 2 diabetes [155]. GAGs and HSPGs enhance the rate of amylin fibrillization *in vitro* [153, 154, 158, 159] and stabilize fibrils once formed [42]. In addition to the mature form of the hormone considered herein, GAGs were also reported to accelerate the fibrillization of the incompletely processed amylin propeptide [152, 160].

Here, we investigate the interactions of the GAG heparin with amylin fibrils. Although heparin is found primarily in the cytoplasmic granules of mast cells, its extensive characterization and similarity to heparan sulfate make it a suitable model for the GAG chains of HSPGs [152, 154, 158, 160, 161]. The availability of fluorescein-tagged heparin made it possible to examine whether GAGs associate with amylin fibrils. The availability of a series of heparin fragments of defined length enabled us to look at how oligosaccharide size and charge content affect binding to amylin monomers, fibrillization kinetics, and amylin cytotoxicity.

Materials and Methods

Materials-Synthetically prepared human amylin with an amidated C terminus and a Cys-2-Cys-7 disulfide bond was from AnaSpec (Freemont, CA). Mature human amylin is naturally amidated at its C terminus, and amidation is required for hormone activity [8]. Except for NMR experiments to look at the interactions of amylin monomers with heparin fragments, all experiments were done with the C-terminally amidated peptide, which is the physiological form of the hormone [8]. For the NMR experiments, we used ^{15}N-labeled recombinant amylin expressed in *Escherichia coli*, which was purchased from rPeptide (Bogart, GA). This peptide has a free-carboxyl group at the C terminus, but we can conclude that the lack of C-terminal amidation has no bearing on results because the NMR signals from the C-terminal half of the peptide are unaffected by the oligosaccharides. Heparin-dp2 was from V-LABS (Covington, LA), whereas the heparin fragments dp4 through dp20 were from Iduron (Manchester, UK). The low molecular weight fraction of heparin (LMWH) (catalog number A16198) was from Alfa Aesar (Ward Hill, MA), and the high molecular weight fraction of heparin (HMWH) (catalog number H3393) was from Sigma. Thioflavin T (ThT) was from Sigma or AnaSpec (ultrapure grade). Fluorescein-labeled heparin (FH) with an average molecular mass of 18 kDa and Alamar Blue were from Invitrogen. All other chemicals for solutions and buffers were from Fisher.

NMR Spectroscopy-Lyophilized aliquots of 0.1 mg of ^{15}Nlabeled amylin were suspended in 500 l of 20 mM sodium phosphate buffer, pH 6.0, in 90% H_2O, 10% D_2O to give a 50 μM peptide concentration. A temperature of 10 °C was used for NMR experiments to avoid exchange of amylin amide protons with solvent. The binding of heparin fragments was monitored using two-dimensional ^{1}H-^{15}N HSQC spectra collected with ^{1}H X ^{15}N spectral windows of 6000 X 1200 Hz

and matrix sizes of 2048 X 32 complex points. The experiments were done on a 600-MHz Varian Inova spectrometer equipped with a cryogenic probe. Assignments for amylin ^{1}H-^{15}N HSQC spectra were from the literature [162].

ThT Assays of Fibrillization Kinetics-Stock solutions of amylin were prepared in 100% DMSO, which disaggregates amylin [23], and stored at 80 °C when not in use. Starting from the 100% DMSO stock solutions, samples for fibrillization reactions were prepared to contain final concentrations of 5M amylin and 10 μM ThT in 20 mM sodium phosphate buffer, pH 7.4, with 4% (v/v) DMSO. To reduce the dead time for the reactions, amylin was the final component added to the solutions. The reaction mixtures of 200 l were placed into 96-well white polystyrene clear-bottom plates from Corning (Corning, NY) and sealed with clear polyester sealing tape from Fisher to prevent evaporation. The plate was incubated at 25 °C without agitation. Fluorescence intensity was recorded at 1-min intervals with excitation at 440 nm and emission at 490 nm on a Fluoroskan Ascent 2.5 fluorescence plate reader.

Fibrillization lag times were obtained from the *x* axis value at the intersection of the lag phase baseline slope and the slope of the steepest part of the growth phase [112]. Fibrillization rates were calculated by omitting the time points for the lag phase and fitting the initial part of the growth curve to the exponential function $y = A + B \exp(-kx)$ [112] where k is the rate constant, B is the initial amplitude, and A is the plateau. ThT fluorescence plateau values were obtained from steady-state fluorescence intensities at 300 min.

Fluorescence Spectroscopy-Proximity between amyloid-bound ThT and FH was analyzed by fluorescence resonance energy transfer (FRET) [163] using a Fluorolog 3-22 spectrophotometer. Samples containing 5 μM amylin, 10 μM ThT, and 0.28 μM FH were loaded into a 4 X 4-mm

quartz cuvette, and emission spectra (460-570 nm) were recorded at 6-min intervals for 3 h using excitation at 440 nm with a 4 nm band-pass filter.

To assess the amount of heparin incorporated into amylin fibrils (37), fibrils grown in the presence of 0.28 μM FH were run through an Amicon Ultra 100-kDa cut-off centrifugal filter at 13,000 rpm for 15 min. The filtrand containing fibrils was washed with deionized water, and the suspension was filtered a second time. Fluorescence spectra of the filtrates and filtrands were used to determine the fraction of FH tightly associated with fibrils.

Fluorescence Microscopy-Total internal reflection fluorescence microscopy (TIRFM) experiments were done on an Andor Revolution XD spinning disk confocal instrument with a Nikon TiE inverted microscope and an iXon EMCCD camera. ThT was excited with a 405 nm laser, and emission was filtered through a 483 nm band-pass filter. FH excitation was achieved with a 488 nm laser, and emission was filtered through a 523 nm band-pass filter.

Transmission Electron Microscopy-Aliquots from the stationary phases of fibrillization reactions containing either amylin or amylin and heparin fragments were blotted for 1 min onto a carbon-coated 400-mesh Maxtaform copper/rhodium grid from Ted Pella Inc. (Redding, CA) followed by negative staining with 1% uranyl acetate. EM images were recorded on an FEI Tecnai G^2 BioTWIN transmission electron microscope equipped with an AMT XR-40 camera.

Cytotoxicity Assays-Cytotoxicity was measured using the mouse insuloma MIN6 cell line model of -pancreatic cells [164], which was a gift from Dr. Anil Rustgi (University of Pennsylvania). Cells were seeded to a density of 20,000/100μL/well in a black clear-bottom 96-well plate from BD Falcon containing DMEM medium from Invitrogen with 15% fetal bovine serum, 25 mM glucose, 2 mM L-glutamine, 500 mM sodium pyruvate, 55 μM β-mercaptoethanol, 1000 units/ml

penicillin, and 100 g/ml streptomycin. After 24 h of incubation at 37 °C, in a humidified incubator with 5% CO_2, the culture medium was removed and replaced with fresh medium containing amylin or controls. The cells were incubated for another 24 h followed by the addition of 10% (v/v) Alamar Blue. Fluorescence, due to the reduction of the Alamar Blue dye by viable cells for 3 h, was measured using excitation and emission wavelengths of 544 and 590 nm, respectively [16]. Cell viability (in percentage) was calculated from the ratio of Alamar Blue fluorescence in treated cells to cells seeded in DMEM media alone. Uncertainties were calculated from the standard errors of measurements done in triplicate.

Amylin was prepared by dissolving lyophilized peptide in 100% DMSO to a 1.1 mM concentration for fresh amylin and 4 mM for experiments with mature amylin fibrils. The stock solutions were sonicated continuously for 5 min at 75 % amplitude before use. To look at the concentration dependence of cytotoxicity with fresh amylin, the amylin stock solution (1.1 mM) was diluted with reaction buffer and culture medium to final concentrations of 1, 5, 10, 40, and 80 μM. For studies with mature amylin fibrils, fibrils were formed for 48 h at 25 °C using amylin monomer concentrations of 10, 50, 100, 400, and 800 μM. Aliquots of the fibril suspensions were then added to the culture medium to achieve final amylin concentrations equivalent to those used with the freshly prepared peptide (1, 5, 10, 40 and 80 μM). For these experiments, we assumed that the higher amylin concentrations used to prepare mature fibrils would affect fibrillization rates but not the cytotoxicity of the fibrils.

To look at the effects of heparin fragments on cytotoxicity with fresh amylin, cells were incubated in the presence of 40 μM amylin and 80 μM oligosaccharides (polymer concentration). For mature fibrils, aliquots of a fibril suspension grown from 400 μM amylin and 800 μM

oligosaccharides over 48 h were diluted 10-fold to obtain equivalent final concentrations expressed in amylin monomer equivalents [114].

Results

Heparin has previously been shown to enhance amylin fibril formation [154, 158]. To explore the interaction between the glycosaminoglycan and the polypeptide, we looked at a series of heparin fragments of defined length ranging from a 2-mer to a 20-mer. The fragments are products of the digestion of porcine high-grade heparin by bacterial heparinase and were purified by high-resolution gel filtration to a uniform fragment length or "degree of polymerization (dp)" [165] : dp2 (0.66 kDa), dp4 (1.33 kDa), dp8 (2.66 kDa), dp12 (4.00 kDa), dp16 (5.32 kDa), and dp20 (6.66 kDa). The main building block of the fragments (75%) is the IS disaccharide IdoUA, 2*S*-GlcNS, 6*S*, which has four negatively charged groups: three sulfates and one carboxylate. Because sulfation of heparin is done by sulfotransferase enzymes after the polymer is synthesized, there is some variation in the sulfate content of the disaccharide building blocks, with about 75% in the trisulfated form and 25% in the mono and disulfated forms [165]. For the molecular masses quoted above, we assumed full sulfation of the parent disaccharides, although in practice, the average sulfation of the heparin parent fragment is 2.5 [158], leading to a 40 dalton lower molecular mass per disaccharide as compared with the fully sulfated form. In addition to the fragments of defined length, we also did experiments on an LMWH with an average molecular mass of 5 kDa (4-6 kDa) and an HMWH that contains fragments from 6 to 30 kDa with most chains in the 17-19 kDa range. When considering the heparin fragments, it is important to note that both the molecular mass and the number of charges increase with increasing fragment length. Unless otherwise stated,

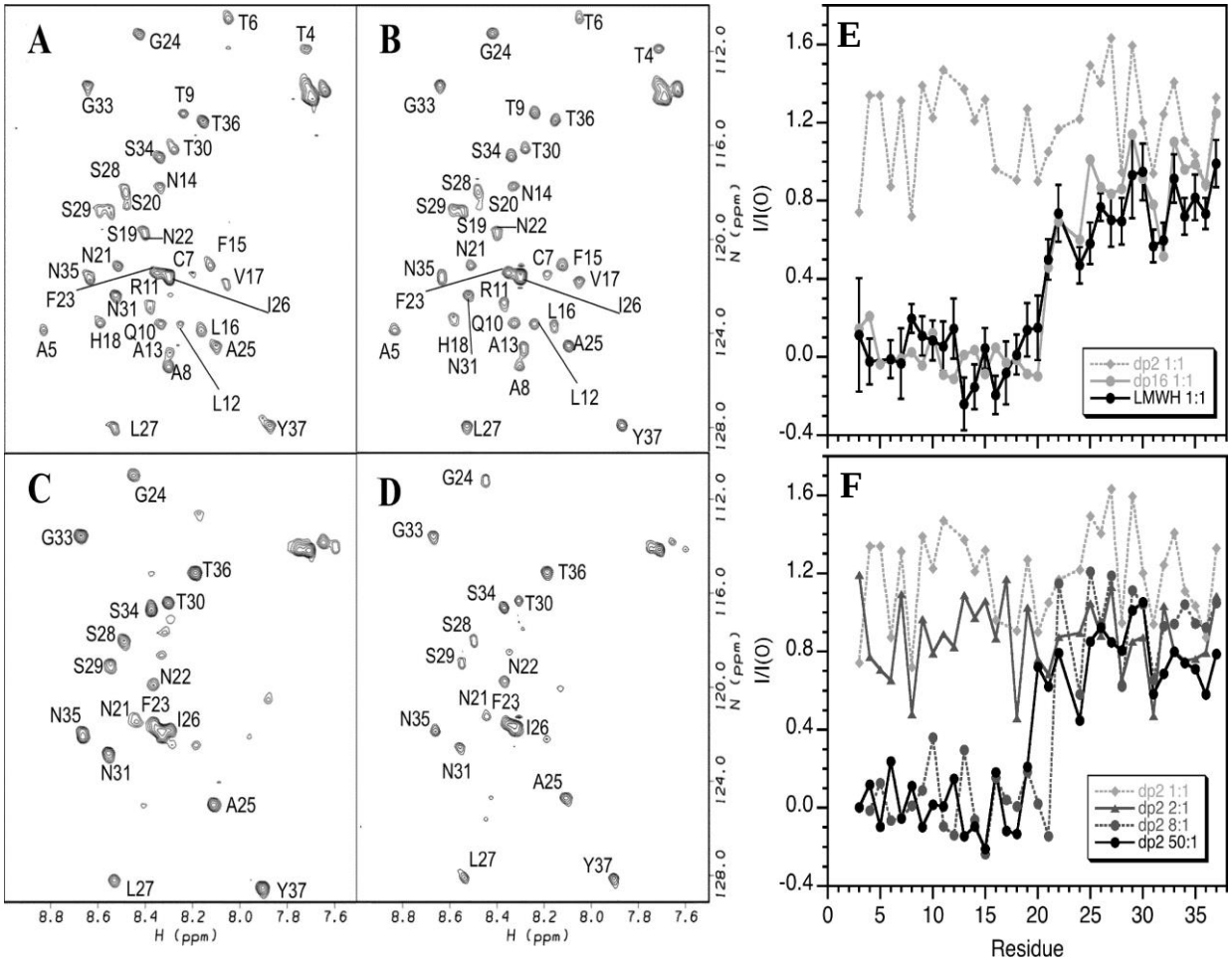

Figure A1.1. Effects of heparin fragments on ^{1}H-^{15}N HSQC spectra of ^{15}N labeled amylin. The degree of polymerization of the heparin fragments is denoted by dp. A, control spectrum of amylin in the absence of heparin. B, amylin in the presence of a 1:1 molar ratio of the dp2 fragment (50 μM dp2). C, amylin in the presence of a 1:1 molar ratio of the dp16 fragment (50 μM dp16). D, amylin in the presence of a 1:8 molar ratio of the dp2 fragment (400 μM dp2). E, Data for equimolar ratios of 50 μM amylin to 50 μM dp2, dp16, and LMWH. F, Data for varying molar ratios of dp2 to 50 μM amylin. The crosspeak broadening data in E and F are presented as I/I(0) where, I is the crosspeak intensity in the presence of a given heparin fragment and I(0) is the control intensity in the absence of heparin.

the concentrations of the heparin fragments quoted in this work are polymer concentrations (*e.g.* dp20 or dp16). For experiments in which we want to vary the chain length but keep the ionic strength constant, it is more useful to work with concentrations expressed in terms of saccharide monomers (*e.g.* (dp20)/20, (dp16)/16), and we explicitly note in those cases that we are reporting the saccharide monomer concentration.

Heparin Binds to the Positively Charged N-terminal Half of Amylin Monomers. Fig. A1.1*A* shows a two-dimensional ^{1}H-^{15}N HSQC spectrum of 50 μM amylin at pH 6 and a temperature of 10 °C. Under these conditions, we see a single set of resonances corresponding to amylin monomers. Any fibrils formed during the 30 min time used to acquire the spectrum would be too large to be seen by NMR. We detected ^{1}H-^{15}N correlations for all 37 residues in the peptide except Lys-1-Asn-3, which are lost due to fast hydrogen exchange with solvent. In the presence of an equimolar concentration of the dp2 heparin fragment, the ^{1}H-^{15}N HSQC spectrum of amylin is unaffected (Fig. A1.1*B*). By contrast, in the presence of an equimolar concentration of the longer dp16 fragment (50 μM), resonances from residues 1-20 are broadened beyond detection, whereas resonances from residues 21-37 persist (Fig. A1.1*C*). The cross-peaks that remain in the presence of dp16 fragment show chemical shift changes that become progressively smaller, going from residue 21 to residue 37. The effects on the NMR spectrum of amylin could be due to the longer size of the dp16 fragment or to the presence of eight times as many negatively charged saccharide monomers as compared with dp2.

To distinguish between these possibilities, we looked at the NMR spectra of amylin in the presence of an excess of the dp2 fragment. At a 2:1 molar ratio of dp2: amylin, the NMR spectrum of amylin is largely unperturbed except for selective partial broadening of cross-peaks from residues 4–6, 10–12, and 18–21. These segments are close to the only four charged groups in the amylin sequence: the -amino group, Lys-1, Arg11, and His-18. Of these, the cross-peak for His-18 shows the most pronounced decrease in intensity. At molar ratios of 8:1 dp2:amylin or above, the effects on the amylin NMR spectrum were similar to those obtained at 50 μM dp16, with residues 1-20 broadened beyond detection (Fig. A1.1D, E and F). Thus when the dp2 concentration

is increased 8-fold to give the same 400 μM charged saccharide monomer concentration as with an equimolar ratio of amylin:dp16, we see analogous effects on the NMR spectrum of the amylin monomer. This indicates that binding of heparin to amylin in its monomeric state depends on the amount of charged saccharide monomers rather than on the length or conformational properties of heparin. The NMR line broadening suggests intermediate exchange on the chemical shift timescale. The range of concentrations over which the effects are observed points to a K_d of 200 μM for the binding of disaccharides to monomeric amylin.

Fibrillization Enhancement Depends on Heparin Oligosaccharide Length. In contrast to the binding of heparin to amylin monomers, enhancement of amylin fibrillization depends on heparin fragment length. Amylin fibrillization kinetics were followed using the ThT assay; the marked changes in the fluorescence properties of this dye when it binds amyloid cross-sheet structures make it a specific probe for fibrils [23, 34, 98, 108, 166]. We first looked at the effects on amylin fibrillization of heparin fragments ranging from 2 to 20 saccharide monomers included in the reactions at a constant polymer concentration of 10 μM (Fig. A1.2*A*). With increasing length, heparin shortens the lag times for fibrillization, increases fibril growth rates, and increases the value of the steady-state ThT fluorescence plateau at the end of the reactions. In addition to the dp2-dp20 series, we also looked at the LMWH and HMWH fractions, using average molecular mass of 5 and 18 kDa to calculate a 10 μM concentration (Fig. A1.2*A*). Although the effects of the heparin fragments of defined length level off beyond dp12, the heterogeneous heparin fractions enhance amylin fibrillization more than any of the dp2–dp20 fragments. The effects of LMWH and HMWH are difficult to interpret because they contain a heterogeneous mixture of heparin fragments with a poorly defined length distribution. LMWH has fragments ranging in size from

dp12 to dp18 and possibly longer, whereas HMWH has fragments in a range between dp18 and dp90. The data for the series of defined-length fragments (dp2-dp20) shows that fibrillization is accelerated with increasing oligosaccharide size. In a mixture of short and large heparin fragments, the effects of the longest would be expected to predominate so that the enhancement of fibrillization would not scale with the average molecular weight. Consequently we did not include LMWH and HMWH in our analysis of amylin fibrillization kinetics.

The trend of increasing fibrillization rates with larger heparin fragments in Fig. A1.2*A* could reflect the increasing length of the oligosaccharide chains or could be due to an increase in the concentration of charged saccharide monomers as seen for the NMR experiments monitoring binding of heparin fragments to amylin monomers (Fig. A1.1). To distinguish between these possibilities, we carried out fibrillization reactions varying the concentration of the smallest dp2 fragment between 50 and 500 μM (Fig. A1.2*B*). The fibrillization kinetics showed only small variations and no systematic trend with increasing concentration of dp2 (Fig. A1.2*B*). This indicates that the enhancement of amylin fibrillization depends primarily on oligosaccharide length rather than on the amount of charged saccharide monomers.

Finally, we carried out fibrillization reactions in the presence of heparin fragments of different lengths, varying the polymer concentration to maintain a fixed saccharide monomer concentration of 200 μM (Fig. A1.2*C*). With the charged saccharide monomer concentration fixed, we once again saw an increase in amylin fibrillization that depended only on the lengths of the heparin oligosaccharides.

Fig. A1.3 summarizes how the three parameters that characterize the kinetics of the amylin fibrillization depend on heparin fragment length. We focus our analysis on the reactions where the

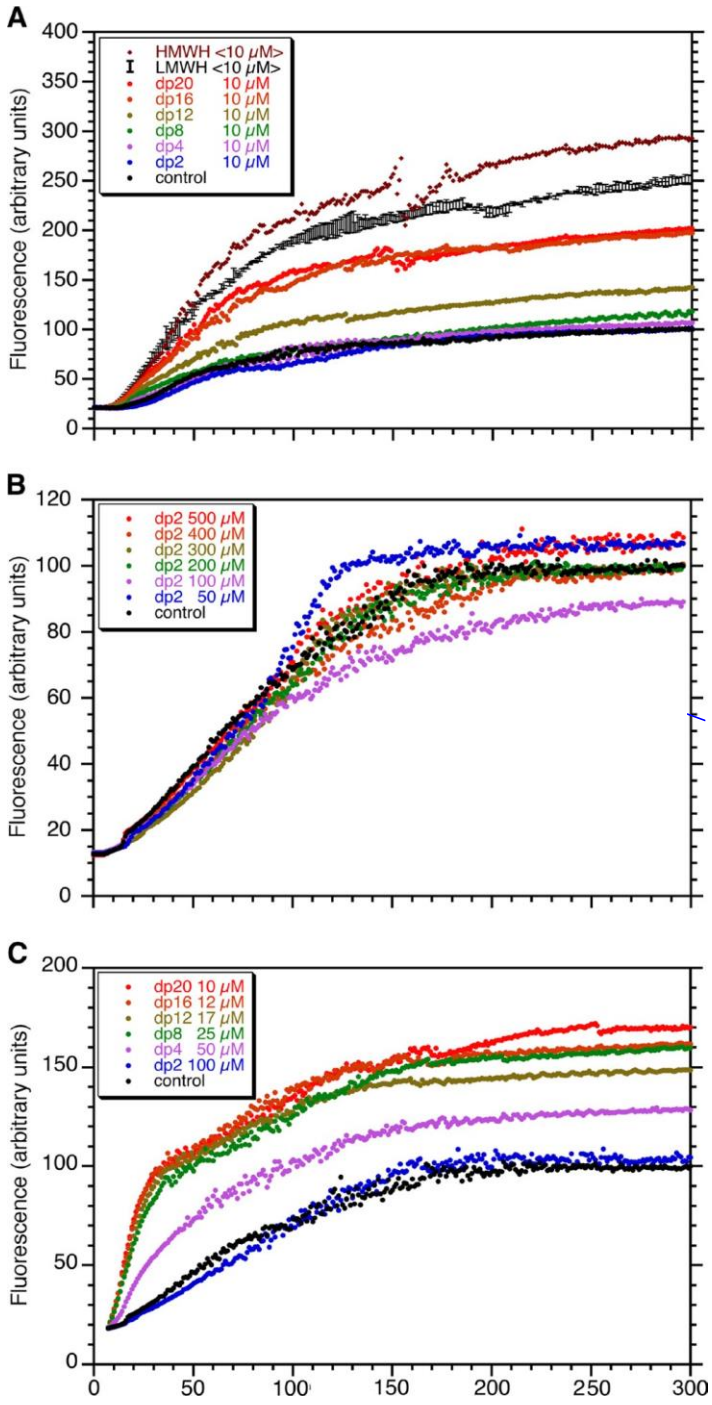

Figure A1.2 Effects of heparin fragments on amylin fibrillization. A, fibrillization at a constant heparin polymer concentration of 10 μM. B, Fibrillization over a 10-fold range of dp2 concentrations from 50 to 500 μM. *C*, fibrillization over a range of fragment concentrations selected to keep the saccharide monomer concentration constant at 200 μM. The control sample in each series is amylin without heparin. The data are presented as averages of duplicate experiments. Representative standard errors are shown for the LMWH sample in *panel A*.

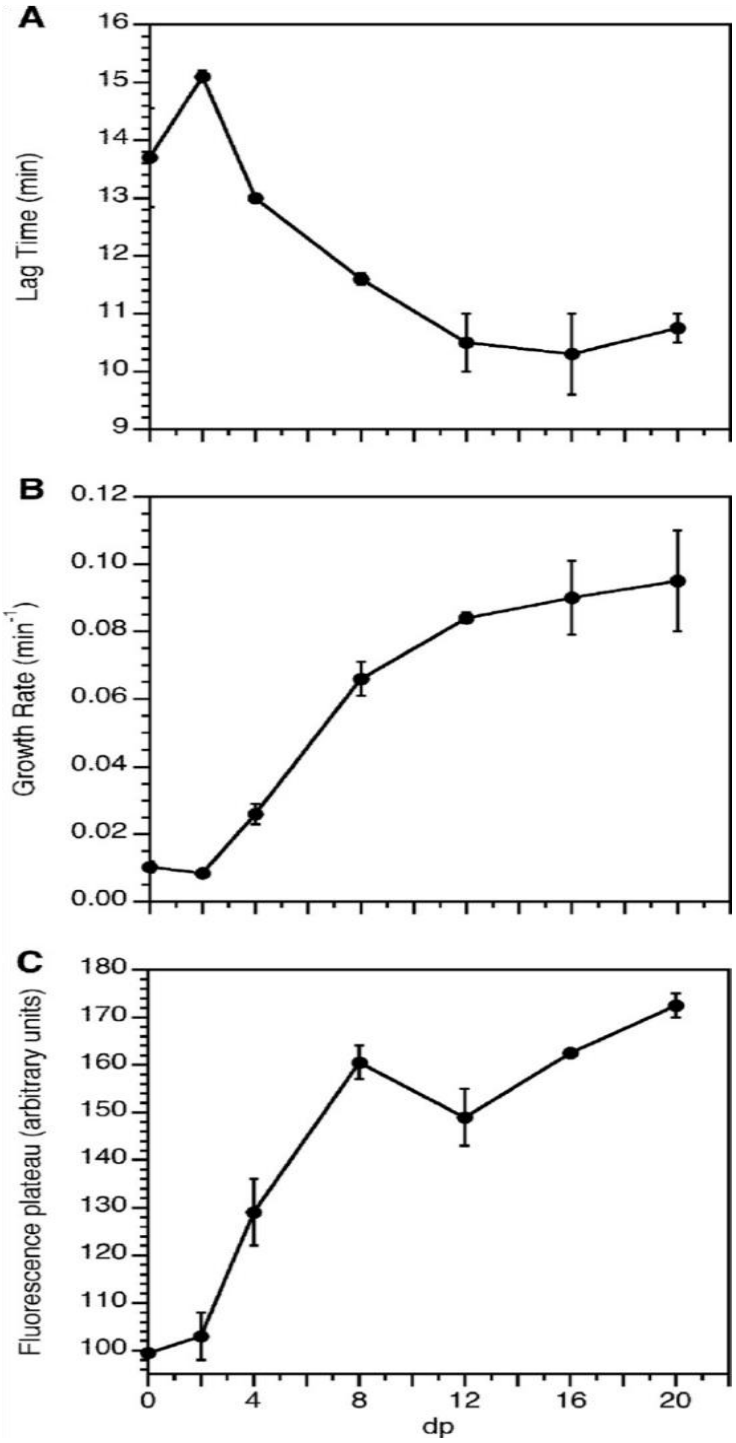

Figure A1.3 Kinetic parameters obtained from the data in Fig. A1.2*C* using a range of heparin fragment concentrations selected to keep the saccharide monomer concentration constant. *A*, lag times. *B*, fibrillization rates. *C*, ThT fluorescence plateaus. The data are averages of kinetic parameters obtained from duplicate runs, shown with their associated standard errors. The dp = 0 point corresponds to amylin in the absence of heparin.

heparin fragment length varies but the charged saccharide monomer concentration is fixed (Fig. A1.2*C*). With increasing oligosaccharide length, the lag time for fibrillization decreases (Fig. A1.3*A*), whereas the elongation rates (Fig. A1.3*B*) and steady-state fluorescence plateaus (Fig. A1.3*C*) increase. All three parameters show a sigmoidal dependence on oligosaccharide length, starting at dp4, reaching a mid-point near dp6, and leveling off beyond dp12.

To demonstrate that fibrils are formed in the presence of heparin fragments, we obtained electron microscopy (EM) data on aliquots taken from the stationary phases of the amylin fibrillization reactions of the control, dp2, dp8, and dp16 samples shown in Fig. A1.2*A* (Fig. A1.4). The images for amylin fibrils grown in the presence of heparin fragments are similar to those obtained for the control sample containing amylin alone. Although EM does not lend itself to quantifying the amounts of fibril formed, we saw a qualitative increase in the number of fibrils in the presence of the longer heparin fragments. The amylin fibrils grown in the presence of dp8 and dp16 fragments also appeared to be longer than those from the dp2 or control samples (Fig. A1.4).

Co-localization of Heparin with Amylin Fibrils by FRET. Immunohistochemical studies have previously shown that the HSPG perlecan is associated with plaques of amylin isolated from patients with type 2 diabetes [155]. Given the complex composition of the amyloid plaques, which can include a variety of proteins and cofactors besides HSPGs [42, 157], we wanted to ascertain more directly whether GAGs are associated with amyloid fibrils using heparin as a model. To this end, we used FH with an average molecular mass of 17 kDa that has one fluorescein conjugated per heparin irrespective of the oligosaccharide size [167].

Fig. A1.5*A* compares amylin fibrillization kinetics in the presence of ThT alone, FH alone, and both dyes. The data in the presence of ThT alone are typical of a fibrillization reaction. With

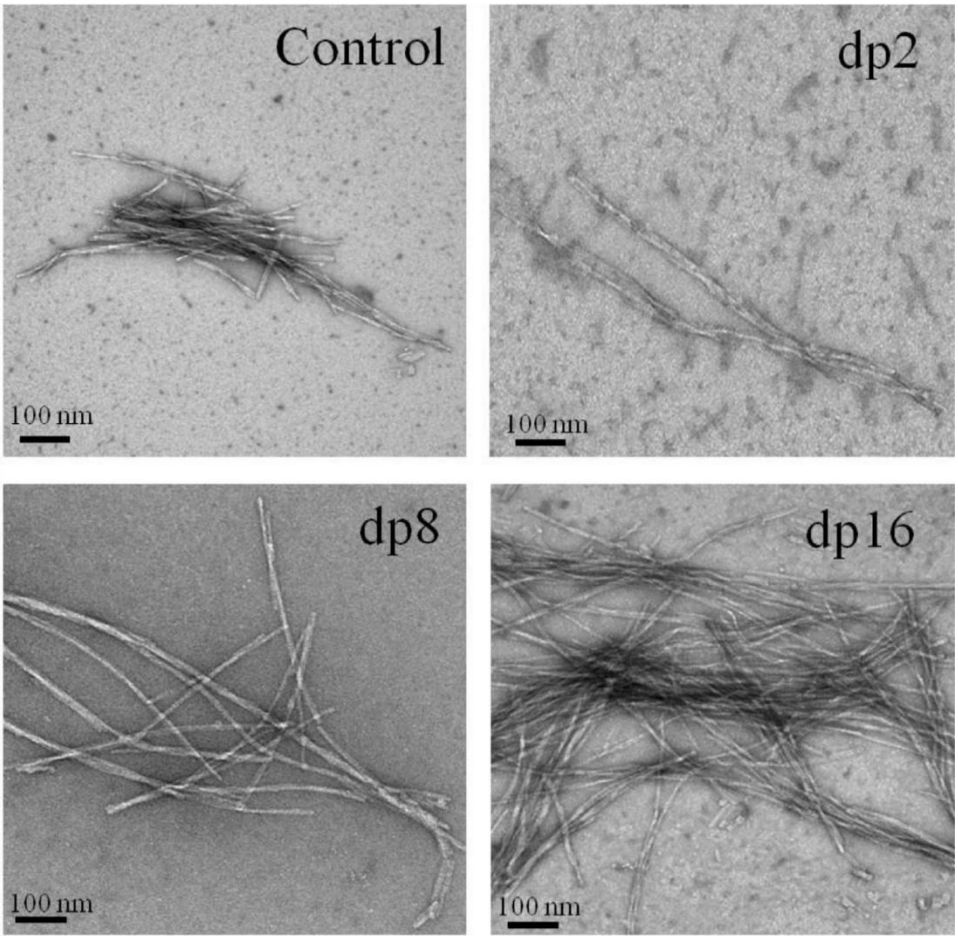

Figure A1.4. EM images of amylin taken from the plateau phases of the fibrillization reactions in Fig. A1.2*A*.

FH alone, the fluorescence is nearly constant as amyloid starts to form. Fluorescein does not undergo the large changes in fluorescence properties that are a hallmark of the binding of ThT dye to amyloid fibrils [98]. Moreover, the spectral parameters were selected for the detection of amyloid-bound ThT (excitation 440 nm, emission 490 nm) rather than fluorescein (excitation 488 nm, emission 518 nm). In the presence of both ThT and FH, we observed 50% reduction in the quantum yield of the amyloid-bound ThT donor due to FRET to the FH acceptor fluorophore (Fig. A1.5*A*). Additional control experiments were done to rule out that the hydrophobic fluorescein dye

could be driving the interaction with amylin fibrils.

To further characterize FRET between FH and amyloid bound ThT, we collected emission spectra on a fluorescence spectrophotometer using excitation at 440 nm (Fig. A1.5*B*). As amylin fibrils started to form in the reaction, between 10 and 158 min, we saw an increase in fluorescence at 478 nm due to fibril-bound ThT [98] and at 508 nm due to FRET between the ThT donor and FH acceptor. The increases in fluorescence are accompanied by a blue shift in the FH emission maximum from 513 to 508 nm (Fig. A1.5*B*) as amylin fibrils start to grow. The increase in fluorescence at 508 nm was about half that at 478 nm (Fig. A1.5*C*), consistent with the previously observed 50% FRET from ThT to FH (Fig. A1.5*A*). The experiments indicate that the two fluorophores come within a 1–10-nm FRET distance [163] of each other in the presence of amylin fibrils.

Co-localization of Heparin with Amylin Fibrils by TIRFM. We next examined the association of FH with amylin fibrils using TIRFM. The TIRFM technique has been previously used to image a variety of amyloid fibrils through the fluorescence of the non-covalently bound dye ThT [33, 34, 166]. In the first experiment, we started with amylin fibrils grown in the presence of ThT, which were imaged using a 483-nm emission filter after excitation with a 405 nm laser. After imaging the fibrils using ThT fluorescence, the solution containing ThT was removed from the coverslip and replaced with a solution containing FH. The same area was used to image fibrils using FH fluorescence, detected using a 523 nm emission filter after excitation with a 488 nm laser. As compared with the ThT image, the FH image is more diffuse, but the same fibrils are observed (Fig. A1.6*A*).

ThT may remain associated to the fibrils after the addition of FH in the experiment shown

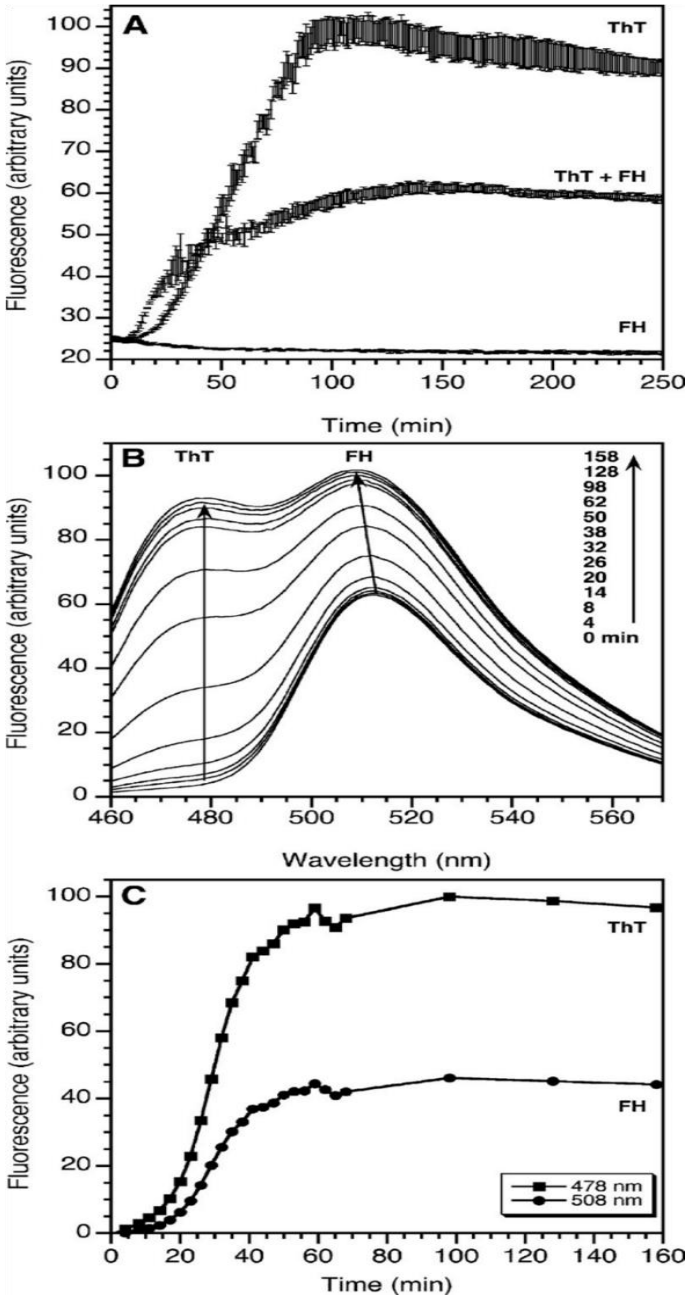

Figure A1.5. FRET between fibril-bound ThT and FH. *A*, fibrillization kinetics of amylin in the presence of ThT only, FH only, or ThT and FH. Fluorescence was measured with a plate reader using an excitation filter of 440 nm and an emission filter of 490 nm. Representative standard errors from duplicate experiments are shown for each reaction. *B*, representative emission spectra for amylin fibrillization in the presence of ThT and FH. The *left arrow* indicates the increase in quantum yield at 478 nm due to amyloid-bound ThT. The *right arrow* indicates the increase in quantum yield, as well as the blue shift in the emission maximum of FH from 513 to 508 nm as amylin fibrillization progresses with time. The experiments were done in a fluorescence spectrophotometer using an excitation wavelength of 440 nm. *C*, kinetics of amylin fibrillization monitored by the increase in fluorescence at 478 nm (ThT) and 508 nm (FRET from ThT to FH). The intensity data are from the spectra in *panel B* after subtracting the baseline spectrum of ThT and FH in the absence of amylin.

Table A1.1 Incorporation of FH into amylin fibrils[a].

Sample	Peak Fluorescence (cps)	Fluorescence Retained (%)	λ_{max} (nm)
Initial fluorescence[b]	7.416×10^6	---	513
Final fluorescence[c]	1.199×10^7	---	508
First filtrate[d]	4.66×10^6	63[f]	512
First filtrand[e]	4.37×10^6	36[g]	508
Second filtrate[d]	4.14×10^5	6[f] (17% of first filtrand)	511
Second filtrand[e]	3.61×10^6	30[g] (83% of first filtrand)	510

[a]Amylin (5 μM) fibrillized in the presence of 0.28 mM FH was filtered through a 100 KDa MW cut-off filter to determine the fraction of FH associated with fibrils.
[b]Fluorescence at the start of the fibrillization reaction.
[c]Fluorescence at the end of the fibrillization reaction.
[d]Fluorescence of the FH fraction that passed through the 100 kDa cut-off filter.
[e]Fluorescence of the FH fraction retained in the 100 kDa cut-off filter.
[f]Fluorescence normalized to the initial value at the start of the reaction, assuming this represents free FH.
[g]Fluorescence normalized to the final value at the end of the reaction, assuming this represents fibrilbound FH.

in Fig. A1.6*A*. The spectral parameters used to obtain the image after the addition of FH (488 nm excitation, 513 nm emission) should be selective for FH, although there is a chance we could still be detecting ThT fluorescence because the emission maxima of ThT and FH are separated by only 25 nm. To rule out that the fibrils were detected through ThT fluorescence, we did a second experiment in which we grew fibrils in the presence of only FH (Fig. A1.6*B*). We once again obtained images of species with a fibrillar morphology detected using FH fluorescence. The solution containing FH was replaced by a ThT solution followed by imaging of the same section replaced with the ThT solution. A number of species with fibrillar morphology of the coverslip using ThT fluorescence filters. As compared with the image obtained using ThT fluorescence, the image obtained using FH fluorescence shows additional globular species, which are no longer seen when the FH solution is replaced with the ThT solution. Presumably these was (indicated by

arrows) are seen in both images, however, demonstrating that FH and ThT bind to the same individual fibrils. In this regard, it is interesting to note that a very recent confocal microscopy study reported co-localization of FH with amyloid fibrils [168]. In a final experiment, we grew amylin fibrils in the absence of fluorophores and then added FH. Within 5 min of adding FH, we saw species with a fibrillar morphology (Fig. A1.6*C*). The experiment demonstrated that like ThT [34], FH can bind rapidly to fibrils after they are formed.

Amylin Fibrils Contain Weakly and Tightly Bound Heparin. To determine whether heparin is incorporated into amylin fibrils, we carried out a fibrillization experiment using 5 μM amylin in the presence of 0.28 μM FH. After the fibrillization reaction was complete, the sample was run through a 100 kDa cutoff centrifugal filter. A 36% fraction of the fluorescence was retained in the filter, whereas 63% passed through the filter corresponding to unbound FH or FH bound to amylin species with a molecular mass smaller than 100 kDa. The fibrils and FH retained in the filter were washed with deionized water and run through the 100 kDa filter a second time. After the second filtration, 30% of the initial fluorescence was retained in the filter, corresponding to an FH that is tightly bound to the fibrils (Table A1.1). The results of the experiment with amylin are similar to those previously reported for -synuclein fibrils grown in the presence of FH [108], where 15% of FH was incorporated into the fibrils, 12% was weakly associated, and the remainder of the FH was not bound [108].

Effect of Heparin Fragments on Amylin Cytotoxicity. We next wanted to see whether heparin fragments had an impact on amylin cytotoxicity to a MIN6 mouse cell line model of pancreatic β cells [164]. There are conflicting reports regarding whether amylin is cytotoxic when added as a freshly dissolved peptide or in its fibrillar form [10-12, 169]. To address this, we first looked at

the dependence of cytotoxicity on amylin concentration using either freshly dissolved amylin or mature amylin fibrils formed over 2 days (48 h). With freshly dissolved amylin, we saw an apparent concentration mid-point at 25 μM amylin, with cell viability reaching 50% asymptotic minimum at amylin concentrations 40 μM (Fig. A1.7*A*, *solid line*). By contrast, with mature amylin fibrils, cytotoxicity appeared to be independent of peptide concentration within experimental error (Fig. A1.7*A*, *dashed line*), giving an average cell viability of 71 ± 4% over the five points sampled in the 1-80 μM amylin concentration range. The lowered cytotoxicity with mature fibrils as compared with freshly dissolved amylin is consistent with previous reports [10, 12, 169]. The lack of a concentration dependence for mature fibrils is puzzling and could signify an equilibrium between non-toxic fibrils and a toxic species. The latter toxic species could be formed simultaneously with the fibrils or could dissociate from them when they are transferred to cell cultures.

The lack of an apparent concentration dependence could be due to a limiting factor for the toxic species such as its solubility. Although with the mature fibrils the reaction has reached a steady state, with fresh amylin, the reaction is ongoing so that the toxic species could be replenished as the reaction proceeds in the presence of the cells. A possible precedent for such a mechanism has been recently reported for mouse prion, where the levels of a distinct toxic species are uncoupled from the titer of infective prion [170].

Fig. A1.7*B* summarizes the effects of heparin on cytotoxicity obtained with either fresh amylin or amylin fibrils. The *first column* shows untreated cells. The Alamar Blue fluorescence of all other experiments was normalized to the untreated cells, which were assigned a cell viability of 100%. The next five experiments show controls. The 1% DMSO vehicle present in all experiments

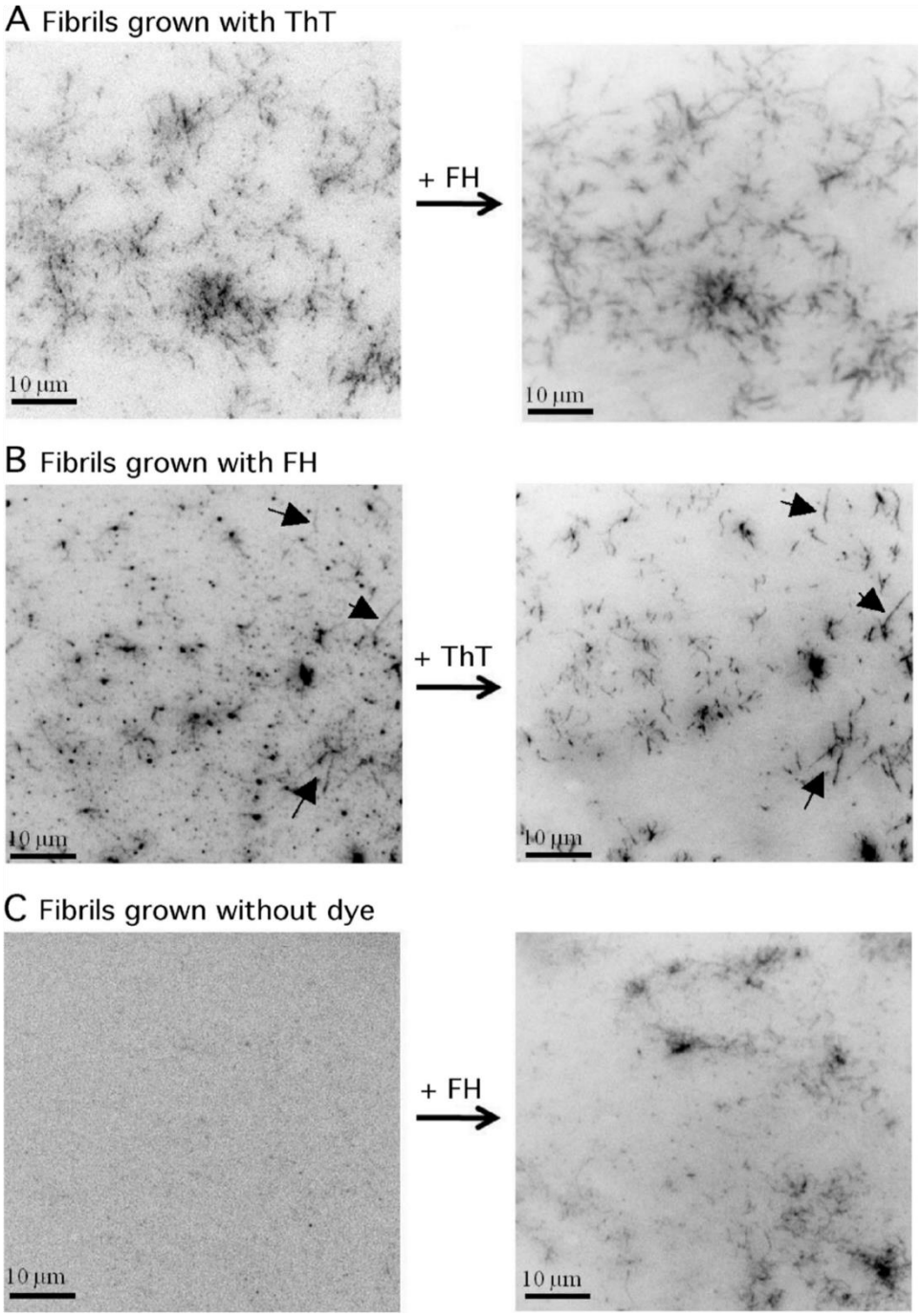

Figure A1.6. TIRFM images of fibrils formed from a 100 µM amylin sample detected with ThT and FH fluorophores. *A*, fibrils grown for 210 min in the presence of 15 µM ThT followed by the addition of FH to a final concentration of 0.3 µM. *B*, fibrils grown for 210 min in the presence of 0.3 µM FH followed by the addition of ThT to a final concentration of 15 µM. *Arrows* indicate examples of species with a fibrillar morphology that are observed in both images. *C*, fibrils grown for 240 min without dye followed by the addition of FH to a final concentration of 1 µM. The images on the right-hand side were obtained within 5 min of adding the respective fluorescence probes.

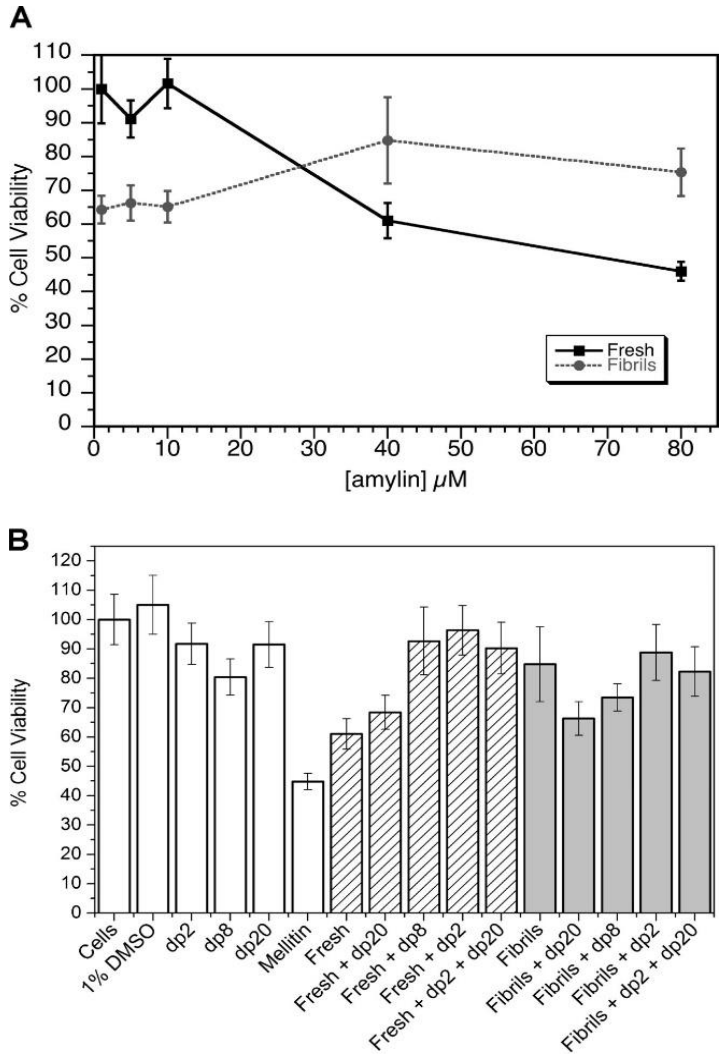

Figure A1.7. Amylin cytotoxicity toward mouse MIN6 cells (38). The data are presented as means S.E. from experiments done in triplicate. *A*, concentration dependence of cytotoxicity for freshly dissolved amylin and amylin fibrillized for 2 days. *B*, effects of heparin fragments on amylin cytotoxicity. The first five experiments (*white bars*) are controls: untreated MIN6 cells; 1% DMSO, which was present in all experiments except the first; dp2, dp8, and dp20 oligosaccharides at 80 μM concentrations in the absence of amylin; and a 5 μM bee venom melittin positive control. The next five experiments (*striped bars*) are for freshly dissolved amylin, alone or in the presence of oligosaccharides. The next five experiments (*gray bars*) are for amylin fibrils formed for 2 days in the absence or presence of the indicated oligosaccharides.

except the untreated cells had no effect on cell viability. The dp2, dp8, and dp20 heparin fragments by themselves also had little effect on cell viability. The bee venom toxin melittin, used as a positive control, reduced cell viability to 45 % at a 5 μM concentration. The next series of five experiments (*striped columns*) looks at the effects of freshly dissolved amylin. Amylin alone at a 40 μM concentration reduced

cell viability to 61%. Amylin together with an 80 μM concentration of the longest dp20 heparin fragment had a similar cell viability of 68%. Inclusion of the short dp8 and dp2 oligosaccharides res cued cell viabilities to levels of 93 and 96%, respectively. We also looked at the effects of adding a mixture of 80 μM dp2 and 80 μM dp20 to 40 μM amylin, which gave a cell viability of 90%. This value is greater than the average of the data for the individual dp2 and dp20 oligosaccharides (82%), indicating that the dp2 disaccharide has a protective effect even in the presence of the longer dp20 heparin fragment. The last set of five experiments looks at amylin fibrils (Fig. A1.7*B*, *gray columns*). The trends are similar, although less clear, because the fibril samples had less of an effect than freshly dissolved amylin. Amylin fibrils grown in the presence of the dp20 and dp8 oligosaccharides showed reduced cell viabilities of 66 and 73%, respectively. Fibrils grown in the presence of dp2 or of a mixture of the dp2 and dp20 fragments gave cell viabilities approaching those of the untreated cells.

Discussion

HSPGs and GAGs are ubiquitous components of the extracellular matrix that are found in association with amyloid deposits formed by a variety of disease-linked proteins [42, 157] including amylin [155]. GAGs have been shown to enhance the fibrillization of amylin *in vitro* [153, 154, 158]. The interaction of heparin with proamylin has also been investigated because GAGs could play a role in amyloidosis of the incompletely processed hormone [152, 160]. Finally, heparin is given as an anticoagulant to diabetic patients receiving pancreas transplants and could contribute to graft dysfunction by stimulating amylin fibrillization [171]. To better understand how GAGs affect amylin dysfunction, we characterized the interaction of heparin with amylin and looked at the effects of heparin fragments on amylin cytotoxicity.

NMR experiments show that heparin binds to the positively charged N-terminal half of amylin

(Fig. A1.1). Binding does not depend on the length of heparin fragments but on the concentration of negatively charged saccharide monomers, in as much as the broadening effects on the amylin NMR spectrum with dp16 can be replicated with an 8-fold excess of the shorter dp2 fragment. Neutralization of the positive charges on amylin by the negative charges on heparin would render the peptide more hydrophobic, thus facilitating aggregation and fibrillization. In this regard, it is worth noting that the loss of a single charge on His-18 at high pH dramatically increases the rate of amylin fibrillization [23, 151].

By contrast, the enhancement of amylin fibrillization by heparin depends on oligosaccharide length rather than the amount of charged monosaccharaides (Fig. A1.2). The oligosaccharide length dependence is sigmoidal (Fig. A1.3), with an enhancement of fibrillogenesis starting at four monomers (dp4) and leveling off beyond 12 monomers (dp12). Heparin adopts a left-handed helix structure with a 2_1 symmetry axis and four sugar residues per turn, based on solution NMR studies [172, 173]. The length dependences of the kinetic parameters in Fig. A1.3 suggest that a minimum of one turn of heparin helix is needed to favor amylin fibrillization and that enhancement of fibrillization begins to level off beyond three turns of the heparin helix. Heparin is the most negatively charged naturally occurring biopolymer known, and its binding to proteins is mediated through electrostatic interactions with basic groups in proteins [174]. We have proposed that electrostatic repulsion between like charges, replicated by the symmetry of the cross- structure along the length of fibrils, could be one of the main forces opposing fibrillogenesis [175]. The heparin polyanion could aid fibrillogenesis by providing a suitable scaffold to complement the positive charges displayed on the surfaces of amylin fibrils. Indeed, it has been shown that the enhancement of amylin fibrillization drops by 86%, going from heparin to completely desulfated heparin, emphasizing the importance of charge-coupling in the interactions between the two polymers [158].

Heparin is composed of the disaccharide unit iduronic acid (IdoUA)-glucosamine (GlcN). In the heparin structure determined by NMR (PDB code: 1HPN), the 6*S* sulfate of residue GlcN (*i*-1), the 2*S* sulfate of residue IdoUA (*i*), the NS sulfate of residue GlcN (*i*1), and the carboxyl C of residue IdoUA (*i*2) form an array of negative charges on one side of the heparin helix. The distances between the charged groups vary between 6.1 Å for the 2*S*(IdoUA) to NS(GlcN) contact and 7.1 Å for the NS(GlcN) to C(IdoUA) contact. After a 7.3 Å contact between C(IdoUA) and 6*S*(GlcN), the pattern is repeated on the same side of the helix for the next four saccharide monomers. In the structure of amylin fibrils based on solid-state NMR [25], the average spacing between positively charged groups on alternate amylin monomers laying along the fibril axis is 5.8 Å for His-18 (Cγ toms) and 6.7 Å for Arg-11 (Cz atoms). Thus the spacing of negative charges in the heparin helix is complimentary to the spacing of positive charges from alternating amylin monomers running along the fibril axis. Because heparin has a flexible structure that can kink to achieve optimal binding to proteins [174, 176] and because side chains can adjust in both polymers, the match may be even better than suggested by considering individual structures. Our conclusions about the structural basis of interactions between amylin fibrils and heparin are supported by recent molecular dynamics modeling of the interactions of amyloid with GAGs [168].

Although amylin fibrils are formed in the presence of heparin fragments of various lengths (Fig. A1.4), the effects of the oligosaccharides on fibrillization could be catalytic or could involve association with the fibrils. Our FRET (Fig. A1.5) and TIRFM (Fig. A1.6) data indicate that heparin associates with amylin fibrils during fibrillogenesis. TIRFM also indicates that heparin can bind to amylin fibrils after they are formed (Fig. A1.6*C*). Filtration experiments suggest that of the fluorescein-tagged heparin bound to amylin fibrils, a fraction of 83% is tightly associated, whereas another 17% is weakly associated. Because heparin affects fibrillization kinetics and associates with fibrils, we wanted to see whether there

is an effect on the biological activity of amylin. GAGs could increase cytotoxicity simply by enhancing fibrillogenesis. Alternatively, fibrils could disrupt normal function by sequestering important components of the extracellular matrix [40]. In contrast to these hypotheses, a number of recent reports indicate that heparin [177-179] as well as other GAGs [180] reduce the cytotoxicity of the Alzheimer amyloid peptide and of the aortic amyloid peptide medin [181]. In the present work, we found that the cytotoxicity of amylin toward a mouse model of -pancreatic cells depends on heparin fragment length (Fig. A1.7). Amylin in the presence of the longest dp20 heparin fragment has a cytotoxicity comparable with amylin alone. By contrast, the shortest dp2 fragment protects against cytotoxicity with both freshly dissolved and fibrillar amylin samples.

The protective effects of the dp2 fragment are intriguing but will need further study to establish a mechanistic basis. Based on the current data, we can conclude that the effects of the heparin fragments on cytotoxicity are probably unrelated to their effects on fibrillization kinetics. The dp2 fragment has negligible effects on amylin fibrillization kinetics (Figs. A1.2*B* and A1.3) yet protects against cytotoxicity (Fig. A1.7*B*). By contrast, the dp20 fragment enhances amylin fibrillization (Figs. A1.2*B* and A1.3), yet amylin cytotoxicity is similar in the presence and absence of dp20 (Fig. A1.7*B*). One possibility is that the heparin fragments exert their effects on soluble amylin oligomers or some other species and that these rather than the fibrils are cytotoxic [10, 12, 169, 179]. The roles of putative intermediates in cytotoxicity remain poorly characterized and controversial not only for amylin but for other amyloidogenic proteins [14, 16]. An alternative possibility is that the structure or surface properties of the fibrils differ in the presence of heparin fragments of different lengths in a way that affects their interactions with β cells [180]. Finally, heparin fragments could affect cofactor molecules [178] that mediate the interactions of amylin with β cells.

Excerpted from: Croke, R. L., Patil, S. M., Quevreaux, J., Kendall, D. A. and Alexandrescu, A. T. (2011), NMR determination of p*K*a values in α-synuclein. Protein Science, 20: 256–269.
I and Dr. Robyn Croke performed NMR experiment and data analysis (Figures A1-1 to A1-5)
Dr. Jason Quevreaux performed protein synthesis

Appendix II: NMR determination of pKa values in α-Synuclein

Abstract

The intrinsically unfolded protein α-Synuclein, which is involved in Parkinson's disease, has an N-terminal domain with seven imperfect repeats of the sequence KTKEGV and a C-terminal domain with a large proportion of acidic residues. To better understand the charge properties of α-Synuclein, 2D ^{1}H-^{15}N HSQC and 3D C(CO)NH NMR experiments were used to determine pK_a values for all 26 sites in the 140 amino acid protein that ionize below pH 7. In the absence of salt, pK_a values of aspartate and glutamate residues from the first 100 residues are systematically lowered compared to random coil model compounds suggestive of weak ion pair interactions between acidic and basic residues in the KTKEGV repeats. By contrast, the pK_a values of acidic residues from the last 40 residues are raised due to electrostatic repulsion between negatively charged residues in the C-terminal tail. The effects are smaller but persist at a physiological salt concentration. Determination of pK_a values for α-Synuclein in a membrane-like environment is hampered by the deterioration of NMR spectra of the protein bound to SDS micelles below pH 5, as the C-terminal tail becomes uncharged. Nevertheless, we could characterize the titration of His50, which has pK_a raised by 1.5 pH units when α-Synuclein is bound to SDS micelles compared to the free monomer. pH titrations for His50 in the disease-linked mutants E46K and A53T show that this shift is primarily due to interactions between the histidine and SDS, with electrostatic interactions between His50 and Glu46 in the a-helical structure playing a much smaller role. Our results indicate that the pK_a values of intrinsically unfolded α-Synuclein differ significantly from those of random coil model compounds and that electrostatic interactions may help nucleate protein misfolding.

Introduction

Alpha-Synuclein (αS) is a 14.5 kDa protein expressed predominantly at the pre-synaptic terminals of brain neurons [182, 183]. The physiological function of the protein remains unknown [182] although a role in synaptic vesicle recycling has been suggested [184, 185]. Misfolding of αS leads to the formation of fibrillar cytoplasmic aggregates [107, 186] called Lewy bodies which are a defining characteristic of Parkinson's disease [187-190]. Because the number of Lewy bodies is often poorly correlated with the severity of Parkinson's disease symptoms controversy surrounds the issue of whether fibrils or smaller soluble oligomers are responsible for the neurotoxicity of misfolded αS [48]. Regardless of the mechanism of neurotoxicity, genetic evidence establishes a link between the αS gene (*SNCA*) and Parkinson's disease. Although 90-95% cases of Parkinson's disease cases are sporadic [191], the autosomal-dominant familial mutations A30P, E46K, A53T, as well as the triplication of the wild-type SNCA gene lead to early onset of the disease [182, 187, 192, 193].

The amino acid sequence of αS can be conceptually subdivided into three domains with an unusual distributions of charged residues (Fig. A2.1A). The first 90 residues of αS contain seven imperfect repeats of the amino acid sequence xKTKEGVxxxx [194], which have been shown to be important for the induction of α-helical structure in αS [195] and for the binding of the protein to the negatively charged lipids it prefers [195-197]. Residues 61-95 of αS correspond to the hydrophobic "non-amyloid-β component" (NAC), the most aggregation-prone part of the protein [198-203]. The name NAC, derives from the occurrence of this segment as a second protein component of the extracellular amyloid-β plaques found in patients with Alzheimer's disease [204]. The mechanism by which the NAC fragment of the intracellular αS is cleaved and comes

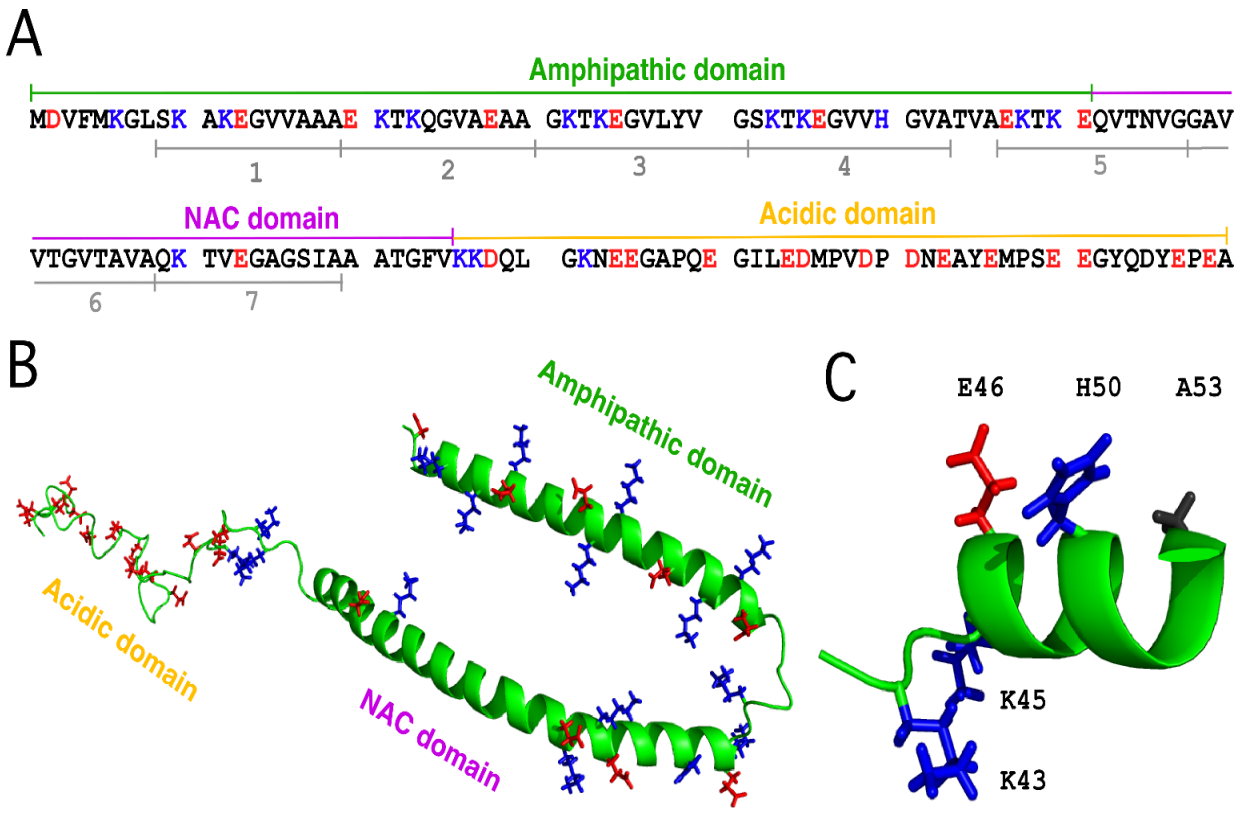

Figure A2.1 Sequence of αS and structure of the protein bound to SDS micelles. (A) The three domains of the αS amino acid sequence and the locations of the seven xKTKEGVxxxx repeats [194]. (B) Structure of αS bound to SDS micelles [197], showing the side-chains of residues that are positively (blue) or negatively charged (red) at neutral pH. (C) Expanded view of the micelle-bound αS structure showing the location of His50 compared to Glu46 and Ala53 (the sites of the familial Parkinson's mutations E46K and A53T).

to be associated with extracellular amyloid-β plaques is unknown. The last two of the KTKEGV repeats occur within the NAC segment [194], however, due to the imperfect nature of the repeats only two charged residues occur in the hydrophobic region 62-95: Lys 80 and Glu 83. The last 40 amino acids of αS contain a large proportion of acidic residues, giving the C-terminal tail of the protein a pronounced negatively charged character at physiological pH.

Monomeric αS is intrinsically unfolded with a fractional population of at most 10-20% α-helix structure [201, 205]. The first ~90 residues of the protein fold into an α-helical

structure in the membrane-like environments provided by micelles, vesicles, or bilayers that contain a large fraction of negatively charged lipids [2, 76, 200, 206, 207]. By contrast, the negatively charged C-terminal tail remains disordered when αS binds to lipid assemblies [2, 27, 76, 197]. The highest-resolution structure available for αS in a membrane environment, is for the protein bound to sodium dodecylsulfate (SDS) micelles [197]. Although the SDS detergent is not physiological, it forms relatively small micelles that are amenable to direct high-resolution NMR studies [27, 197]. When bound to SDS micelles, the amphipathic N-terminal domain forms two long α-helices that lie on the surface of the micelle. The hairpin structure is likely an artifact of the small size of SDS micelles. With larger lipid assemblies that approach the sizes of synaptic vesicles, αS folds into a single uninterrupted α-helix [206, 208]. The structure of αS bound to SDS micelles is shown in Fig. A2.1B. The view of the structure is opposite to the face of the protein that interacts with SDS micelles [197]. Charged residues are shown in blue (positive) and red (negative). In an α-helix, residues separated by three or four positions in the sequence have the potential to form ion-pairs [209]. Consideration of the αS sequence and structure suggests that residues in the amphipathic domain of the protein are poised to form electrostatic interactions between acidic and basic amino acids, including the pairs Asp2-Lys6, Lys10-Glu13, Glu20-Lys23, Glu28-Lys32, Lys32-Glu35, Lys42-Glu46, Glu46-His50, Glu57-Lys60, Lys58-Glu61, and Lys80-Glu83. By contrast, the negatively charged residues in the C-terminal tail could be subject to electrostatic repulsion due to a high density of like charges. It is important to note that the structure of αS bound to SDS micelles was determined entirely with perdeuterated protein samples using NMR experiments that look at the protein backbone [197]. As such there is no information on the

conformations of side-chains in the αS structure; these are shown in random orientations in Fig. A.1B and A2.1C.

To better understand the role of charges in αS structure we determined pK_a values for the 26 sites in monomeric αS that ionize below pH 7. In the absence of salt, we see pK_a deviations up to 0.6 pH units compared to random coil model compounds. Sites in the first 100 residues have pK_a values lowered compared to random coil values, while those in the last 40 residues are raised. The pH titrations were repeated in the presence of 150 mM NaCl. While the effects are smaller the same sequence pattern is observed. We tried obtaining titration data for αS bound to SDS micelles but the NMR spectrum of the protein deteriorates below pH 5 as the acidic residues in the C-terminal tail become neutralized. We thus focused on the pH titration of His50, a residue of particular interest. His50 has been identified as the high-affinity binding-site for Cu^{2+}, a metal which has been implicated in Parkinson's disease and that markedly increases the fibrillization rates of αS [210]. Moreover, in the αS structure His50 is within one turn of α-helix of the sites of the two familial Parkinson's disease mutations E46K and A53T (Fig. A2.1C). We wanted to obtain data on the ionization of His50 to test the hypothesis that the E46K and A53T mutations perturb the electrostatic properties of His50.

The pK_a data reported in this work provides a foundation for understanding the roles of charges in the αS structure. A number of studies have shown that pK_a values of unfolded proteins deviate from random coil model compounds [211-215]. The unusual distribution of charged residues in αS provides a stringent test of the assumption that pK_a values of residues in unfolded proteins are approximated by those in random coils. The unfolded state is an important reference state for theoretical calculations of the roles of charges in protein structure

stabilization [212, 215-217]. Accurate pK_a values for unfolded αS will help the analysis of the effects of protonation of residues on the structures of membrane-bound and fibrillar αS.

Materials and Methods

Materials - The peptides Ac-AADAA-NH_2 and Ac-AAEAA-NH_2 used to obtain random coil pKa values for Asp and Glu were prepared by solid-phase synthesis at > 95% purity by NEO-Peptide (Cambridge, MA). Deuterated SDS (d_{25}-sodium dodecyl sulfate) was from Cambridge Isotopes (Andover, MA). The chemical shift standard 2, 2-Dimethyl-2-silapentane-5-sulfonate (DSS) was from Sigma (St. Louis, MO).

Site-Directed Mutagenesis of αS - The E46K and A53T mutants were prepared starting from the *pT7-7/asyn-WT* vector [218] which was a gift from the Lansbury lab (Harvard Medical School). Oligonucleotide primers were purchased from Integrated DNA Technologies (Coralville, IA). For E46K, the forward primer was 5'-CC AAA ACC AAG AAG GGA GTG GTG-3' and the reverse primer 5'-CAC CAC TCC CTT CTT GGT TTT GG-3'. For A53T, the forward primer was 5'-GTG CAT GGT GTG ACG ACA GTG GCT GAG-3' and the reverse primer 5'-CTC AGC CAC TGT CGT CAC ACC ATG CAC-3'. Site-directed mutagenesis was performed using the QuikChange protocol, utilizing PFU Turbo Polymerase from Stratagene (La Jolla, CA). The PCR product was purified using digestion with the restriction endonuclease DpnI from New England Biolabs (Ipswich, MA) at 37 ºC, followed by transformation into Stratagene *E. coli* BL21 (DE3)-pLysS cells according to the manufacturer's instructions. Sequences of the αS clones were verified using Beckman Coulter CEQ 2000 Dye Terminator Cycle Sequencing at the UConn Biotechnology facility.

Expression and Purification of αS - Expression and purification of αS was carried out

according to published methods [205, 219]. Cells were grown in M9 minimal media supplemented with 1 g/L ^{15}N ammonium chloride and/or 3 g/L ^{13}C-glucose at a temperature of 37°C and a shaker speed of 250 rpm. To make unlabeled protein the M9 media was supplemented with the same amounts of ammonium chloride and glucose at natural isotopic abundance. Ampicillin (100 µg/mL) was used to select for the *ampicillin* resistance marker in the *pT7-7/asyn-WT* vector, and 37 µg/mL chloramphenicol was used to maintain the pLysS copy number. When the cells reached an OD_{600} of 0.6, αS expression was induced by addition of IPTG to a final concentration of 1 mM, and the cells were incubated for an additional 4 h at 37°C. Cells were collected by sedimentation at 4 ºC for 30 min in a GSA rotor operating at 4294 rpm. The cell pellet was resuspended in lysis buffer (10mM Tris at pH 8.0, 1 mM EDTA, 1 mM PMSF, 1mM DTT and a few crystals of RNase, DNase and lysozyme) and sonicated at 70% (pulse 45 sec, delay 15 sec) for ten minutes on a Fisher Scientific Sonic Dismembrator Model 500. After sonication, the cell lysate was boiled for 20 min and the cell debris was separated by sedimentation for 30 min at 12,800 rpm at a temperature of 4 °C. The supernatant was boiled again for 20 min, taking advantage of the heat stability of αS to achieve partial purification from other proteins in the lysate [220, 221], and the precipitate was removed by sedimentation for 30 min at 12,800 rpm and 4 ºC. The resulting supernatant was subject to ammonium sulfate precipitation (361g/L) for 1 hr at 4°C, followed by collection of the pellet containing αS by sedimentation for 30 min at 12,800 rpm, 4°C. The ammonium sulfate precipitate containing αS was resuspended in 20 mM Na_2HPO_4, pH 7.4 and dialyzed overnight against the same buffer, followed by application on an Amersham Q-Sepharose™ Fast Flow anion exchange column. A linear 1M NaCl gradient was used to elute αS. SDS-PAGE was

used to identify column fractions containing αS, the fractions were pooled and dialyzed for 24h against 20 mM Na_2HPO_4, pH 7.4. The αS purified in this way was determined to be at least 90% homogeneous by 15% tricine gel electrophoresis and electrospray ionization (ESI) mass spectroscopy. Final yields of purified αS were about 50 mg per liter of *E. coli* culture. Prior to use, purified αS samples were stored at –80°C in 20 mM Na_2HPO_4, pH 7.4 containing 0.02% NaN_3.

pH Titrations - The pH titrations of free αS (Fig. A2.2 and A2.3), αS in the presence of SDS micelles (Fig. A2.4), and random coil model peptides were performed on samples dissolved in 90% H_2O /10% D_2O. All αS and peptide samples used in this study were initially in 20 mM sodium phosphate buffer at pH 7.4. The sample pH was adjusted by adding aliquots of 1 M HCl and NaOH stock solutions. For comparisons of the titration of His50 in WT αS, E46K-αS and A53T-αS in the presence of d_{25}-SDS micelles (Fig. A2.5) samples were dissolved in 99.96% D_2O and pH adjustments were made using 1 M stock solutions of DCl and NaOD.

For pH measurements in aqueous solution we used a Mettler (Columbus, OH) Inlab Micro pH glass electrode. For any solutions containing SDS we used a PH46-SS probe metal electrode from IQ Scientific (Loveland, CO) since trace amounts of KCl from glass electrodes precipitate SDS. Three-point electrode calibrations (pH 4, 7, 10) were done before each pH titration. Solution pH values were measured before and after each experiment with typical differences between measurements of less than 0.05 to 0.1 pH units. The average of the pH measurements before and after the NMR experiment was taken as the solution pH. We found that the following protocol reduces fluctuations in pH measurements before and after NMR experiments. The pH after the NMR experiment is measured by transferring the sample from

the NMR tube to an Eppendorf tube. For the next pH value, HCl or NaOH are added to adjust the pH, the sample is stirred on a Vortex mixer, transferred to the NMR tube, and then back to the Eppendorf for the pH measurement before the NMR experiment. This minimizes pH fluctuations from traces of the sample before the pH adjustment that remain in the NMR tube. The same NMR tube, Eppendorf tube, and pipette for transferring samples were used throughout the entire pH titration. For the pH titrations samples were contained in 5 mm (Wilmad 535-pp) NMR tubes, with a larger initial volume (0.75 to 1.0 ml) than the recommended 0.6 ml, to make up for sample losses due to pipetting and pH measurements during the titration.

NMR Spectroscopy - NMR experiments were done on a Varian 600 MHz instrument equipped with a cryogenic probe. The αS concentration for all experiments was 0.25 mM. DSS was used as an internal ^{1}H chemical shift reference standard for all experiments. ^{13}C and ^{15}N chemical shifts were referenced indirectly as described in the literature [222]. The pH titration of ^{13}C,^{15}N-labeled αS in the absence of salt was characterized with twelve 3D C(CO)NH and 2D ^{1}H-^{15}N HSQC experiments recorded between pH 7.4 and pH 1.5. Eleven experiments over the same pH range and were used to determine pK_a values for αS in the presence of 150 mM NaCl. An additional four 2D ^{1}H-^{15}N HSQC experiments were recorded up to pH 8.1 for each titration, to define the high pH chemical shift plateau of the His 50 backbone ^{15}N resonance. Experiments on αS in the absence of micelles were done at 10 ^{o}C to prevent loss of amide proton signals due to fast exchange with solvent [205]. Experiments of αS in the presence of SDS micelles were done at 37 ^{o}C since lower temperatures reduce the quality of NMR spectra [2].

The peptides Ac-AADAA-NH_2 and Ac-AAEAA-NH_2, dissolved to 3 mM concentrations in 90% H_2O /10 % D_2O were used to determine random coil pK_a values for Asp and Glu. The titration of the peptides in the absence of salt was followed using twelve 1D ^1H NMR spectra recorded between 6.7 and 1.7. For experiments in the presence of 150 mM NaCl ten spectra were obtained between pH 6.4 and 2.4. All peptide experiments were done at a temperature of 10 ^oC for direct comparison with the αS data.

The titration of ^{13}C, ^{15}N-labeled αS in the presence of SDS micelles was characterized with sixteen 2D ^1H-^{15}N HSQC and 1D ^{13}C-filtered aromatic spectra (50 mM SDS) collected between pH 10.4 and 4.2. Four representative pH points that show the deterioration of ^1H-^{15}N HSQC spectra below ~pH 5.0 are shown in Fig. A2.4. The titration of His50 in WT, E46K and A53T αS was monitored by 1D ^1H NMR using with protein samples at natural isotopic abundance in the presence of 50 mM d_{25}-SDS dissolved in 99.96% D_2O. For each of the experiments at least twelve spectra were recorded between pH 9.7 and 5.6 (Fig. A2.5)

The following spectral parameters were used for NMR experiments. 1D ^1H NMR spectra were collected with spectral windows of 8000 Hz digitized into 2048 complex points. 2D ^1H-^{15}N HSQC spectra were acquired with ^1H x ^{15}N spectral windows of 1024 x 128 Hz digitized into 6000 x 1380 complex points. The total acquisition time for each spectrum was 10 min. 3D C(CO)NH spectra were acquired with ^1H x ^{13}C x ^{15}N spectral windows of 6000 x 8800 x 1380 Hz digitized into 1024 x 64 x 32 complex points. The total acquisition time for each spectrum was 12 hr.

NMR Data Analysis - Identification of NMR signals over the pH range studied was facilitated by published ^1H, ^{15}N and ^{13}C assignments for αS at pH 7 [223], pH 3 [201], as

well as data on the pH dependence of αS NMR spectra from our lab [205]. For 1D spectra, chemical shifts at the various pH values were obtained from the center of the peak envelope. For 2D and 3D spectra, 1D traces were extracted along the frequency of the nucleus of interest. The traces were phased as necessary before measuring chemical shifts from the center of the peak envelope.

The pH dependence of chemical shifts was analyzed using non-linear least squares fits of the data to the modified Henderson-Hasselbach equation [224, 225]:

$$\delta = \delta\,\mathrm{low} - \frac{\delta\,\mathrm{low} - \delta\,\mathrm{high}}{1+10^{n(\mathrm{pKa}-\mathrm{pH})}} \qquad \text{Eq. A2.1}$$

Where, the pK_a is the ionization constant, δ_{low} is the low pH chemical shift plateau, δ_{high} is the high pH chemical shift plateau, and n is the apparent Hill coefficient. The parameters obtained from the fits and their associated standard errors are given in Table A2.1.

Results

pKa Values for αS in the Absence of Salt. Ionization constants for aspartate and glutamate residues in αS were obtained from 3D C(CO)NH experiments recorded at different pH values. The C(CO)NH experiment [226] correlates the amide of a given residue with all the aliphatic ^{13}C resonances of the preceding residue. The experiment circumvents the spectral overlap typically encountered for Asp and Glu side-chains, which is particularly severe for an unfolded protein like αS, by correlating these spin systems with the well dispersed nitrogens of the following residues in the amino acid sequence. Fortuitously, the strongest crosspeaks were from the aliphatic carbons closest to the titrating carboxyl groups of the acidic residues.

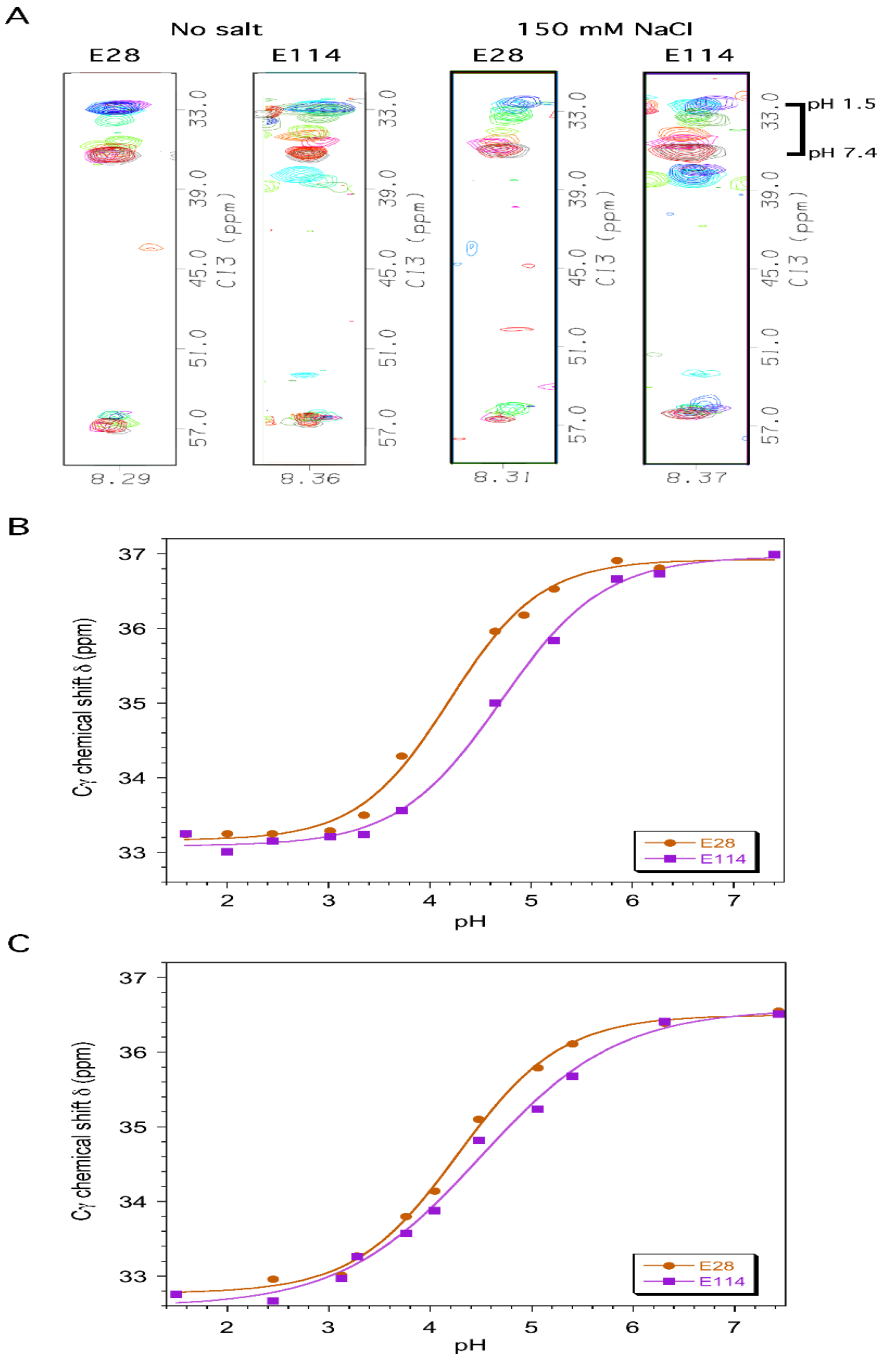

Figure A2.2 Representative pH titration data. (A) Superposed 2D strips from twelve 3D C(CO)NH experiments used to determine pK_a values for Glu and Asp residues in the absence and presence of 150 mM NaCl. Contours are shown for residues Glu28 and Glu114 on a red (neutral) to blue (acidic) color ramp using data collected between pH 7.4 (black) and pH 1.5 (blue). The individual pH values are shown in panels B and C. The width of the strips in the HN dimension is 0.1 ppm. The contours centered at ~38 ppm in the strips for Glu114 are from another spin system that appears in the same HN and N frequency range at low pH. (B) pH titration data for Glu28 and Glu114 in the absence of salt. (C) pH titration data for Glu28 and Glu114 in the presence of 150 mM NaCl. The curves are non-linear least squares fits of the data to Eq. A2.1, used to obtain the titration parameters in Table A2.1.

Representative data for Glu28 and Glu114 showing superimpositions of 2D slices from the 3D C(CO)NH experiments obtained at pH values between 7.4 and 1.5 are shown in Fig. A2.2A. The pH dependence of the Cγ chemical shifts of Glu28 and Glu114 in the absence of salt is shown in Fig. A2.2B. The glutamate Cγ carbons shift from ~37 ppm at neutral pH, to ~33 ppm at acidic pH. For the aspartate Cβ carbons the corresponding shift is between ~42 and ~38 ppm. The Cα resonances are also sensitive to the titration of the carboxyl groups but the pH dependence of these shifts is much smaller, typically from ~57.0 to ~56.0 ppm for glutamate and ~54.5 to ~53.0 ppm for aspartate between neutral and acidic pH.

The 3D C(CO)NH experiment enabled us to obtain data for 21 of the 26 sites that ionize between neutral and acidic pH in αS. The sites that could not be characterized with the C(CO)NH experiment were His50, Glu61, Asp119, Glu137, and the α-carboxyl group at the C-terminus. Two of these sites are in the residue pairs D119-P120 and E137-P138 since prolines lack an amide proton we could not use the 3D C(CO)NH experiment to follow the pH titration of the preceding residues. Similarly, the α-carboxyl group is at the end of the sequence (Ala140) and the titration of His50 involves the ionization of an aromatic side-chain that cannot be detected in the C(CO)NH experiment. For these sites pK_a values were obtained by monitoring the pH dependence of ^{1}H-^{15}N correlations in 2D ^{1}H-^{15}N HSQC spectra. In the case of Glu61, the E61(Cγ)-Q62(HN) spin system occurs as a partially overlapped shoulder on the E114(Cγ)-D115(HN) spin system throughout most of the pH transition. While we could obtain accurate data for the Cγ resonance of Glu114 from the C(CO)NH experiments the titration of Glu61 was more accurately determined from the ^{15}N resonance in 2D ^{1}H-^{15}N HSQC experiments. Consistent with previous results on unfolded proteins [227] we found that the ^{15}N shifts of

ionizable residues in αS are dominated by the protonation of the residue's own side-chain. Protonation of residues more than one position removed in the amino acid sequence have negligible effects on backbone ^{15}N chemical shifts.

The KTKEGV repeats in the amphipathic region of αS give seven instances of Glu-Gly pairs (Fig. A2.1A). In the 3D C(CO)NH experiments the E83(Cγ)-G84(HN) and E131(Cγ)-G132(HN) spin systems are well resolved so that unambiguous pK_a values were obtained for Glu83 and Glu131. The two correlations E35(Cγ)-G36(HN) and E110(Cγ)-G111(HN) overlap between pH 7.4 and 4.0 but separate at lower pH. We based our assignments on a slightly more downfield ^{15}N chemical shift of 110.9 for Gly111 compared to 110.5 for Gly36 [201]. The assignment is tentative, however, as indicated in Table A2.1. The three correlations E13(Cγ)-G14(HN), E46(Cγ)-G47(HN) and E105(Cγ)-G106(HN) are unresolved throughout the entire pH range in the absence of salt. We assigned the parameters obtained from the unresolved pH titration of the group to all three residues Glu13, Glu46, and Glu105. We estimate the pK_a values of the three individual residues differ by at most 0.1 pH unit from the unresolved pK_a of 4.21. pH titration parameters for αS are summarized in Table A2.1. In the absence of salt, the pK_a values of the 18 Glu residues in αS are spread over 0.8 pH units while those of the 6 Asp residues are spread over 1.0 pH units. The ranges are large for an unfolded protein and comparable to those of ionizable residues on the surfaces of folded proteins [212, 214, 216]. The pK_a values of the intrinsically unfolded αS show a pronounced dependence on residue position in the amino acid sequence (Table A2.1). Acidic residues within the first 100 amino acids of αS have lowered pK_a values indicating a lower affinity for protons (hydronium ions) such that they resist losing their negative charge.

Table A2.1. pK_a Values of αS in the absence and presence of salt.[a]

	No salt				150 mM NaCl				
Site	**pK_a**	**n**	**δ_{low}**	**δ_{high}**	**pK_a**	**n**	**δ_{low}**	**δ_{high}**	**Resonance**
Asp2	3.61±0.05	1.30±0.21	38.64±0.09	41.99±0.06	3.63±0.04	1.00±0.08	122.81±0.05	124.92±0.03	Cβ/N[d]
Glu13[c]	4.21±0.06	0.90±0.08	33.11±0.08	36.79±0.08	4.32±0.09	1.42±0.35	32.85±0.14	36.24±0.16	Cγ
Glu20	4.07±0.04	0.93±0.06	33.10±0.05	36.74±0.04	4.24±0.04	0.90±0.08	32.77±0.19	36.49±0.18	Cγ
Glu28	4.20±0.06	0.96±0.09	33.16±0.08	36.92±0.08	4.27±0.04	0.85±0.06	32.77±0.06	36.50±0.06	Cγ
Glu35[b]	4.17±0.06	0.93±0.08	33.11±0.07	36.69±0.07	4.08±0.13	0.88±0.20	30.42±0.41	36.39±0.29	Cγ
Glu46[c]	4.21±0.06	0.90±0.08	33.11±0.08	36.79±0.08	4.31±0.10	0.86±0.15	32.99±0.18	36.39±0.13	Cγ
His50	6.78±0.04	1.08±0.08	123.11±0.02	125.05±0.06	6.52±0.07	1.52±0.37	123.45±0.02	125.05±0.05	N
Glu57	4.20±0.05	0.94±0.08	33.10±0.07	36.87±0.07	4.33±0.09	0.76±0.11	32.89±0.13	36.49±0.13	Cγ
Glu61	4.04±0.27	0.86±0.35	121.05±0.07	121.70±0.08	3.97±0.06	1.12±0.22	121.35±0.04	122.07±0.02	N
Glu83	4.35±0.05	1.07±0.10	33.14±0.06	36.71±0.07	4.33±0.03	0.91±0.05	32.70±0.05	36.32±0.05	Cγ
Asp98	3.68±0.06	0.87±0.11	38.23±0.10	41.56±0.07	4.00±0.03	1.44±0.16	38.60±0.05	41.01±0.04	Cβ
Glu104	4.39±0.13	1.12±0.26	33.13±0.15	36.74±0.17	4.51±0.11	1.01±0.17	33.02±0.12	36.36±0.14	Cγ
Glu105[c]	4.21±0.06	0.90±0.08	33.10±0.08	36.79±0.08	4.49±0.17	1.04±0.35	33.85±0.18	36.33±0.20	Cγ
Glu110[b]	4.50±0.09	0.98±0.19	34.34±0.06	36.71±0.08	4.31±0.07	0.85±0.09	32.65±0.12	36.36±0.10	Cγ
Glu114	4.70±0.05	0.86±0.08	33.09±0.06	36.97±0.09	4.49±0.09	0.64±0.08	32.59±0.13	36.58±0.14	Cγ
Asp115	4.15±0.05	0.76±0.06	38.18±0.06	41.69±0.05	4.18±0.09	0.94±0.16	38.10±0.12	41.11±0.11	Cβ
Asp119	4.02±0.07	0.69±0.06	122.85±0.08	125.87±0.06	3.99±0.02	0.77±0.03	123.27±0.03	126.20±0.02	N
Asp121	4.62±0.06	0.97±0.08	39.11±0.03	41.43±0.06	4.39±0.03	0.78±0.04	117.42±0.03	119.36±0.03	Cβ/N[d]
Glu123	4.87±0.05	0.77±0.06	33.16±0.05	36.95±0.08	4.69±0.10	0.78±0.12	32.69±0.13	36.46±0.16	Cγ
Glu126	4.89±0.06	0.97±0.18	32.53±0.08	36.72±0.14	4.55±0.10	0.91±0.16	32.03±0.16	36.12±0.19	Cγ
Glu130	4.53±0.06	0.85±0.09	33.09±0.09	36.82±0.09	4.40±0.09	1.09±0.22	33.05±0.14	36.38±0.15	Cγ
Glu131	4.58±0.05	0.93±0.09	33.26±0.06	36.84±0.07	4.71±0.15	0.61±0.12	32.80±0.22	37.09±0.27	Cγ
Asp135	4.16±0.07	0.70±0.06	38.18±0.08	41.74±0.08	4.05±0.06	0.77±0.07	37.88±0.09	41.16±0.07	Cβ
Glu137	4.82±0.16	0.56±0.11	123.36±0.11	125.77±0.17	4.42±0.03	0.92±0.05	123.88±0.02	125.56±0.02	N
Glu139	4.69±0.04	0.97±0.10	33.14±0.06	36.99±0.08	4.54±0.06	0.84±0.09	32.72±0.09	36.62±0.11	Cγ
α-CO_2^-	3.65±0.03	1.10±0.07	8.537±0.006	8.081±0.003	3.67±0.03	1.01±0.06	8.541±0.007	8.087±0.005	HN(A140)

[a]All values are for a temperature of 10 °C.
[b]The assignments for Glu35 and Glu110 are tentative due to spectral overlap and may be reversed.
[c] Glu13, Glu46 and Glu105 titrate as a single unresolved group and the three residues are assigned the same parameters in the absence of salt. The pH titration of the three residues can be resolved in the presence of 150 mM NaCl.
[d]The pK_a values of Asp2 and Asp121 were determined from Cβ chemical shifts in the absence of salt and ^{15}N chemical shifts in the presence of 150 mM salt.

Sites within the last 40 residues have raised pK_a values indicating a higher affinity for protons, which would facilitate the neutralization of acidic residues in the C-terminal tail compared to the N-terminal amphipathic domain.

pKa Values for αS in the Presence of Salt. Deviations of pK_a values from random coil model compounds have been reported for other unfolded proteins [211, 212, 214, 215] and the differences were found to decrease with increasing salt concentration [213]. To obtain pK_a data at a physiological salt concentration we characterized the pH titration of αS in the presence of 150 mM NaCl (Fig. A2.2A, C). The analysis of the data was similar to that for αS in the absence of salt. We determined pK_a values for 20 of 26 sites from 3D C(CO)NH experiments. The pH titrations of His50, Asp119, Glu137 and the C-terminal α-carboxyl group are not amenable to C(CO)NH spectroscopy and were determined using 2D ^{1}H-^{15}N HSQC spectra (Table A2.1). The pK_a values for two additional residues (Asp2, Asp121) were determined from ^{15}N shifts in ^{1}H-^{15}N HSQC spectra because of overlap in the C(CO)NH experiments. For αS in the presence of 150 mM NaCl we were able to resolve the pH titrations of all seven Glu(Cγ)-Gly(HN) spin systems although the assignments of E35 and E110 remain tentative and could be reversed (Table A2.1). The spread of pK_a values in the presence of 150 mM NaCl is smaller than in the absence of salt, as exemplified by the representative titrations of residues E28 and E114 (compare Fig. A2.2B,C). The distribution of smaller pK_a values in the N-terminal domain and larger pK_a values in the C-terminal domain is less pronounced but persists when αS is studied in the presence of 150 mM NaCl (Table A2.1).

Differences from Random Coil pK_a Values - To analyze the pK_a data for αS we needed to obtain reference values for residues in random coil conformations. Random coil pK_a values are available in the literature [228-230] but to obtain accurate values for Glu and Asp residues which account for 24 of the 26 ionizable sites in this study, we carried out ^{1}H NMR pH titrations on the model peptides Ac-AADAA-NH_2 and Ac-AAEAA-NH_2 under the exact same conditions used for

the pH titrations for αS. The two Hα protons of the aspartate in the Ac-AADAA-NH_2 peptide, which gave the same pK_a within experimental uncertainty, were used to obtain an ionization constant for aspartate. The Hγ protons of the glutamate in the Ac-AAEAA-NH_2, which have degenerate chemical shifts throughout the entire pH range studied, were used to obtain an ionization constant for glutamate. The random coil pK_a values we obtained for aspartate were 4.00 ± 0.02 in the absence of salt and 3.94 ± 0.02 in the presence of salt. For glutamate the pK_a values were 4.42 ± 0.02 in the absence of salt and 4.38 ± 0.02 in the presence of 150 mM NaCl. Our values are somewhat higher than those recently determined by the Pace group (3.67 for Asp, 4.25 for Glu) using potentiometry of the same peptides at a temperature of 25 ^{o}C and in the presence of 100 mM NaCl [230]. The values we obtained are in very good agreement with those reported for model peptides at 25 ^{o}C by potentiometry [228] (4.0 for Asp, 4.4 Glu) and NMR [229] (3.84 for Asp, 4.32 for Glu) respectively. For histidine which occurs only once at position 50 in αS, we used a published random coil pK_a of 6.54 ± 0.04 [228-230]. For the α-carboxyl group at the C-terminus we used a random coil pK_a of 3.67 ± 0.03 [230].

Differences between random coil and αS pK_a values are shown in Fig. A2.3A for the protein without salt and Fig. A2.3B for the protein in the presence of 150 mM NaCl. Uncertainty bars were calculated from the propagation of standard errors obtained from the least squares fits of the αS and the model peptide pH titration data. Alternatively, if we consider that the primary source of errors in the pH titrations is the accuracy of the pH measurements which in our study is on the order of 0.05 to 0.1 pH units, the uncertainties in the pK_a differences are between 0.07 to 0.14 pH units. Acidic residues from the N-terminal amphipathic domain of αS show uniformly negative differences (Fig. A2.3A) with pK_a values lowered on average by 0.24 pH units from random coil

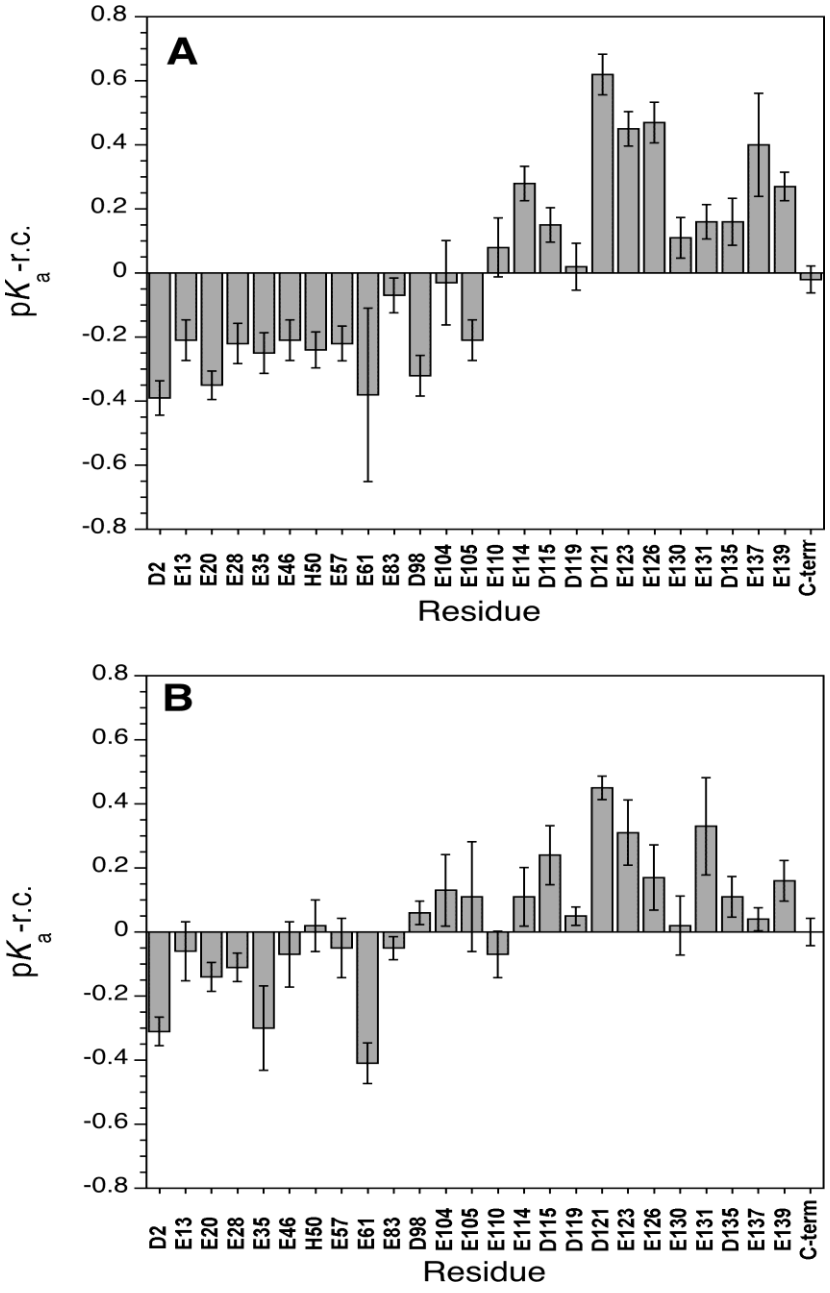

Figure A2.3 Differences between αS and random coil pK_a values (p$K_{a,\,\alpha S}$ – p$K_{a,\,r.c.}$). (A) αS In the absence of salt, (B) αS in the presence of 150 mM NaCl. The pK_a values for αS are given in Table A2.1. Random coil values were obtained from NMR titrations of the model peptides Ac-AAEAA-NH2 and Ac-AADAA-NH_2 as described in the text. Random coil values for a histidine side-chain and the C-terminal α-carboxyl group were taken from published values [230]. For His50 the difference was multiplied by -1 since this group gains a positive charge, in contrast to the acidic groups which lose a negative charge at low pH. Uncertainty bars were calculated using propagation of the standard errors obtained from fits of the αS pH titration data (Table A2.1) and the model peptide pH titration data. All data were obtained at a temperature of 10 °C.

values. In the C-terminal tail the differences are positive, with pK_a values of acidic residues raised on average by 0.24 pH units compared to the corresponding random coil values. The switch-point from positive to negative differences occurs between residues Glu105 and Glu110, just outside the amphipathic and NAC domains, at the start of the acidic C-terminal tail. In the presence of 150 mM NaCl (Fig. A2.3B) the differences between αS and random coil pK_a values are lowered but maintain the same pattern, with residues from the N-terminal domain showing negative differences (average = 0.10) and those from the C-terminus showing positive differences (average = 0.15). The switch-point in the sequence occurs roughly nearby the demarcation of the amphipathic and acidic domains between residues D98 and E114.

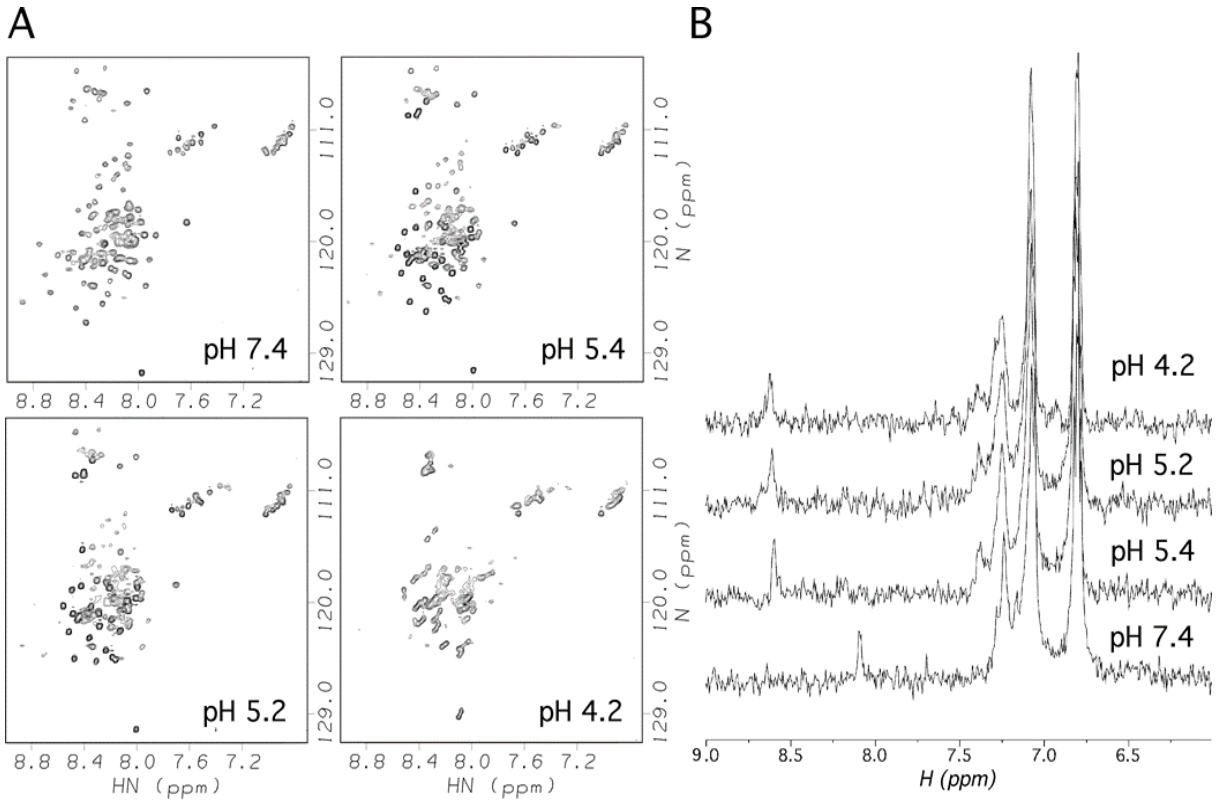

Figure A2.4 Representative data from a pH titration of αS bound to SDS micelles. (A) ^{1}H-^{15}N HSQC spectra showing the deterioration of backbone ^{1}H-^{15}N below pH ~5.4. (B) ^{13}C-filtered aromatic spectra of αS in the presence of SDS showing the titration of the His50 Hε1 proton, which shifts from 7.6 to 8.6 ppm as the pH is lowered. Samples contained 0.2 mM αS and 40 mM SDS in 90% H_2O/10% D_2O, and were recorded at a temperature of 37 ºC.

The N- and C-terminal domains also show small differences in the parameter *n*, the Hill coefficient for the pH titration. The Hill coefficient (Eq. A2.1) describes the cooperativity of pH titrations [231]. Values of *n* less than 1 are associated with negative cooperativity, while *n* greater than 1 corresponds to positive cooperativity [231, 232]. The Hill coefficients for most sites in αS are very close to unity (Table A2.1). Nevertheless, the average values for residues 1-105 are significantly larger than for residues 110-140: 0.98 versus 0.86 (statistical significance, $P < 0.03$) in the absence of salt; 1.06 versus 0.84 ($P < 0.01$) in the presence of salt. The ionization of sites at the N-terminus thus appears to be more cooperative than at the C-terminus.

pH Titration of αS Bound to SDS Micelles. We next tried to obtain information on ionization constants in the membrane-like environment provided by SDS micelles, where αS adopts the α-helical hairpin structure shown in Fig. A2.1 [197]. As shown in Fig. A2.4A, ^{1}H-^{15}N HSQC spectra of αS in the presence of 50 mM SDS markedly deteriorate below ~pH 5.4 resulting in loss of cross-peaks due to line-broadening accompanying the protonation of Asp and Glu residues in the protein. The mid-point of the transition occurs near pH 5.2, about 0.8 and 1.2 pH units above the random coil pK_a values of Glu and Asp, respectively. As we have described for amyloid-beta(1-40), the pK_a values of acidic residues are uniformly raised in proteins bound to SDS micelles, due to electrostatic repulsion between the negatively charged side-chains and negatively charged sulfate groups on the SDS micelles [41]. At the present time we do not know the cause of the line-broadening of NMR signals from micelle-bound αS at low pH. One possibility is that the affinity of αS for SDS micelles decreases at low pH, which would result in loss of resonances due to fast solvent exchange from the αS monomers dissociated from the micelles at the 37 ^{o}C. This seems unlikely, however, since the loss of negative charges at low pH should favor the binding of αS to

negatively charged SDS micelles. A more likely explanation is that neutralization of the negative charges in the C-terminal domain perturbs the structure of the αS-micelle complex, possibly by favoring aggregation of the protein through the C-terminal tail which at physiological pH is kept unfolded and away from the micelle by the high density of negatively charged residues in its sequence. The poor quality of the spectra below pH 5.4 precluded the analysis of the protonation of Asp and Glu residues.

By contrast to the backbone ^{1}H and ^{15}N resonances, the aromatic Cε1 proton of His50 can still be seen at low pH presumably because of the high flexibility of this side-chain in the complex (Fig. A2.4B). In the WT αS bound to SDS micelles His50 titrates with a pK_a of 8.06, with the titration reaching a low-pH chemical shift plateau by pH 6 (Fig. A2.5). Note that the titration of His50 is complete (Fig. A2.5) before broadening of crosspeaks is observed in ^{1}H-^{15}N HSQC spectra below pH 5.4 (Fig. A2.4A). The changes in the spectrum associated with the protonation of the C-terminal tail do not affect the pK_a value obtained for His 50. Under the same conditions (37 ºC, 99.96% D2O) free αS has a pK_a of 6.3 [41]. The pK_a of His50 is thus raised by ~1.8 pH units when WT αS binds to SDS micelles compared to the unbound state. The raised pK_a of His50 indicates that protonation is facilitated in the micelle bound state, either because the charged form of the histidine ion-pairs with Glu46 in the α-helical structure adopted by the micelle-bound protein (Fig. A2.1) or because the positively charged histidine interacts with the negatively charged sulfate groups of SDS. To distinguish between these possibilities we collected titration data for His 50 in the Parkinson's disease-linked mutants E46K and A53T (Fig. A2.5). Glu46 is the only negatively charged residue positioned to form an ion pair with the charged form of His50 in the α-helical structure of micelle-bound αS. The E46K mutant, which replaces the glutamate with a positively

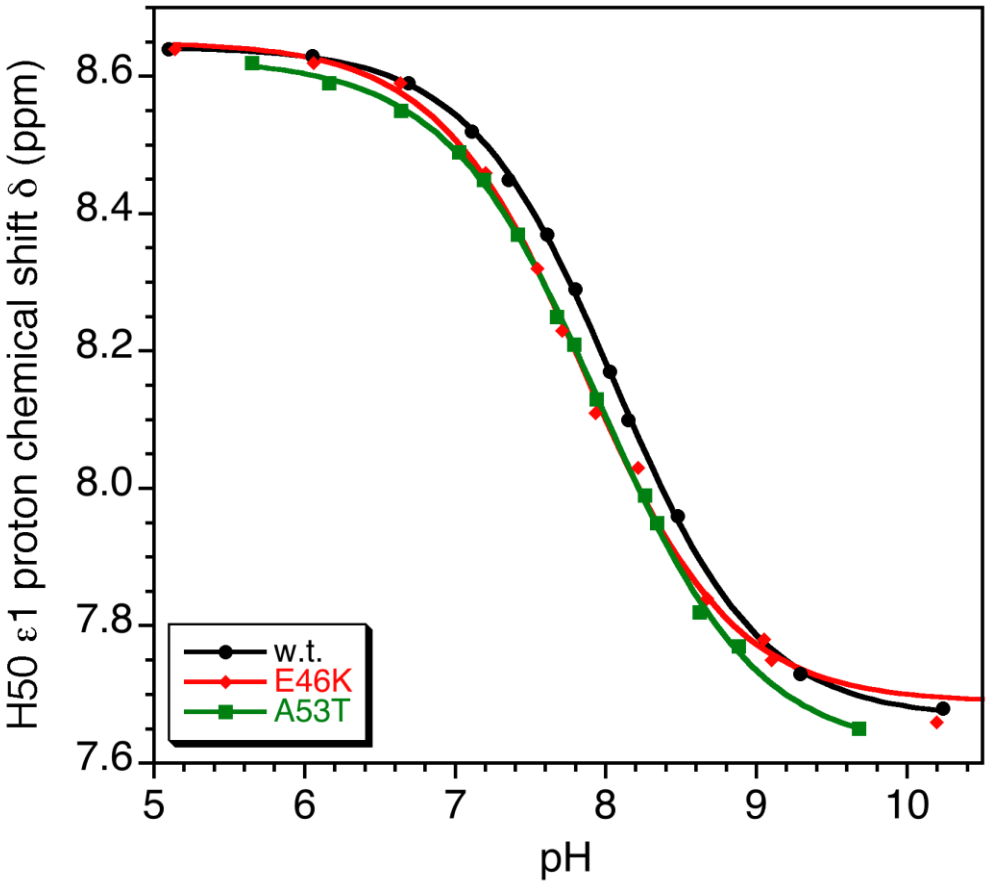

Figure A2.5 pH titrations for the His50 Hε1 proton of αS bound to SDS micelles. The samples contained 99.96% D_2O solutions of 0.2 mM protein and 50 mM SDS (0.8 mM SDS micelles). All data were collected at 37 °C. The parameters obtained from least-squares fits of the titration data were: WT - pK_a = 8.06 ± 0.01, n = 0.90 ± 0.02; E46K - pK_a = 7.86 ± 0.03, n = 0.89 ± 0.06; A53T - pK_a = 7.97 ± 0.02, n = 0.85 ± 0.02. For WT αS under the same conditions in the absence of SDS micelles [41], we obtained pK_a = 6.33 ± 0.02, n = 0.99 ± 0.04.

charged lysine gives a pK_a of 7.86 for His50 in micelle-bound αS (Fig. A2.5). The pK_a shift of -0.2 pH units from the WT is comparable to the shifts for residues positioned to form ion pairs in the N-terminal domain of uncomplexed αS (Table A2.1, Fig. A2.3). For A53T the pK_a shift of -0.1 pH units is intermediate and close to the experimental uncertainty. With both mutants the pK_a perturbations are much smaller than the difference of ~1.8 pH units between free and micelle-bound αS. We can thus safely conclude that the pK_a perturbation of His50 in micelle bound αS is

dominated by the interaction of the histidine cation with the negatively charged sulfate groups on the surface of the micelle.

We looked for alternative membrane mimetics amenable to NMR studies of αS including micelles composed of the negatively charged lipid LPPG (1-palmitoyl-2-hydroxy-sn-glycero-3-phospho-RAC-(1-glycerol)), the neutral lipid LMPC (1-myristoyl-2-hydroxy-sn-glycero-3-phosphocholine) and the neutral detergent DPC (dodecyl phosphocholine). Besides SDS, only LPPG gave a complete set of ^{1}H-^{15}N HSQC resonances for αS but the NMR spectra were of poorer quality than with SDS micelles (A.T.A and Andrew Mehta, unpublished results). High-quality NMR spectra have been recently demonstrated [223] for αS complexed to micelles of the surfactant SLAS (sodium lauroyl sarcosinate) but like SDS and LPPG, the detergent is negatively charged and would be expected to perturb the pK_a values of αS. With neutral DPC micelles, we confirmed that αS binds only weakly [198], such that most of the ^{1}H-^{15}N HSQC correlations from the N-terminal domain of αS are lost due to fast hydrogen exchange through the free form of the protein, which is in dynamic equilibrium with the micelle bound form. Since αS requires negatively charged lipids to bind to membranes we explored the amenability of mixed DPC/SDS micelles for NMR studies. Starting from micelles composed of the neutral DPC detergent we gradually added negatively charged SDS detergent. Below DPC: SDS molar ratios of 70:30 the ^{1}H-^{15}N HSQC spectra of αS were poor with most ^{1}H-^{15}N resonances lost due to fast solvent exchange. At a DPC:SDS molar ratio of 70:30 the ^{1}H-^{15}N HSQC spectrum was comparable to that of αS with pure SDS micelles [197] but resonances were still too broad for the more demanding C(CO)NH experiments used to determine pK_a values. Thus the characterization of pK_a values for αS in a membrane-like environment is limited by the requirement of a small micelle size

amenable to direct NMR studies coupled with the requirement of micelles containing a high proportion of negatively charged lipids or surfactants that interfere with the characterization of ionization constants of titratable groups from the protein. While charge coupling between Glu46 and His50 is small when αS is bound to SDS micelles, this need not be the case when the protein is bound to physiological lipid bilayers with a lower proportion of negatively charged lipids.

Discussion

The pK_a values obtained for αS in this work show surprisingly large differences from random coil values considering that the protein is intrinsically unfolded (Fig. A2.3). The results are consistent with previous findings that ionizable sites in unfolded proteins can have electrostatic environments that are poorly approximated by random coil models of proteins [211, 212, 214, 215, 233]. Site-specific pK_a values are important for modeling the contributions of charges to protein structure [212, 216, 217, 233] and we anticipate that our data for the unfolded reference state will help analyze the contributions of charges to the fibrillar and membrane bound structures of αS.

The sequence of αS is organized into an amphipathic domain (residues 1-100) consisting of seven imperfect KTKEGV repeats that have the potential to form ion pairs between acidic and basic residues and a C-terminal domain (residues 101-140) that has a high density of negatively charged residues at neutral pH. The uniformly raised pK_a values of acidic groups from the C-terminal domain suggest that these sites experience electrostatic repulsion between like charges, which should have the effect of keeping this segment in extended disordered conformations. Functionally, the C-terminal tail may help αS recognize binding partners on the surfaces of lipid membranes [2]. Neutralization of the charges in the C-terminal tail by polycations [234] or low pH [201-203] enhances the aggregation and fibrillization of αS. Similarly deletion of the C-

terminal tail enhances the rate of fibrillization [84]. The loss of charges from the C-terminal tail of αS at low pH also appears to increase the aggregation of the protein in the membrane-like environment provided by SDS micelles (Fig. A2.4A). For the free protein it has been recently shown that removal of charges from the C-terminal tail causes a conformational transition that leads to transient interactions between the C-terminal and the non-polar NAC domain. This state of αS aggregates with faster rates than the state populated at neutral pH [201-203]. The conformational transition leads to small changes in backbone chemical shifts of ~0.3 ppm for the Cα carbons of residues from the C-terminus [201, 202] but is unlikely to affect the pK_a measurements in the present study. First, the pH titrations of most residues in αS were followed by side-chain carbons which undergo much larger changes in chemical shifts with pH, on the order of 3 to 4 ppm (Table A2.1, Fig. A2. 2). The chemical shifts of side-chain carbons from acidic residues are affected by the protonation of carboxyl groups but are much less sensitive to any residual secondary structure in the protein. Second, the differences in pK_a values correspond to differences in the mid-points of the pH transitions. The limiting low- and high-pH chemical shift plateau values of side-chain ^{13}C resonances in αS are similar and show no dependence on residue position in the sequence (Table A2.1).

In contrast to the C-terminal tail, residues from the N-terminal domain show pK_a values that are uniformly lowered compared to random coil values (Fig. A2.3). This behavior indicates that acidic residues from the N-terminal domain resist losing their negative charges, becoming neutralized at larger hydronium ion concentrations (lower pH) than the corresponding amino acids from the C-terminal tail of αS, or random coil peptides. The lowered pK_a values suggest that the negatively charged acidic sites in the N-terminal domain form nascent ion-pair interactions with

positively charged basic amino acids in the KTKEGV repeats. Although 150 mM NaCl screens the nascent electrostatic interactions they persist at a physiological salt concentration (Fig. A2.3B). The observed average pK_a shifts of -0.10 (with salt) to -0.25 (no salt) pH units for acidic residues in the N-terminal domain of αS, correspond to stabilizing $\Delta\Delta G_{titr}$ contributions of only -0.1 to -0.3 kcal/mol at 10 ^oC. As such the effects of individual ion pairs on the stability of α-helix structure in αS are negligible being less than 1 kT (0.56 kcal/mol at 10 ^oC). In analogy to other proteins, rather than stabilizing structure, nascent ion pair interactions may be more important in nucleating the folding of α-helix structure [235, 236]. Once an ion pair is formed it would allow localized folding which could then propagate α-helical structure through the rest of the N-terminal amphipathic domain. The slightly raised *n* values for the acidic residues in the N-terminal domain are consistent with cooperativity amongst the ionization reactions of these residues. Nucleation of αS folding could occur in the cytosol, with α-helical structures selected for membrane binding. Alternatively, the folding of α-helix structure may occur after the protein binds to the surfaces of lipid bilayers. In addition to facilitating folding of αS into an α-helix structure, nascent ion-pairs in the N-terminal domain may decrease the rates of misfolding of the protein into alternative toxic conformations. That is, the sequence of the N-terminal domain could offer protection from αS misfolding additional to that provided by the highly negatively charged sequence of the C-terminal tail. In this regard, it is interesting to note that reducing the number of KTKEGV repeats in αS increases the rate of fibrillization, while increasing the number of repeats has the opposite effect [194].

αS is primarily distributed in the cytosol [237]. The membrane-bound protein which accounts for only ~15% of Synuclein in the brain, however, is probably the functional form, and

membranes may play role in αS aggregation [187, 237]. It would clearly be desirable to have information on the electrostatic properties of αS in membrane-like environments. The highest-resolution structural data for αS in a membrane-like environment has come from NMR but the technique is limited by the sizes and types of complexes that can be studied. Although indirect NMR studies have recently provided information on the interactions of αS with lipid assemblies as large as vesicles [200], direct NMR studies which afford the highest resolution, typically require that the protein is tightly bound to lipid assemblies and that the sizes of the complexes are below ~50 kDa [197]. While not physiological, micelles composed of the detergent SDS meet the requirements of tight association and small complex size for detailed NMR studies [76, 197, 238]. For the purposes of investigating pK_a values, SDS micelles pose the complication of presenting a high density of negative charges from the sulfate groups on the surface of the micelle. Studies with the Aβ (1-40) peptide show that SDS micelles strongly perturb the electrostatic properties of ionizable residues with both acidic and basic residues experiencing increases in pK_a values of 1 to 2 pH units. These effects are specific to proteins and peptides since the pK_a of single amino acids are unperturbed in the presence of SDS micelles [239]. The pK_a shifts observed for proteins bound to SDS micelles, however, do not appear to depend on the context of the ionizable site within the protein structure or on the degree of interaction with the micelle [41].

When αS is bound to SDS micelles the pK_a values of His50 is raised by 1.8 pH units compared to the free protein. This residue is of particular interest since it is flanked within a turn of α-helix by the sites of the early-onset Parkinson's disease mutations E46K and A53T. The E46K mutant breaks the pattern of acidic residues alternating with basic residues with an i, i+3 or i, i+4 spacing in the N-terminal domain of αS (Fig. A2.1A). To see if the raised pK_a value of His50

in αS complexed to SDS micelles is due to an electrostatic interaction within the protein or between the histidine and the micelle, we obtained titration data for His50 in the micelle-bound form of the E46K mutant. In the E46K mutant the pK_a value of His 50 is lowered by 0.2 pH units from 8.06 to 7.86 but is still 1.6 pH units higher than that of the histidine in natively unfolded WT αS. Based on these observations we conclude that there is only a weak charge-charge interaction between Glu46 and His50. The large pK_a shift of His50 when αS binds to SDS micelles is due to ion pairing between the histidine cation and the anionic sulfate groups on the surface of the micelle. In more physiological membrane where the density of negatively charged lipids is lower the interaction between Glu46 and His50 may be stronger. Considering the sequence of αS (Fig. A2.1A) the possibility also exists that Glu46 could interact with Lys43 in addition or in lieu of His50. Lys43 occurs in the break between the two α-helices in the structure of αS bound to SDS micelles so that it is not positioned to interact with Glu46 (Fig. A2.1B, C). In lipid vesicles, however, αS folds into a single uninterrupted α-helix [206, 208] so it is possible that the two residues ion-pair when αS folds into an uninterrupted α-helix on the surfaces of physiological lipid bilayers.

Acknowledgements

The authors thank Prof. Peter Lansbury and Dr. Michael J. Volles (Harvard Medical School) for the *pT7-7/asyn-WT* expression vector used in this work and Dr. Suman Jha for comments on the manuscript.

References

[1] L. Hou, H. Shao, Y. Zhang, H. Li, N.K. Menon, E.B. Neuhaus, J.M. Brewer, I.J. Byeon, D.G. Ray, M.P. Vitek, T. Iwashita, R.A. Makula, A.B. Przybyla, M.G. Zagorski, Solution NMR studies of the A beta(1-40) and A beta(1-42) peptides establish that the Met35 oxidation state affects the mechanism of amyloid formation, J Am Chem Soc, 126 (2004) 1992-2005.
[2] D. Eliezer, E. Kutluay, R. Bussell, Jr., G. Browne, Conformational properties of alpha-synuclein in its free and lipid-associated states, J Mol Biol, 307 (2001) 1061-1073.
[3] C.H. Trinh, D.P. Smith, A.P. Kalverda, S.E. Phillips, S.E. Radford, Crystal structure of monomeric human beta-2-microglobulin reveals clues to its amyloidogenic properties, Proc Natl Acad Sci U S A, 99 (2002) 9771-9776.
[4] P. Westermark, A. Andersson, G.T. Westermark, Islet amyloid polypeptide, islet amyloid, and diabetes mellitus, Physiol Rev, 91 (2011) 795-826.
[5] S.K. Maji, M.H. Perrin, M.R. Sawaya, S. Jessberger, K. Vadodaria, R.A. Rissman, P.S. Singru, K.P. Nilsson, R. Simon, D. Schubert, D. Eisenberg, J. Rivier, P. Sawchenko, W. Vale, R. Riek, Functional amyloids as natural storage of peptide hormones in pituitary secretory granules, Science, 325 (2009) 328-332.
[6] D. Romero, C. Aguilar, R. Losick, R. Kolter, Amyloid fibers provide structural integrity to Bacillus subtilis biofilms, Proc Natl Acad Sci U S A, 107 (2010) 2230-2234.
[7] F. Chiti, C.M. Dobson, Protein misfolding, functional amyloid, and human disease, Annual review of biochemistry, 75 (2006) 333-366.
[8] G.J. Cooper, Amylin compared with calcitonin gene-related peptide: structure, biology, and relevance to metabolic disease, Endocr Rev, 15 (1994) 163-201.
[9] S.A. Jayasinghe, R. Langen, Membrane interaction of islet amyloid polypeptide, Biochim Biophys Acta, 1768 (2007) 2002-2009.
[10] J. Janson, R.H. Ashley, D. Harrison, S. McIntyre, P.C. Butler, The mechanism of islet amyloid polypeptide toxicity is membrane disruption by intermediate-sized toxic amyloid particles, Diabetes, 48 (1999) 491-498.
[11] A. Lorenzo, B. Razzaboni, G.C. Weir, B.A. Yankner, Pancreatic islet cell toxicity of amylin associated with type-2 diabetes mellitus, Nature, 368 (1994) 756-760.
[12] A.V. Matveyenko, P.C. Butler, ILAR J., 47 (2006) 225.
[13] M. Anguiano, R.J. Nowak, P.T. Lansbury, Jr., Protofibrillar islet amyloid polypeptide permeabilizes synthetic vesicles by a pore-like mechanism that may be relevant to type II diabetes, Biochemistry, 41 (2002) 11338-11343.
[14] M.F. Engel, Membrane permeabilization by Islet Amyloid Polypeptide, Chem Phys Lipids, 160 (2009) 1-10.
[15] L. Haataja, T. Gurlo, C.J. Huang, P.C. Butler, Endocr. Rev., 29 (2008) 303.
[16] F. Meng, P. Marek, K.J. Potter, C.B. Verchere, D.P. Raleigh, Biochemistry, 47 (2008) 6016.
[17] S. Sakagashira, T. Sanke, T. Hanabusa, H. Shimomura, S. Ohagi, K.Y. Kumagaye, K. Nakajima, K. Nanjo, Missense mutation of amylin gene (S20G) in Japanese NIDDM patients, Diabetes, 45 (1996) 1279-1281.
[18] Z. Ma, G.T. Westermark, Effects of free fatty acid on polymerization of islet amyloid polypeptide (IAPP) in vitro and on amyloid fibril formation in cultivated isolated islets of transgenic mice overexpressing human IAPP, Mol Med, 8 (2002) 863-868.

[19] Z. Ma, G.T. Westermark, S. Sakagashira, T. Sanke, A. Gustavsson, H. Sakamoto, U. Engstrom, K. Nanjo, P. Westermark, Enhanced in vitro production of amyloid-like fibrils from mutant (S20G) islet amyloid polypeptide, Amyloid : the international journal of experimental and clinical investigation : the official journal of the International Society of Amyloidosis, 8 (2001) 242-249.
[20] I.T. Yonemoto, G.J. Kroon, H.J. Dyson, W.E. Balch, J.W. Kelly, Amylin proprotein processing generates progressively more amyloidogenic peptides that initially sample the helical state, Biochemistry, 47 (2008) 9900-9910.
[21] T.J. Rink, K. Beaumont, J. Koda, A. Young, Structure and biology of amylin, Trends Pharmacol Sci, 14 (1993) 113-118.
[22] S.M. Patil, A. Mehta, S. Jha, A.T. Alexandrescu, Heterogeneous amylin fibril growth mechanisms imaged by total internal reflection fluorescence microscopy, Biochemistry, 50 2808-2819.
[23] A. Abedini, D.P. Raleigh, The role of His-18 in amyloid formation by human islet amyloid polypeptide, Biochemistry, 44 (2005) 16284-16291.
[24] A.V. Kajava, U. Aebi, A.C. Steven, The parallel superpleated beta-structure as a model for amyloid fibrils of human amylin, J Mol Biol, 348 (2005) 247-252.
[25] S. Luca, W.M. Yau, R. Leapman, R. Tycko, Peptide conformation and supramolecular organization in amylin fibrils: constraints from solid-state NMR, Biochemistry, 46 (2007) 13505-13522.
[26] M. Coles, W. Bicknell, A.A. Watson, D.P. Fairlie, D.J. Craik, Solution structure of amyloid beta-peptide(1-40) in a water-micelle environment. Is the membrane-spanning domain where we think it is?, Biochemistry, 37 (1998) 11064-11077.
[27] T.S. Ulmer, A. Bax, Comparison of structure and dynamics of micelle-bound human alpha-synuclein and Parkinson disease variants, J Biol Chem, 280 (2005) 43179-43187.
[28] R.P. Nanga, J.R. Brender, J. Xu, G. Veglia, A. Ramamoorthy, Structures of rat and human islet amyloid polypeptide IAPP(1-19) in micelles by NMR spectroscopy, Biochemistry, 47 (2008) 12689-12697.
[29] A. Mascioni, F. Porcelli, U. Ilangovan, A. Ramamoorthy, G. Veglia, Conformational preferences of the amylin nucleation site in SDS micelles: an NMR study, Biopolymers, 69 (2003) 29-41.
[30] G. Pappalardo, D. Milardi, A. Magri, F. Attanasio, G. Impellizzeri, C. La Rosa, D. Grasso, E. Rizzarelli, Environmental factors differently affect human and rat IAPP: conformational preferences and membrane interactions of IAPP17-29 peptide derivatives, Chemistry, 13 (2007) 10204-10215.
[31] A. Clark, M.R. Nilsson, Islet amyloid: a complication of islet dysfunction or an aetiological factor in Type 2 diabetes?, Diabetologia, 47 (2004) 157-169.
[32] C.B. Andersen, H. Yagi, M. Manno, V. Martorana, T. Ban, G. Christiansen, D.E. Otzen, Y. Goto, C. Rischel, Branching in amyloid fibril growth, Biophys J, 96 (2009) 1529-1536.
[33] T. Ban, Y. Goto, Direct observation of amyloid growth monitored by total internal reflection fluorescence microscopy, Methods Enzymol, 413 (2006) 91-102.
[34] T. Ban, D. Hamada, K. Hasegawa, H. Naiki, Y. Goto, Direct observation of amyloid fibril growth monitored by thioflavin T fluorescence, J Biol Chem, 278 (2003) 16462-16465.

[35] T. Ban, M. Hoshino, S. Takahashi, D. Hamada, K. Hasegawa, H. Naiki, Y. Goto, Direct observation of Abeta amyloid fibril growth and inhibition, J Mol Biol, 344 (2004) 757-767.
[36] D. Ozawa, H. Yagi, T. Ban, A. Kameda, T. Kawakami, H. Naiki, Y. Goto, Destruction of amyloid fibrils of a beta2-microglobulin fragment by laser beam irradiation, J Biol Chem, 284 (2009) 1009-1017.
[37] F.A. Ferrone, J. Hofrichter, W.A. Eaton, Kinetics of sickle hemoglobin polymerization. II. A double nucleation mechanism, J Mol Biol, 183 (1985) 611-631.
[38] S.B. Padrick, A.D. Miranker, Islet amyloid: phase partitioning and secondary nucleation are central to the mechanism of fibrillogenesis, Biochemistry, 41 (2002) 4694-4703.
[39] A.M. Ruschak, A.D. Miranker, Fiber-dependent amyloid formation as catalysis of an existing reaction pathway, Proc Natl Acad Sci U S A, 104 (2007) 12341-12346.
[40] M. Calamai, J.R. Kumita, J. Mifsud, C. Parrini, M. Ramazzotti, G. Ramponi, N. Taddei, F. Chiti, C.M. Dobson, Nature and significance of the interactions between amyloid fibrils and biological polyelectrolytes, Biochemistry, 45 (2006) 12806-12815.
[41] S.R. Sheftic, R.L. Croke, J.R. LaRochelle, A.T. Alexandrescu, Electrostatic contributions to the stabilities of native proteins and amyloid complexes., Methods in Enzymology, 466 (2009) 233-258.
[42] A.T. Alexandrescu, Amyloid accomplices and enforcers, Protein Sci, 14 (2005) 1-12.
[43] S. Jha, S.M. Patil, J. Gibson, C.E. Nelson, N.N. Alder, A.T. Alexandrescu, Mechanism of amylin fibrillization enhancement by heparin, J Biol Chem, 286 (2011) 22894-22904.
[44] E.A. Greenbaum, C.L. Graves, A.J. Mishizen-Eberz, M.A. Lupoli, D.R. Lynch, S.W. Englander, P.H. Axelsen, B.I. Giasson, The E46K mutation in alpha-synuclein increases amyloid fibril formation, J Biol Chem, 280 (2005) 7800-7807.
[45] K.E. Paleologou, A.W. Schmid, C.C. Rospigliosi, H.Y. Kim, G.R. Lamberto, R.A. Fredenburg, P.T. Lansbury, Jr., C.O. Fernandez, D. Eliezer, M. Zweckstetter, H.A. Lashuel, Phosphorylation at Ser-129 but not the phosphomimics S129E/D inhibits the fibrillation of alpha-synuclein, J Biol Chem, 283 (2008) 16895-16905.
[46] P. Cao, L.H. Tu, A. Abedini, O. Levsh, R. Akter, V. Patsalo, A.M. Schmidt, D.P. Raleigh, Sensitivity of amyloid formation by human islet amyloid polypeptide to mutations at residue 20, J Mol Biol, 421 (2012) 282-295.
[47] S.T. Ferreira, M.N. Vieira, F.G. De Felice, Soluble protein oligomers as emerging toxins in Alzheimer's and other amyloid diseases, IUBMB Life, 59 (2007) 332-345.
[48] P.T. Lansbury, H.A. Lashuel, A century-old debate on protein aggregation and neurodegeneration enters the clinic, Nature, 443 (2006) 774-779.
[49] C.A. Ross, M.A. Poirier, Protein aggregation and neurodegenerative disease, Nature medicine, 10 Suppl (2004) S10-17.
[50] S. Chimon, M.A. Shaibat, C.R. Jones, D.C. Calero, B. Aizezi, Y. Ishii, Evidence of fibril-like beta-sheet structures in a neurotoxic amyloid intermediate of Alzheimer's beta-amyloid, Nature structural & molecular biology, 14 (2007) 1157-1164.
[51] H.A. Lashuel, D. Hartley, B.M. Petre, T. Walz, P.T. Lansbury, Jr., Neurodegenerative disease: amyloid pores from pathogenic mutations, Nature, 418 (2002) 291.
[52] K. Wuthrich, NMR studies of structure and function of biological macromolecules (Nobel lecture), Angewandte Chemie, 42 (2003) 3340-3363.

[53] P. Dux, B. Whitehead, R. Boelens, R. Kaptein, G.W. Vuister, Measurement of (15)N- (1)H coupling constants in uniformly (15)N-labeled proteins: Application to the photoactive yellow protein, Journal of biomolecular NMR, 10 (1997) 301-306.
[54] S.J. Archer, M. Ikura, D.A. Torchia, A. Bax, An alternative 3D NMR technique for correlating backbone 15N with side chain Hβ resonances in larger proteins, Journal of Magnetic Resonance (1969), 95 (1991) 636-641.
[55] D.A. Case, H.J. Dyson, P.E. Wright, Use of chemical shifts and coupling constants in nuclear magnetic resonance structural studies on peptides and proteins, Methods Enzymol, 239 (1994) 392-416.
[56] G.W. Vuister, A. Bax, Quantitative J correlation: a new approach for measuring homonuclear three-bond J(HNH.alpha.) coupling constants in 15N-enriched proteins, Journal of the American Chemical Society, 115 (1993) 7772-7777.
[57] A.T. Brunger, A system for X-ray crystallography and NMR. X-PLOR Version 3.1, Yale University Press, New Haven, 1992.
[58] A.M. Gronenborn, D.R. Filpula, N.Z. Essig, A. Achari, M. Whitlow, P.T. Wingfield, G.M. Clore, A novel, highly stable fold of the immunoglobulin binding domain of streptococcal protein G, Science, 253 (1991) 657-661.
[59] N.A. Farrow, O. Zhang, J.D. Forman-Kay, L.E. Kay, Comparison of the backbone dynamics of a folded and an unfolded SH3 domain existing in equilibrium in aqueous buffer, Biochemistry, 34 (1995) 868-878.
[60] A.T. Alexandrescu, D. Shortle, Backbone dynamics of a highly disordered 131 residue fragment of staphylococcal nuclease, J Mol Biol, 242 (1994) 527-546.
[61] B.R. Brooks, R.D. Bruccoleri, B.D. Olafson, D.J. States, S. Swaminathan, M. Karplus, CHARMM: A program for macromolecular energy minimisation and molecular dynamics., J. Comp. Chem., 4 (1983) 187-193.
[62] G. Lipari, A. Szabo, Model-free approach to the interpretation of nuclear magnetic resonance relaxation in macromolecules. 1. Theory and range of validity, Journal of the American Chemical Society, 104 (1982) 4546-4559.
[63] P. Dosset, J.C. Hus, M. Blackledge, D. Marion, Efficient analysis of macromolecular rotational diffusion from heteronuclear relaxation data, Journal of biomolecular NMR, 16 (2000) 23-28.
[64] M. Lindberg, J. Jarvet, U. Langel, A. Graslund, Secondary structure and position of the cell-penetrating peptide transportan in SDS micelles as determined by NMR, Biochemistry, 40 (2001) 3141-3149.
[65] J.A. Williamson, A.D. Miranker, Direct detection of transient alpha-helical states in islet amyloid polypeptide, Protein Sci, 16 (2007) 110-117.
[66] I.V. Nesmelova, D. Idiyatullin, K.H. Mayo, Measuring protein self-diffusion in protein-protein mixtures using a pulsed gradient spin-echo technique with WATERGATE and isotope filtering, Journal of magnetic resonance, 166 (2004) 129-133.
[67] J. Jarvet, J. Danielsson, P. Damberg, M. Oleszczuk, A. Graslund, Positioning of the Alzheimer Abeta(1-40) peptide in SDS micelles using NMR and paramagnetic probes, Journal of biomolecular NMR, 39 (2007) 63-72.

[68] D.S. Wishart, C.G. Bigam, A. Holm, R.S. Hodges, B.D. Sykes, 1H, 13C and 15N random coil NMR chemical shifts of the common amino acids. I. Investigations of nearest-neighbor effects, Journal of biomolecular NMR, 5 (1995) 67-81.
[69] M.A. Jimenez, F.J. Blanco, M. Rico, J. Santoro, J. Herranz, J.L. Nieto, Periodic properties of proton conformational shifts in isolated protein helices. An experimental study, European journal of biochemistry / FEBS, 207 (1992) 39-49.
[70] R. Wiltscheck, R.A. Kammerer, S.A. Dames, T. Schulthess, M.J. Blommers, J. Engel, A.T. Alexandrescu, Heteronuclear NMR assignments and secondary structure of the coiled coil trimerization domain from cartilage matrix protein in oxidized and reduced forms, Protein Sci, 6 (1997) 1734-1745.
[71] M.J. McLeish, K.J. Nielsen, L.V. Najbar, J.D. Wade, F. Lin, M.B. Doughty, D.J. Craik, Conformation of a peptide corresponding to T4 lysozyme residues 59-81 by NMR and CD spectroscopy, Biochemistry, 33 (1994) 11174-11183.
[72] N.E. Zhou, B.Y. Zhu, B.D. Sykes, R.S. Hodges, Relationship between amide proton chemical shifts and hydrogen bonding in amphipathic .alpha.-helical peptides, Journal of the American Chemical Society, 114 (1992) 4320-4326.
[73] R. Koradi, M. Billeter, K. Wuthrich, MOLMOL: a program for display and analysis of macromolecular structures, Journal of molecular graphics, 14 (1996) 51-55, 29-32.
[74] S.F. Altschul, T.L. Madden, A.A. Schaffer, J. Zhang, Z. Zhang, W. Miller, D.J. Lipman, Gapped BLAST and PSI-BLAST: a new generation of protein database search programs, Nucleic Acids Res, 25 (1997) 3389-3402.
[75] A. Bairoch, B. Boeckmann, S. Ferro, E. Gasteiger, Swiss-Prot: juggling between evolution and stability, Brief Bioinform, 5 (2004) 39-55.
[76] S. Chandra, X. Chen, J. Rizo, R. Jahn, T.C. Sudhof, A broken alpha -helix in folded alpha -Synuclein, J Biol Chem, 278 (2003) 15313-15318.
[77] A.T. Alexandrescu, and Croke, R. L., Protein Misfolding (O Doherty, C. B., and Byrne, A. C, eds), (2008).
[78] M. Apostolidou, S.A. Jayasinghe, R. Langen, Structure of alpha-helical membrane-bound human islet amyloid polypeptide and its implications for membrane-mediated misfolding, J Biol Chem, 283 (2008) 17205-17210.
[79] D.F. Moriarty, D.P. Raleigh, Effects of sequential proline substitutions on amyloid formation by human amylin20-29, Biochemistry, 38 (1999) 1811-1818.
[80] K. Lycknert, T. Rundlöf, G. Widmalm, Solution Structure of a Type 1 H Antigen Trisaccharide at a Micellar Surface: NMR Relaxation and Molecular Dynamics Simulation Studies, The Journal of Physical Chemistry B, 106 (2002) 5275-5280.
[81] J. Jarvet, J. Zdunek, P. Damberg, A. Graslund, Three-dimensional structure and position of porcine motilin in sodium dodecyl sulfate micelles determined by 1H NMR, Biochemistry, 36 (1997) 8153-8163.
[82] C.S. Gangabadage, A. Najda, D. Bogdan, S.S. Wijmenga, M. Tessari, Dependence of the size of a protein-SDS complex on detergent and Na+ concentrations, The journal of physical chemistry. B, 112 (2008) 4242-4245.
[83] T. Luhrs, C. Ritter, M. Adrian, D. Riek-Loher, B. Bohrmann, H. Dobeli, D. Schubert, R. Riek, 3D structure of Alzheimer's amyloid-beta(1-42) fibrils, Proc Natl Acad Sci U S A, 102 (2005) 17342-17347.

[84] M. Vilar, H.T. Chou, T. Luhrs, S.K. Maji, D. Riek-Loher, R. Verel, G. Manning, H. Stahlberg, R. Riek, The fold of alpha-synuclein fibrils, Proc Natl Acad Sci U S A, 105 (2008) 8637-8642.
[85] L.M. Gierasch, J.E. Lacy, K.F. Thompson, A.L. Rockwell, P.I. Watnick, Conformations of model peptides in membrane-mimetic environments, Biophys J, 37 (1982) 275-284.
[86] M.F. Engel, H. Yigittop, R.C. Elgersma, D.T. Rijkers, R.M. Liskamp, B. de Kruijff, J.W. Hoppener, J. Antoinette Killian, Islet amyloid polypeptide inserts into phospholipid monolayers as monomer, J Mol Biol, 356 (2006) 783-789.
[87] A. Young, Receptor pharmacology, Advances in pharmacology, 52 (2005) 47-65.
[88] A. Young, Amylin and the integrated control of nutrient influx, Advances in pharmacology, 52 (2005) 67-77.
[89] Y.A. Domanov, P.K. Kinnunen, Islet amyloid polypeptide forms rigid lipid-protein amyloid fibrils on supported phospholipid bilayers, J Mol Biol, 376 (2008) 42-54.
[90] S.A. Jayasinghe, R. Langen, Lipid membranes modulate the structure of islet amyloid polypeptide, Biochemistry, 44 (2005) 12113-12119.
[91] J.D. Knight, A.D. Miranker, Phospholipid catalysis of diabetic amyloid assembly, J Mol Biol, 341 (2004) 1175-1187.
[92] R.P.R. Nanga, J.R. Brender, S. Vivekanandan, A. Ramamoorthy, Structure and membrane orientation of IAPP in its natively amidated form at physiological pH in a membrane environment, Biochimica et Biophysica Acta (BBA) - Biomembranes, 1808 (2011) 2337-2342.
[93] J.R. Cort, Z. Liu, G.M. Lee, K.N. Huggins, S. Janes, K. Prickett, N.H. Andersen, Solution state structures of human pancreatic amylin and pramlintide, Protein engineering, design & selection : PEDS, 22 (2009) 497-513.
[94] R.P. Nanga, J.R. Brender, J. Xu, K. Hartman, V. Subramanian, A. Ramamoorthy, Three-dimensional structure and orientation of rat islet amyloid polypeptide protein in a membrane environment by solution NMR spectroscopy, J Am Chem Soc, 131 (2009) 8252-8261.
[95] J.R. Brender, K. Hartman, K.R. Reid, R.T. Kennedy, A. Ramamoorthy, A single mutation in the nonamyloidogenic region of islet amyloid polypeptide greatly reduces toxicity, Biochemistry, 47 (2008) 12680-12688.
[96] K.N. Fish, Total internal reflection fluorescence (TIRF) microscopy, Curr Protoc Cytom, Chapter 12 (2009) Unit12 18.
[97] H. Schneckenburger, Total internal reflection fluorescence microscopy: technical innovations and novel applications, Curr Opin Biotechnol, 16 (2005) 13-18.
[98] H. LeVine, 3rd, Thioflavine T interaction with synthetic Alzheimer's disease beta-amyloid peptides: detection of amyloid aggregation in solution, Protein Sci, 2 (1993) 404-410.
[99] S.R. Collins, A. Douglass, R.D. Vale, J.S. Weissman, PLoS Biol., 2 (2004) e321.
[100] Y. Inoue, A. Kishimoto, J. Hirao, M. Yoshida, H. Taguchi, J. Biol. Chem., 276 (2001) 35227.
[101] Y. Liang, D.G. Lynn, K.M. Berland, J. Am. Chem. Soc., 132 (2010) 6306.
[102] G.R.B. Qin Qiao, and Xuhui Huang, Dynamics of an Intrinsically Disordered Protein Reveal Metastable Conformations That Potentially Seed Aggregation, Journal of the American Chemical Society, 135 (2013) 16092.

[103] J.D. Green, C. Goldsbury, J. Kistler, G.J. Cooper, U. Aebi, Human amylin oligomer growth and fibril elongation define two distinct phases in amyloid formation, J Biol Chem, 279 (2004) 12206-12212.
[104] J.W. Wu, L. Breydo, J.M. Isas, J. Lee, Y.G. Kuznetsov, R. Langen, C. Glabe, J. Biol. Chem., 285 (2010) 6071.
[105] C.M. Dobson, Protein folding and misfolding, Nature, 426 (2003) 884-890.
[106] C. Goldsbury, J. Kistler, U. Aebi, T. Arvinte, G.J. Cooper, Watching amyloid fibrils grow by time-lapse atomic force microscopy, J Mol Biol, 285 (1999) 33-39.
[107] J.D. Harper, P.T. Lansbury, Jr., Models of amyloid seeding in Alzheimer's disease and scrapie: mechanistic truths and physiological consequences of the time-dependent solubility of amyloid proteins, Annual review of biochemistry, 66 (1997) 385-407.
[108] J.A. Cohlberg, J. Li, V.N. Uversky, A.L. Fink, Heparin and other glycosaminoglycans stimulate the formation of amyloid fibrils from alpha-synuclein in vitro, Biochemistry, 41 (2002) 1502-1511.
[109] M.J. Volles, P.T. Lansbury, J. Mol. Biol., 366 (2007) 1510.
[110] F.A. Ferrone, M. Ivanova, R. Jasuja, Heterogeneous nucleation and crowding in sickle hemoglobin: an analytic approach, Biophys J, 82 (2002) 399-406.
[111] H. Yagi, Y. Abe, N. Takayanagi, Y. Goto, Elongation of amyloid fibrils through lateral binding of monomers revealed by total internal reflection fluorescence microscopy, Biochim Biophys Acta, 1844 (2014) 1881-1888.
[112] P. Hortschansky, V. Schroeckh, T. Christopeit, G. Zandomeneghi, M. Fandrich, The aggregation kinetics of Alzheimer's beta-amyloid peptide is controlled by stochastic nucleation, Protein Sci, 14 (2005) 1753-1759.
[113] T.P. Knowles, C.A. Waudby, G.L. Devlin, S.I. Cohen, A. Aguzzi, M. Vendruscolo, E.M. Terentjev, M.E. Welland, C.M. Dobson, An analytical solution to the kinetics of breakable filament assembly, Science, 326 (2009) 1533-1537.
[114] W.F. Xue, S.W. Homans, S.E. Radford, Systematic analysis of nucleation-dependent polymerization reveals new insights into the mechanism of amyloid self-assembly, Proc Natl Acad Sci U S A, 105 (2008) 8926-8931.
[115] V. Fodera, S. Cataldo, F. Librizzi, B. Pignataro, P. Spiccia, M. Leone, Self-organization pathways and spatial heterogeneity in insulin amyloid fibril formation, The journal of physical chemistry. B, 113 (2009) 10830-10837.
[116] S. Jha, J.M. Snell, S.R. Sheftic, S.M. Patil, S.B. Daniels, F.W. Kolling, A.T. Alexandrescu, pH dependence of amylin fibrillization, Biochemistry, 53 (2014) 300-310.
[117] S.M. Patil, S. Xu, S.R. Sheftic, A.T. Alexandrescu, Dynamic alpha-helix structure of micelle-bound human amylin, J Biol Chem, 284 (2009) 11982-11991.
[118] S.M. Patil, A. Mehta, S. Jha, A.T. Alexandrescu, Heterogeneous amylin fibril growth mechanisms imaged by total internal reflection fluorescence microscopy, Biochemistry, 50 (2011) 2808-2819.
[119] L. Haataja, T. Gurlo, C.J. Huang, P.C. Butler, Islet amyloid in type 2 diabetes, and the toxic oligomer hypothesis, Endocr Rev, 29 (2008) 303-316.
[120] H. Gubler, U. Schopfer, E. Jacoby, Theoretical and experimental relationships between percent inhibition and IC50 data observed in high-throughput screening, Journal of biomolecular screening, 18 (2013) 1-13.

[121] P.J. Marek, V. Patsalo, D.F. Green, D.P. Raleigh, Ionic strength effects on amyloid formation by amylin are a complicated interplay among Debye screening, ion selectivity, and Hofmeister effects, Biochemistry, 51 (2012) 8478-8490.
[122] J.A. Hebda, I. Saraogi, M. Magzoub, A.D. Hamilton, A.D. Miranker, A peptidomimetic approach to targeting pre-amyloidogenic states in type II diabetes, Chem Biol, 16 (2009) 943-950.
[123] A. Hassanpour, C.A. De Carufel, S. Bourgault, P. Forgione, Synthesis of 2,5-diaryl-substituted thiophenes as helical mimetics: towards the modulation of islet amyloid polypeptide (IAPP) amyloid fibril formation and cytotoxicity, Chemistry, 20 (2014) 2522-2528.
[124] L. Khemtemourian, E. Domenech, J.P. Doux, M.C. Koorengevel, J.A. Killian, Low pH acts as inhibitor of membrane damage induced by human islet amyloid polypeptide, J Am Chem Soc, 133 (2011) 15598-15604.
[125] Y. Li, W. Xu, Y. Mu, J.Z. Zhang, Acidic pH retards the fibrillization of human islet amyloid polypeptide due to electrostatic repulsion of histidines, J Chem Phys, 139 (2013) 055102.
[126] R. Mishra, B. Bulic, D. Sellin, S. Jha, H. Waldmann, R. Winter, Small-molecule inhibitors of islet amyloid polypeptide fibril formation, Angewandte Chemie, 47 (2008) 4679-4682.
[127] I. Saraogi, J.A. Hebda, J. Becerril, L.A. Estroff, A.D. Miranker, A.D. Hamilton, Synthetic alpha-helix mimetics as agonists and antagonists of islet amyloid polypeptide aggregation, Angewandte Chemie, 49 (2010) 736-739.
[128] M.H. Viet, C.Y. Chen, C.K. Hu, Y.R. Chen, M.S. Li, Discovery of dihydrochalcone as potential lead for Alzheimer's disease: in silico and in vitro study, PloS one, 8 (2013) e79151.
[129] B. Matharu, G. Gibson, R. Parsons, T.N. Huckerby, S.A. Moore, L.J. Cooper, R. Millichamp, D. Allsop, B. Austen, Galantamine inhibits beta-amyloid aggregation and cytotoxicity, Journal of the neurological sciences, 280 (2009) 49-58.
[130] A.F. McKoy, J. Chen, T. Schupbach, M.H. Hecht, A novel inhibitor of amyloid beta (Abeta) peptide aggregation: from high throughput screening to efficacy in an animal model of Alzheimer disease, J Biol Chem, 287 (2012) 38992-39000.
[131] A. Quist, I. Doudevski, H. Lin, R. Azimova, D. Ng, B. Frangione, B. Kagan, J. Ghiso, R. Lal, Amyloid ion channels: a common structural link for protein-misfolding disease, Proc Natl Acad Sci U S A, 102 (2005) 10427-10432.
[132] S. Zraika, R.L. Hull, C.B. Verchere, A. Clark, K.J. Potter, P.E. Fraser, D.P. Raleigh, S.E. Kahn, Toxic oligomers and islet beta cell death: guilty by association or convicted by circumstantial evidence?, Diabetologia, 53 (2010) 1046-1056.
[133] M.F. Engel, L. Khemtemourian, C.C. Kleijer, H.J. Meeldijk, J. Jacobs, A.J. Verkleij, B. de Kruijff, J.A. Killian, J.W. Hoppener, Membrane damage by human islet amyloid polypeptide through fibril growth at the membrane, Proc Natl Acad Sci U S A, 105 (2008) 6033-6038.
[134] S.H. Shim, R. Gupta, Y.L. Ling, D.B. Strasfeld, D.P. Raleigh, M.T. Zanni, Two-dimensional IR spectroscopy and isotope labeling defines the pathway of amyloid formation with residue-specific resolution, Proc Natl Acad Sci U S A, 106 (2009) 6614-6619.
[135] S. Bedrood, Y. Li, J.M. Isas, B.G. Hegde, U. Baxa, I.S. Haworth, R. Langen, Fibril structure of human islet amyloid polypeptide, J Biol Chem, 287 (2012) 5235-5241.

[136] C. Soto, E.M. Sigurdsson, L. Morelli, R.A. Kumar, E.M. Castano, B. Frangione, Beta-sheet breaker peptides inhibit fibrillogenesis in a rat brain model of amyloidosis: implications for Alzheimer's therapy, Nature medicine, 4 (1998) 822-826.
[137] J.M. Mason, N. Kokkoni, K. Stott, A.J. Doig, Design strategies for anti-amyloid agents, Current opinion in structural biology, 13 (2003) 526-532.
[138] C. Miller, G.H. Zerze, J. Mittal, Molecular simulations indicate marked differences in the structure of amylin mutants, correlated with known aggregation propensity, The journal of physical chemistry. B, 117 (2013) 16066-16075.
[139] M. Duan, J. Fan, S. Huo, Conformations of islet amyloid polypeptide monomers in a membrane environment: implications for fibril formation, PloS one, 7 (2012) e47150.
[140] J.J. Wiltzius, S.A. Sievers, M.R. Sawaya, D. Eisenberg, Atomic structures of IAPP (amylin) fusions suggest a mechanism for fibrillation and the role of insulin in the process, Protein Sci, 18 (2009) 1521-1530.
[141] H. Jang, F. Teran Arce, S. Ramachandran, R. Capone, R. Lal, R. Nussinov, Structural convergence among diverse, toxic beta-sheet ion channels, The journal of physical chemistry. B, 114 (2010) 9445-9451.
[142] R. Soong, J.R. Brender, P.M. Macdonald, A. Ramamoorthy, Association of highly compact type II diabetes related islet amyloid polypeptide intermediate species at physiological temperature revealed by diffusion NMR spectroscopy, J Am Chem Soc, 131 (2009) 7079-7085.
[143] G. Calloni, C. Lendel, S. Campioni, S. Giannini, A. Gliozzi, A. Relini, M. Vendruscolo, C.M. Dobson, X. Salvatella, F. Chiti, Structure and dynamics of a partially folded protein are decoupled from its mechanism of aggregation, J Am Chem Soc, 130 (2008) 13040-13050.
[144] L. Jean, C.F. Lee, C. Lee, M. Shaw, D.J. Vaux, Competing discrete interfacial effects are critical for amyloidogenesis, FASEB journal : official publication of the Federation of American Societies for Experimental Biology, 24 (2010) 309-317.
[145] M. Pannuzzo, A. Raudino, D. Milardi, C. La Rosa, M. Karttunen, alpha-helical structures drive early stages of self-assembly of amyloidogenic amyloid polypeptide aggregate formation in membranes, Scientific reports, 3 (2013) 2781.
[146] C.Y. Lin, T. Gurlo, R. Kayed, A.E. Butler, L. Haataja, C.G. Glabe, P.C. Butler, Toxic human islet amyloid polypeptide (h-IAPP) oligomers are intracellular, and vaccination to induce anti-toxic oligomer antibodies does not prevent h-IAPP-induced beta-cell apoptosis in h-IAPP transgenic mice, Diabetes, 56 (2007) 1324-1332.
[147] T. Gurlo, S. Ryazantsev, C.J. Huang, M.W. Yeh, H.A. Reber, O.J. Hines, T.D. O'Brien, C.G. Glabe, P.C. Butler, Evidence for proteotoxicity in beta cells in type 2 diabetes: toxic islet amyloid polypeptide oligomers form intracellularly in the secretory pathway, Am J Pathol, 176 (2010) 861-869.
[148] D. Kajihara, R. Abe, I. Iijima, C. Komiyama, M. Sisido, T. Hohsaka, FRET analysis of protein conformational change through position-specific incorporation of fluorescent amino acids, Nature methods, 3 (2006) 923-929.
[149] E.T. Jaikaran, M.R. Nilsson, A. Clark, Pancreatic beta-cell granule peptides form heteromolecular complexes which inhibit islet amyloid polypeptide fibril formation, Biochem J, 377 (2004) 709-716.
[150] J.D. Knight, J.A. Williamson, A.D. Miranker, Protein Sci., 17 (2008) 1850.

[151] J.R. Brender, K. Hartman, R.P. Nanga, N. Popovych, R. de la Salud Bea, S. Vivekanandan, E.N. Marsh, A. Ramamoorthy, Role of zinc in human islet amyloid polypeptide aggregation, J Am Chem Soc, 132 (2010) 8973-8983.
[152] A. Abedini, S.M. Tracz, J.H. Cho, D.P. Raleigh, Characterization of the heparin binding site in the N-terminus of human pro-islet amyloid polypeptide: implications for amyloid formation, Biochemistry, 45 (2006) 9228-9237.
[153] G.M. Castillo, W. Lukito, T.N. Wight, A.D. Snow, The sulfate moieties of glycosaminoglycans are critical for the enhancement of beta-amyloid protein fibril formation, Journal of neurochemistry, 72 (1999) 1681-1687.
[154] D.J. Watson, A.D. Lander, D.J. Selkoe, Heparin-binding properties of the amyloidogenic peptides Abeta and amylin. Dependence on aggregation state and inhibition by Congo red, J Biol Chem, 272 (1997) 31617-31624.
[155] I.D. Young, L. Ailles, S. Narindrasorasak, R. Tan, R. Kisilevsky, Localization of the basement membrane heparan sulfate proteoglycan in islet amyloid deposits in type II diabetes mellitus, Archives of pathology & laboratory medicine, 116 (1992) 951-954.
[156] R.H. Garrett, and Grisham, C. M. , Biochemistry, 2nd Ed.,, (1999) pp. 234-237.
[157] J.B. Ancsin, *Amyloid*, 10 (2003) 67-79.
[158] G.M. Castillo, J.A. Cummings, W. Yang, M.E. Judge, M.J. Sheardown, K. Rimvall, J.B. Hansen, A.D. Snow, Sulfate content and specific glycosaminoglycan backbone of perlecan are critical for perlecan's enhancement of islet amyloid polypeptide (amylin) fibril formation, Diabetes, 47 (1998) 612-620.
[159] S. Potter-Perigo, R.L. Hull, C. Tsoi, K.R. Braun, S. Andrikopoulos, J. Teague, C. Bruce Verchere, S.E. Kahn, T.N. Wight, Proteoglycans synthesized and secreted by pancreatic islet beta-cells bind amylin, Arch Biochem Biophys, 413 (2003) 182-190.
[160] K. Park, C.B. Verchere, Identification of a heparin binding domain in the N-terminal cleavage site of pro-islet amyloid polypeptide. Implications for islet amyloid formation, J Biol Chem, 276 (2001) 16611-16616.
[161] R. Kisilevsky, Review: amyloidogenesis-unquestioned answers and unanswered questions, Journal of structural biology, 130 (2000) 99-108.
[162] J.A. Williamson, J.P. Loria, A.D. Miranker, Helix stabilization precedes aqueous and bilayer-catalyzed fiber formation in islet amyloid polypeptide, J Mol Biol, 393 (2009) 383-396.
[163] E.A. Jares-Erijman, T.M. Jovin, FRET imaging, Nature biotechnology, 21 (2003) 1387-1395.
[164] J. Miyazaki, K. Araki, E. Yamato, H. Ikegami, T. Asano, Y. Shibasaki, Y. Oka, K. Yamamura, Endocrinology, 127 (1990) 126.
[165] B. Goger, Y. Halden, A. Rek, R. Mosl, D. Pye, J. Gallagher, A.J. Kungl, Different affinities of glycosaminoglycan oligosaccharides for monomeric and dimeric interleukin-8: a model for chemokine regulation at inflammatory sites, Biochemistry, 41 (2002) 1640-1646.
[166] S.M. Patil, A. Mehta, S. Jha, A.T. Alexandrescu, Heterogeneous Amylin Fibril Growth Mechanisms Imaged by Total Internal Reflection Fluorescence Microscopy, Biochemistry, 50 (2011) 2808-2819.
[167] H. Uchiyama, K. Nagasawa, Preparation of biologically active fluorescent heparin composed of fluorescein-labeled species and its behavior to antithrombin III, Journal of biochemistry, 89 (1981) 185-192.

[168] J.J. Valle-Delgado, M. Alfonso-Prieto, N.S. de Groot, S. Ventura, J. Samitier, C. Rovira, X. Fernandez-Busquets, Modulation of Abeta42 fibrillogenesis by glycosaminoglycan structure, FASEB journal : official publication of the Federation of American Societies for Experimental Biology, 24 (2010) 4250-4261.
[169] B. Konarkowska, J.F. Aitken, J. Kistler, S. Zhang, G.J. Cooper, The aggregation potential of human amylin determines its cytotoxicity towards islet beta-cells, FEBS J, 273 (2006) 3614-3624.
[170] M.K. Sandberg, H. Al-Doujaily, B. Sharps, A.R. Clarke, J. Collinge, Prion propagation and toxicity in vivo occur in two distinct mechanistic phases, Nature, 470 (2011) 540-542.
[171] K. Potter, K. Park, Heparin induces amyloid formation in cultured human isletss, 2007, (2007).
[172] B. Mulloy, M.J. Forster, C. Jones, D.B. Davies, N.m.r. and molecular-modelling studies of the solution conformation of heparin, Biochem J, 293 (Pt 3) (1993) 849-858.
[173] Z. Zhang, S.A. McCallum, J. Xie, L. Nieto, F. Corzana, J. Jiménez-Barbero, M. Chen, J. Liu, R.J. Linhardt, Solution Structures of Chemoenzymatically Synthesized Heparin and Its Precursors, Journal of the American Chemical Society, 130 (2008) 12998-13007.
[174] S. Khan, J. Gor, B. Mulloy, S.J. Perkins, Semi-Rigid Solution Structures of Heparin by Constrained X-ray Scattering Modelling: New Insight into Heparin–Protein Complexes, Journal of Molecular Biology, 395 (2010) 504-521.
[175] S.R. Sheftic, R.L. Croke, J.R. LaRochelle, A.T. Alexandrescu, Electrostatic contributions to the stabilities of native proteins and amyloid complexes, Methods in enzymology, 466 (2009) 233-258.
[176] R. Raman, G. Venkataraman, S. Ernst, V. Sasisekharan, R. Sasisekharan, Structural specificity of heparin binding in the fibroblast growth factor family of proteins, Proceedings of the National Academy of Sciences, 100 (2003) 2357-2362.
[177] L. Bergamaschini, C. Donarini, E. Rossi, A. De Luigi, C. Vergani, M.G. De Simoni, Heparin attenuates cytotoxic and inflammatory activity of Alzheimer amyloid-beta in vitro, Neurobiology of aging, 23 (2002) 531-536.
[178] L. Bergamaschini, E. Rossi, C. Storini, S. Pizzimenti, M. Distaso, C. Perego, A. De Luigi, C. Vergani, M.G. De Simoni, Peripheral treatment with enoxaparin, a low molecular weight heparin, reduces plaques and beta-amyloid accumulation in a mouse model of Alzheimer's disease, J Neurosci, 24 (2004) 4181-4186.
[179] E. Sandwall, P. O'Callaghan, X. Zhang, U. Lindahl, L. Lannfelt, J.P. Li, Heparan sulfate mediates amyloid-beta internalization and cytotoxicity, Glycobiology, 20 (2010) 533-541.
[180] R. Bravo, M. Arimon, J.J. Valle-Delgado, R. Garcia, N. Durany, S. Castel, M. Cruz, S. Ventura, X. Fernandez-Busquets, Sulfated polysaccharides promote the assembly of amyloid beta(1-42) peptide into stable fibrils of reduced cytotoxicity, J Biol Chem, 283 (2008) 32471-32483.
[181] J. Madine, D.A. Middleton, Comparison of aggregation enhancement and inhibition as strategies for reducing the cytotoxicity of the aortic amyloid polypeptide medin, European biophysics journal : EBJ, 39 (2010) 1281-1288.
[182] J.M. George, The synucleins, Genome Biol, 3 (2002) REVIEWS3002.
[183] L. Maroteaux, J.T. Campanelli, R.H. Scheller, Synuclein: a neuron-specific protein localized to the nucleus and presynaptic nerve terminal, J Neurosci, 8 (1988) 2804-2815.

[184] S. Bellani, V.L. Sousa, G. Ronzitti, F. Valtorta, J. Meldolesi, E. Chieregatti, The regulation of synaptic function by alpha-synuclein, Commun Integr Biol, 3 106-109.
[185] S. Chandra, G. Gallardo, R. Fernandez-Chacon, O.M. Schluter, T.C. Sudhof, Alpha-synuclein cooperates with CSPalpha in preventing neurodegeneration, Cell, 123 (2005) 383-396.
[186] S.J. Wood, J. Wypych, S. Steavenson, J.C. Louis, M. Citron, A.L. Biere, alpha-synuclein fibrillogenesis is nucleation-dependent. Implications for the pathogenesis of Parkinson's disease, J Biol Chem, 274 (1999) 19509-19512.
[187] M.R. Cookson, The biochemistry of Parkinson's disease, Annual review of biochemistry, 74 (2005) 29-52.
[188] M.G. Spillantini, M.L. Schmidt, V.M. Lee, J.Q. Trojanowski, R. Jakes, M. Goedert, Alpha-synuclein in Lewy bodies, Nature, 388 (1997) 839-840.
[189] J. Xu, S.Y. Kao, F.J. Lee, W. Song, L.W. Jin, B.A. Yankner, Dopamine-dependent neurotoxicity of alpha-synuclein: a mechanism for selective neurodegeneration in Parkinson disease, Nature medicine, 8 (2002) 600-606.
[190] A. Takeda, M. Mallory, M. Sundsmo, W. Honer, L. Hansen, E. Masliah, Abnormal accumulation of NACP/alpha-synuclein in neurodegenerative disorders, Am J Pathol, 152 (1998) 367-372.
[191] H. Tomiyama, I. Mizuta, Y. Li, M. Funayama, H. Yoshino, L. Li, M. Murata, M. Yamamoto, S. Kubo, Y. Mizuno, T. Toda, N. Hattori, LRRK2 P755L variant in sporadic Parkinson's disease, J Hum Genet, 53 (2008) 1012-1015.
[192] M. Goedert, Alpha-synuclein and neurodegenerative diseases, Nat Rev Neurosci, 2 (2001) 492-501.
[193] D.J. Moore, A.B. West, V.L. Dawson, T.M. Dawson, Molecular pathophysiology of Parkinson's disease, Annu Rev Neurosci, 28 (2005) 57-87.
[194] J.C. Kessler, J.C. Rochet, P.T. Lansbury, Jr., The N-terminal repeat domain of alpha-synuclein inhibits beta-sheet and amyloid fibril formation, Biochemistry, 42 (2003) 672-678.
[195] R.J. Perrin, W.S. Woods, D.F. Clayton, J.M. George, Interaction of human alpha-Synuclein and Parkinson's disease variants with phospholipids. Structural analysis using site-directed mutagenesis, J Biol Chem, 275 (2000) 34393-34398.
[196] M. Bisaglia, I. Tessari, L. Pinato, M. Bellanda, S. Giraudo, M. Fasano, E. Bergantino, L. Bubacco, S. Mammi, A topological model of the interaction between alpha-synuclein and sodium dodecyl sulfate micelles, Biochemistry, 44 (2005) 329-339.
[197] T.S. Ulmer, A. Bax, N.B. Cole, R.L. Nussbaum, Structure and dynamics of micelle-bound human alpha-synuclein, J Biol Chem, 280 (2005) 9595-9603.
[198] M. Bisaglia, A. Trolio, M. Bellanda, E. Bergantino, L. Bubacco, S. Mammi, Structure and topology of the non-amyloid-beta component fragment of human alpha-synuclein bound to micelles: implications for the aggregation process, Protein Sci, 15 (2006) 1408-1416.
[199] A.M. Bodles, D.J. Guthrie, P. Harriott, P. Campbell, G.B. Irvine, Toxicity of non-abeta component of Alzheimer's disease amyloid, and N-terminal fragments thereof, correlates to formation of beta-sheet structure and fibrils, European journal of biochemistry / FEBS, 267 (2000) 2186-2194.
[200] C.R. Bodner, A.S. Maltsev, C.M. Dobson, A. Bax, Differential phospholipid binding of alpha-synuclein variants implicated in Parkinson's disease revealed by solution NMR spectroscopy, Biochemistry, 49 (2010) 862-871.

[201] M.K. Cho, G. Nodet, H.Y. Kim, M.R. Jensen, P. Bernado, C.O. Fernandez, S. Becker, M. Blackledge, M. Zweckstetter, Structural characterization of alpha-synuclein in an aggregation prone state, Protein Sci, 18 (2009) 1840-1846.
[202] S. McClendon, C.C. Rospigliosi, D. Eliezer, Charge neutralization and collapse of the C-terminal tail of alpha-synuclein at low pH, Protein Sci, 18 (2009) 1531-1540.
[203] K.P. Wu, D.S. Weinstock, C. Narayanan, R.M. Levy, J. Baum, Structural reorganization of alpha-synuclein at low pH observed by NMR and REMD simulations, J Mol Biol, 391 (2009) 784-796.
[204] K. Ueda, H. Fukushima, E. Masliah, Y. Xia, A. Iwai, M. Yoshimoto, D.A. Otero, J. Kondo, Y. Ihara, T. Saitoh, Molecular cloning of cDNA encoding an unrecognized component of amyloid in Alzheimer disease, Proc Natl Acad Sci U S A, 90 (1993) 11282-11286.
[205] R.L. Croke, C.O. Sallum, E. Watson, E.D. Watt, A.T. Alexandrescu, Hydrogen exchange of monomeric alpha-synuclein shows unfolded structure persists at physiological temperature and is independent of molecular crowding in Escherichia coli, Protein Sci, 17 (2008) 1434-1445.
[206] C.C. Jao, B.G. Hegde, J. Chen, I.S. Haworth, R. Langen, Structure of membrane-bound alpha-synuclein from site-directed spin labeling and computational refinement, Proc Natl Acad Sci U S A, 105 (2008) 19666-19671.
[207] J.N. Rao, C.C. Jao, B.G. Hegde, R. Langen, T.S. Ulmer, A combinatorial NMR and EPR approach for evaluating the structural ensemble of partially folded proteins, J Am Chem Soc, 132 8657-8668.
[208] A.J. Trexler, E. Rhoades, Alpha-synuclein binds large unilamellar vesicles as an extended helix, Biochemistry, 48 (2009) 2304-2306.
[209] S. Marqusee, R.L. Baldwin, Helix stabilization by Glu-...Lys+ salt bridges in short peptides of de novo design, Proc Natl Acad Sci U S A, 84 (1987) 8898-8902.
[210] R.M. Rasia, C.W. Bertoncini, D. Marsh, W. Hoyer, D. Cherny, M. Zweckstetter, C. Griesinger, T.M. Jovin, C.O. Fernandez, Structural characterization of copper(II) binding to alpha-synuclein: Insights into the bioinorganic chemistry of Parkinson's disease, Proc Natl Acad Sci U S A, 102 (2005) 4294-4299.
[211] A.T. Alexandrescu, P.A. Evans, M. Pitkeathly, J. Baum, C.M. Dobson, Structure and dynamics of the acid-denatured molten globule state of alpha-lactalbumin: a two-dimensional NMR study, Biochemistry, 32 (1993) 1707-1718.
[212] W.M. Matousek, B. Ciani, C.A. Fitch, B. Garcia-Moreno, R.A. Kammerer, A.T. Alexandrescu, Electrostatic contributions to the stability of the GCN4 leucine zipper structure, J Mol Biol, 374 (2007) 206-219.
[213] Y.J. Tan, M. Oliveberg, B. Davis, A.R. Fersht, Perturbed pKA-values in the denatured states of proteins, J Mol Biol, 254 (1995) 980-992.
[214] M. Tollinger, K.A. Crowhurst, L.E. Kay, J.D. Forman-Kay, Site-specific contributions to the pH dependence of protein stability, Proc Natl Acad Sci U S A, 100 (2003) 4545-4550.
[215] S.T. Whitten, E.B. Garcia-Moreno, pH dependence of stability of staphylococcal nuclease: evidence of substantial electrostatic interactions in the denatured state, Biochemistry, 39 (2000) 14292-14304.
[216] C.A. Castaneda, C.A. Fitch, A. Majumdar, V. Khangulov, J.L. Schlessman, B.E. Garcia-Moreno, Molecular determinants of the pKa values of Asp and Glu residues in staphylococcal nuclease, Proteins, 77 (2009) 570-588.

[217] A.H. Elcock, Realistic modeling of the denatured states of proteins allows accurate calculations of the pH dependence of protein stability, J Mol Biol, 294 (1999) 1051-1062.
[218] K.A. Conway, S.J. Lee, J.C. Rochet, T.T. Ding, R.E. Williamson, P.T. Lansbury, Jr., Acceleration of oligomerization, not fibrillization, is a shared property of both alpha-synuclein mutations linked to early-onset Parkinson's disease: implications for pathogenesis and therapy, Proc Natl Acad Sci U S A, 97 (2000) 571-576.
[219] B.C. McNulty, A. Tripathy, G.B. Young, L.M. Charlton, J. Orans, G.J. Pielak, Temperature-induced reversible conformational change in the first 100 residues of alpha-synuclein, Protein Sci, 15 (2006) 602-608.
[220] R. Jakes, M.G. Spillantini, M. Goedert, Identification of two distinct synucleins from human brain, FEBS letters, 345 (1994) 27-32.
[221] P.H. Weinreb, W. Zhen, A.W. Poon, K.A. Conway, P.T. Lansbury, Jr., NACP, a protein implicated in Alzheimer's disease and learning, is natively unfolded, Biochemistry, 35 (1996) 13709-13715.
[222] D.S. Wishart, C.G. Bigam, J. Yao, F. Abildgaard, H.J. Dyson, E. Oldfield, J.L. Markley, B.D. Sykes, 1H, 13C and 15N chemical shift referencing in biomolecular NMR, Journal of biomolecular NMR, 6 (1995) 135-140.
[223] J.N. Rao, Y.E. Kim, L.S. Park, T.S. Ulmer, Effect of pseudorepeat rearrangement on alpha-synuclein misfolding, vesicle binding, and micelle binding, J Mol Biol, 390 (2009) 516-529.
[224] S.A. Dames, R.A. Kammerer, D. Moskau, J. Engel, A.T. Alexandrescu, Contributions of the ionization states of acidic residues to the stability of the coiled coil domain of matrilin-1, FEBS letters, 446 (1999) 75-80.
[225] J. Markley, Observation of Histidine Residues in Proteins by Means of Nuclear Magnetic Resonance Spectroscopy, Acc. Chem. Res., 8 (1975) 70-80.
[226] S. Grzesiek, J. Anglister, A. Bax, Correlation of backbone amide and aliphatic side-chain resonances in 13C/15N-enriched proteins by isotropic mixing of 13C magnetization, Journal of magnetic resonance, B101 (1993) 114-119.
[227] M. Pujato, A. Navarro, R. Versace, R. Mancusso, R. Ghose, M.L. Tasayco, The pH-dependence of amide chemical shift of Asp/Glu reflects its pKa in intrinsically disordered proteins with only local interactions, Biochim Biophys Acta, 1764 (2006) 1227-1233.
[228] Y. Nozaki, C. Tanford, Examination of titration behavior., Methods Enzymol., 11 (1967) 715-734.
[229] J. Song, M. Laskowski, Jr., M.A. Qasim, J.L. Markley, NMR determination of pKa values for Asp, Glu, His, and Lys mutants at each variable contiguous enzyme-inhibitor contact position of the turkey ovomucoid third domain, Biochemistry, 42 (2003) 2847-2856.
[230] R.L. Thurlkill, G.R. Grimsley, J.M. Scholtz, C.N. Pace, pK values of the ionizable groups of proteins, Protein Sci, 15 (2006) 1214-1218.
[231] J.L. Markley, Observation of histidine residues in proteins by means of nuclear magnetic resonance spectroscopy, Accounts of Chemical Research, 8 (1975) 70-80.
[232] G. Kaslik, W.M. Westler, L. Graf, J.L. Markley, Properties of the His57-Asp102 dyad of rat trypsin D189S in the zymogen, activated enzyme, and alpha1-proteinase inhibitor complexed forms, Arch Biochem Biophys, 362 (1999) 254-264.

[233] B. Kuhlman, D.L. Luisi, P. Young, D.P. Raleigh, pKa values and the pH dependent stability of the N-terminal domain of L9 as probes of electrostatic interactions in the denatured state. Differentiation between local and nonlocal interactions, Biochemistry, 38 (1999) 4896-4903.
[234] C.O. Fernandez, W. Hoyer, M. Zweckstetter, E.A. Jares-Erijman, V. Subramaniam, C. Griesinger, T.M. Jovin, NMR of alpha-synuclein-polyamine complexes elucidates the mechanism and kinetics of induced aggregation, EMBO J, 23 (2004) 2039-2046.
[235] R.A. Kammerer, T. Schulthess, R. Landwehr, A. Lustig, J. Engel, U. Aebi, M.O. Steinmetz, An autonomous folding unit mediates the assembly of two-stranded coiled coils, Proc Natl Acad Sci U S A, 95 (1998) 13419-13424.
[236] M.O. Steinmetz, I. Jelesarov, W.M. Matousek, S. Honnappa, W. Jahnke, J.H. Missimer, S. Frank, A.T. Alexandrescu, R.A. Kammerer, Molecular basis of coiled-coil formation, Proc Natl Acad Sci U S A, 104 (2007) 7062-7067.
[237] H.J. Lee, C. Choi, S.J. Lee, Membrane-bound alpha-synuclein has a high aggregation propensity and the ability to seed the aggregation of the cytosolic form, J Biol Chem, 277 (2002) 671-678.
[238] D. Eliezer, Amyloid ion channels: a porous argument or a thin excuse?, J Gen Physiol, 128 (2006) 631-633.
[239] K. Ma, E.L. Cancy, Y. Zhang, D.G. Ray, K. Wollenberg, M.G. Zagorski, Residue-Specific pKa Measurements of the Abeta-Peptide and Mechanism of pH-Induced Amyloid Formation, J. Am. Chem. Soc., 120 (1999) 8698-8706.